CHARACTERIZATION OF THE SURFACE PLASMON MODES IN PLANAR METAL-INSULATOR-METAL WAVEGUIDES BY AN ATTENUATED TOTAL REFLECTION APPROACH

A Thesis
Presented to
The Academic Faculty

by

Chien-I Lin

In Partial Fulfillment
of the Requirements for the Degree
Doctor of Philosophy in the
School of Electrical and Computer Engineering

Georgia Institute of Technology
December 2011

CHARACTERIZATION OF THE SURFACE PLASMON MODES IN PLANAR METAL-INSULATOR-METAL WAVEGUIDES BY AN ATTENUATED TOTAL REFLECTION APPROACH

Approved by:

Professor Thomas K. Gaylord,
Committee Chair
School of Electrical and Computer Engineering
Georgia Institute of Technology

Professor Ali Adibi
School of Electrical and Computer Engineering
Georgia Institute of Technology

Professor Gee-Kung Chang
School of Electrical and Computer Engineering
Georgia Institute of Technology

Professor William Alan Doolittle
School of Electrical and Computer Engineering
Georgia Institute of Technology

Professor Phillip N. First
School of Physics
Georgia Institute of Technology

Date Approved: August 15, 2011

To my parents,

Chuan-Fu and Yu-Chen

ACKNOWLEDGEMENTS

During my time at Georgia Tech, there has been a great deal of help and support from many people. Without them, I would not have survived, let alone completed this work. There is so much I owe them that there may not be a chance to repay fully, but, at least, I would like to express my gratitude in this more permanent form.

It has been a pleasure and a privilege to have Prof. Thomas K. Gaylord as an advisor. His astute advices and extensive knowledge constantly not only guide me to the correct direction, but also inspire numerous valuable new ideas. His dedication, prudence, and energy toward research are absolutely admirable and are something I will keep in mind and try very hard to incorporate in my future career.

I would also like to thank the other members of my Ph.D. thesis committee, Prof. Ali Adibi, Prof. Gee-Kung Chang, Prof. William Alan Doolittle, and Prof. Phillip First. Their encouragement and constructive comments have greatly helped me make this research more complete in all aspects.

All of the past and present members of the Georgia Tech Optics group, Lieutenant Colonel Matt Burrow, Prof. Yin-Jung Chang, Dr. Donald D. Davis, Michael Hutsel (soon to be Dr.), Micah Jenkins, Prof. Gregory Kilby, Joe Kummer, Matthieu Leibovici, Jonathan Maikisch, and Dr. Justin Stay, have highly enriched my research life here. In addition to all their great help academically, every Friday lunch meetings and all the cheerful events, from various parties held by Prof. Gaylord, Mike's wedding, to the π-mile racing, were good relaxations for the sometimes stressful research life.

Friends that I have made in Atlanta these years are also invaluable to me. They have not only helped me with numerous living things, but also allowed me to enjoy the life outside the lab. All the gatherings, parties, or even simply dinners/lunches

together, are precious moments that I would miss more than the research these years.

Finally, I want to thank my family: my father Chuan-Fu, my mother Yu-Chen, and my sister Wan-Leng; without their encouragement and support, it is unlikely for me to complete my Ph.D. study. There are no words for me to fully express what their love and support mean to me throughout this journey. They provide a haven that always opens for me and allow me to concentrate on the front without worrying the back.

Chien-I Lin

Georgia Institute of Technology
September 2011

TABLE OF CONTENTS

ACKNOWLEDGEMENTS iv

LIST OF TABLES x

LIST OF FIGURES xi

LIST OF SYMBOLS AND ABBREVIATIONS xvi

SUMMARY xxi

CHAPTER 1 INTRODUCTION 1

1.1 Background 2

1.2 Research Objectives 6

1.3 Thesis Overview 9

CHAPTER 2 REVIEW OF SURFACE PLASMONS (SPS) 12

2.1 SP at a Metal/Dielectric Interface 12

2.2 SP in a Metal-Dielectric-Metal (MIM) Waveguide Structure 18

2.3 Comparison of MIM Waveguides with Parallel-Plate Waveguides . . 26

2.3.1 Drude Free-Electron Gas Model 26

2.3.2 Parallel-Plate Waveguides in Microwave Regime 27

2.3.3 Transition from Visible to Microwave Regime 30

2.4 Conventional Experimental Characterization Techniques for MIM Structures 34

2.4.1 Near-Field Scanning Optical Microscopy (NSOM) 34

2.4.2 Usage of Multiple Samples with Various Propagation Distances 40

2.5 Summary 43

CHAPTER 3 TRANSVERSE TRANSMISSION/REFLECTION (TTR) METHOD 44

3.1 Transmission Matrix Analysis 44

3.1.1 SP Modes 46
3.2 Theory of the Transverse Transmission/Reflection (TTR) Method . 48
3.3 Attenuated Total Reflection (ATR) Configuration 48
3.4 ATR Configuration for MIM Structures 52
3.5 Summary 56
CHAPTER 4 THEORETICAL PERFORMANCE OF THE TTR METHOD 58
4.1 ARROW Structure 59
4.2 Leaky and Lossy Thin-Film Waveguide Structure 64
4.3 Silver-Oxide-Silver Structure 67
4.4 Silver-Air-Silver Structure 70
4.4.1 Sensitivity Analysis 70
4.5 Summary 75
CHAPTER 5 EXPERIMENTAL VERIFICATION OF THE TTR METHOD 77
5.1 Fabrication of MIM Structures 77
5.1.1 Optical Constants of Silicon Dioxide 77
5.1.2 Optical Constants of Gold 83
5.2 Metricon Prism Coupler and Alignment of the Laser Beam 85
5.3 TTR Measurements for Single-Mode MIM Waveguides 90
5.3.1 Oxide Core Thickness of 200 nm 91
5.3.2 Oxide Core Thickness of 50 nm 96
5.4 Sensitivity Analysis 100
5.4.1 Effects of the Air-Gap Thickness Between the Prism and the Waveguide 100
5.4.2 Effects of the Thickness of the Top Metal Cladding 100
5.5 Summary 106

CHAPTER 6 MULTIMODE MIM WAVEGUIDES 107
6.1 Theoretical Performance of Multimode MIM Waveguides 107
6.2 TTR Measurements for Multimode MIM Waveguides 110
6.2.1 Oxide Core Thickness of 730 nm 111
6.2.2 Oxide Core Thickness of 1460 nm 114
6.3 Summary 119
CHAPTER 7 EFFECTS OF THE LASER BEAM ON THE EXPERIMENTAL RESULTS 120
7.1 Effect of the Angular Distribution of Incident Laser Beam 120
7.2 Effect of the Laser Beam Linewidth 133
7.3 Limitations on the Range of Detectable Loss 134
7.3.1 Lower Limit 134
7.3.2 Upper Limit 135
7.4 Summary 136
CHAPTER 8 CONCLUSIONS 138
8.1 Summary of Results 138
8.1.1 Review of Surface Plasmons 138
8.1.2 Transverse Transmission/Reflection (TTR) Method 139
8.1.3 Theoretical Performance of the TTR Method 140
8.1.4 Experimental Verification of the TTR Method 141
8.1.5 Multimode MIM Waveguides 142
8.1.6 Effects of the Laser Beam on the Experimental Results . . . 142
8.2 Future Work 143
8.2.1 Application of the TTR Method to Ridge or Channel MIM Waveguides 144

8.2.2 Application of the TTR Method to Asymmetric MIM Structures 145

8.2.3 Scattering Loss induced by Surface/Interface Roughness . . 148

8.3 Concluding Remarks 149

8.4 Summary 150

APPENDIX A COMPARISON OF THE EXACT MODE PROFILE WITH THE FIELD PROFILE EXCITED AT RESONANT ANGLE 151

APPENDIX B DETAILED ERROR ANALYSIS 153

APPENDIX C METHOD OF DETERMINING CORRECTED ATTENUATION COEFFICIENTS 157

REFERENCES 158

VITA 175

LIST OF TABLES

1.1 Loss characterization methods for the MIM structure. 7

4.1 TTR simulation results for the structure in Fig. 4.1. 60

4.2 TTR simulation results for the structure in Fig. 4.5. 65

4.3 TTR simulation results for the structure in Fig. 4.8. 69

4.4 TTR simulation results for the structure in Fig. 4.11. 73

5.1 Measured effective mode indices and fitted refractive index and thickness of the PECVD oxide thin film in Fig. 5.3(a). 80

5.2 Measured effective mode indices and fitted refractive index and thickness of the thermal oxide thin film. 83

7.1 TTR simulation results for the structure in Fig. 7.3 at various incidence condition. 132

LIST OF FIGURES

1.1 Operating speeds and critical dimensions of various technologies. . . . 4

2.1 Schematic diagram of a metal/dielectric interface. 12

2.2 Dispersion relation and field profile for the SP mode at a metal/dielectric interface. 17

2.3 Schematic diagram of a metal-insulator-metal (MIM) structure. . . . 18

2.4 Dispersion relations and field profiles for the TM modes in an MIM structure. 22

2.5 Structural dispersion relation for the TM modes in an MIM structure. 24

2.6 Propagation lengths as functions of dielectric core thickness for various modes in an MIM structure. 25

2.7 Material Dispersion for Au from ultra-violet to microwave wavelengths using Drude free-electron-gas model. 28

2.8 Schematic diagram of a parallel-plate waveguide in microwave regime. 29

2.9 Dispersion relation for the modes in a parallel-plate waveguide. 31

2.10 Comparison of TM field profiles in a parallel-plate waveguide and an MIM waveguide at various wavelengths. 33

2.11 Schematic diagram of the experimental configuration for NSOM. . . . 36

2.12 SEM and NSOM images for a metal-groove SP waveguide. 37

2.13 Optical signal intensity as a function of the propagation distance along the metal-groove SP waveguide. 38

2.14 Alternative way of characterizing the MIM structure using near-field scanning. 39

2.15 Light transmission measurements in multiple MIM waveguides with various propagation distances. 41

2.16 Propagation lengths as functions of wavelength in slab MIM waveguides. 42

3.1 Schematic diagram of a multilayer structure. 45

3.2 Schematic diagram of Fig. 3.1 with an added high-index layer. 50

3.3 Schematic diagram of a prism-loaded MIM structure and its dissections. 53

3.4 Angular reflection power spectrum for a prism-air-silver configuration at various air gap thicknesses. 55

4.1 Schematic diagram of an (prism-loaded) ARROW structure. 59

4.2 Angular reflection power spectrum for the structure in Fig. 4.1. . . . 61

4.3 Error analysis of the TTR simulation for the structure in Fig. 4.1 at various air gap thicknesses. 62

4.4 Comparison of the exact mode profiles with the resonant field profiles in the structure in Fig. 4.1. 63

4.5 Schematic diagram of a (prism-loaded) leaky and lossy thin-film waveguide. 64

4.6 Angular reflection power spectrum for the structure in Fig. 4.5. . . . 65

4.7 Comparison of the exact mode profiles with the resonant field profiles in the structure in Fig. 4.5. 66

4.8 Schematic diagram of a prism-loaded MIM structure with silver claddings and a 50 nm SiO_2 core. 67

4.9 Angular reflection power spectrum for the structure in Fig. 4.8 with $d_m = 80$ nm. 69

4.10 Angular reflection power spectrum for the structure in Fig. 4.8 with $d_m = \infty$. 70

4.11 Schematic diagram of a prism-loaded MIM structure with silver claddings and an air core. 71

4.12 Angular reflection power spectrum for the structure in Fig. 4.11 with $d_m = 100$ nm. 73

4.13 Angular reflection power spectrum for the structure in Fig. 4.11 with $d_m = 80$ nm. 74

4.14 Angular reflection power spectrum for the structure in Fig. 4.11 with $d_m = 60$ nm. 74

4.15 Angular reflection power spectrum for the structure in Fig. 4.11 with $d_m = \infty$. 75

5.1 Refractive index of PECVD oxide as a function of the RF power. . . 79

5.2 Refractive index of PECVD oxide as a function of the RF power. . . 79

5.3 Angular TE reflection power spectrum for a PECVD oxide thin-film structure. 81

5.4 Angular TE reflection power spectrum for a thermal oxide thin-film structure. 82

5.5 Measured dielectrics constant of Au as functions of wavelengths. . . . 84

5.6 Schematic diagram of a Metricon Prism Coupler system. 86

5.7 Schematic diagram of the laser beam movements and alignments near a coupling spot. 87

5.8 Experimental angular reflection power spectrum measured at various fluid ($n_g = 1.4459$) gap thicknesses. 89

5.9 Schematic diagram of the ATR configuration applied to the MIM structures. 91

5.10 TTR measurement results for the structure in Fig. 5.9 with $d_i = 200$ nm. 93

5.11 Simulated angular TM reflection power spectrum for the structure in Fig. 5.9 with $d_i = 200$ nm and $d_m = 75$ nm. 95

5.12 Simulated angular TM reflection power spectrum for the structure in Fig. 5.9 with $d_i = 200$ nm and $d_m = 66$ nm. 95

5.13 Comparison of the simulated reflection power spectrum and the measured reflection power spectrum for the structure in Fig. 5.9 with $d_i = 200$ nm at $P_c = 40$ psi. 96

5.14 TTR measurement results for the structure in Fig. 5.9 with $d_i = 50$ nm. 98

5.15 Simulated angular TM reflection power spectrum for the structure in Fig. 5.9 with $d_i = 50$ nm and $d_m = 75$ nm. 99

5.16 Comparison of the simulated reflection power spectrum and the measured reflection power spectrum for the structure in Fig. 5.9 with $d_i = 50$ nm at $P_c = 40$ psi. 99

5.17 Schematic diagram of the ATR configuration applied to the MIM structures with $d_i = 190$ nm and various values of d_m. 101

5.18 TTR measurement results for an MIM structure with $d_i = 190$ nm and $d_i = 85$ nm. 103

5.19 TTR measurement results for an MIM structure with $d_i = 190$ nm and $d_i = 75$ nm. 104

5.20 TTR measurement results for an MIM structure with $d_i = 190$ nm and $d_i = 85$ nm. 105

6.1 Effective mode indices and propagation lengths as functions of dielectric core thickness for various modes in an MIM waveguide. 109

6.2 Schematic diagram of the ATR configuration applied to the MIM structures. 110

6.3 TTR measurement results for the structure in Fig. 6.2 with $d_i = 730$ nm. 113

6.4 TTR measurement results for the structure in Fig. 6.2 with $d_i = 1460$ nm. 117

7.1 Intensity profile of the laser in the Metricon Prism Coupler. 121

7.2 Schematic diagram of the light path in the prism coupler. 124

7.3 Schematic diagram of the prism-loaded MIM (Au-SiO_x-Au) structure used in the simulation. 125

7.4 Effect of the 1 mm×1 mm incident laser beam. 128

7.5 Effect of the 1.5 mm×1.5 mm incident laser beam. 129

7.6 Effect of the 2 mm×2 mm incident laser beam. 130

7.7 Effect of the 3 mm×3 mm incident laser beam. 131

7.8 Simulated broadening effects for various laser beams on Lorentzian functions with various HWHMs. 133

7.9 Simulated dispersion relation of the TM_0 mode in a 200 nm-core MIM (Au-SiO_x-Au) waveguide around $\lambda = 1550$ nm. 134

8.1 Schematic diagram of applying the TTR method to an array of parallel channel MIM waveguides. 145

8.2 Calculated dispersion curves for Ag-Si_3N_4-Ag and Au-Si_3N_4-Ag MIM structures with 50 nm cores. 146

8.3 Schematic diagram of the structure fabricated to demonstrate negative refraction. 147

B.1 Detailed error analysis for applying the TTR method to MIM structures. 155

B.2 Error caused by background variations in the reflection power spectra. 156

C.1 Error correction scheme for background variations in the reflection power spectra. 159

LIST OF SYMBOLS AND ABBREVIATIONS

A	Field Amplitude Coefficient
a	Air (as subscript)
AC	Alternating Current
Ag	Silver
α	Imaginary Propagation Constant/Attenuation Coefficient
α'	Value of α Obtained by the TTR Method
α''	Value of α' after Correction Procedure
APM	Argument Principle Method
ARROW	AntiResonant Reflecting Optical Waveguide
ATR	Attenuated Total Reflection
Au	Gold
B	Magnetic Field
β	Real Propagation Constant
β'	Value of β Obtained by the TTR Method
$\beta_{hf}^{\pm}$	β Value at Upper/Lower Half-Minimum
c	Freespace Light Speed
c	Cover (as subscript)
$C_{\pm\pm}$	Transmission Matrix Element Coefficient
cl	Cladding (as subscript)
CPU	Central Processing Unit
d	Dielectric (as subscript)
d	Thickness
D_a	Distance between Aperture and Observation Plane
DC	Direct Current
Δ	Small Difference/Step Size

δ	Skin Depth
δ	Field Angle
ΔN_θ	Effective Index Resolution
d_{g1}	Small Gap Thickness
d_{g2}	Medium Gap Thickness
d_{g3}	Large Gap Thickness
d'_m	Thickness of Bottom Gold Layer
E	Electric Field
ϵ	Permittivity
ε	Relative Permittivity
ε'_c	Dielectric Constant of an Added High-Index Layer
$\widetilde{\varepsilon}$	Complex Dielectric Cconstant
f	Polarization-Dependent Ratio
f	Film (as subscript)
f	Frequency
FDTD	Finite-Difference Time-Domain
g	Dielectric/Air/Fluid Gap (as subscript)
γ	Complex Propagation Constant
γ	Damping Rate
γ'	Value of γ Obtained by the TTR Method
H	Magnetizing Field
$\hbar$	Reduced Planck Constant
HWHM	Half Width at Half Maximum/Minimum
I	Imaginary Part of a Complex Number(as subscript)
i	Insulator (as subscript)
I_a	Normalized Airy-Disk Profile
IMI	Insulator-Metal-Insulator

j	Integer Layer Index (as subscript)
J_1	First-Order Bessel Function of the First Kind
k	Wavevector Magnitude
k_0	Freespace Wavevector Magnitude
κ	Complex Wavevector Magnitude
κ_c'	Complex Wavevector Magnitude in an Added High-Index Layer
L	Propagation Length
λ	Freespace Wavelength
λ_p	Plasma Wavelength
LRSP	Long-Range Surface Plasmon
m	Metal (as subscript)
m	Integer
m'	Integer
m''	Integer
M'	Transmission Matrix of Structure with an Added High-Index Layer
m^*	Electron Effective Mass
m_{ij}	Transmission Matrix Element
m_{ij}'	Transmission Matrix Element
MIM	Metal-Insulator-Metal
M_p	Number of Poles
μ	Relative Permeability
n	Refractive Index
n	Mode Number (as subscript)
n_c'	Refractive Index of an Added High-Index Layer
n_e	Extraordinary Refractive Index
n_o	Ordinary Refractive Index
$\widetilde{n}$	Complex Refractive Index

N	Bulk Electron Charge Density
N_{eff}	Effective Mode Index
N'_{eff}	Value of N_{eff} Obtained by the TTR Method
NI	Negative Refractive Index
NSOM	Near-Field Scanning Optical Microscopy
ω	Radian Frequency
ω_p	Plasma Radian Frequency
p	Prism (as subscript)
P_c	Pressure Applied to Coupling Head
PEC	Perfect Electric Conductor
PECVD	Plasma-Enhanced Chemical Vapor Deposition
ϕ	Phase Coefficient
ϕ	Angle between Waveguide Axis and Prism Axis
ϕ_p	Angle of Prism Base
q	Index of Pole
R	Real Part of a Complex Number(as subscript)
r	Reflection Coefficient
r_a	Radius of Aperture
r'_c	Reflection Coefficient for Structure with an Added High-Index Layer
RF	Radio Frequency
ρ_f	Free Surface Charge
r.m.s.	Root Mean Square
s	Substrate (as subscript)
s	Slowly Varying Function
SEM	Scanning Electron Microscope
Si	Silicon
Si_3N_4	Silicon Nitride

σ	Conductivity
σ	Standard Deviation
σ_0	DC Conductivity
SiO_2	Silicon Dioxide
SP	Surface Plasmon
t	Time
t	Transmission Coefficient
τ	Momentum Scattering Time
TE	Transverse Electric
TEM	Transverse Electromagnetic
θ	Arbitrary Angle
θ	Angle of Incidence from an Added High-Index Layer (e.g. Prism)
θ_a	Angle of Incidence from Air into the Lateral Surface of Prism
θ_p	Angle of Incidence at Prism/Air Gap Interface
TM	Transverse Magnetic
TTR	Transverse Transmission/Reflection
U	Slowly Varying Function
V	Slowly Varying Function
v_g	Group Velocity
v_p	Phase Velocity
x	Position Coordinate
x	Unknown Variable (as subscript)
y	Position Coordinate
z	Position Coordinate

SUMMARY

Surface plasmons (SPs) are of interest for various applications, including optical interconnects and devices, light sources, nanolithography, biosensors, solar cells, and negative-refraction prisms or superlenses. Some of the most important applications are SP-based optical interconnects and devices, which offer the potential of realizing integrated optical nanocircuitry due to the subwavelength confinement and the slow-wave nature of SPs. The fundamental building element of these applications is the plasmonic waveguide. Among the family of various plasmonic waveguides, the metal-insulator-metal (MIM) waveguide has superior lateral confinement because of the relatively shallow field penetration into the metal claddings (about a skin depth – usually tens of nanometers). Such subwavelength confinement cannot be achieved by conventional dielectric optical waveguides. However, the loss in the MIM waveguide is substantial due to the strong absorption of metal in the visible or near-infrared spectrum. Therefore, the design, simulation, and measurement of the loss in the MIM waveguide are critically important in the development of SP-based nanocircuitry.

Owing to the subwavelength sizes of MIM waveguides, the excitation of an MIM plasmonic mode typically requires end-fire coupling with tapered fibers or waveguides. Further, the conventional loss measurements require the usage of a near-field scanning optical microscopy (NSOM) or multiple waveguide samples with various length scales; however, the two aforementioned techniques are both complicated and have issues of sensitivity to uncontrollable environmental factors or variations in coupling strength, respectively. These experimental challenges have been a primary reason for the slow experimental development of the MIM waveguide and device. The research

in this thesis focuses on the development of the transverse transmission/reflection (TTR) method, which is a more reliable, accurate, and straightforward method of characterizing the plasmonic modes in the MIM waveguide.

The theory of the TTR method, which incorporates an attenuated total reflection (ATR) configuration, is developed based on the transmission matrix formulation. A methodology for obtaining the propagation constant and attenuation coefficient of a plasmonic mode in an MIM waveguide is illustrated. Using the Metricon Prism Coupler, the TTR method is experimentally applied to planar, single-mode MIM (Au-SiO_2-Au) waveguides with various core thicknesses at $\lambda = 1550$ nm. The experimental results are in very good agreement with the theoretical results. It is also shown experimentally that the TTR method is robust against difficult-to-quantify parameters such as the metal cladding thickness and the air gap thickness between the prism and the waveguide. As a result, the TTR method can be readily applied by using other similar ATR or prism-coupler configurations, without concern for the sensitivity issues caused by the subtle differences between various configurations.

Moreover, the TTR method is also experimentally applied to planar, multimode MIM waveguides. Multimode MIM waveguides, which have larger core sizes, may be of interest for applications in low-loss interconnects or tapered end-couplers. Thanks to the superior angular selectivity of the ATR configuration, the TTR method is capable of detecting the propagation constant and attenuation coefficient of each mode. To the best of the author's knowledge, this is the first time the propagation constant of each mode in a multimode MIM waveguide has been individually measured. Also, to the best of the author's knowledge, this is the first time the attenuation coefficient of each mode in a multimode MIM waveguide has been individually measured.

The TTR method is proved to be a reliable, accurate, and straightforward approach to characterize plasmonic modes in MIM waveguides. Future research will target the extension of the TTR method to 2D MIM waveguides, asymmetric MIM waveguides, and inclusion of scattering loss. Taking full advantage of the TTR method, the development of plasmonic devices can be potentially accelerated.

CHAPTER 1

INTRODUCTION

During the past few years, surface plasmons (SPs) have been the subject of intensive research [1–6]. SPs are of interest for various applications, including optical interconnects and devices [7–12], light sources [13–16], nanolithography [17, 18], biosensors [19–22], solar cells [23–25], and negative-refraction prisms or superlenses [26–28]. Some of the most important applications are SP-based optical interconnects and devices, which offer the potential of realizing integrated optical nanocircuitry due to the subwavelength confinement and the "slow-wave" nature of SPs [3, 11, 29–31]. The fundamental building element of these applications is the plasmonic waveguide. Among the family of various plasmonic waveguides, the metal-insulator-metal (MIM) waveguide has the best lateral confinement because of the relatively shallow field penetration to the skin depth (usually tens of nanometers) of the metal claddings [1, 30]. Such subwavelength confinement cannot be achieved by conventional dielectric optical waveguides.

In spite of the advantages of the MIM waveguide, they do not come without limitations: the loss in the MIM waveguide is substantial owing to the intrinsic loss of the metal and is further magnified with enhanced transverse modal confinement [1, 30], which is essential in the integration of SP-based nanocircuitry. Therefore, the design, simulation, and measurement of the loss in the MIM waveguide are critically important in the development of SP-based nanocircuitry. However, the modal profile of a typical MIM waveguide is usually below the diffraction limit [30, 32]. As a result, the excitation of an MIM plasmonic mode typically requires end-fire coupling of tapered fibers or waveguides, and the loss measurements require multiple waveguide

samples with various length scales [33–35] or the usage of the near-field scanning optical microscopy (NSOM) [36–38]. With multiple waveguide samples, the variations in the coupling strength and waveguide defects are difficult to determine. On the other hand, the NSOM measurements are very sensitive to uncontrollable environmental factors (e.g. waveguide defects, vibration, temperature, etc.) and tend to produce very noisy signals. These experimental challenges have been a primary reason for the slow experimental development of the MIM waveguide and device.

The objective of the proposed research is to develop an accurate and straightforward method of characterizing the plasmonic modes in the MIM waveguide. It is proposed to accomplish this by developing and applying the transverse transmission/reflection (TTR) method [39–41]. Based on the transmission matrix formulation, the TTR method together with its experimental implementation is potentially a very powerful tool for determining the propagation and attenuation characteristics of MIM plasmonic waveguides. Due to its transverse nature, propagation and loss measurements based on the TTR method eliminate the need for tapered end-couplers in traditional attenuation measurement configurations or the need for NSOM in scattered light measurements. In the present research, it is proposed to develop an experimental configuration that implements the TTR method by utilizing the attenuated total reflection (ATR) [42–44] or prism coupler [45–47] geometrical arrangement. Using this facility, a series of MIM structures will be fabricated in the Nanotechnology Research Center and tested in the Optics Laboratory to demonstrate the viability of the TTR method.

1.1 Background

Over the past five decades, the development of integrated electronic circuits has realized remarkable data processing and transport capabilities and greatly changed our lives. The number of transistors that can be placed on a central processing unit

(CPU) has approximately doubled every two years, and so does the corresponding performance, as described by the Moore's law. However, as the dimension of the state-of-the-art transistors comes down to the order of 50 nm or less, the signal delay and thermal issues associated with electronic interconnections prevent significant increases in processor speed [3]. One of the most promising solutions is integrated optical nanocircuitry, which can potentially carry digital data with a much higher capacity than electronic circuits. However, the sizes of conventional dielectric optical devices are subject to the diffraction limit [32] and are usually on the order of free-space wavelength of light, which is one or two orders of magnitude larger than the sizes of modern electronic devices. This significant size mismatch is a major obstacle in realizing integrated optical nanocircuitry. Devices that can carry optical signals with nanometer-scale features are therefore urgently required to satisfy the rapidly growing demand on computation capability.

The surface plasmon (SP)-based interconnect and device may be the solution to this dilemma. The SP is an electromagnetic wave that propagates at a metal/dielectric interface, where electrons collectively oscillate at optical frequency [31]. The electromagnetic field of the SP wave is existent only near the interface, and the fields in both media decay exponentially away from the interface. The decay length of the SP wave into the metal is approximately equal to the skin depth of the metal, which is usually a few tens of nanometers. Moreover, the momentum of the SP wave is higher than that of a conventional optical wave in the same bulk dielectric medium. This higher momentum corresponds to a smaller phase velocity, which is unique to the SP mode, in contrast to the modes in a conventional dielectric optical waveguide. The group velocity of the SP wave could also be very small as the frequency approaches the resonant frequency given by the Drude free-electron-gas model [48, 49] of metals. This "slow-wave" property is essential in realizing some critical components for optical nanocircuitry, such as optical delay lines [50–52]. Due to the nanometer-scale

confinement and the slow wave nature of SPs [3, 11, 29–31], SP-based interconnects and devices have been considered as promising candidates in realizing optical nano-circuitry. The role of the SP-based technology (also termed as "plasmonics") with the the conventional optical and electronic technology is shown in Fig. 1.1 [3].

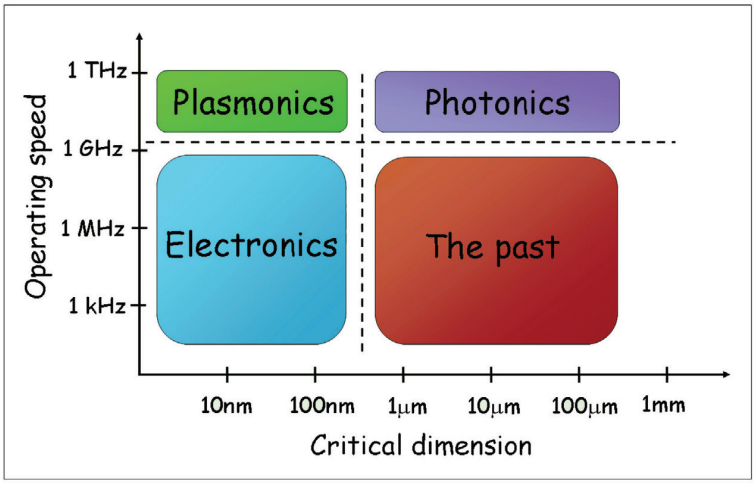

Figure 1.1: Operating speeds and critical dimensions of various technologies [3].

Based on the SP mode at a single metal/dielectric interface, a plasmonic waveguide can be realized by introducing two or more metal/dielectric interfaces into the structure. One example is the insulator-metal-insulator (IMI) structure. This geometry provides the longest propagation length (up to a few millimeters) among the family of plasmonic waveguides due to the smaller percentage of the entire field in the metal core, whose ohmic loss is the source of the waveguide loss. As a result, the IMI structure is usually referred to as the long-range surface plasmon (LRSP) [9, 42–44, 53]. However, the transverse modal size of the IMI structure is in the order of a few wavelengths, which is comparable with that in conventional dielectric optical waveguides. The complementary structure, the metal-insulator-metal (MIM) waveguide, offers the possibility of subwavelength confinement. The transverse modal size in the MIM structure is significantly smaller than that in the IMI structure because of the relatively shallow field penetration to the skin depth of the metal claddings. Such small penetration also makes the MIM structure less sensitive to interface/surface

defects, index mismatch of cladding layers, and crosstalk [30]. However, the loss in the MIM waveguide is substantial owing to the larger portion of the field in the metal claddings. Moreover, the loss is further magnified with enhanced transverse modal confinement [1,3,11,30], which, in turn, is essential in integration of SP-based nanocircuitry. That is, there is a basic trade-off in all plasmonic waveguide geometries between modal size and propagation loss. Therefore, the design, simulation, and measurement of the loss in the MIM waveguide are critically important in the development of SP-based integrated optical nanocircuitry.

Although considerable research achievements have been made on the theoretical developments, including the design and simulation of novel MIM structures and devices [30, 54–58], the experimental characterization of the MIM plasmonic modes is still relatively challenging. The primary obstacle is the subwavelength modal profile and aperture of the MIM structure. Owing to the subwavelength aperture, the excitation of an MIM plasmonic mode typically requires end-fire coupling of tapered fibers or waveguides. Further, the propagation loss can be measured by comparing the output light intensities from samples with various propagation distances [33–35]. However, the coupling strength and waveguide defects may vary from sample to sample and are difficult to quantify. Another measurement technique is based on the near-field scanning optical microscopy (NSOM) [36–38]. By detecting the scattered light in the near-field along the propagation direction of the waveguide, the loss can be calculated by the variations in light intensity. However, NSOM is very sensitive to uncontrollable environmental factors, such as variations in waveguide defects, vibration, and temperature. As a result, NSOM tends to produce very noisy signals [38]. These experimental challenges, especially the complexity and reliability issues, have been a primary reasons for the slow experimental development of the MIM waveguide and device.

The loss measurement techniques mentioned above are all based on variations in

light intensity with various distances of propagation. In contrast, another type experimental configuration based on the attenuated total reflection (ATR) [42–44], which has a similar geometrical arrangement to the prism coupler [45–47], is also used to measure the waveguide loss. The prism coupler was first developed to measure the propagation constants in the conventional dielectric waveguide, and the conceptually similar ATR configuration was applied to measure the loss in the IMI structure. However, to date, to the best of the author's knowledge, no such theories or experiments have been developed and applied to characterize the MIM plasmonic mode. In this proposed research, based on the prism coupler and the ATR configuration, the transverse transmission/reflection (TTR) method [39–41] is presented to circumvent the complicated and unreliable loss measurements mentioned above. A brief comparison between the TTR method and the other loss characterization methods is summarized in Table 1.1. It is shown that only the TTR method can obviate the need for tapered end-couplers, quantitative coupling efficiency, sample-to-sample uniformity, and control over environmental factors. The theoretical development and the proposed experimental implementation of the TTR method are discussed in detail in the following sections.

1.2 Research Objectives

Given the superior lateral confinement and its slow-wave property, the MIM waveguide is a promising fundamental element in realizing a SP-based optical nanocircuitry. However, for plasmonics technology to be successful, a reliable and straightforward experimental characterization technique is required. The conventional characterization techniques for plasmonic modes in MIM waveguides have some severe limitations and issues of reliability. The main objective of this research is to develop a much more reliable and straightforward technique for characterizing plasmonic modes in MIM waveguides.

Table 1.1: Loss characterization methods for the MIM structure.

Loss Characterization Method	Exempt from requirements of				Inexpensive
	Tapered end-couplers	Quantitative coupling efficiency	Sample-to-sample uniformity	Control over environmental factors	
Multiple samples with various propagation distances	Yes/No	No	No	Yes	Yes
NSOM	No	Yes	Yes	No	No
TTR method	Yes	Yes	Yes	Yes	Yes

The main objectives/contributions of this research are given below.

1. The relation between the MIM waveguides and the geometrically identical structure, parallel-plate waveguide used in microwave technology, is discussed in detail.

2. The attenuated total reflection (ATR) configuration, which is also known as a prism coupler, is analyzed by using the transmission matrix formulation. It is shown that the mode condition $m_{22} = 0$ corresponds to a measurable resonance in such a configuration.

3. The transverse transmission/reflection (TTR) method is proposed based on the ATR configuration. It is shown that, by performing an angular reflection measurement on the ATR configuration, the propagation constants and attenuation coefficients of waveguide modes can be obtained by the locations of the resonance minima and the widths of the resonances, respectively.

4. The TTR simulation is applied to various leaky/lossy waveguides and MIM waveguides. All the TTR simulation results agree well with the theoretical results. It is also shown that the TTR simulation is insensitive to difficult-to-quantify parameters such as air gap thicknesses and metal cladding thicknesses.

5. The effect of the laser beam alignment in the Metricon Prism Coupler is illustrated.

6. The TTR method is experimentally applied to single-mode MIM waveguides at $\lambda = 1550$ nm. The experimental results are in good agreement with the theoretical results.

7. The propagation constants and attenuation coefficients are calculated for the TM_0 to TM_3 modes in Au-based MIM waveguides with various core thicknesses at $\lambda = 1550$ nm.

8. The TTR method is experimentally applied to multimode MIM waveguides at $\lambda = 1550$ nm. To the best of the author's knowledge, this is the first time the propagation constant of each mode in a multimode MIM waveguide has been individually measured. Also, to the best of the author's knowledge, this is the first time the attenuation coefficient of each mode in a multimode MIM waveguide has been individually measured.

9. The laser beam profile in the Metricon Prism Coupler is characterized, and the effects on the TTR measurement results are quantified.

10. The range of detectable loss for the TTR method is estimated.

1.3 Thesis Overview

The research objectives discussed in the previous section are rigorously examined in subsequent chapters.

Chapter 2 reviews the concepts of surface plasmon (SP) at a single metal/dielectric interface and in an MIM structure. The dispersion relations, loss characteristics, and mode profiles are calculated. The relation between the MIM structure and the geometrically identical structure, parallel-plate waveguide used in microwave technology, is also illustrated. Moreover, the conventional characterization techniques for plasmonic modes in MIM structures are also reviewed, and the limitations are pointed out.

Chapter 3 provides a systematic analysis of the attenuated total reflection (ATR) configuration, which is also known as the prism coupler, based on the transmission matrix formulation. The theory of the transverse transmission/reflection (TTR) method, which can be used to characterize the propagation constants and attenuation coefficients of waveguide modes based on an ATR configuration, is also introduced. Specifically, the application of the TTR method to an MIM structure is analyzed.

Chapter 4 illustrates the theoretical performance of the TTR method on various waveguide structures, including an AntiResonant Reflecting Optical Waveguide (ARROW), a simultaneously leaky and lossy waveguide, and two MIM waveguides. For the MIM waveguides, the sensitivity analysis is performed using various values of hard-to-quantify paramters, such as the thicknesses of the air gap between the prism and the waveguide and the thicknesses of the metal cladding.

Chapter 5 presents the TTR measurement results for two fabricated single-mode MIM (Au-SiO_x-Au) waveguides at $\lambda = 1550$ nm. The experiments are performed by using Metricon Prism Coupler. The optical properties of the oxide films and gold films are reviewed. The effects of the laser beam alignment in Metricon Prism Coupler are illustrated. The propagation constants and attenuation coefficients of the plasmonic modes in the MIM structures are measured. Moreover, the experiments on the MIM structures are performed at various air gap thicknesses and metal cladding thicknesses, in order to determine the sensitivity of the TTR method on these hard-to-quantify parameters.

Chapter 6 provides an extensive discussion on the multimode MIM waveguide. The dispersion relation and attenuation coefficients of multimode MIM (Au-SiO_x-Au) waveguides at $\lambda = 1550$ nm are calculated. Moreover, the TTR measurement results for two fabricated multimode MIM waveguides are also presented. The propagation constants and attenuation coefficients of various modes in the MIM waveguides are measured individually.

Chapter 7 describes the effects of the angular distribution and linewidth of the laser beam on the results obtained by the TTR method, which utilizes a single-wavelength, plane-wave incidence. The simulation is performed using various incidence conditions and various waveguide modes. The range of detectable loss is also estimated based on the experimental arrangement.

Chapter 8 summarizes the research presented in this thesis. Potential areas of

future research are discussed.

Included within this thesis are three appendices. Appendix A provides the detailed analysis on the comparison of the unperturbed mode profile with the resonant field profile in an ATR configuration.

Appendix B provides a detailed error analysis for applying the TTR method to an MIM waveguide.

Appendix C illustrates the scheme for recovering from the errors discussed in Appendix B. An example case is presented.

CHAPTER 2

REVIEW OF SURFACE PLASMONS (SPS)

2.1 SP at a Metal/Dielectric Interface

Considering a plasmonic transverse magnetic (TM) mode ($E_y = 0, H_x = H_z = 0$) propagating in the $+z$ direction at a metal/dielectric interface as shown in Fig. 2.1, the fields in the dielectric can be expressed as

$$\vec{E}_d(x,z) = (E_{x,d}\hat{x} + E_{z,d}\hat{z})\exp[j(\omega t - k_{z,d}z)]\exp(\kappa_{x,d}x), \tag{2.1}$$

$$\vec{H}_d(x,z) = H_{y,d}\hat{y}\exp[j(\omega t - k_{z,d}z)]\exp(\kappa_{x,d}x), \tag{2.2}$$

and the fields in the metal as

$$\vec{E}_m(x,z) = (E_{x,m}\hat{x} + E_{z,m}\hat{z})\exp[j(\omega t - k_{z,m}z)]\exp(-\kappa_{x,m}x), \tag{2.3}$$

$$\vec{H}_m(x,z) = H_{y,m}\hat{y}\exp[j(\omega t - k_{z,m}z)]\exp(-\kappa_{x,m}x), \tag{2.4}$$

where k_z is the wavevector in the $+z$ direction and $\kappa_x = (k_z^2 - k_0^2\varepsilon)^{1/2}$ is the complex wavevector in the $+x$ direction with $k_0 \equiv 2\pi/\lambda$ being the freespace wavevector magnitude. It should be noted that both the dielectric and the metal are assumed to be lossless, that is, both ε_d and ε_m are real numbers with ε_d being positive and ε_m being

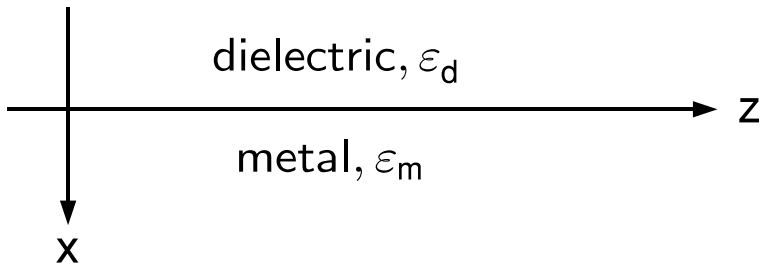

Figure 2.1: Configuration and coordinate system of a metal/dielectric interface for an SP mode. The structure is invariant in the y direction.

negative.

To satisfy the boundary conditions at the metal/dielectric interface, the k_z values must be equal,

$$k_{z,d} = k_{z,m} = \beta, \tag{2.5}$$

and the tangential components of the electric field (E_z) must be continuous across the boundary ($x = 0$),

$$E_{z,d} = E_{z,m}, \tag{2.6}$$

Moreover, for the case that there are no free surface charges (ρ_f), the normal component of the electric displacement ($D_x \equiv \epsilon E_x$) must be continuous across the boundary,

$$\epsilon_d E_{x,d} = \epsilon_m E_{x,m}. \tag{2.7}$$

Further, using the Maxwell's curl of H equation,

$$\nabla \times \vec{H} = \frac{\partial \vec{D}}{\partial t}, \tag{2.8}$$

E_z, E_x, and H_y can be interrelated by

$$j\beta H_y \hat{x} \pm \kappa_x H_y \hat{z} = j\omega\epsilon(E_x \hat{x} + E_z \hat{z}), \tag{2.9}$$

or equivalently

$$H_y = \frac{\omega\epsilon}{\beta} E_x = \pm j \frac{\omega\epsilon}{\kappa_x} E_z, \tag{2.10}$$

where the positive sign is for the dielectric and the negative sign is for the metal. Using Eq. (2.6), (2.7), and (2.10), it can be shown that

$$\frac{\kappa_{x,d}}{\kappa_{x,m}} = -\frac{E_{x,m}}{E_{x,d}} = -\frac{\varepsilon_d}{\varepsilon_m}. \tag{2.11}$$

Solving Eq. (2.11) by using $\kappa_{x,d/m} = (\beta^2 - k_0^2 \varepsilon_{d/m})^{1/2}$ yields the dispersion relation for the SP mode at a single metal/dielectric interface,

$$\beta = k_0 \left(\frac{\varepsilon_d \varepsilon_m}{\varepsilon_d + \varepsilon_m} \right)^{1/2}. \tag{2.12}$$

It should be noted that Eq. (2.12) implies that the SP mode exists only when $\varepsilon_d < -\varepsilon_m$. This inequality is usually referred to as the cutoff condition for the SP mode at a single metal/dielectric interface.

A transverse electric (TE) mode ($H_y = 0, E_x = E_z = 0$) propagating in the $+z$ direction can be analyzed by following a similar procedure to that above and using Maxwell's curl equation of E

$$\nabla \times \vec{E} = -\frac{\partial \vec{B}}{\partial t}. \tag{2.13}$$

The characteristic equation for a TE mode at a single metal/dielectric interface is then given by

$$\frac{\kappa_{x,d}}{\kappa_{x,m}} = -\frac{H_{x,m}}{H_{x,d}} = -\frac{\mu_d}{\mu_m}. \tag{2.14}$$

Therefore, unless μ_d and μ_m are opposite in sign, Eq. (2.14) has no solutions for real $\kappa_{x,d}$ and $\kappa_{x,m}$, which indicates that TE modes cannot exist in a single metal/dielectric interface configuration.

The dispersion relation given by Eq. (2.12) can be further analyzed by considering the frequency dependence of ε_m and ε_d. The dielectric constant of the metal, ε_m, exhibits resonant behavior and is therefore strongly frequency dependent. The dielectric constant of the dielectric, ε_d, has a modest material dispersion frequency dependence. The variation of ε_d will thus be neglected and ε_d treated as a constant. For the metal, the dielectric constant ε_m can be approximated by a lossless Drude free-electron-gas model [48, 49]. From this model, the plasma dispersion law is

$$\varepsilon_m = 1 - \frac{\omega_p^2}{\omega^2}, \tag{2.15}$$

where ω_p is the plasma radian frequency. In a metal this is the natural frequency of the entire electron gas oscillating about the positive ion cores. The resonant frequency, ω_p, is given by

$$\omega_p = \left(\frac{Ne^2}{m^*\epsilon_0}\right)^{1/2}, \tag{2.16}$$

where N is the bulk electron charge density, e is the electronic charge, and m^* is the electron effective mass. Substituting Eq. (2.15) into Eq. (2.12) gives the dispersion relation as

$$\beta = k_0 \left[\frac{\left(1 - \frac{\omega_p^2}{\omega^2}\right) \varepsilon_d}{\left(1 - \frac{\omega_p^2}{\omega^2}\right) + \varepsilon_d} \right]^{1/2}. \tag{2.17}$$

The corresponding dispersion curve is shown in Fig. 2.2(a). The light line for propagation in the bulk dielectric in Fig. 2.2(a) appears as a straight line through the origin with a slope $= 1/\varepsilon_d^{1/2}$. For small values of β, the dispersion curve approaches the light line. However, the $\omega(k)$ curve is always to the right of the light line. At large values of β, the value of ω approaches

$$\omega = \frac{\omega_p}{(1 + \varepsilon_d)^{1/2}}, \tag{2.18}$$

which is the maximum surface plasmon frequency. It is noteworthy that at this frequency, $\varepsilon_d = -\varepsilon_m$, which is the cutoff condition for the SP mode at a single metal/dielectric interface. Since the dispersion curve is to the right of the light line, the plasmon momentum $\hbar k_{\mathrm{SP}}$ is always greater than the photon momentum $\hbar k = \hbar \varepsilon_d^{1/2} \omega / c$. Due to this momentum deficiency, incident light cannot directly couple into the SP mode. There are three main techniques to provide the missing momentum. The first utilizes a high-index layer (e.g. prism) to enhance the momentum of the incident light [59, 60]. The second makes use of a periodic grating structure on the metal surface [31, 61, 62]. The diffraction of light by a metallic grating allows the incident light to be matched in momentum and thus coupled to a SP mode. The third technique involves scattering from topological defects on the surface, such as subwavelength rods or holes, which provide a convenient way to generate SP modes locally [63, 64].

Figures 2.2(b), (c), and (d) show the normalized field profiles (H_y) corresponding to the three labeled points in Fig. 2.2(a). Figure 2.2(b) shows an SP mode that is very close to the light line, therefore the evanescent tail in the dielectric is relatively

long. In Figs. 2.2(c) and (d), the SP modes have relatively smaller phase velocities $v_p = \omega/\beta$ and shorter evanescent tails in the dielectric. It should also be noted that the as $\omega/\omega_p \to 1/(1+\varepsilon_d)^{1/2}$ asymptotically, the group velocity $v_g = d\omega/d\beta \to 0$. This "slow-wave" nature [3, 11, 30, 31] of the SP is one of the crucial properties required in future integrated optical elements, such as optical delay lines [50–52]. However, the dispersion relation and lateral confinement for the SP mode at a single metal/dielectric interface are mainly controlled by the frequency dependence of ε_m of the metal. In order to engineer the SP mode properties, a waveguide structure with two coupled metal/dielectric interfaces should logically be used. This includes two possible waveguide structures, the metal-insulator-metal (MIM) and the insulator-metal-insulator (IMI). However, the decaying tail in the dielectric is usually on the order of several wavelengths, therefore the dielectric-metal-dielectric structure cannot guarantee a subwavelength confinement, which is essential in realizing integrated optical nanocircuitry. In contrast, the confinement in a metal-dielectric-metal structure is determined by the thickness of the dielectric because of the relatively shallow field penetration (approximately a skin depth) into the metal claddings. More details about MIM structures will be introduced in Sec. 2.2.

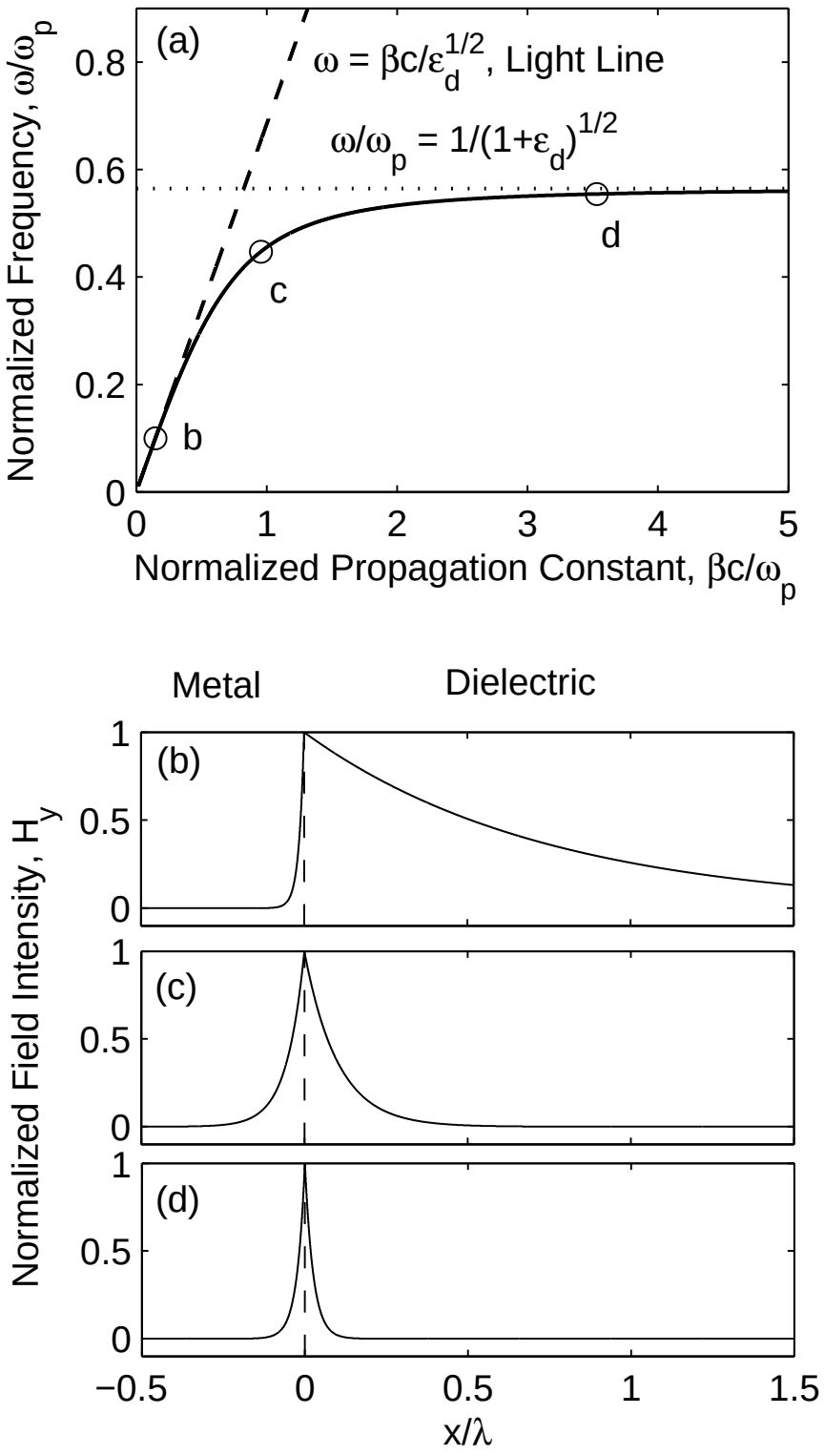

Figure 2.2: (a) Dispersion relation for the SP mode at a metal/dielectric interface. The value of ε_m is given by a Drude free-electron-gas model, while the value of ε_d is treated as a constant = 2.25. The field profiles of the three labeled points, b, c, and d, are shown in (b), (c), and (d), respectively.

2.2 SP in a Metal-Dielectric-Metal (MIM) Waveguide Structure

Considering a TM mode ($E_y = 0, H_x = H_z = 0$) propagating in the $+z$ direction in an MIM structure shown in Fig. 2.3, the magnetic fields in the three regions can be represented by

$$H_y = A_1 \exp(\kappa_m x) \qquad x < 0 \tag{2.19}$$

$$H_y = B_1 \exp(\kappa_d x) + B_2 \exp(-\kappa_d x) \qquad 0 < x < d_d \tag{2.20}$$

$$H_y = A_2 \exp(-\kappa_m x) \qquad x > d_d, \tag{2.21}$$

where $\kappa_m = (\beta^2 - k_0^2 \varepsilon_m)^{1/2}$ and $\kappa_d = (\beta^2 - k_0^2 \varepsilon_d)^{1/2}$ are the complex wavevectors in the $+x$ direction in the metal and insulator, respectively, with β being the propagation constant in $+z$ direction and $k_0 \equiv \lambda/2\pi$ being the freespace wavevector magnitude; the A's and B's are unknown constants to be determined by solving the boundary condition equations. It is assumed that both the insulator and the metal cladding are lossless, that is, both ε_d and ε_m are real with ε_d being positive and ε_m being negative. It should also be noted that the values of κ_d can be either real or imaginary, which correspond to plasmonic modes or oscillatory modes, respectively [30]. By using Maxwell's curl of H equation [Eq. (2.8)], the tangential electric field (E_z) can be

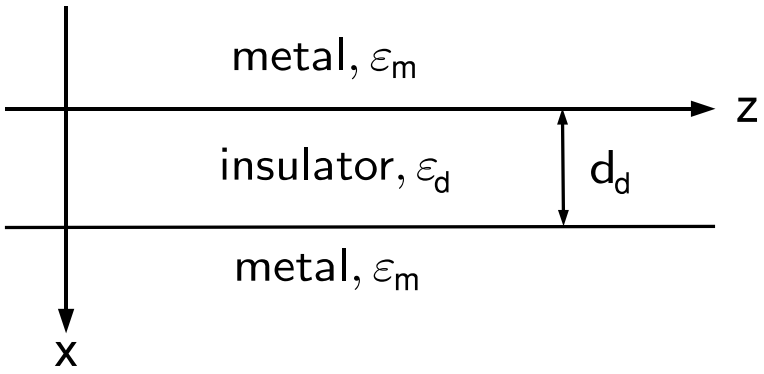

Figure 2.3: Configuration and coordinate system of a metal-insulator-metal (MIM) structure. The structure is invariant in the y direction.

represented as

$$E_z = \frac{1}{j\omega\epsilon}\frac{\partial H_y}{\partial x}. \tag{2.22}$$

The tangential electric fields in each of the three regions of the MIM structure are

$$E_z = \frac{\kappa_m}{j\omega\epsilon_0\varepsilon_m}A_1\exp(\kappa_m x) \qquad x < 0 \tag{2.23}$$

$$E_z = \frac{\kappa_d}{j\omega\epsilon_0\varepsilon_d}[B_1\exp(\kappa_d x) - B_2\exp(-\kappa_d x)] \qquad 0 < x < d_d \tag{2.24}$$

$$E_z = -\frac{\kappa_m}{j\omega\epsilon_0\varepsilon_m}A_2\exp(-\kappa_m x) \qquad x > d_d. \tag{2.25}$$

To satisfy the boundary conditions at $x = 0$ and $x = d_d$, H_y and E_z must be continuous at both interfaces. In brief, there are four equations of boundary conditions and five unknowns (A_1, A_2, B_1, B_2, and β). Therefore, by algebraic manipulation, for real κ_d, the characteristic equation for β is given as

$$\tanh(\kappa_d d_d) = -\frac{2}{\left(\frac{\kappa_m}{\kappa_d}\frac{\varepsilon_d}{\varepsilon_m} + \frac{\kappa_d}{\kappa_m}\frac{\varepsilon_m}{\varepsilon_d}\right)}. \tag{2.26}$$

Recalling the hyperbolic function identity

$$\tanh(\theta) \equiv -\frac{2}{\tanh\frac{\theta}{2} + \coth\frac{\theta}{2}}, \tag{2.27}$$

it is clear that the solutions of Eq. (2.26) have two possibilities. The first possibility is

$$\tanh(\frac{\kappa_d d_d}{2}) = -\frac{\kappa_m}{\kappa_d}\frac{\varepsilon_d}{\varepsilon_m} \tag{2.28}$$

and the second possibility is

$$\tanh(\frac{\kappa_d d_d}{2}) = -\frac{\kappa_d}{\kappa_m}\frac{\varepsilon_m}{\varepsilon_d}. \tag{2.29}$$

The first possibility corresponds to the TM_0 plasmonic mode, which has a symmetric mode profile in H_y and the field components are evanescent (i.e. κ_d is real) in the insulator core. It is a plasmonic mode for all values of β. The second possibility corresponds to the TM_1 plasmonic mode, which has odd symmetry in H_y. It is a

plasmonic mode for sufficiently large values of β, but an oscillatory mode (i.e. κ_d is imaginary and the field components in the insulator core are sinusoidal) for small values of β. There is a smooth transition from an oscillatory mode at low frequencies to an evanescent mode at higher frequencies. The transition occurs at the light line of the insulator. The characteristic equations for the TM oscillatory modes (imaginary κ_d) can be obtained in a similar way as their plasmonic counterparts, yielding

$$\tan(\frac{k_d d_d}{2}) = -\frac{\kappa_m}{k_d}\frac{\varepsilon_d}{\varepsilon_m} \tag{2.30}$$

and

$$\tan(\frac{k_d d_d}{2}) = -\frac{k_d}{\kappa_m}\frac{\varepsilon_m}{\varepsilon_d}, \tag{2.31}$$

where $k_d = (k_0^2\varepsilon_d - \beta^2)^{1/2} = -j\kappa_d$ is the wavevector in $+x$ direction in the insulator. Equation (2.30) corresponds to symmetric oscillatory TM_2, TM_4, TM_6,... modes, while Eq. (2.31) corresponds to antisymmetric oscillatory TM_1, TM_3, TM_5,... modes.

Also, TE modes may exist in an MIM structure as shown in Fig. 2.3. Following a similar approach as for the TM modes, the characteristic equations for the TE modes are given as

$$\tan(\frac{k_d d_d}{2}) = -\frac{\kappa_m}{k_d} \tag{2.32}$$

and

$$\tan(\frac{k_d d_d}{2}) = -\frac{k_d}{\kappa_m}. \tag{2.33}$$

Equation (2.32) corresponds to symmetric oscillatory TE_0, TE_2, TE_4,... modes, while Eq. (2.33) corresponds to antisymmetric oscillatory TE_1, TE_3, TE_5,... modes.

The dispersion relation for the TM and TE modes in an MIM structure can be further analyzed by considering the frequency dependence of ε_m and ε_d [48,65]. The ε_d is a constant and $\varepsilon_m = 1 - \omega_p^2/\omega^2$ (Drude free-electron-gas model), same as the assumption for the SP mode at a single metal/dielectric interface in Sec. 2.1. The calculated dispersion curves for the TM modes in an MIM waveguide structure are presented in Fig. 2.4(a). The plasma wavelength is $\lambda_p = 137$ nm in the lossless

Drude model, and the thickness of the dielectric core is $d_d = 0.2$ μm. The light line $\omega = \beta c/\varepsilon_d^{1/2}$ is shown as the dashed line and the maximum plasmon frequency is $\omega/\omega_p = 1/(1+\varepsilon_d)^{1/2}$, which is shown as the dotted line. The curves to the right of the light line, that is, the TM_0 and high-frequency part of the TM_1, are plasmonic modes, which have evanescent fields in the dielectric core. The low-frequency part of the TM_1 mode and all the higher-order modes are similar to the conventional TM modes in dielectric slab waveguides, which have sinusoidal fields in the core. It is noteworthy that the TM_0 mode has no cutoff frequency. There is a TM_0 mode for any frequency above zero frequency. In contrast, the TM_1 mode has a cutoff frequency below which even an oscillatory TM_1 mode cannot exist. Moreover, the TM_1 mode makes a transition between an oscillatory mode to a plasmonic mode. It is worth mentioning that, for both the TM_0 and TM_1 modes, as $\omega/\omega_p \to 1/(1+\varepsilon_d)^{1/2}$ asymptotically, the group velocity $v_g = d\omega/d\beta \to 0$. Figure 2.4(b) shows the detailed comparison of the TM_0 and TM_1 modes in the MIM structure with the SP mode at a single metal/dielectric interface with the same ε_m and ε_d as those in the MIM structure. It is observed that at a given frequency, β_{TM_0} is always greater than β_{SP} of the single interface SP mode, while β_{TM_1} is always smaller than β_{SP}. Figures 2.4(c)-(h) show the field profiles corresponding to the labeled points in Fig. 2.4(a). Figure 2.4(c) shows a TM_0 mode profile whose two metal/dielectric interfaces are strongly coupled. It implies that β_{TM_0} is close to the light line. Figure 2.4(d) shows an oscillatory TM_1 mode profile, which is located to the left of the light line. Figure 2.4(e) shows a TM_1 mode profile at the transition point from the oscillating to plasmonic mode. It corresponds to a point precisely on the light line. The corresponding field profile in the dielectric core is also at the transition point between sinusoidal and evanescent, that is, it is a straight line. Figures 2.4(f) and (g) show TM_0 and TM_1 mode profiles whose metal/dielectric interfaces are weakly coupled, respectively. The propagation constants of the TM_0 and TM_1 modes are therefore very close to those

of the uncoupled SP modes. Figure 2.4(h) shows a TM_2 mode profile, which has a sinusoidal field in the dielectric core.

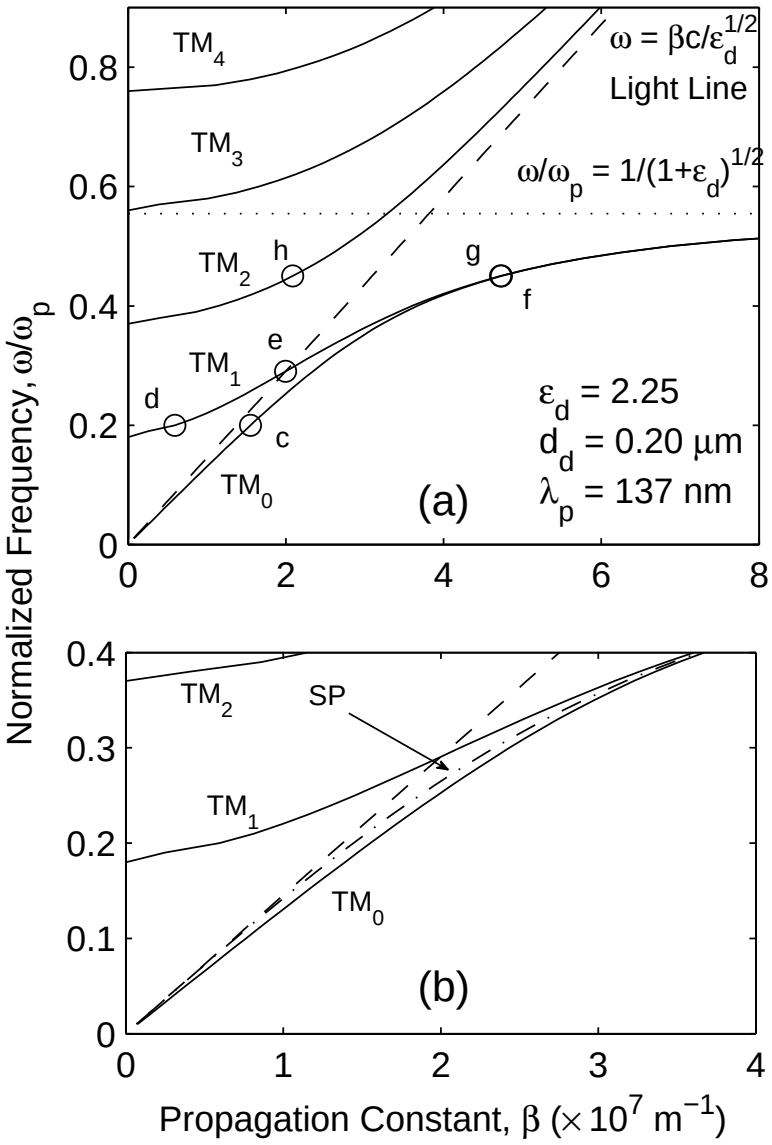

Figure 2.4: (a) Dispersion diagram for the TM modes in an MIM waveguide structure. The value of ε_m is given by the lossless Drude free-electron-gas model with a plasma wavelength $\lambda_p = 137$ nm, while the value of ε_d is treated as a constant= 2.25. The dielectric core thickness is $d_d = 0.2$ μm. The light line corresponds to the light propagation in bulk dielectric. (b) The dispersion curves of the TM_0 and TM_1 compared with the dispersion curve for the SP mode at a single metal/insulator interface (dotted-dash line).

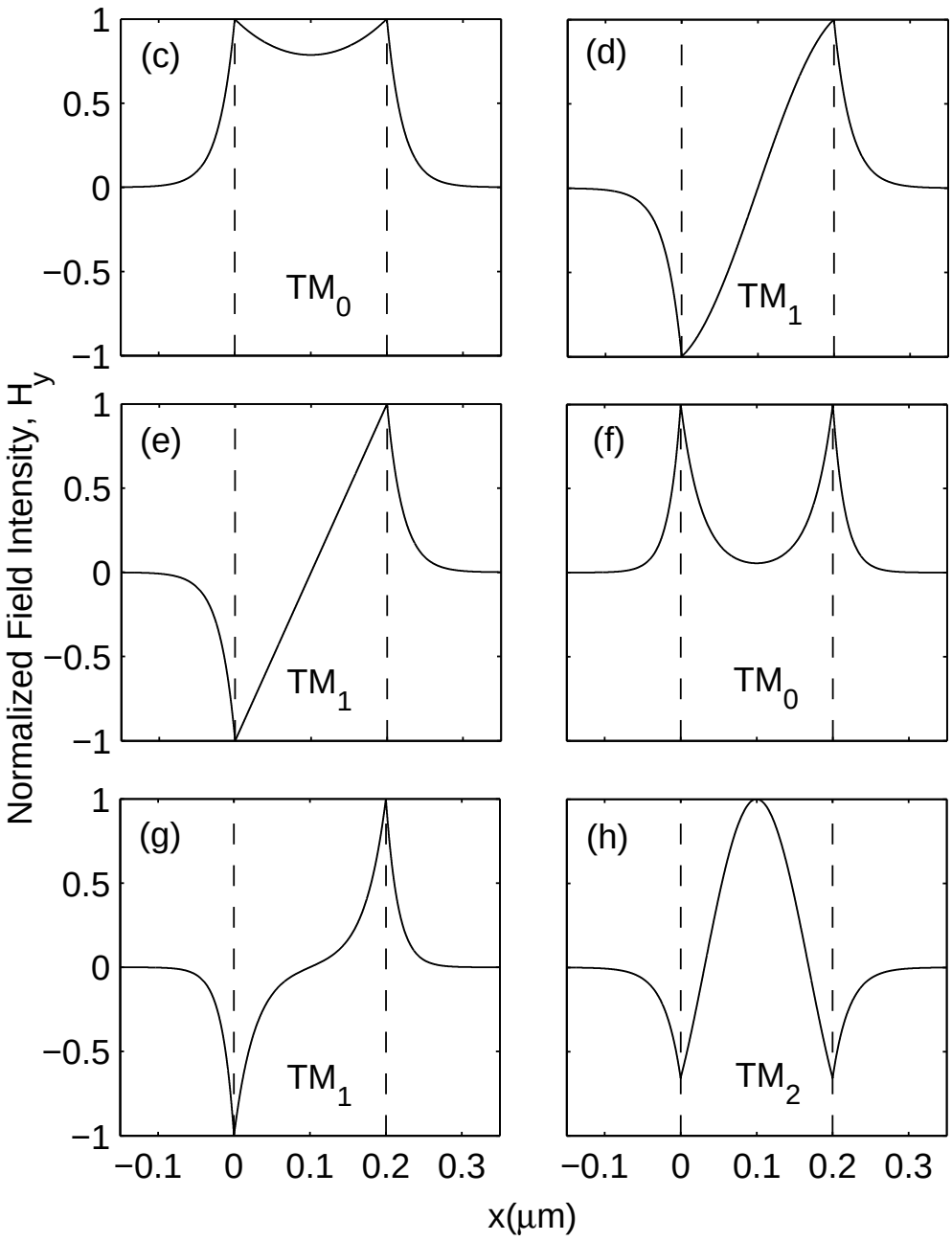

Figure 2.4 (cont.): Field profiles of (c) a plasmonic TM_0 mode at low frequency, (d) an oscillatory TM_1 mode at low frequency, (e) a TM_1 mode at the transition between an oscillatory and a plasmonic mode, (f) a plasmonic TM_0 mode at high frequency, (g) a plasmonic TM_1 mode at high frequency, and (h) an oscillatory TM_2 mode at high frequency.

Figure 2.5 shows the normalized propagation constant β/k_0 as a function of the normalized dielectric core thickness d_d/λ at fixed values of ε_m, ε_d, and ω. In this case, $\varepsilon_m = -5$ and $\varepsilon_d = 2.25$ are used. Similar to Fig. 2.4, the TM_0 mode has no cutoff thickness and the TM_1 mode has a cutoff thickness and makes a transition across the light line from an oscillatory mode to a plasmonic mode as d_d increases. At a large d_d value, both β_{TM_0} and β_{TM_1} approach β_{SP}, due to the weak coupling between the two metal/dielectric interfaces in the MIM structure. The higher-order TM_2, TM_3, TM_4,... modes have larger cutoff thicknesses and can only exist as oscillatory modes.

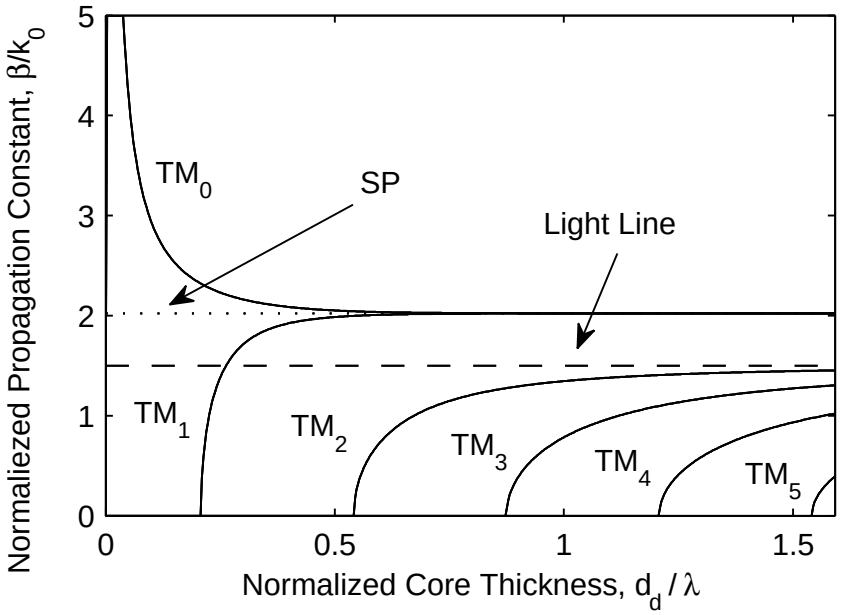

Figure 2.5: Normalized propagation constant β/k_0 as a function of the dielectric core thickness d_d in an MIM structure. The dielectric constants of the metal and the dielectric core are $\varepsilon_m = -5$ and $\varepsilon_d = 2.25$, respectively. The SP line is the propagation constant for the SP mode at a single metal/dielectric interface with the same material parameters, or equivalently, for $d_d = \infty$ in an MIM structure.

According to Fig. 2.5, the TM_0 mode in an MIM structure exists for any dielectric core size d_d, which, theoretically, can be infinitesimally small. However, when the material loss of the metal is taken into account, the loss of the plasmonic modes could limit the minimum practical value of d_d. Figure 2.6 shows the propagation lengths L

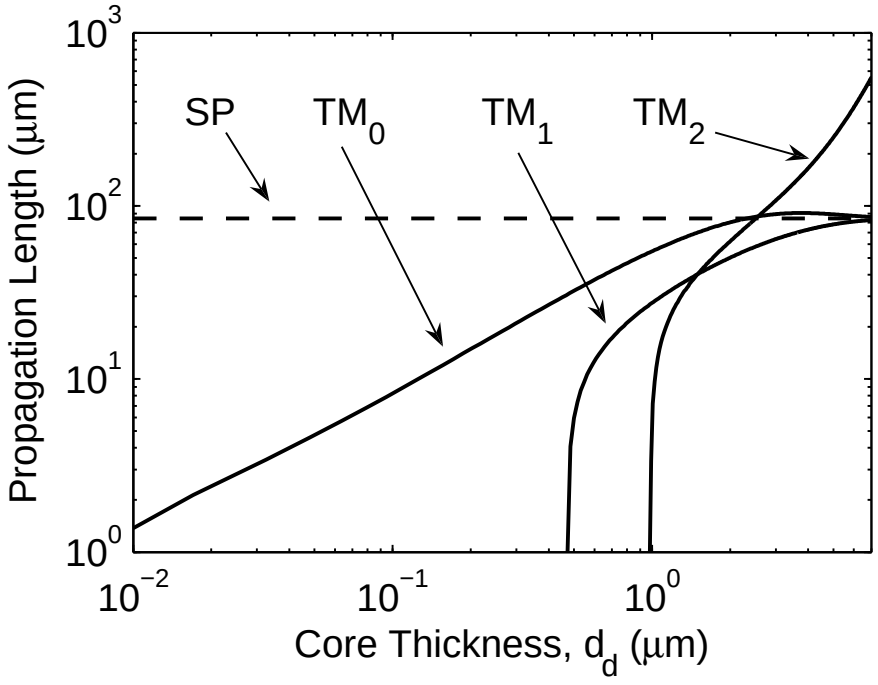

Figure 2.6: Propagation lengths $L \equiv 1/(2|\alpha|)$ for the TM_0, TM_1, and TM_2 modes as functions of the dielectric core thickness d_d in an MIM structure. It is assumed in this case that the metal is Au at $\lambda = 1550$ nm, with a dielectric constant $\widetilde{\varepsilon}_{\text{Au}} = -115 - j11.3$ [66]. The dielectric constant of the dielectric core is $\varepsilon_d = 2.25$. The curves for the MIM TM_x modes and the single gold/dielectric interface are labeled as TM_x and SP, respectively.

as functions of d_d for various mode in an MIM structure. The propagation length is defined as the $1/e$ decay length for the field intensity, or equivalently, $L \equiv 1/(2|\alpha|)$, where α is the imaginary part of the complex propagation constant γ for the modes in the MIM structure. The dielectric constant of the metal (Au at $\lambda = 1550$ nm) and the dielectric core are $\widetilde{\varepsilon}_m = -115 - j11.3$ [66] and $\varepsilon_d = 2.25$, respectively. At large d_d, the propagation lengths of the TM_0 and TM_1 modes approaches that of the SP mode at a single Au/dielectric interface, which is nearly 100 μm in this case. This is intuitive, since both TM_0 and TM_1 modes are plasmonic, the two interfaces are practically decoupled and each mode propagates as two independent SP modes at the interfaces. The propagation length of the TM_2 mode, on the other hand, does not approach that of the SP mode because the TM_2 mode is oscillatory. The loss in the

TM_2 mode decreases as d_d value increases, which corresponds to smaller portion of the field in the metal claddings. However, for strongly confined, subwavelength values of d_d, especially when $d_d/\lambda < 0.1$, the loss in the MIM structure is substantial and the mode can only propagate for a few microns even for the TM_0 mode. This extremely high loss could severely hinder any practical use of the structure. In brief, there is a trade-off between confinement and loss. Moreover, due to the subwavelength size of the dielectric core, coupling light into an MIM structure is challenging. Therefore, the propagation constant and loss measurement for MIM structures [33, 35, 37, 38] are critically important in the design and testing of MIM-based integrated optical nanocircuitry. The theoretical and experimental characterization of the loss in MIM structures is thus the main issue addressed in this work. More details about the conventional loss measurement techniques for MIM structures are discussed in Sec. 2.4.

2.3 Comparison of MIM Waveguides with Parallel-Plate Waveguides

The MIM structures discussed in Sec. 2.2 have been an area of intensive research, primarily due to their subwavelength confinement and therefore potential to realize integrated optical nanocircuitry. The operating frequency for such application is in the visible light and near-infrared regime. However, one may recall that a similar structure has been studied and well known in microwave technology – the parallel-plate waveguide [67]. The parallel-plate waveguide supports a transverse electromagnetic (TEM) mode and a series of waveguide modes [68]. In this section, the similarities and differences between the MIM waveguides and parallel-plate waveguides will be discussed in detail.

2.3.1 Drude Free-Electron Gas Model

In order to analyze the parallel-plate waveguide, the properties of metal in microwave regime must be known. According to the Drude free-electron-gas model [49, 67], the

dielectric constant of metal can be expressed as

$$\widetilde{\varepsilon}_m(\omega) = 1 + \frac{j\sigma(\omega)}{\epsilon_0 \omega}, \tag{2.34}$$

where $\sigma(\omega)$ is the AC conductivity

$$\sigma(\omega) = \frac{\sigma_0}{1 - j\omega\tau} \tag{2.35}$$

with σ_0 being the DC conductivity and τ being the momentum scattering time. Take Au for example, $\sigma_0 = 4.52 \times 10^7$ (S/m) at 20 °C and $\tau = 2.7 \times 10^{-14}$ sec [49]. Using Eq. (2.34), the dielectric constant and refractive index of Au can then be plotted as functions of ω, as shown in Fig. 2.7(a) and (b), respectively. The subscripts R and I in Fig. 2.7 represent the real and the imaginary parts, respectively. The x-axis scale is logarithm from 10^9 to 10^{15} rad/s and linear from 10^{15} to 10^{16} rad/s. Figures 2.7(a) shows that the absolute value of $\varepsilon_{\rm R}$ is much larger than $\varepsilon_{\rm I}$ for frequencies above mide-infrared. In the entire microwave regime, it can be observed from Fig. 2.7(a) that the the absolute value of $\varepsilon_{\rm R}$ is much smaller than $\varepsilon_{\rm I}$, and both $\varepsilon_{\rm R}$ and $\varepsilon_{\rm I}$ are very large. This observation agrees with Eq. (2.34) and (2.35) at low frequency limit: $\sigma(\omega) \simeq \sigma_0$, which is a large number for a good conductor, and therefore $\widetilde{\varepsilon}_m \simeq j\sigma_0/(\varepsilon_0\omega)$ is also a large number. This property will be applied in Sec. 2.3.2.

2.3.2 Parallel-Plate Waveguides in Microwave Regime

In this section, following the low frequency limit results from Sec. 2.3.1 and using the fact that σ_0 is very large for good conductors (e.g. $\sigma_0 = 6.30 \times 10^7$ S/m for Ag, $\sigma_0 = 5.96 \times 10^7$ S/m for Cu, and $\sigma_0 = 4.52 \times 10^7$ S/m for Au), the dielectric constant of the metal in microwave regime is approximated as $\widetilde{\varepsilon}_m \to j\infty$.

The schematic diagram of a parallel-plate waveguide is shown in Fig. 2.8. It is equivalent to the MIM structure shown in Fig. 2.3 except that the metal claddings have $\widetilde{\varepsilon}_m \to j\infty$. In this work, the parallel-plate waveguide refers to the MIM structure in microwave regime. Using the same analysis as in Sec. 2.2, for TM polarization,

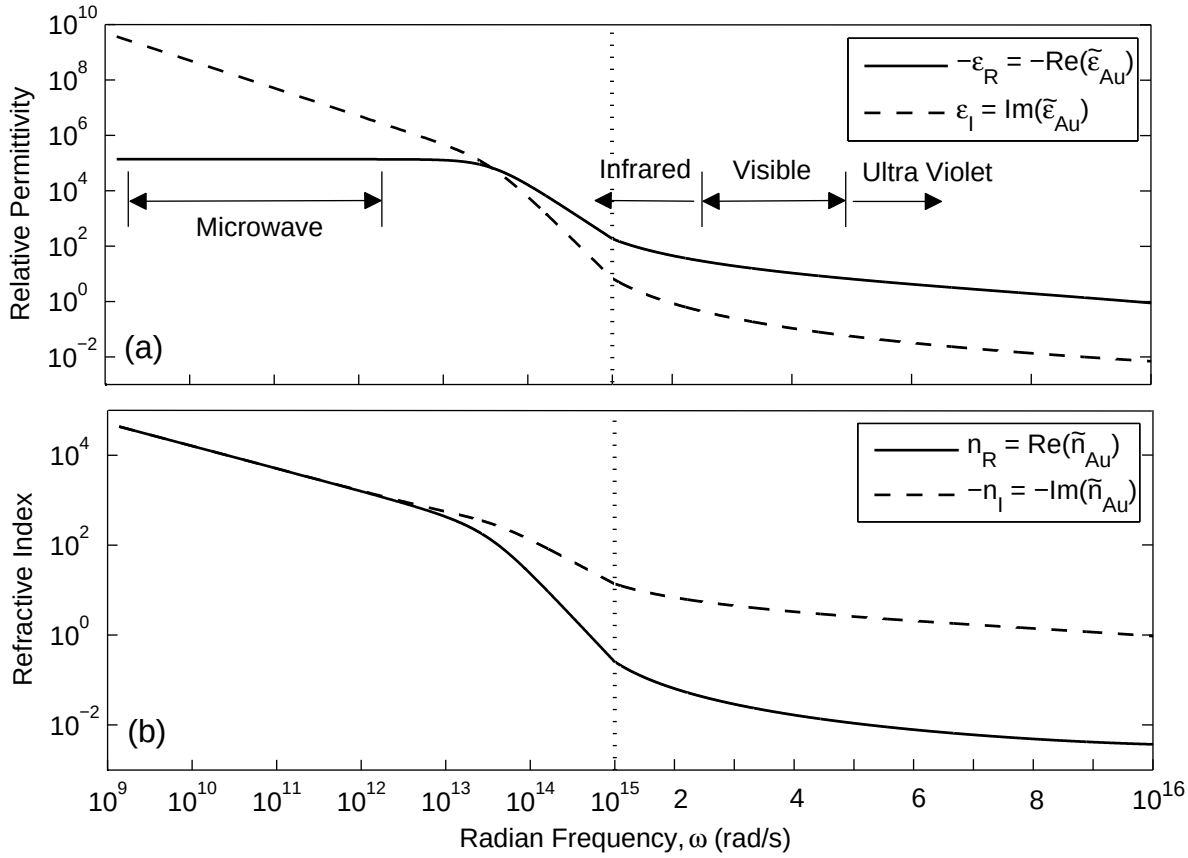

Figure 2.7: Using Drude free-electron-gas model, the theoretical (a) real and imaginary parts of the dielectric constant of Au as functions of radian frequency ω and (b) real and imaginary parts of the refractive index of Au as functions of ω. The subscripts R and I represent the real and the imaginary parts, respectively. The x-axis scale is logarithm from 10^9 to 10^{15} rad/s and linear from 10^{15} to 10^{16} rad/s.

the characteristic equations for the symmetric plasmonic mode, Eq. (2.28), and the antisymmetric plasmonic mode, Eq. (2.29), become

$$\tanh(\frac{\kappa_d d_d}{2}) = 0 \tag{2.36}$$

and

$$\tanh(\frac{\kappa_d d_d}{2}) = \tilde{\infty}, \tag{2.37}$$

respectively. The symbol $\tilde{\infty}$ represents a complex infinity, whose absolute value is ∞ and phase is typically nonzero. Equation (2.36) requires that $\kappa_d = (\beta^2 - k_0^2 \varepsilon_d)^{1/2} = 0$ and therefore $\beta = k_0 \varepsilon_d^{1/2}$. That is, the wave propagates with the same propagation

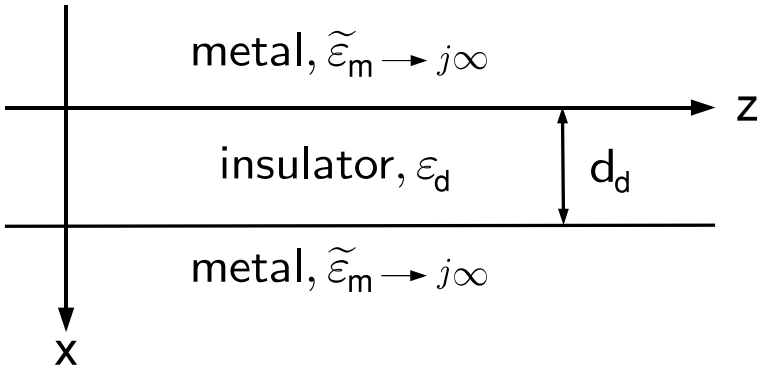

Figure 2.8: Configuration and coordinate system of a parallel-plate waveguide in microwave regime. The structure is invariant in the y direction.

constant as in the bulk insulator. This is the well known TEM mode, with electric field in the x direction and magnetic field in the y direction in the insulator, and the corresponding dispersion relation is the same as the light line. It is noteworthy that the TEM mode has no cutoff frequency. On the other hand, Eq. (2.37) does not have a solution for κ_d. It implies that there is no antisymmetric plasmonic mode in a parallel-plate waveguide.

Similarly, by using $\widetilde{\varepsilon}_m \to j\infty$ for the metal claddings, the characteristic equations for the symmetric oscillatory TM modes, Eq. (2.30), and the antisymmetric oscillatory TM modes, Eq. (2.31), become

$$\tan(\frac{k_d d_d}{2}) = 0 \tag{2.38}$$

and

$$\tan(\frac{k_d d_d}{2}) = \tilde{\infty}, \tag{2.39}$$

respectively. Equation (2.38) requires that

$$k_d = \frac{2m'\pi}{d}, m' = 1, 2, 3, ... \tag{2.40}$$

And Eq. (2.39) requires that

$$k_d = \frac{(2m'' - 1)\pi}{d}, m'' = 1, 2, 3, ... \tag{2.41}$$

Combining Eq. (2.40) and (2.41), the dispersion relation for the oscillatory TM modes in the parallel-plate waveguide is given as

$$k_d = \frac{m\pi}{d}, m = 1, 2, 3, ... \tag{2.42}$$

The TE modes in a parallel-plate waveguide can also be analyzed in the same manner. Following a similar approach as for the TM modes, the characteristic equations for the symmetric oscillatory TE modes, Eq. (2.32), and the antisymmetric oscillatory TE modes, Eq. (2.33), become

$$\tan(\frac{k_d d_d}{2}) = \tilde{\infty} \tag{2.43}$$

and

$$\tan(\frac{k_d d_d}{2}) = 0, \tag{2.44}$$

respectively. The dispersion relation is then given as

$$k_d = \frac{m\pi}{d}, m = 1, 2, 3, ... \tag{2.45}$$

The calculated dispersion curves for the TEM, TE, and TM modes in a parallel-plate waveguide are presented in Fig. 2.9. The dielectric core thickness is $d_d = 2$ mm, and the dielectric constant of the core is treated as a constant, $\varepsilon_d = 1.0$. The curve corresponding to the TEM mode is equivalent to the light line. All the higher-order TM and TE modes lie to the left of the light line and approach the light line as frequency increases. The TEM mode has no cutoff frequency, and the higher-order modes have higher cutoff frequencies.

2.3.3 Transition from Visible to Microwave Regime

The transition from visible to microwave wavelengths can be further clarified by examining the MIM field profiles at various wavelengths. Owing to the drastic change in wavelength, the core thickness is varied proportionally with wavelength, in order to remove the effects of waveguide dispersion. Waveguide dispersion is caused solely by

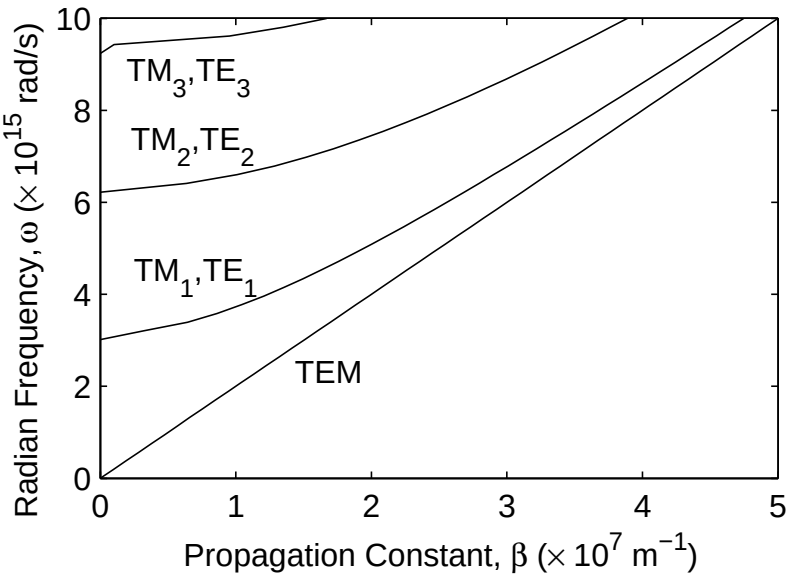

Figure 2.9: Dispersion diagram for the TEM, TE, and TM modes in a parallel-plate waveguide. The thickness of the dielectric core is $d_d = 2$ mm, and the dielectric constant of the core is $\varepsilon_d = 1.0$.

geometric factors, that is, without considering any wavelength-dependent properties of the materials [69].

Figure 2.10 compares the H_y field profiles of the TM_0 and TM_1 modes in Au MIM waveguides at various wavelengths $\lambda = 0.5$ μm, 2 μm, 10 μm, and 100 μm. The core thickness is a function of wavelength, $d_d = \lambda/2$. The dielectric constants of Au are calculated using the parameters and Eq. (2.34) in Sec. 2.3.1. It is observed that the TM_0 field profile in the core becomes flatter, and the field penetration into the metal claddings decreases as the wavelength increases. Similarly, for the TM_1 modes, the field profile in the core becomes more obviously sinusoidal, and the the field penetration into the metal claddings decreases as the wavelength increases. At $\lambda = 100$ μm, the H_y field for the TM_0 mode is nearly constant in the core, which agrees with the TEM mode profile in a perfect electric conductor (PEC) parallel-plate waveguide. Further, the TM_1 mode agrees with the TM_1 mode in a PEC parallel-plate waveguide. That is, at sufficiently long wavelength, an MIM structure approaches a PEC parallel-plate waveguide in all aspects.

In summary, the parallel-plate waveguide is a special case of the MIM waveguide. They both have a fundamental mode (TEM in the parallel-plate waveguide and TM_0 in the MIM waveguide) without a cutoff frequency. This property implies that both the TEM mode and the TM_0 mode may propagate with a subwavelength confinement. However, the TEM mode in the parallel-plate waveguide does not have a slow-wave property: the group velocity, as well as the phase velocity, are always equivalent to the light line of the core. At higher frequency or with a larger core size, both MIM and parallel-plate waveguides have higher-order modes. The primary difference is that the TM_1 mode profile in the parallel-plate waveguide is always sinusoidal, while the TM_1 mode profile is evanescent in the MIM waveguide at sufficiently high frequencies.

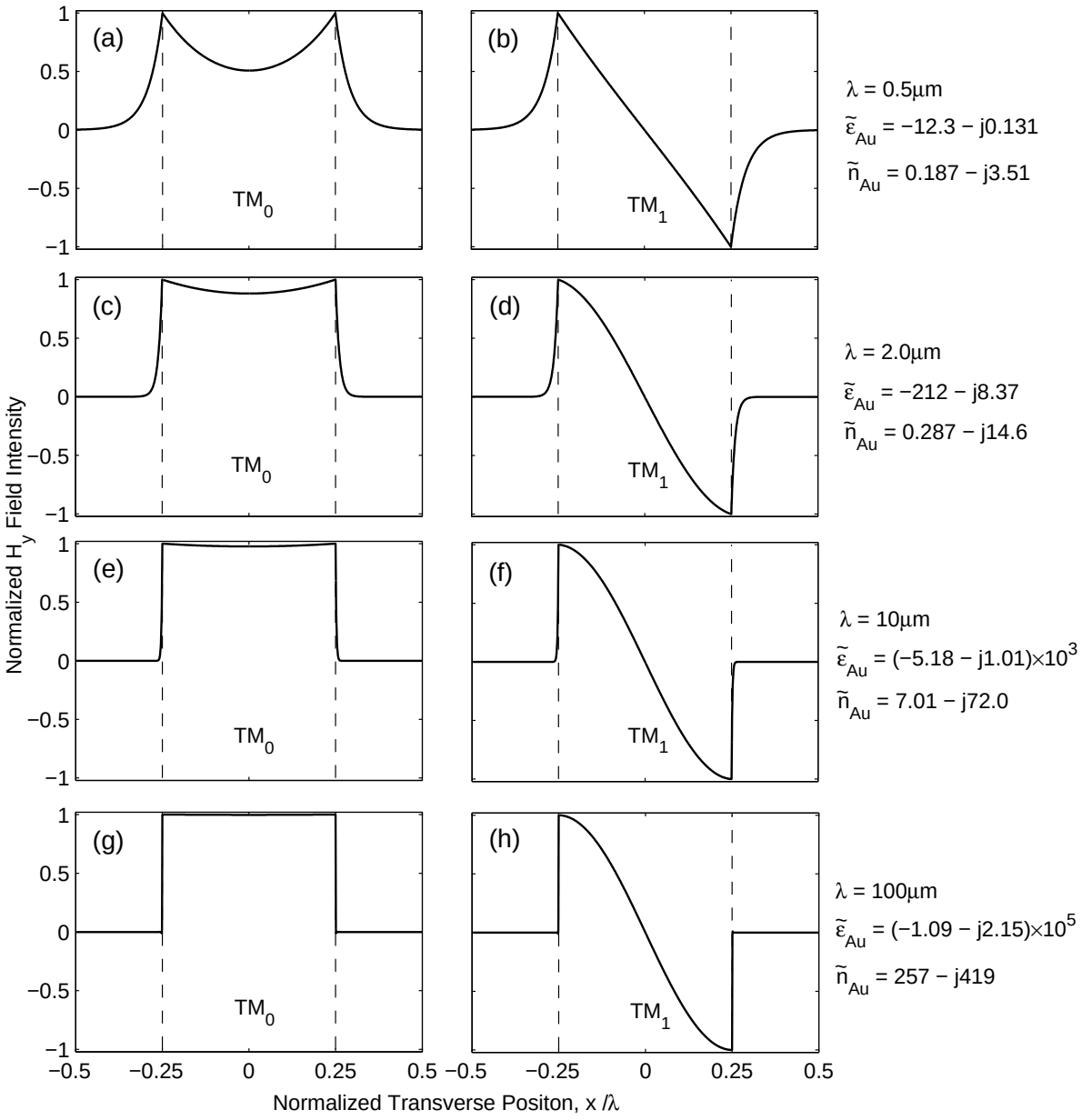

Figure 2.10: Field profiles of (a), (c), (e), (g) the TM_0 modes and (b), (d), (f), (h) the TM_1 modes in MIM waveguides at wavelengths $\lambda = 0.5$ μm, 2 μm, 10 μm, and 100 μm, respectively. The core thicknesses of the MIM waveguides are $d_d = \lambda/2$.

2.4 Conventional Experimental Characterization Techniques for MIM Structures

As mentioned in previous sections, the experimental characterizations of the MIM plasmonic modes is challenging due to the subwavelength modal profile and aperture of the MIM structure. Owing to the subwavelength aperture, the excitation of an MIM plasmonic mode typically requires end-fire coupling of tapered fibers or waveguides. Further, the propagation loss can be measured by detecting the variation of light intensity as a function of propagation distance, and the propagation constant may be obtained from the periodicity of the far-field modal pattern from the end of the waveguide [33]. In this section, the two major types of conventional MIM characterization techniques are reviewed, and their pros and cons are discussed.

2.4.1 Near-Field Scanning Optical Microscopy (NSOM)

Optical microscopy provides a convenient and economical way to observe micron-scale features in research and development. However, conventional optical microscopy is limited by optical diffraction, and the resolution is $\sim \lambda/2$ [70]. In the visible light regime, this corresponds to a resolution of ~ 200 nm. Therefore, as scientific interest shifts to subwavelength optical devices, such as surface plasmon (SP)-based devices, the resolving power of conventional optical microscopy becomes insufficient.

Fortunately, near-field optics provides a possible way to go beyond the diffraction limit [71, 72]. By putting a light source or detector with subwavelength dimension in close proximity (typically $< \lambda/50$) to a sample, images with resolution better than the diffraction limit can be achieved [73, 74]. The conventional use of a stethoscope has applied this concept for many years [36, 74]. In 1972, Ash and co-workers applied near-field scanning for imaging purpose using 3 cm-wavelength microwave [75]. They achieved a resolution of $\lambda/60$. Nowadays, the near-field scanning optical microscopy (NSOM) has been applied in a wide range of scientific research, from detection of

erbium distribution in Er-doped fibers [76] to single molecule observation [77]. The achievable resolution is approximately $\lambda/20$ in visible spectrum.

Owing to the superior resolution and ability to characterize optical properties, NSOM has also been used to image the mode profiles or measure the propagation constants and losses in various types of waveguides, including conventional dielectric ridge waveguides [78–80], photonic crystal waveguides [81], metal-strip SP waveguides [37, 82], and metal-groove SP waveguides [38]. In all of these cases, NSOM probes (typically made of tapered fiber tip) are placed in close proximity to the waveguide surface. The distance is controlled by "shear-force" feedback [73, 81] and typically kept at a constant 10 nm. The evanescent field intensity, which is proportional to the field intensity within the waveguide, can then be detected.

Figure 2.11 shows the experimental configuration for applying NSOM to a photonic crystal waveguide [81]. The same configuration was also used to characterize a metal-groove SP waveguide [38], which can be regarded as one type of MIM structures. The Scanning Electron Microscope (SEM) cross-sectional image and NSOM image of the metal-groove SP waveguide are shown in Fig. 2.12. The periodic pattern in Fig. 2.12(c) is related to the interference between the SP mode and scattered field components caused by the surface roughness [38, 81]. Owing to insufficient knowledge about the periodic pattern, no direct information about the propagation constant of the SP mode can be obtained in this case. Similar patterns were also observed in previous NSOM images for various types of waveguides [78–81], and the authors claimed that the periods of the patterns are equal to λ/N_{eff}, where N_{eff} is the effective mode index.

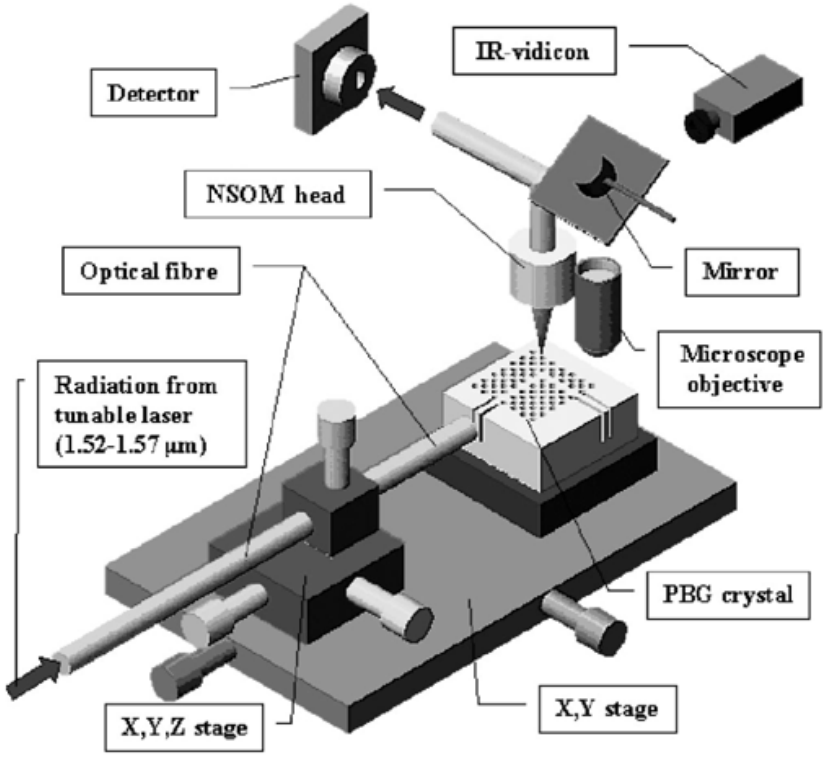

Figure 2.11: Schematic diagram of the experimental configuration for NSOM [81].

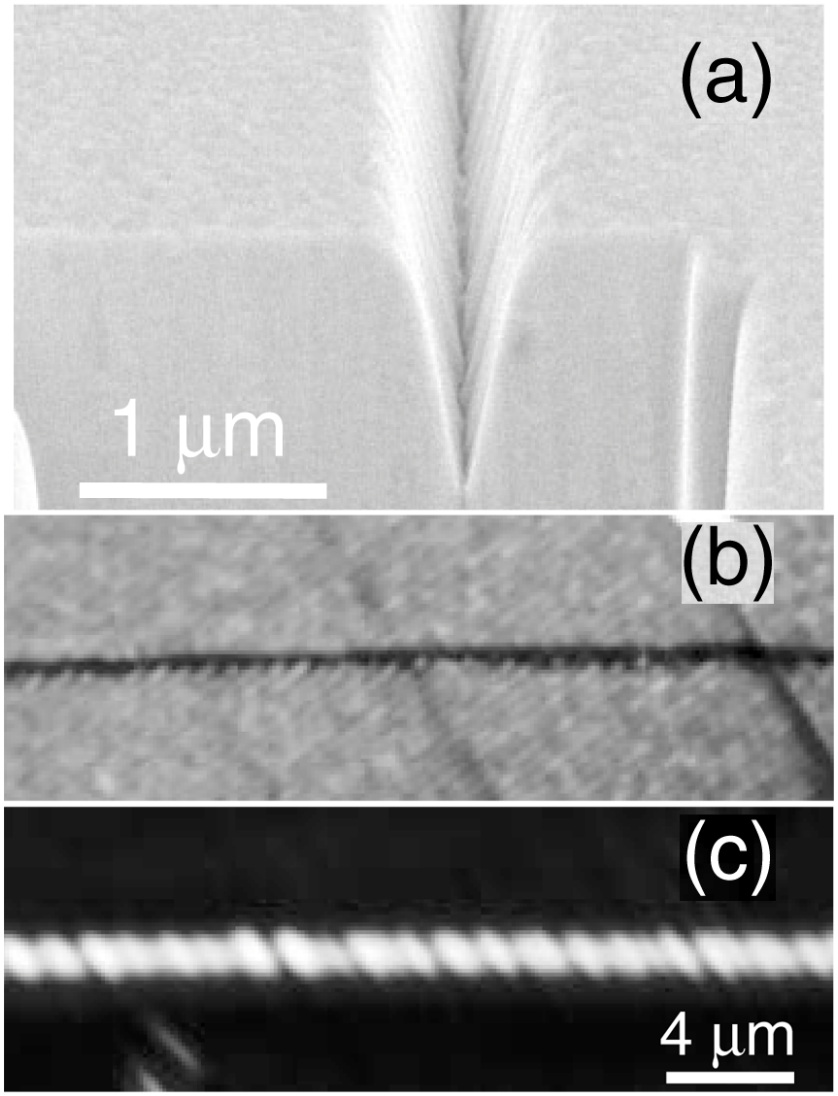

Figure 2.12: (a)Scanning Electron Microscope (SEM) cross-sectional image, (b) topographical image, and (c) NSOM image (taken at $\lambda = 1.44$ μm) of a metal-groove SP waveguide. The SP mode propagates from left to right in (c) [38].

By detecting the variation of light intensity along the waveguide, the propagation loss can be determined. Figure 2.13 shows the optical signal intensity as a function of the propagation distance along the metal-groove waveguide in Fig. 2.12. The fitted loss corresponds to a propagation length of $\sim$ 100 μm. Such loss characterization has not been performed in the NSOM measurements for conventional dielectric ridge waveguides and photonic crystal waveguides [78–81]. This may be due to the relatively small propagation losses or insufficient signal strengths in these cases.

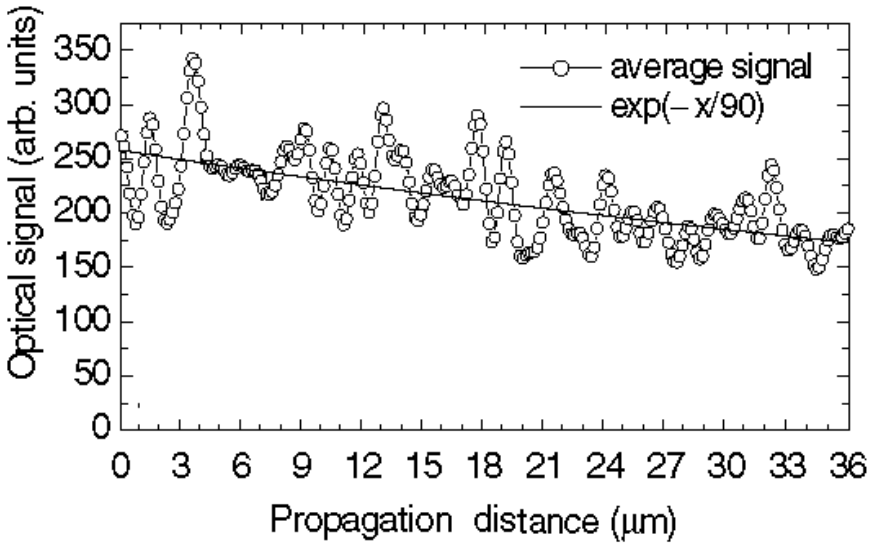

Figure 2.13: Optical signal intensity as a function of the propagation distance along the metal-groove SP waveguide [38].

Figure 2.14(a) illustrates the schematic diagram of an alternative way of using near-field scanning to characterize the SP mode in an MIM structure [83]. The near-field probe is a hollow Al pyramid, whose tip aperture has a diameter smaller than 100 nm. The probe acts as an excitation source with light incident from the transverse direction of the MIM structure. The MIM structure has a 50 nm Si_3N_4 core and a 35 nm Ag top cladding, and a slit is fabricated on the back side of the sample for the exit and detection of light. Figure 2.14(b) shows the H-field mode profiles of the SP mode in the MIM structure and the SP mode at the MIM's interface with air. The detected light intensity at the slit is plotted as a function of the probe tip-slit distance

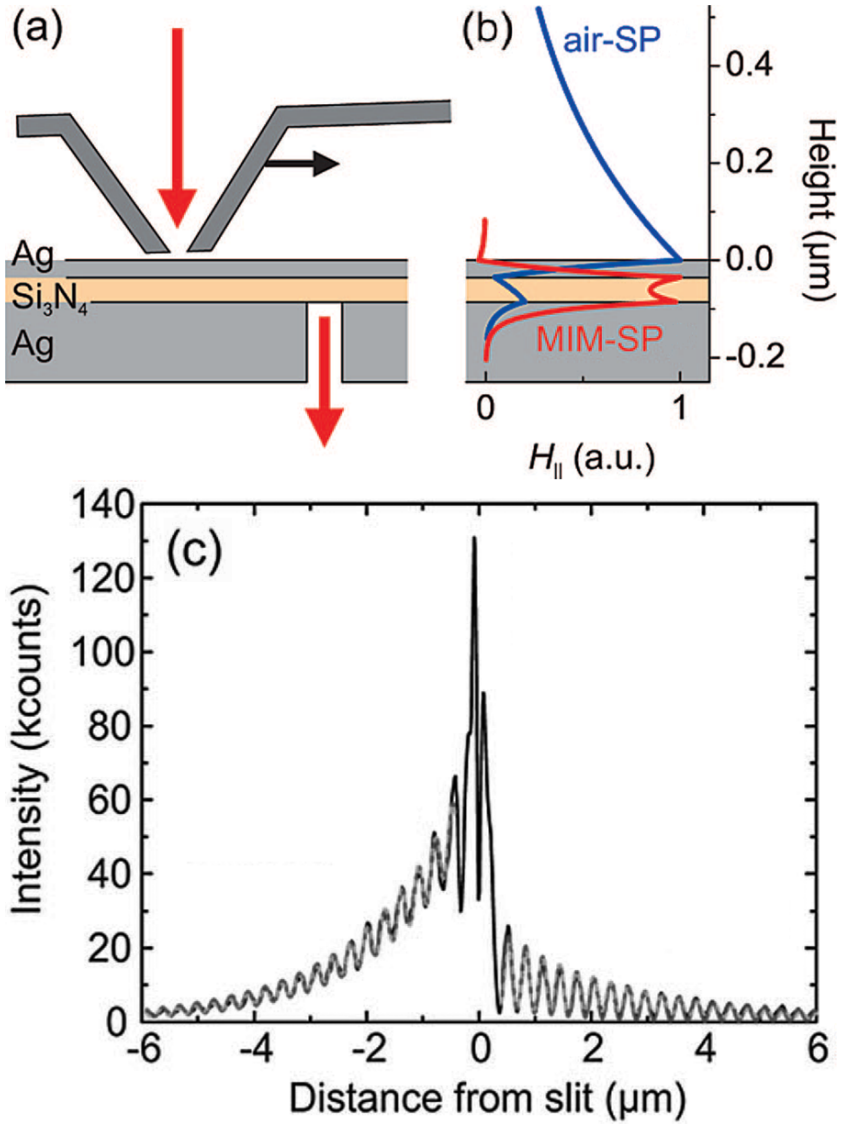

Figure 2.14: (a) Schematic diagram of the measurement geometry. Laser light is incident upon the aperture of an Al near-field probe. Light propagating through the MIM waveguide is collected from the slit in the lower Ag film. (b) H-field mode profiles of the SP mode in the MIM structure and at the MIM's interface with air. (c) Collected light intensity at the slit as a function of the tip-slit distance [83].

in Fig. 2.14(c). The oscillations in the signal represents the interference of the SP mode in MIM and the SP mode at the Ag/air interface. The propagation constant and loss of the SP mode in MIM can then be obtained by fitting. The fitted loss has a $\sim 50\%$ discrepancy with the theoretical value, however. The asymmetries observed in Fig. 2.14(c) of the interference pattern on either side of the slit, according to the

authors, "can be ascribed to a small asymmetry in the tip shape." In spite of that NSOM provides a way to observe directly the light transmission in MIM waveguides with subwavelength apertures, there are some fundamental restrictions. The near-field intensity is very strongly related to the distance between the probe tip and the waveguide surface, therefore the signal is very sensitive to environmental factors, such as temperature and vibration [81, 83]. Moreover, surface roughness produces interference effects with the waveguide modes and causes periodic patterns on the images [38, 78–81]; probe artifacts may also further affect the interference and distort the image [83]. The propagation constants of the SP modes in MIM structures may, therefore, not be obtained correctly from such periodic patterns [38, 83]. Moreover, the near-field signals are inherently weak, which further impairs the reliability of the measurement results. For example, the signals in Fig. 2.13 come with apparently strong noise, which inevitably decreases the accuracy of the loss measurement result.

2.4.2 Usage of Multiple Samples with Various Propagation Distances

Another method of measuring the propagation loss in subwavelength-aperture MIM is through the use of multiple samples with various propagation distances [33–35]. Figure 2.15(a) illustrates the schematic diagram of the slab MIM structure used in [33]. Light was coupled into the waveguide via the input slit using an unpolarized lamp source, transported through the waveguide, and coupled out and collected from the output slit. Multiple samples were fabricated with various distances between the input and ouput slits d'. Figure 2.15(b) shows the measured spectra for the slab MIM structures with 50 nm Si_3N_4 cores, and d' is varied from 2 to 8 μm. The propagation loss can be obtained by comparing the variation of light intensity for the various-length samples. Similar results for MIM waveguides with 100 nm Si_3N_4 cores are shown in Fig. 2.15(c). Figure 2.15(d) shows the results for the MIM waveguides with a 100 nm Si_3N_4 core and $d' = 2$ μm with unpolarized, TE, and TM incident light. The

detected TE light intensity increases as the wavelength decreases, which indicates the existence of a TE mode at shorter wavelength.

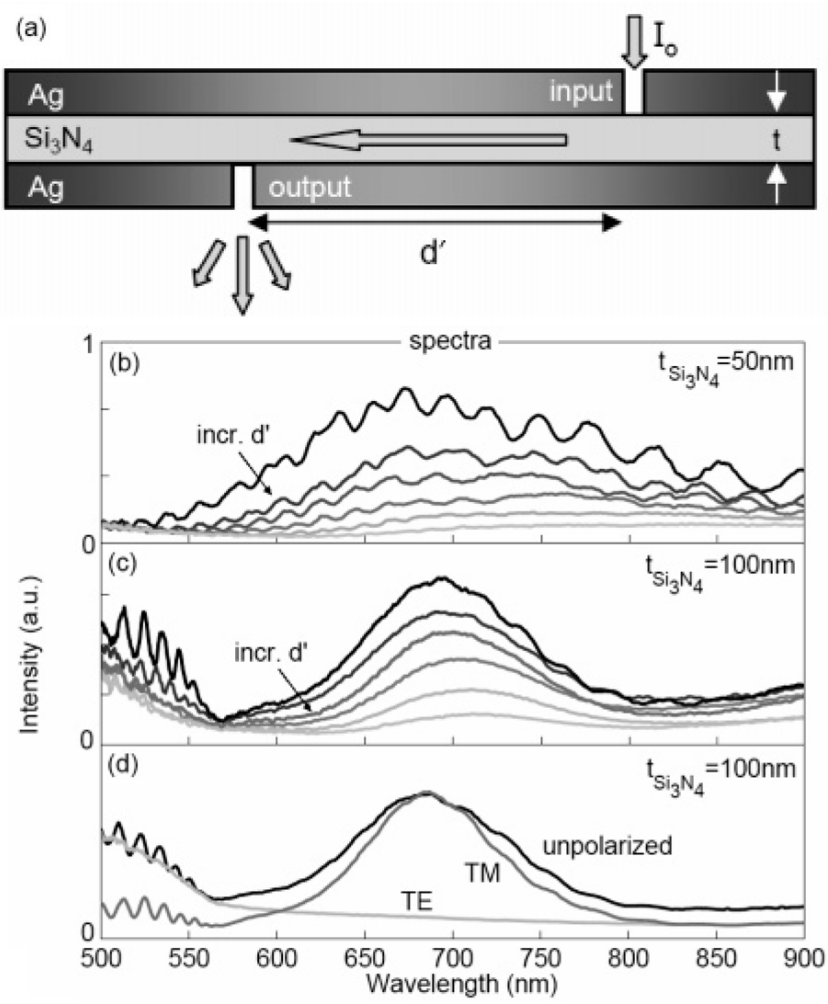

Figure 2.15: (a) Schematic diagram of the measurement geometry of the multiple-samples various-propagation-distances method. Light is coupled into and out of the waveguide via the subwavelength slits and collected at the output slit. (b) Experimental spectra for the slab waveguides with 50 nm Si_3N_4 cores. (c) Experimental spectra for the slab waveguides with 100 nm Si_3N_4 cores. The distances between the input and output slits $d' = 2, 3, 4, 5, 7$, and 8 μm in (b) and (c). The light source is an unpolarized lamp in (b) and (c). (d) TE and TM experimental spectra for the slab waveguide with a 100 nm Si_3N_4 core and $d' = 2$ μm [33].

Figure 2.16 plots the propagation lengths as functions of wavelengths. The dots represent experimental results obtained from the spectra shown in Fig. 2.15 (b) and (c). The solid lines are simulated results. It is shown that the experimental results have longer propagation lengths, or equivalently, smaller loss. According to the authors, this mismatch likely results from the higher-quality Ag film used in the experimental measurements [33]. On the other hand, the effective mode index N_{eff} can be determined from the far-field intensity distribution at the output slit. For the 50 nm-core samples, the fitted N_{eff} is between 6.9 and 5.7 for wavelengths between 600 and 900 nm. The values of N_{eff} are exceptionally high compared with those from similar structures [38].

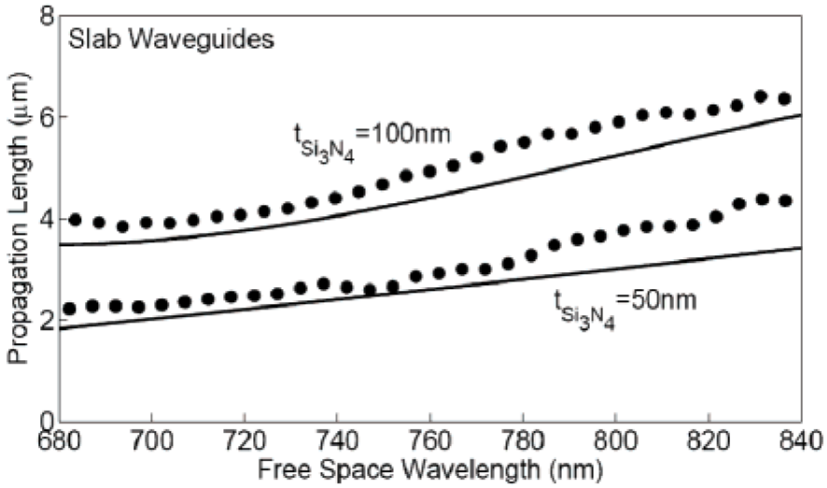

Figure 2.16: Propagation lengths as functions of wavelength for slab MIM waveguides with 50 nm and 100 nm Si_3N_4 cores. The dots represent experimental results, and the solid lines represent theoretical calculations [33].

The approach described in this section provides a straightforward way of characterizing the SP mode in subwavelength MIM structures. However, it is extremely difficult to ensure that the coupling efficiencies are the same for various-length samples. The fabrication imperfections and/or coupling techniques may all contribute to non-uniform coupling efficiencies. Moreover, it is infeasible to quantify the effects of sample-to-sample uniformity, which is critical when comparing the results from

various samples. For example, Fig. 2.15(b) shows obvious sample-to-sample non-uniformity on the oscillation features. These uncertainties need to be resolved before the results can be confirmed.

2.5 Summary

In this chapter, the properties of the SP mode at a single metal/dielectric interface and TM and TE modes in an MIM waveguide were discussed in detail in Sec. 2.1 and 2.2. Because of the superior lateral confinement and slow-wave property, MIM-based devices and interconnects offer the potential of realizing integrated optical nanocircuitry. However, the subwavelength sizes of MIM structures make the coupling and any further measurements very challenging. The light is typically coupled into the subwavelength MIM structure via a tapered fiber or waveguide. The MIM waveguide modes can be characterized by using NSOM or multiple samples with various propagation distances. In the former, NSOM allows direct observations of the near-field light field on a waveguide surface. However, the measurement is very sensitive to uncontrollable environmental factors. In the latter, the sample-to-sample non-uniformity and the differences in coupling efficiencies among samples are difficult to quantify. More details were presented in Sec. 2.4. In the following chapters, a much more reliable and straightforward experimental technique for MIM characterization, which is called the Transverse Transmission/Reflection (TTR) method, will be developed and realized.

Further, it is also shown in Sec. 2.3 that the well-known parallel-plate waveguide in microwave technology is simply an MIM waveguide operated at microwave wavelengths. The TEM mode in a parallel-plate waveguide can be guided with subwavelength confinement as can the TM_0 mode in an MIM structure. However, the TEM mode propagates at light speed, whereas the TM_0 mode propagates more slowly, especially at higher frequency.

CHAPTER 3

TRANSVERSE TRANSMISSION/REFLECTION (TTR) METHOD

3.1 Transmission Matrix Analysis

The transmission matrix provides the basis for a systematic approach for analyzing a multilayer structure as shown in Fig. 3.1. For a transverse magnetic (TM) wave traveling in the $+z$ direction in the ith layer ($x_{i-1} \leq x \leq x_i$), the magnetic field is $\vec{H}_i = \hat{y} H_{yi}(x) \exp[j(\omega t - \gamma z)]$, where $\hat{y}$ is the unit vector in the $+y$ direction and $\gamma = \beta - j\alpha$ is the complex propagation constant with β and α being the phase and attenuation propagation constants, respectively. The effective index N_{eff} is defined as $N_{\text{eff}} \equiv \beta/k_0$, where $k_0 = 2\pi/\lambda_0$ and λ_0 is the freespace wavelength. The total magnetic field in the ith layer is the summation of the $+x$ and $-x$ propagating waves, which can be expressed as

$$H_{yi}(x) = A_i \exp[-\kappa_{x,i}(x - x_{i-1})] + B_i \exp[+\kappa_{x,i}(x - x_{i-1})], \tag{3.1}$$

where A_i and B_i are the complex field amplitudes corresponding to the $+x$ and $-x$ propagating waves in the ith layer respectively, $\kappa_{x,i} = (\gamma^2 - k_0^2 \varepsilon_i)^{1/2}$ is the complex transverse wavevector in the ith layer, and x_i defines the boundary between the ith and $(i+1)$th layer (Fig. 3.1). For a waveguide mode, the sum of the propagating fields in the x direction produces a standing wave. By matching the tangential components of the electric and magnetic fields at every interface, the field coefficients at the cover and substrate boundaries can be related via the matrix equation

$$\begin{pmatrix} A_s \\ B_s \end{pmatrix} = M_{j-1} M_{j-2} \cdots M_1 M_0 \begin{pmatrix} A_c \\ B_c \end{pmatrix} = \begin{pmatrix} m_{11} & m_{12} \\ m_{21} & m_{22} \end{pmatrix} \begin{pmatrix} A_c \\ B_c \end{pmatrix}, \tag{3.2}$$

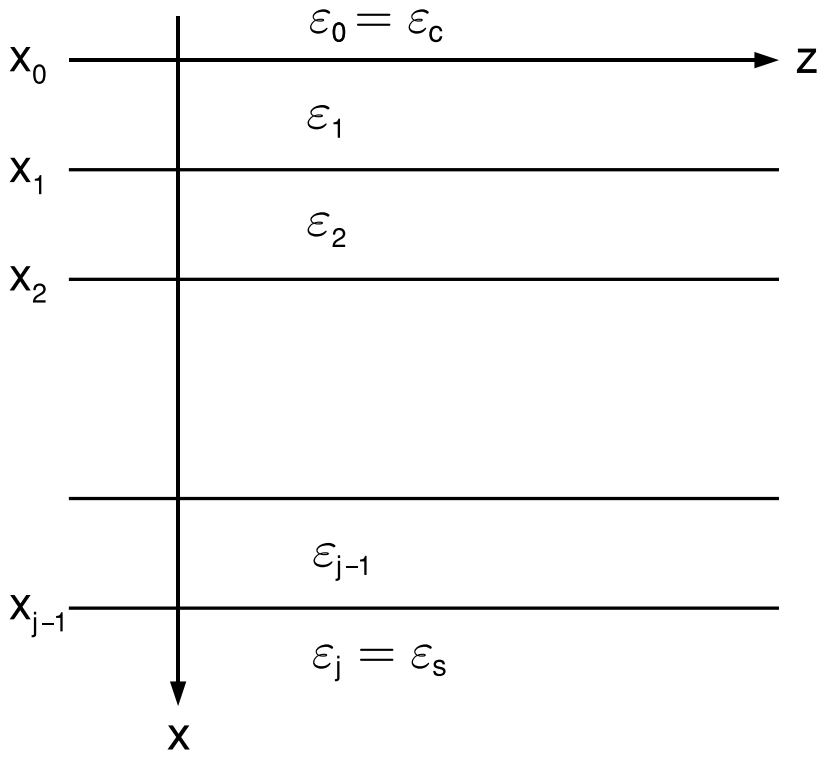

Figure 3.1: Schematic diagram and coordinate system of a multilayer structure. The subscript "c" indicates "cover" and "s" indicates "substrate".

where the transmission matrix for the ith layer, M_i, is represented by

$$M_i = \frac{1}{2}\begin{pmatrix} (1+f_i\frac{\kappa_{x,i}}{\kappa_{x,i+1}})\exp(-\kappa_{x,i}d_i) & (1-f_i\frac{\kappa_{x,i}}{\kappa_{x,i+1}})\exp(\kappa_{x,i}d_i) \\ (1-f_i\frac{\kappa_{x,i}}{\kappa_{x,i+1}})\exp(-\kappa_{x,i}d_i) & (1+f_i\frac{\kappa_{x,i}}{\kappa_{x,i+1}})\exp(\kappa_{x,i}d_i) \end{pmatrix} \text{ for } i = 0, \cdots, j-1, \tag{3.3}$$

where for TE waves $f_i = 1$ while for TM waves $f_i = \varepsilon_{i+1}/\varepsilon_i$, and d_i is the thickness of the ith layer. By Eq. (3.2), the complex amplitude transmission and reflection coefficients are represented as

$$\text{Cover incidence } (B_s = 0) \quad : \quad \begin{pmatrix} t_s \\ 0 \end{pmatrix} = \begin{pmatrix} m_{11} & m_{12} \\ m_{21} & m_{22} \end{pmatrix} \begin{pmatrix} 1 \\ r_c \end{pmatrix} \tag{3.4}$$

$$\text{Substrate incidence } (A_c = 0) \quad : \quad \begin{pmatrix} r_s \\ 1 \end{pmatrix} = \begin{pmatrix} m_{11} & m_{12} \\ m_{21} & m_{22} \end{pmatrix} \begin{pmatrix} 0 \\ t_c \end{pmatrix} \tag{3.5}$$

By algebraic manipulation,

$$r_c = -\frac{m_{21}}{m_{22}},\ r_s = \frac{m_{12}}{m_{22}},\ t_c = \frac{1}{m_{22}},\ t_s = \frac{m_{11}m_{22} - m_{12}m_{21}}{m_{22}}. \tag{3.6}$$

The fraction of the power reflected is

$$R_c = |r_c|^2,\ R_s = |r_s|^2. \tag{3.7}$$

The fraction of the power transmitted is

$$T_c = T_s = |t_c|^2 \frac{\kappa_c}{\kappa_s}\frac{\varepsilon_s}{\varepsilon_c} = |t_s|^2 \frac{\kappa_s}{\kappa_c}\frac{\varepsilon_c}{\varepsilon_s}. \tag{3.8}$$

By Eq. (3.6) and (3.8) we can also obtain

$$m_{11}m_{22} - m_{12}m_{21} = \frac{\kappa_c}{\kappa_s}\frac{\varepsilon_s}{\varepsilon_c}. \tag{3.9}$$

For a waveguide mode to exist, the field intensities have to converge at $x = \pm\infty$, i.e. $A_c = B_s = 0$. As a result, the following relation has to be satisfied,

$$\text{Waveguide mode } (A_c = B_s = 0): \begin{pmatrix} A_s \\ 0 \end{pmatrix} = \begin{pmatrix} m_{11} & m_{12} \\ m_{21} & m_{22} \end{pmatrix} \begin{pmatrix} 0 \\ B_c \end{pmatrix}. \tag{3.10}$$

For non-trivial solutions to exist in Eq. (3.10), it is required that $m_{22} = 0$. It should be noted that this relation is satisfied for both guided modes and leaky/lossy modes [84]; the former corresponds to real solutions of γ and the latter to complex solutions of γ. On the other hand, by applying $m_{22} = 0$ to Eq. (3.6), it shows that r and t approach $\pm\infty$ for a mode; this implies that, physically, the waveguide modes cannot be directly excited from the cover or substrate. To overcome this, a high-index layer has to be added adjacent to the cover layer to enable evanescent-field coupling. More details about this are described in Sec. 3.3.

3.1.1 SP Modes

The structures supporting SP modes (see Sec. 2.1 and 2.2) can also be analyzed by using the transmission matrix formulation. Consider the single metal/dielectric

interface in Fig. 2.1, the corresponding transmission matrix for TM waves can be expressed as

$$M_{\rm SP} = \frac{1}{2}\begin{pmatrix} 1+\frac{\varepsilon_d}{\varepsilon_m}\frac{\kappa_{x,m}}{\kappa_{x,d}} & 1-\frac{\varepsilon_d}{\varepsilon_m}\frac{\kappa_{x,m}}{\kappa_{x,d}} \\ 1-\frac{\varepsilon_d}{\varepsilon_m}\frac{\kappa_{x,m}}{\kappa_{x,d}} & 1+\frac{\varepsilon_d}{\varepsilon_m}\frac{\kappa_{x,m}}{\kappa_{x,d}} \end{pmatrix}. \tag{3.11}$$

By using $m_{22}=0$, the characteristic equation of the SP mode at the metal/dielectric interface can be expressed by

$$\frac{\varepsilon_m}{\varepsilon_d} = -\frac{\kappa_{x,m}}{\kappa_{x,d}}, \tag{3.12}$$

which is identical to the characteristic equation [Eq. (2.11)] obtained in Sec. 2.1 based on plane-wave analysis and boundary condition equations.

Similarly, the TM-wave transmission matrix for the MIM structure in Fig. 2.3 can be expressed as

$$\begin{aligned} M_{\rm MIM} =& \frac{1}{4}\begin{pmatrix} (1+\frac{\varepsilon_m}{\varepsilon_d}\frac{\kappa_{x,d}}{\kappa_{x,m}})\exp(-\kappa_{x,d}d_d) & (1-\frac{\varepsilon_m}{\varepsilon_d}\frac{\kappa_{x,d}}{\kappa_{x,m}})\exp(\kappa_{x,d}d_d) \\ (1-\frac{\varepsilon_m}{\varepsilon_d}\frac{\kappa_{x,d}}{\kappa_{x,m}})\exp(-\kappa_{x,d}d_d) & (1+\frac{\varepsilon_m}{\varepsilon_d}\frac{\kappa_{x,d}}{\kappa_{x,m}})\exp(\kappa_{x,d}d_d) \end{pmatrix} \\ & \times \begin{pmatrix} 1+\frac{\varepsilon_d}{\varepsilon_m}\frac{\kappa_{x,m}}{\kappa_{x,d}} & 1-\frac{\varepsilon_d}{\varepsilon_m}\frac{\kappa_{x,m}}{\kappa_{x,d}} \\ 1-\frac{\varepsilon_d}{\varepsilon_m}\frac{\kappa_{x,m}}{\kappa_{x,d}} & 1+\frac{\varepsilon_d}{\varepsilon_m}\frac{\kappa_{x,m}}{\kappa_{x,d}} \end{pmatrix} \\ =& \begin{pmatrix} C_{++}\exp(-\kappa_{x,d}d_d)+C_{--}\exp(\kappa_{x,d}d_d) & C_{+-}\exp(-\kappa_{x,d}d_i)+C_{-+}\exp(\kappa_{x,i}d_d) \\ C_{-+}\exp(-\kappa_{x,d}d_d)+C_{+-}\exp(\kappa_{x,d}d_d) & C_{--}\exp(-\kappa_{x,d}d_i)+C_{++}\exp(\kappa_{x,i}d_d) \end{pmatrix}, \end{aligned} \tag{3.13}$$

where

$$C_{\pm\pm} = (1 \pm \frac{\varepsilon_m}{\varepsilon_d}\frac{\kappa_{x,d}}{\kappa_{x,m}})(1 \pm \frac{\varepsilon_d}{\varepsilon_m}\frac{\kappa_{x,m}}{\kappa_{x,d}}). \tag{3.14}$$

Applying $m_{22}=0$ to Eq. (3.13) gives the characteristic equation for the MIM structure

$$\exp(2\kappa_{x,d}d_d) = -\frac{C_{--}}{C_{++}} = \frac{\frac{\varepsilon_m}{\varepsilon_d}\frac{\kappa_{x,d}}{\kappa_{x,m}}+\frac{\varepsilon_d}{\varepsilon_m}\frac{\kappa_{x,m}}{\kappa_{x,d}}-2}{\frac{\varepsilon_m}{\varepsilon_d}\frac{\kappa_{x,d}}{\kappa_{x,m}}+\frac{\varepsilon_d}{\varepsilon_m}\frac{\kappa_{x,m}}{\kappa_{x,d}}+2}. \tag{3.15}$$

Equivalently,

$$\tanh(\kappa_{x,d}d_d) = \frac{\exp(2\kappa_{x,d}d_d)-1}{\exp(2\kappa_{x,d}d_d)+1} = -\frac{2}{\frac{\varepsilon_m}{\varepsilon_d}\frac{\kappa_{x,d}}{\kappa_{x,m}}+\frac{\varepsilon_d}{\varepsilon_m}\frac{\kappa_{x,m}}{\kappa_{x,d}}}, \tag{3.16}$$

which is identical to the characteristic equation [Eq. (2.26)] for the MIM plasmonic mode obtained in Sec. 2.2.

3.2 Theory of the Transverse Transmission/Reflection (TTR) Method

From Eq. (3.6), t and r are infinite when $m_{22} = 0$. In the TTR method, the fraction of power transmitted/reflected is calculated as a function of the z-component of the wavevector, $\beta = \mathrm{Re}(\gamma)$. The essence of the TTR method is based on expressing the fraction of the power transmitted approximately as a rational function of the poles of the complex propagation constants γ_q for leaky modes and lossy modes [39,85,86]. That is,

$$T = \left|\frac{1}{m_{22}}\right|^2 \frac{\kappa_c}{\kappa_s}\frac{\varepsilon_s}{\varepsilon_c} \simeq U(\beta)\left|\frac{1}{\prod_{q=1}^{M_p}(\beta - \gamma_q)}\right|^2, \tag{3.17}$$

where $U(\beta)$ is a slowly varying function of β and M_p is the number of poles. The γ_q values which make the transmission coefficients infinite correspond to the propagation constants of guided or leaky/lossy modes of the waveguide structure. This is consistent with guided modes and leaky/lossy modes being solutions of $m_{22} = 0$. Given that $U(\beta)$ varies sufficiently slowly with β, the fractional transmitted power $T(\beta)$ has Lorentzian-type peaks located at $\beta = \mathrm{Re}(\gamma_q)$ and has HWHMs equal to $\alpha = \mathrm{Im}(\gamma_q)$. In the case that all the layers have zero or negligible loss, i.e. $|\mathrm{Im}(\varepsilon)| \ll |\mathrm{Re}(\varepsilon)|$, the fractional reflected power can be approximated as $R = 1 - T$ [39]. Therefore under these circumstances, the $R(\beta)$ has Lorentzian-type minima at $\beta = \mathrm{Re}(\gamma_q)$ and has HWHMs $= \alpha = \mathrm{Im}(\gamma_q)$.

3.3 Attenuated Total Reflection (ATR) Configuration

When light is incident from the cover (see Fig. 3.1), the achievable effective index N_{eff} ranges from 0 to n_c. The angular spectrum of the reflected power for $N_{\mathrm{eff}} > n_c$ is

not shown since the corresponding incident angles are not accessible from the cover. Moreover, when light is incident from the cover, total internal reflection occurs when $N_{\text{eff}} > n_s$, consequently the modes with $N_{\text{eff}} > n_s$ are also not accessible from the cover. As a result, both n_c and n_s are required to be larger than the N_{eff} of the modes of interest to enable the TTR method to detect all the modes. This shortcoming can be overcome by adding a layer(s) with a refractive index higher than the effective index of any of the waveguide modes to the original cover and/or the substrate. Figure 3.2 shows the case with a high-index layer n_c' added above the cover, and the angle of incidence from the added high-index layer is θ. The effective index N_{eff} can then be expressed as a function of θ, $N_{\text{eff}} = n_c' \sin\theta$. The resulting structure will be a perturbed version of the original structure, with a slightly shifted real part of the propagation constant and a slightly larger attenuation coefficient compared with those of the original mode. It should be noted that the β' and α' characterized by the TTR method are for the perturbed structure, which contains the added high-index layer. The "prime" indicates results obtained by the TTR method. To minimize the perturbation, weak coupling is required, as in a conventional prism coupler [45–47]. Calculations have shown that the gap between the prism and the waveguide structure should be larger than half a wavelength to satisfy the weak coupling condition [87–89]. With a sufficiently large gap, the β' and α' obtained by the TTR method approach the unperturbed propagation constants of the waveguide modes, β and α, respectively.

Based on the transmission matrix formulation, the perturbation caused by the added high-index layer can be analyzed. Let the transmission matrix for the structure in Fig. 3.1 be

$$M = \begin{pmatrix} m_{11} & m_{12} \\ m_{21} & m_{22} \end{pmatrix}, \tag{3.18}$$

then the transmission matrix for the structure loaded with a high-index layer (see

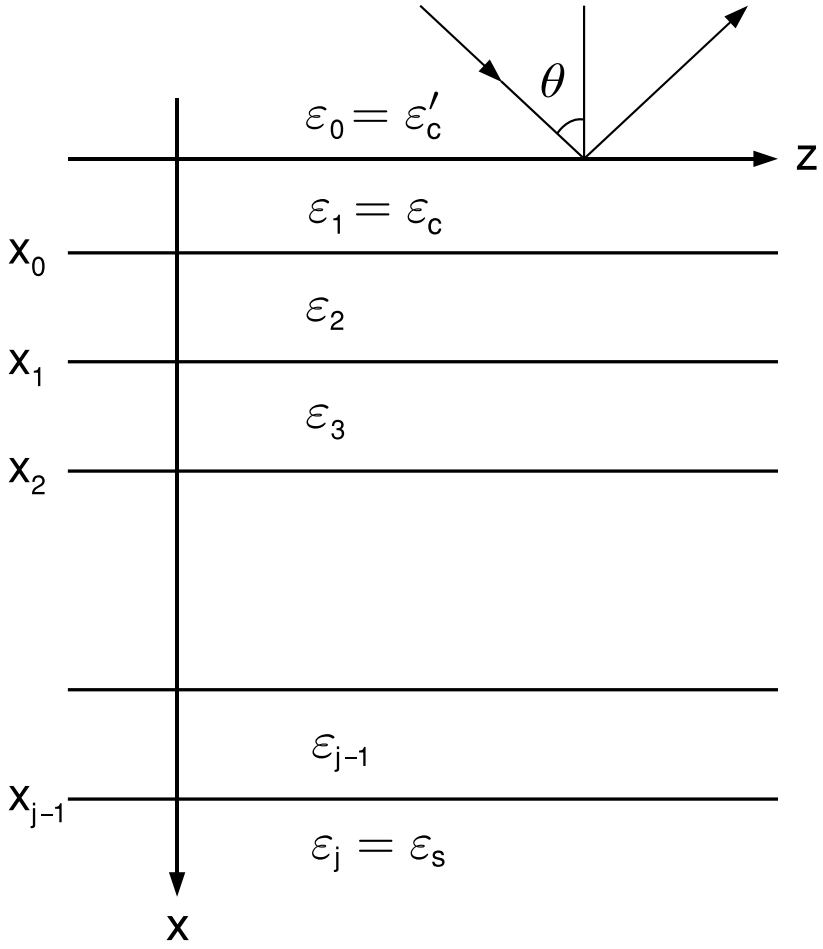

Figure 3.2: Schematic diagram and coordinate system of the multilayer structure in Fig. 3.1 with an added high-index layer, $\varepsilon_0 = \varepsilon_c'$.

Fig. 3.2) is

$$
\begin{aligned}
M' &= \frac{1}{2}\begin{pmatrix} m_{11} & m_{12} \\ m_{21} & m_{22} \end{pmatrix}\begin{pmatrix} \left(1+f_{i=0}\frac{\kappa_c'}{\kappa_c}\right)\exp(-\kappa_c d_c) & \left(1-f_{i=0}\frac{\kappa_c'}{\kappa_c}\right)\exp(-\kappa_c d_c) \\ \left(1-f_{i=0}\frac{\kappa_c'}{\kappa_c}\right)\exp(\kappa_c d_c) & \left(1+f_{i=0}\frac{\kappa_c'}{\kappa_c}\right)\exp(\kappa_c d_c) \end{pmatrix} \\
&= \frac{1}{2}\begin{pmatrix} m_{12}\left(1-f_{i=0}\frac{\kappa_c'}{\kappa_c}\right)\exp(\kappa_c d_c) + m_{11}\left(1+f_{i=0}\frac{\kappa_c'}{\kappa_c}\right)\exp(-\kappa_c d_c) \\ m_{22}\left(1-f_{i=0}\frac{\kappa_c'}{\kappa_c}\right)\exp(\kappa_c d_c) + m_{21}\left(1+f_{i=0}\frac{\kappa_c'}{\kappa_c}\right)\exp(-\kappa_c d_c) \end{pmatrix} \\
&\quad \begin{pmatrix} m_{12}\left(1+f_{i=0}\frac{\kappa_c'}{\kappa_c}\right)\exp(\kappa_c d_c) + m_{11}\left(1-f_{i=0}\frac{\kappa_c'}{\kappa_c}\right)\exp(-\kappa_c d_c) \\ m_{22}\left(1+f_{i=0}\frac{\kappa_c'}{\kappa_c}\right)\exp(\kappa_c d_c) + m_{21}\left(1-f_{i=0}\frac{\kappa_c'}{\kappa_c}\right)\exp(-\kappa_c d_c) \end{pmatrix}. \qquad (3.19)
\end{aligned}
$$

Therefore, the reflection coefficient for the light incident from the added high-index

layer $n = n'_c$ is

$$r'_c = -\frac{M'(2,1)}{M'(2,2)}$$
$$= -\frac{m_{12}\left(1 + f_{i=0}\frac{\kappa'_c}{\kappa_c}\right)\exp(\kappa_c d_c) + m_{11}\left(1 - f_{i=0}\frac{\kappa'_c}{\kappa_c}\right)\exp(-\kappa_c d_c)}{m_{22}\left(1 + f_{i=0}\frac{\kappa'_c}{\kappa_c}\right)\exp(\kappa_c d_c) + m_{21}\left(1 - f_{i=0}\frac{\kappa'_c}{\kappa_c}\right)\exp(-\kappa_c d_c)}. \tag{3.20}$$

In the case that $\exp(\kappa_c d_c) \gg 1$, Eq. (3.20) can be approximated as

$$r'_c \simeq -\frac{1 - f_{i=0}\frac{\kappa'_c}{\kappa_c}}{1 + f_{i=0}\frac{\kappa'_c}{\kappa_c}}\left[1 + \frac{4m_{21}f_{i=0}\frac{\kappa'_c}{\kappa_c}\exp(-2\kappa_c d_c)}{m_{22}\left(1 - f^2_{i=0}\frac{\kappa'^2_c}{\kappa^2_c}\right)}\right]. \tag{3.21}$$

For a mode to exist, $n_c < \beta/k_0 < n'_c$, therefore κ_c is real and κ'_c is imaginary, given the typically small α value. Equation (3.21) can then be approximated as

$$r'_c \simeq \exp(j\phi)\left[1 - s(\beta)\frac{\exp(-2\kappa_c d_c)}{\beta - \gamma_q}\right], \tag{3.22}$$

where $\exp(j\phi)$ is a phase factor and $s(\beta)$ is a slowly varying function defined as

$$s(\beta) = -4m_{21}\frac{f_{i=0}\frac{\kappa'_c}{\kappa_c}}{1 - f^2_{i=0}\frac{\kappa'^2_c}{\kappa^2_c}}. \tag{3.23}$$

Equation (3.22) implies that, given $s(\beta)$ varies sufficiently slowly near $\beta = \mathrm{Re}(\gamma_q)$ and $\exp(2\kappa_c d_c) \gg 1$, the fractional reflected power $R_c \equiv |r_c|^2$ has a Lorentzian-shaped resonance near $\beta = \mathrm{Re}(\gamma_q)$ and a half-width at half-minimum (HWHM)$= \alpha = \mathrm{Im}(\gamma_q)$. It should be noted that $\exp(2\kappa_c d_c) \gg 1$ corresponds to the weak coupling condition [87–89], which is required to minimize the perturbation caused by the added high-index layer n'_c. The detailed analysis based on applying the ATR configuration to MIM structures is provided in Sec. 3.4.

Moreover, the field profile excited at the resonance angle can be related to the corresponding mode profile based on the transmission matrix formulation. For example, in a leaky waveguide structure loaded with a high-index layer n'_c as shown in Fig. 3.2, the complex propagation constant of a particular mode is assumed to be $\beta_q - j\alpha_q$, which satisfies the equation $m_{22} = 0$; the corresponding mode profile

therefore contains waves that propagate away from the waveguide into the high-index layer and the substrate, while there are no waves incident on the waveguide from these two regions. On the other hand, for a wave incident from this high-index layer at the incident resonant angle θ_q such that $n_c' \sin\theta_q = \beta_q/k_0$, this wave can excite a resonant field that is very similar to the corresponding mode profile if there is no low-index layer other than the coupling layer $n_1 = n_c$ (see Fig. 3.2). The field profile excited at resonant angle differs from the exact mode profile to within a first-order perturbation factor proportional to α_q (see Appendix A). This fact can be utilized to obtain the mode profile of a leaky waveguide without the knowledge of a very accurate complex propagation constant, which is typically required for determining the leaky mode profile. In addition, based on the previous discussion in this section, the transmitted wave is maximized when $n_c' \sin\theta_q = \beta_q/k_0$, therefore the excited field strength in the waveguide structure, which is approximately proportional to the transmitted wave field amplitude (see Appendix A), is also maximized.

3.4 ATR Configuration for MIM Structures

When applying the ATR configuration to an MIM structure, some modifications need to be made. Because the claddings in the MIM structure are metal, one of the two metal claddings has to be made thinner for transverse light coupling. Moreover, it is difficult to avoid an air gap between the prism and the MIM structure unless the MIM waveguide structure is directly deposited on the prism. The prism-loaded MIM structure is shown in Fig. 3.3(c), which can be divided into two parts, as shown in Fig. 3.3(a) and (b).

The structure in Fig. 3.3(a) is commonly referred as an Otto configuration [59]. The SP is excited at the metal/dielectric interface by frustrated total internal reflection of the light incident upon the prism. Compared with a simple metal/dielectric

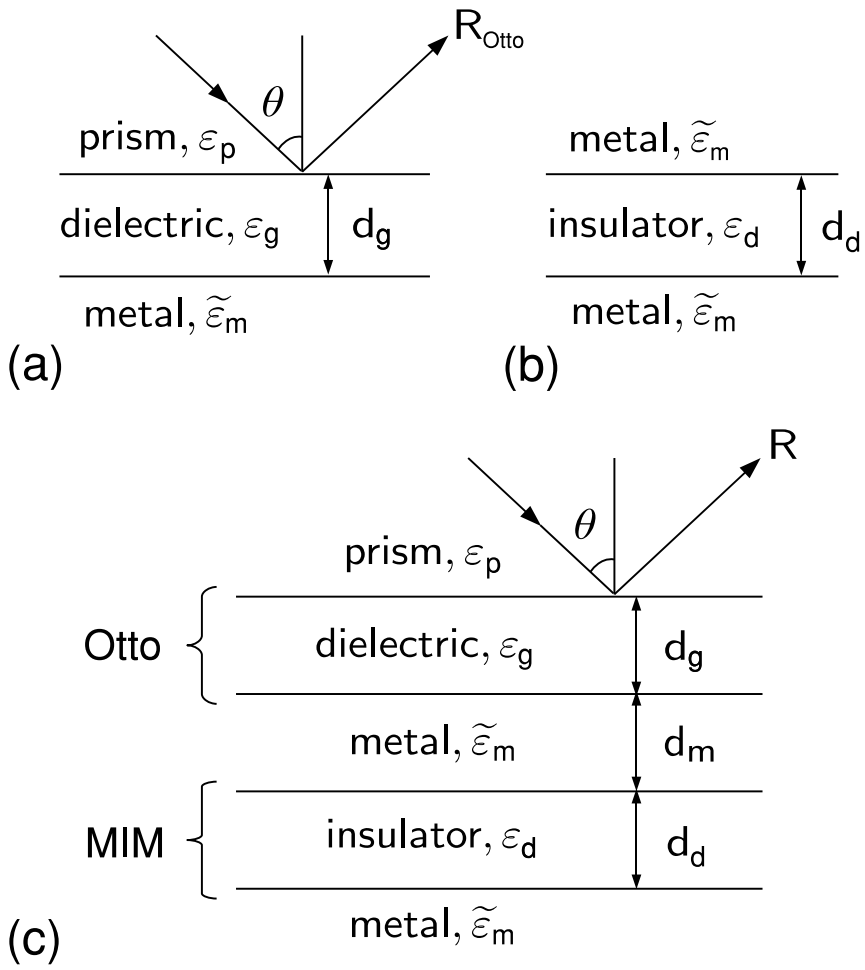

Figure 3.3: (a) Schematic diagram of a single metal/dielectric interface-SP structure (Otto configuration). (b) A symmetric MIM structure. (c) The MIM structure in (b) loaded with a prism.

interface, whose dispersion relation is given by

$$\beta_{\mathrm{SP}} = k_0 \left(\frac{\varepsilon_m \varepsilon_g}{\varepsilon_m + \varepsilon_g} \right)^{1/2}, \tag{3.24}$$

the Otto configuration supports a perturbed SP mode due to the existence of the prism. In an Otto configuration, the thickness of the dielectric is not infinite, so part of the energy in the SP mode at the metal/dielectric interface can be coupled back into the prism. Therefore, the SP mode supported by the Otto configuration is perturbed by this leakage loss, which grows with decreasing gap dielectric thickness d_g. The complex propagation constant γ_{Otto} of the perturbed SP mode can be obtained by

solving the transmission matrix equation. Defining the transmission matrix of this structure [Fig. 3.3(a)] as

$$M_{\text{Otto}} = \begin{pmatrix} m'_{11} & m'_{12} \\ m'_{21} & m'_{22} \end{pmatrix}_{\text{Otto}} \tag{3.25}$$

then the reflection coefficient is

$$r_{\text{Otto}} = -\frac{m'_{21}}{m'_{22}}. \tag{3.26}$$

The complex propagation constant γ_{Otto} is the solution of $m'_{22} = 0$. Figure 3.4 shows the simulated angular reflection power spectrum for a prism-air-silver configuration at various air gap thicknesses d_g. The fractional reflected power is $R_{\text{Otto}} = |r_{\text{Otto}}|^2$ and the effective index is $N_{\text{eff}} = n_p \sin\theta$, where $n_p = 2.5$ is the refractive index of the prism and θ is the angle of incidence from the prism at the prism/air gap interface. At $\lambda = 632.8$ nm, the dielectric constant of the silver is $\widetilde{\varepsilon}_{\text{Ag}} = -15.9 - j1.07$, or equivalently, $\widetilde{n}_{\text{Ag}} = 0.135 - j3.99$ [90]. As d_g decreases, the loss of the SP mode increases and the HWHM of the fractional reflected power R_{Otto} resonance increases, and the center of the R_{Otto} resonance moves from β_{SP} to higher β values.

Based on the transmission matrix formulation, the prism-loaded MIM structure in Fig. 3.3(c) can be analyzed. The transmission matrix for this structure can be represented as

$$\begin{aligned} M &= \begin{pmatrix} m_{11} & m_{12} \\ m_{21} & m_{22} \end{pmatrix}_{\text{MIM}} \begin{pmatrix} \exp(-\kappa_m d_m) & 0 \\ 0 & \exp(\kappa_m d_m) \end{pmatrix} \begin{pmatrix} m'_{11} & m'_{12} \\ m'_{21} & m'_{22} \end{pmatrix}_{\text{Otto}} \\ &= \begin{pmatrix} m_{12}m'_{21}\exp(\kappa_m d_m) + m_{11}m'_{11}\exp(-\kappa_m d_m) \\ m_{22}m'_{21}\exp(\kappa_m d_m) + m_{21}m'_{11}\exp(-\kappa_m d_m) \end{pmatrix} \\ &\quad \begin{matrix} m_{12}m'_{22}\exp(\kappa_m d_m) + m_{11}m'_{12}\exp(-\kappa_m d_m) \\ m_{22}m'_{22}\exp(\kappa_m d_m) + m_{21}m'_{12}\exp(-\kappa_m d_m) \end{matrix} \end{aligned} \tag{3.27}$$

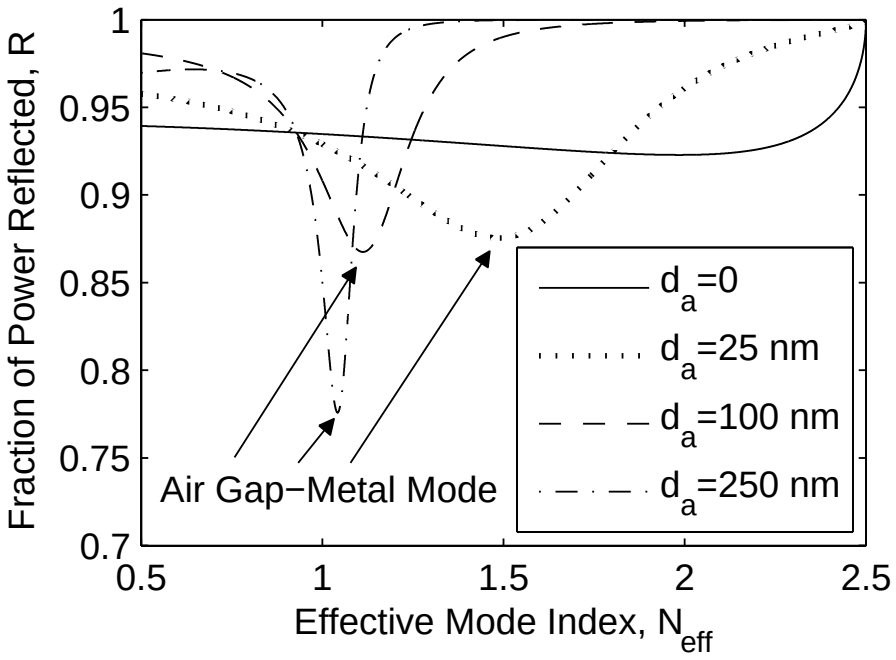

Figure 3.4: Angular reflection power spectrum for a prism-air-silver configuration at various air gap thickness d_g at $\lambda = 632.8$ nm. The dielectric constants of silver and the prism are $\widetilde{\varepsilon}_{\rm Ag} = -15.9 - j1.07$ and $\varepsilon_p = 6.25$, respectively.

Therefore, the reflection coefficient for the light incident at the prism is

$$\begin{aligned} r &= -\frac{M(2,1)}{M(2,2)} \\ &= -\frac{m'_{21}}{m'_{22}} \frac{1 + \frac{m_{21}m'_{11}}{m_{22}m'_{21}} \exp(-2\kappa_m d_m)}{1 + \frac{m_{21}m'_{12}}{m_{22}m'_{22}} \exp(-2\kappa_m d_m)} \\ &= -\frac{m'_{21}}{m'_{22}} \left[1 + \frac{\frac{m_{21}}{m_{22}} \frac{m'_{11}m'_{22} - m'_{12}m'_{21}}{m'_{22}m'_{21}} \exp(-2\kappa_m d_m)}{1 + \frac{m_{21}m'_{12}}{m_{22}m'_{22}} \exp(-2\kappa_m d_m)} \right]. \end{aligned} \tag{3.28}$$

In the case that $(m_{21}m'_{12})/(m_{22}m'_{22}) \exp(-2\kappa_m d_m) \ll 1$, and using $m_{22} \simeq C \cdot (\beta - \gamma_{\rm MIM})$ from Eq. (3.17), where C is a constant and $\gamma_{\rm MIM} \equiv \beta_{\rm MIM} - j\alpha_{\rm MIM}$ is the complex propagation constant of a plasmonic or oscillatory TM mode in the MIM structure, Eq. (3.30) can be approximated as

$$\begin{aligned} r &\simeq -\frac{m'_{21}}{m'_{22}} \left[1 + \frac{m_{21}}{m_{22}} \frac{m'_{11}m'_{22} - m'_{12}m'_{21}}{m'_{22}m'_{21}} \exp(-2\kappa_m d_m) \right] \\ &= r_{\rm Otto} \left[1 + \frac{V(\beta)}{\beta - \gamma_{\rm MIM}} \right], \end{aligned} \tag{3.29}$$

where the quantity $V(\beta) = (\kappa_p \varepsilon_m / \kappa_m \varepsilon_p)[m_{21} \exp(-2\kappa_m d_m)/(C m'_{21} m'_{22})]$, using $m'_{11} m'_{22} - m'_{12} m'_{21} = \kappa_p \varepsilon_m / \kappa_m \varepsilon_p$, is a slowly varying function of β. Based on Eq. (3.29), the fractional reflected power $R = |r|^2$ can be expressed as

$$\begin{aligned} R &\simeq R_{\text{Otto}} \left\{ 1 + 2 \cdot \text{Re} \left[\frac{V(\beta)}{\beta - \gamma_{\text{MIM}}} \right] \right\} \\ &= R_{\text{Otto}} \left\{ 1 + 2 \cdot \frac{(\beta - \beta_{\text{MIM}}) \cdot \text{Re}[V(\beta)] + \alpha_{\text{MIM}} \cdot \text{Im}[V(\beta)]}{(\beta - \beta_{\text{MIM}})^2 + \alpha_{\text{MIM}}^2} \right\}. \end{aligned} \tag{3.30}$$

Equation (3.30) shows that R is similar to R_{Otto}, which has a resonance near the pole of m'_{22}, but the former has one or more extra resonances corresponding to the plasmonic or oscillatory TM modes in the MIM structure near the poles of m_{22}. Equation (3.30) also implies that if the numerator of the second component is a negative constant (i.e. $V(\beta) = V \exp(3\pi/2)$, where V is a positive constant), R/R_{Otto} has a Lorentzian-type resonance centered at $N_{\text{MIM}} = \beta_{\text{MIM}}/k_0$ and a HWHM $= \alpha_{\text{MIM}}/k_0$. Therefore, by simulating or experimentally measuring such an ATR configuration, the propagation constants and attenuation coefficients for the MIM structure can be obtained. However, because $V(\beta)$ is not a constant and the phase of $V(\beta)$ is shifted due to the material loss in the metal, the HWHM of R/R_{Otto} is not precisely equal to α_{MIM}/k_0. Moreover, the approximation $[(m_{21} m'_{12})/(m_{22} m'_{22})] \exp(-2\kappa_m d_m) = 0$ made in Eq. (3.29) also causes errors since the metal thickness d_m is finite. The detailed analysis of these errors is given in Appendix B and a step-by-step procedure for correcting for the errors is given in Appendix C.

3.5 Summary

In this chapter, the theory of TTR method is developed based on the transmission matrix formulation. It is shown that, for a waveguiding structure, the zeros of m_{22} component of the transmission matrix correspond to the guided or leaky/lossy modes. As a result, as light is incident into the structure at a resonant angle, it will cause a maximum/minimum in the transmission/reflection spectrum. However, a waveguide

mode cannot be directly excited by light incident from the transverse direction. One common way to solve this problem is by using an attenuated total reflection (ATR) configuration, which is also known as the prism coupler. In this configuration, light is coupled into the waveguide through the evanescent wave in the gap between the prism and the waveguide. Specifically, the application of the ATR configuration to an MIM structure was discussed in detail in Sec. 3.4. It was shown that resultant reflection spectrum contains a downward resonance, whose central resonant angle and width correspond to the real and imaginary part of the propagation constant of an MIM mode. This downward resonance can be extracted by subtracting out the background variation caused by the SP mode at the air gap/metal interface. More simulation results will be presented in Chapter 4, and experimental results for MIM waveguide will be presented in Chapter 5. In Chapter 6, both the simulation and experimental results for multimode MIM waveguides will be presented.

CHAPTER 4

THEORETICAL PERFORMANCE OF THE TTR METHOD

In this chapter, the simulation performance and accuracy of the TTR method applied to various leaky/lossy waveguides and MIM waveguides are examined. The TTR simulation results are compared with rigorous results calculated by the Argument Principle Method (APM) [91]. The first example chosen is a multimode AntiResonant Reflecting Optical Waveguide (ARROW) structure which supports numerous modes with nearly equal effective mode indices. This case demonstrates the performance of the TTR method in detecting all of the overlapping leaky modes. The second example is a lossy thin-film waveguide with a 1 μm cladding layer and a high-index substrate. This case demonstrates the performance of the TTR method in detecting a mode that is simultaneously leaky and lossy. The third example is an MIM (silver-oxide-silver) structure with a 50 nm core at $\lambda = 1.55$ μm. This structure has a small core size and a higher β_{MIM}, therefore the gap between the prism and the MIM structure is filled with a high-index material (e.g. fluid) to facilitate the light coupling. The fourth example is another MIM (silver-air-silver) structure, which has a 200 nm core at $\lambda = 0.6328$ μm. A sensitivity analysis is performed on this case by using various thicknesses of air gap and top metal cladding, both of which are difficult to measure precisely experimentally. The simulations show that the results obtained by the TTR method are insensitive to these two parameters, in the case that the weak coupling condition [47, 87–89] is satisfied.

4.1 ARROW Structure

ARROWs are multilayer waveguides that are primarily used to eliminate high leakage losses in waveguides formed on the top of higher refractive index substrates [92]. ARROWs utilize thin and highly reflective layers between the guiding layer and the substrate to reduce the ARROW mode radiation losses. In this particular case [Fig. 4.1(a)], the original cover is air, therefore a high-index layer must be added above the air layer to excite leaky modes with effective indices larger than 1.0. Since the effective indices of the modes of interest are smaller than 1.46, the refractive index of the added layer is chosen to be 1.46. The thickness of the air gap, d_a, is chosen to be 0.5λ to achieve the appropriate coupling strength. Figure 4.1(b) shows the structure with an added high-index layer n_c' that is used in the TTR simulation. The freespace wavelength of operation for this structure is 0.6328 μm.

The angular reflection power spectrum for the ARROW structure with the added high-index layer [Fig. 4.1(b)] is given in Table 4.1 and in Fig. 4.2. For two modes that are close in effective index, such as the TE_2 and TE_3 modes, the values of β' and α' can be determined by fitting the two resonances with the product of two Lorentzian

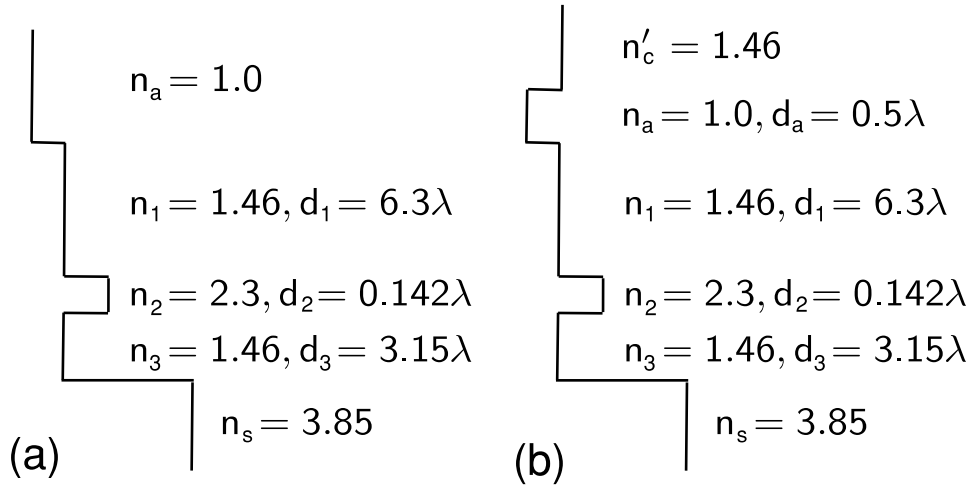

Figure 4.1: (a) Schematic diagram of the ARROW structure in [93]. (b) The ARROW structure loaded with a high-index layer n_c'.

functions or alternatively by using the HWHM obtained from the side of the resonance away from the overlap region. The "prime" indicates the values obtained by the TTR method. It is shown that the TTR simulation results are in good agreement with APM ones for all the leaky modes. However, for overlapping modes, for example, the TE_2 and TE_3 modes, the accuracy of the TTR simulation result is slightly reduced. Nevertheless, even for the worst case for this structure, the error of the TTR method is still $< 0.1\%$ for the real parts and $\lesssim 10\%$ for the imaginary parts of the propagation constants, compared to the unperturbed propagation constants, β and α, respectively, as shown in Table 4.1. The β and α values are calculated by the rigorous APM method.

Table 4.1: TE_n leaky mode normalized complex propagation constants $\gamma'_n/k_0 \equiv (\beta'_n - j\alpha'_n)/k_0 = N'_{\text{eff}} - j\text{HWHM}_n$ calculated by the TTR method, for the ARROW structure shown in Fig. 4.1(b). The rigorous complex propagation constant for the TE_n modes of the ARROW structure without prism loaded [Fig. 4.1(a) or Fig. 4.1(b) with $d_a = \infty$] is calculated by the APM.

Mode TE_n	APM ($d_a = \infty$)	TTR Method ($d_a = 0.5\lambda$)
TE_1	$1.45794 - j5.419 \times 10^{-8}$	$\simeq 1.45794$
TE_2	$1.45192 - j5.287 \times 10^{-5}$	$1.45192 - j4.97 \times 10^{-5}$
TE_3	$1.45117 - j1.920 \times 10^{-4}$	$1.45122 - j1.78 \times 10^{-4}$
TE_4	$1.44137 - j4.375 \times 10^{-6}$	$1.44137 - j5.47 \times 10^{-6}$
TE_5	$1.42741 - j2.137 \times 10^{-4}$	$1.42740 - j2.02 \times 10^{-4}$
TE_6	$1.42445 - j7.667 \times 10^{-4}$	$1.42462 - j7.15 \times 10^{-4}$
TE_7	$1.40768 - j3.358 \times 10^{-5}$	$1.40769 - j3.96 \times 10^{-5}$
TE_8	$1.38565 - j4.897 \times 10^{-4}$	$1.38563 - j4.70 \times 10^{-4}$
TE_9	$1.37900 - j1.726 \times 10^{-3}$	$1.37934 - j1.64 \times 10^{-3}$
TE_{10}	$1.35567 - j1.286 \times 10^{-4}$	$1.35569 - j1.52 \times 10^{-4}$
TE_{11}	$1.32510 - j8.935 \times 10^{-4}$	$1.32505 - j8.74 \times 10^{-4}$
TE_{12}	$1.31320 - j3.095 \times 10^{-3}$	$1.31370 - j3.01 \times 10^{-3}$
TE_{13}	$1.28330 - j3.531 \times 10^{-4}$	$1.28330 - j4.31 \times 10^{-4}$
TE_{14}	$1.24321 - j1.444 \times 10^{-3}$	$1.24310 - j1.48 \times 10^{-3}$
TE_{15}	$1.22418 - j4.949 \times 10^{-3}$	$1.22474 - j5.05 \times 10^{-3}$
TE_{16}	$1.18720 - j8.063 \times 10^{-4}$	$1.18713 - j1.07 \times 10^{-3}$
TE_{17}	$1.13592 - j2.151 \times 10^{-3}$	$1.13556 - j2.46 \times 10^{-3}$
TE_{18}	$1.10700 - j7.469 \times 10^{-3}$	$1.10728 - j8.34 \times 10^{-3}$
TE_{19}	$1.06241 - j1.665 \times 10^{-3}$	$1.06138 - j2.66 \times 10^{-3}$

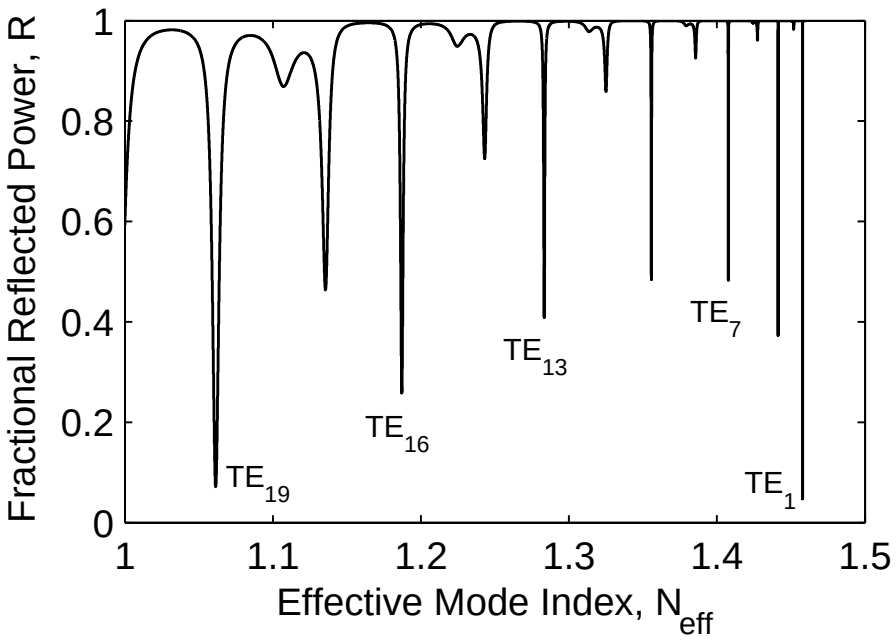

Figure 4.2: Angular reflection power spectrum for the ARROW structure in Fig. 4.1(b). The x-axis is the effective index $N_{\text{eff}} \equiv \beta/k_0 = n_p \sin\theta$ and the y-axis is the fraction of power reflected.

Figure 4.3(a) illustrates the TTR simulation results for $d_a = 0.3\lambda$ to 0.7λ. A smaller d_a produces a larger perturbation in the original waveguide and theoretically, a larger error. The perturbations in the normalized propagation constants, $|\Delta\beta|/k_0 \equiv |(\beta' - \beta)|/k_0$ and $\Delta\alpha/k_0 \equiv (\alpha' - \alpha)/k_0$, are calculated by APM and are shown in Fig. 4.3(b) and (c) as a function of d_a/λ. The $\Delta\beta$ values can be positive or negative for various modes, but $\Delta\alpha$ values are always positive because extra losses are introduced by the loading of the high-index layer. For a given leaky mode, the ratio $\Delta\alpha/\alpha$ can then be regarded as the ratio of the power leaking into the loading high-index layer to the power leaking into the substrate. It is found that $|\Delta\beta|$ and α are approximately in proportion to $\exp(-2\kappa_a d_a)$, which is consistent with the values calculated for the prism-loaded thin-film waveguides [46]. However, as d_a increases, the fraction of power reflected approaches unity due to the decrease in coupling strength. Therefore, the reflection resonance of a given mode may not be detectable when the air gap is so large that only a small amount of light is coupled into the waveguide.

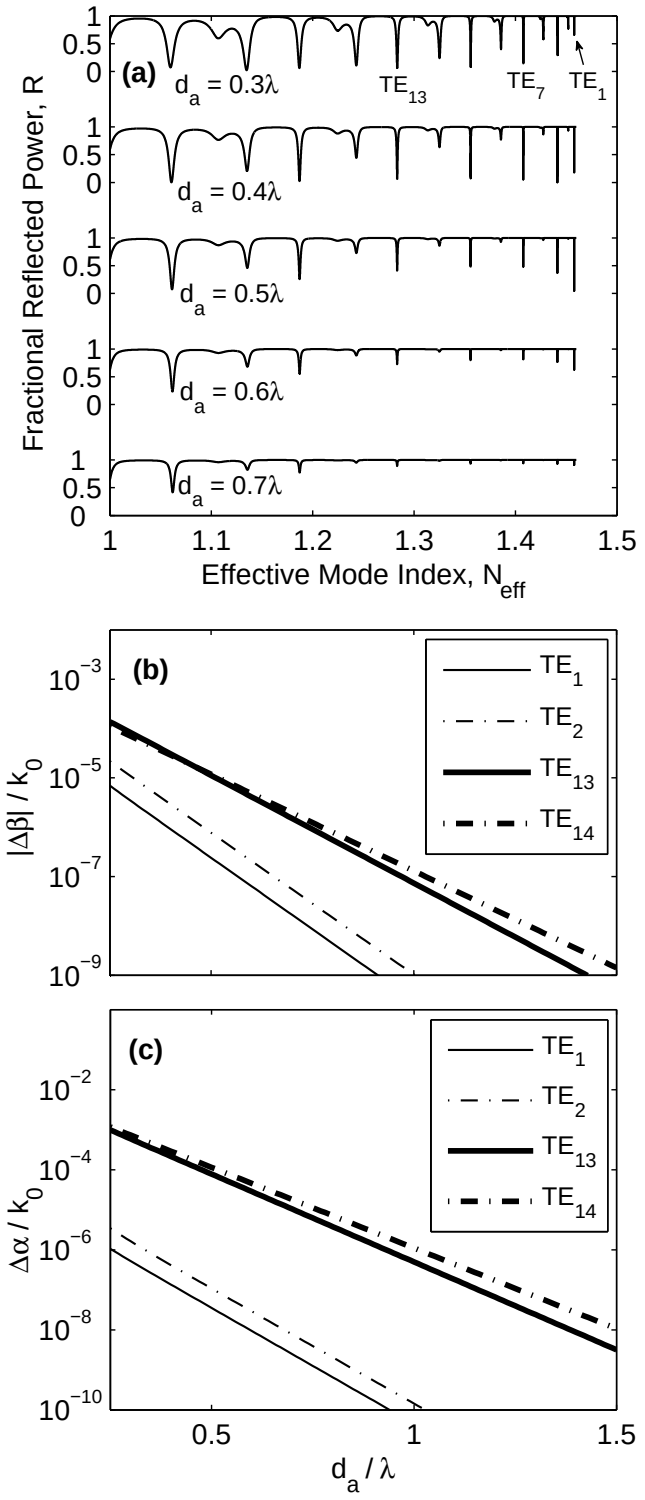

Figure 4.3: (a) Angular reflection power spectra for the ARROW structure in Fig. 4.1(b) with various d_a values. (b) Absolute error in the real part of the normalized propagation constant, $|\Delta\beta|/k_0$, as a function of d_a/λ for some selected TE modes for the ARROW structure. (c) Error in normalized attenuation coefficient, $\Delta\alpha/k_0$, as a function of d_a/λ for some selected TE modes for the ARROW structure.

Figure 4.4 shows the comparison of the exact TE_1 to TE_4 mode profiles with the field profiles excited at the corresponding resonant angles. Both the exact mode profiles and the resonant field profiles are calculated for the perturbed structure in Fig. 4.1(b). The agreement of the profiles is excellent for low-loss modes such as the TE_1 and TE_4 modes; the agreement degenerates as the leakage of the mode increases, such as in the case of the TE_3 mode. It should also be noted that the profiles will not match in the incident region in general, since for the resonant field profile there is a partial standing wave and for the mode profile there is only a wave propagating away from the waveguide. A more detailed discussion is provided in Appendix A.

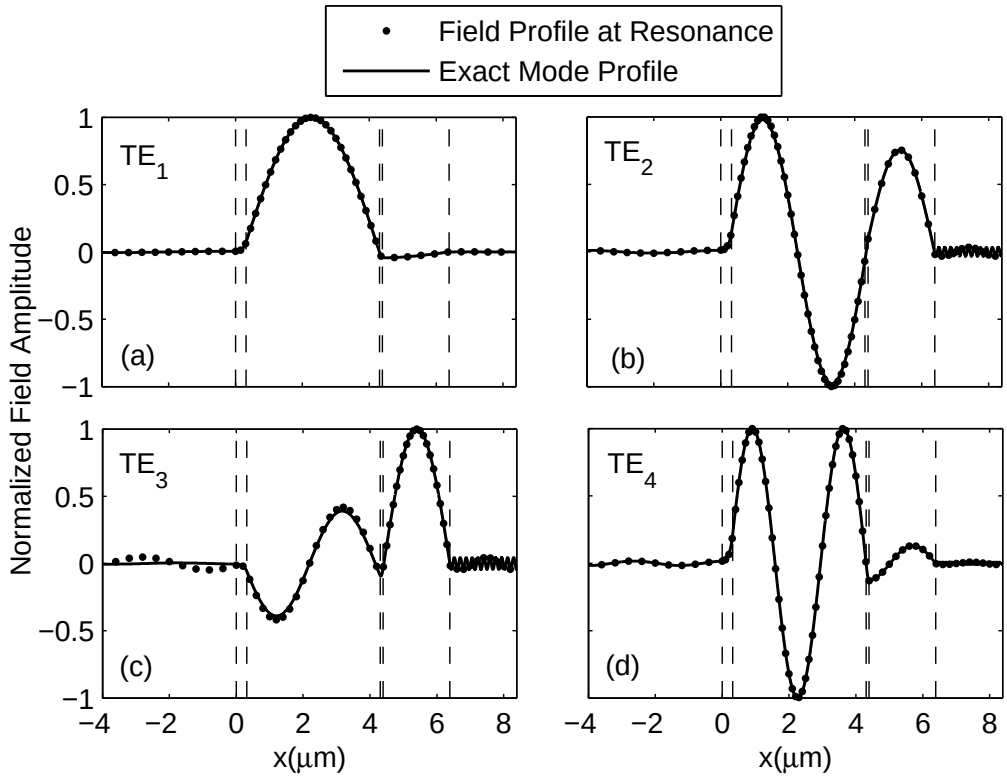

Figure 4.4: Comparison of the exact mode profiles with the field profiles excited at the corresponding resonant angles for the (a) TE_1, (b) TE_2, (c) TE_3, and (d) TE_4 modes of the ARROW structure in Fig. 4.1(b).

4.2 Leaky and Lossy Thin-Film Waveguide Structure

Figure 4.5(a) shows a leaky and lossy thin-film waveguide structure with a 6 μm film $\widetilde{n}_f = 1.50 - jn_{\text{I}}$, where n_{I} is the imaginary part of the refractive index, on top of a 1 μm cladding ($n_{cl} = 1.46$) and a high-index substrate. For a dielectric material, the value of n_{I} is approximately proportional to the absorption loss in the material. To apply the TTR method, a high-index layer with $n'_c = 1.5$ is added above the original cover (i.e. air). The air-gap thickness is chosen to be 0.5λ to achieve the appropriate coupling strength. Figure 4.5(b) shows the perturbed structure used in the TTR simulation. The freespace wavelength of operation for this structure is 1.55 μm.

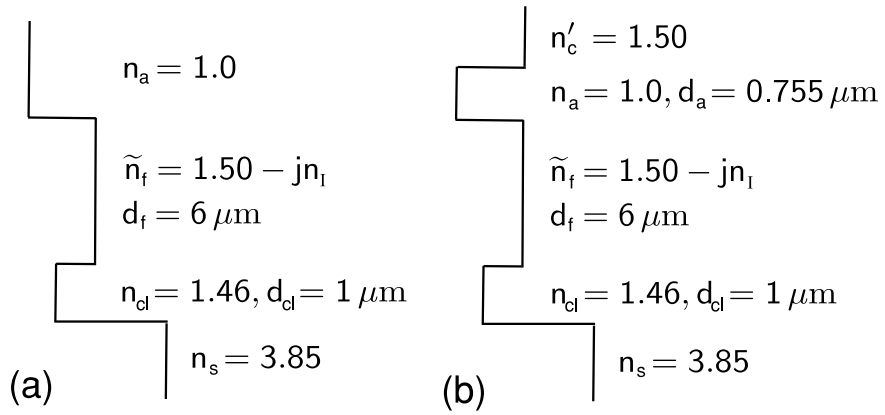

Figure 4.5: (a) Schematic diagram of a simultaneously leaky and lossy thin-film waveguide structure with a 1 μm cladding and a high-index substrate. (b) The leaky and lossy waveguide structure loaded with an added high-index layer.

The angular reflection power spectrum for the structure in Fig. 4.5(b) is given in Table 4.2 and Fig. 4.6. It is shown that the TTR simulation results are in good agreement with APM for all the leaky and lossy modes. For $n_{\text{I}} = 1 \times 10^{-5}$, the errors of the TTR method are $< 1\%$ for the imaginary parts of the complex propagation constants, α'; for $n_{\text{I}} = 1 \times 10^{-3}$, the errors are $< 5\%$ for α' values. The errors in the real parts of the complex propagation constants, β', are virtually zero in both cases.

Table 4.2: TE_n leaky mode normalized complex propagation constants $\gamma'_n/k_0 \equiv (\beta'_n - j\alpha'_n)/k_0 = N'_{\text{eff}} - j\text{HWHM}_n$ calculated by the TTR method, for the leaky and lossy waveguide structure shown in Fig. 4.5(b). The rigorous complex propagation constant for the TE_n modes of the leaky and lossy waveguide structure without prism loaded [Fig. 4.5(a) or Fig. 4.5(b) with $d_a = \infty$] is calculated by APM.

Mode TE_n	APM ($d_a = \infty, n_{\text{I}} = 1 \times 10^{-5}$)	TTR Method ($d_a = 0.5\lambda, n_{\text{I}} = 1 \times 10^{-5}$)
TE_0	$1.49574 - j2.960 \times 10^{-5}$	$1.49574 - j2.970 \times 10^{-5}$
TE_1	$1.48297 - j1.003 \times 10^{-4}$	$1.48297 - j1.012 \times 10^{-4}$
TE_2	$1.46170 - j2.649 \times 10^{-4}$	$1.46171 - j2.683 \times 10^{-4}$
Mode TE_n	APM ($d_a = \infty, n_{\text{I}} = 1 \times 10^{-3}$)	TTR Method ($d_a = 0.5\lambda, n_{\text{I}} = 1 \times 10^{-3}$)
TE_0	$1.49574 - j1.016 \times 10^{-3}$	$1.49569 - j1.066 \times 10^{-3}$
TE_1	$1.48297 - j1.074 \times 10^{-3}$	$1.48296 - j1.088 \times 10^{-3}$
TE_2	$1.46171 - j1.217 \times 10^{-3}$	$1.46169 - j1.229 \times 10^{-3}$

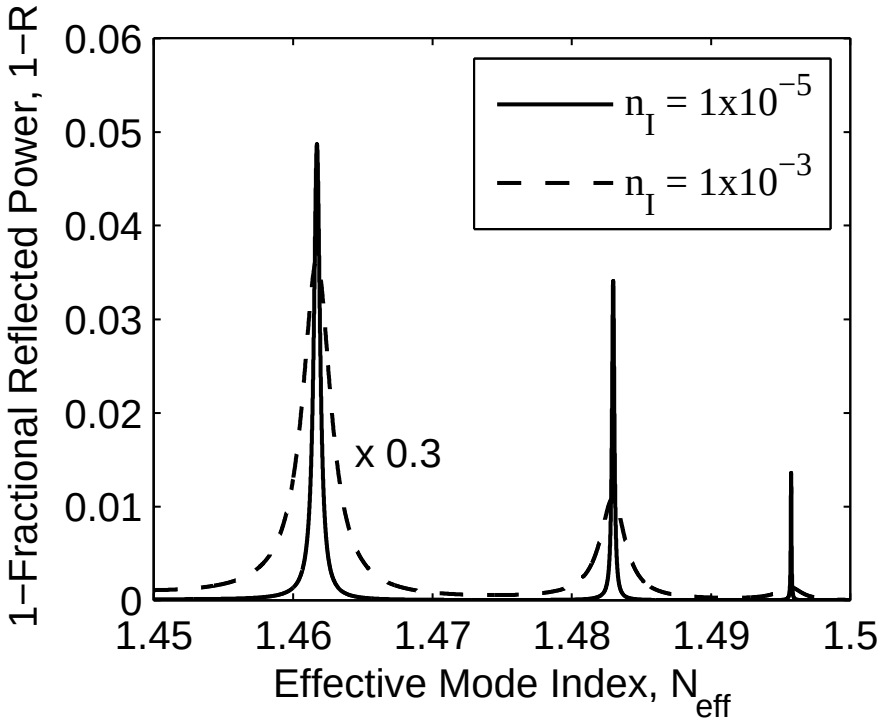

Figure 4.6: Angular reflection power spectrum for the leaky and lossy waveguide structure in Fig. 4.5(b) with $n_{\text{I}} = 1 \times 10^{-5}$ and 1×10^{-3}. The curve for $n_{\text{I}} = 1 \times 10^{-3}$ has been multiplied by 3.33.

Figure 4.7 shows the comparison of the exact TE_0 to TE_2 mode profiles with the field profiles excited at the corresponding resonant angles for the structure in Fig. 4.5(b) with $n_{\text{I}} = 1 \times 10^{-5}$. The agreement of the profiles is excellent for all the modes. This case shows the performance of the TTR method in detecting a mode that is simultaneously leaky and lossy.

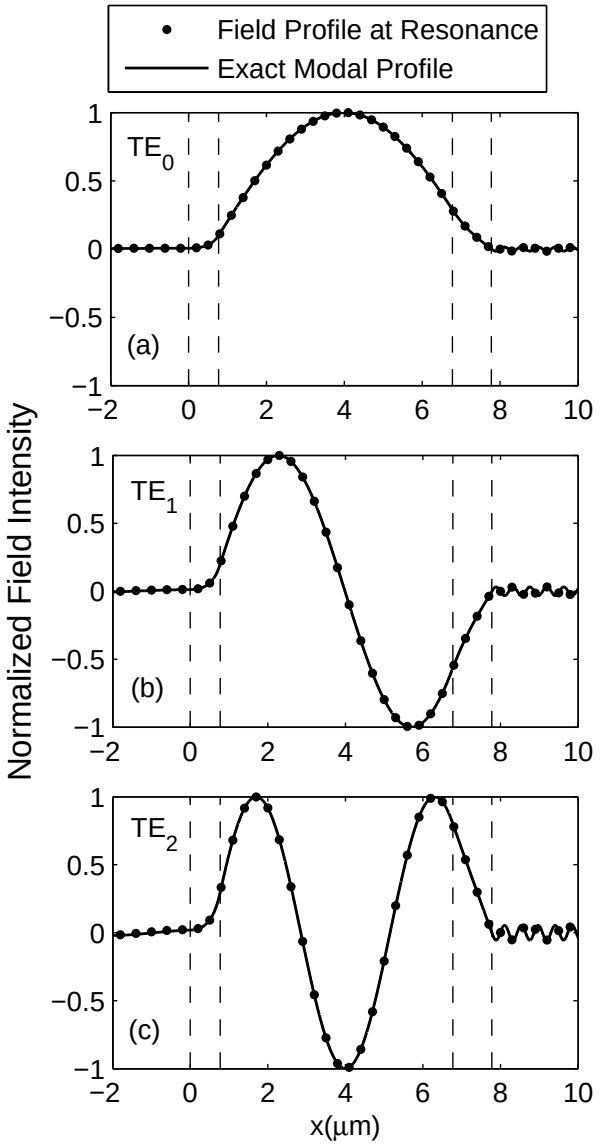

Figure 4.7: Comparison of the exact mode profiles with the field profiles excited at the corresponding resonant angles for the (a) TE_0, (b) TE_1, and (c) TE_2 modes of the leaky and lossy waveguide structure in Fig. 4.5(b) with $n_{\text{I}} = 1 \times 10^{-5}$.

4.3 Silver-Oxide-Silver Structure

Figure 4.8 shows an MIM structure with a 50 nm SiO_2 core and silver claddings. At $\lambda = 1.55$ μm, the silver has a complex dielectric constant $\widetilde{\varepsilon}_{\text{Ag}} = -86.6 - j8.74$, or equivalently a refractive index $\widetilde{n}_{\text{Ag}} = 0.469 - j9.32$ [90]. The normalized propagation constant γ_{MIM}/k_0 of the TM_0 mode calculated by APM is $2.11140 - j0.02967$, which corresponds to a loss of 1.04 dB/μm. The relatively high N_{MIM} in this case is the result of the higher index and small size of the core insulator. Owing to the high N_{MIM}, the gap between the prism and the MIM structures is filled with fluid with $n_g = 1.5$ to enhance the coupling strength.

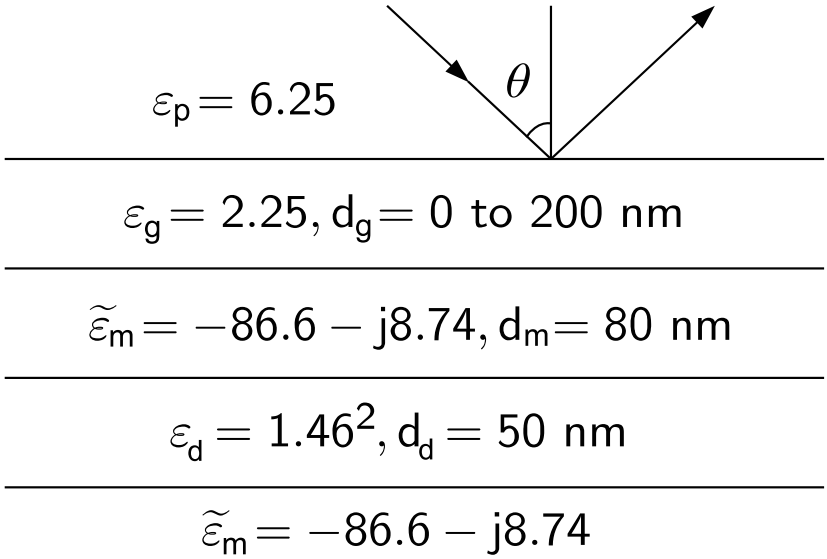

Figure 4.8: Schematic diagram of a prism-loaded MIM structure with a 50 nm SiO_2 core. The metal is silver with complex dielectric constant $\widetilde{\varepsilon}_m = -86.6 - j8.74$, or equivalently refractive index $\widetilde{n}_m = 0.469 - j9.32$ [90]. The operating wavelength is 1.55 μm.

In order to apply the TTR method to this structure, one of the silver claddings is made thinner and a prism is placed adjacent to the MIM structure. In this case, the skin depth (i.e. the distance in which the field amplitude attenuated by a factor $1/e$) of silver is $\delta \simeq 26$ nm, so d_m is chosen to be 80 nm to allow the appropriate coupling strength, as shown in Fig. 4.8. The prism index n_p has to be sufficiently higher than

N_{MIM} and is chosen to be 2.5.

The angular reflection power spectrum for the structure in Fig. 4.8 is shown in Fig. 4.9 and summarized in Table 4.3. The simulations are performed at various fluid gap thicknesses d_g, because, experimentally, d_g is difficult to quantify precisely. The angular reflection power spectrum for the Otto configuration (Fig. 4.8 with $d_m = \infty$) is shown in Fig. 4.10 for comparison. It is clear that R_{Otto} (Fig. 4.10) is simply the background variation in R (Fig. 4.9). According to the analysis in Sec. 3.4, the effective index N'_{MIM} of the TM_0 mode is located at the minimum of the R/R_{Otto} resonance and the normalized attenuation coefficient $\alpha'_{\mathrm{MIM}}/k_0$ is equal to the HWHM, where the prime denotes results obtained by the TTR method, in contrast to the rigorous results obtained by APM. R_{Otto} can also be obtained by qualitatively subtracting out the TM_0 resonance from R for each d_g. It is shown in Table 4.3 that the results of the TTR method are in good agreement with the the rigorous result. The error in α'_{MIM} is less than 5% for $d_g = 100$ and 200 nm and less than 10% for $d_g = 0$ and 50 nm.

Following Appendix B, the error in α'_{MIM} can be estimated. The error due to finite thickness of the metal layer d_m is usually smaller than the half resonance strength of R/R_{Otto} as $d_g \to 0$, that is, $\lesssim 6\%$. Following the procedure described in Appendix C, the phase shift is fitted as $\Delta\phi_V \simeq 20^\circ$ and the normalized attenuation coefficient after correction is $\alpha''_{\mathrm{MIM}}/k_0 \simeq 0.0297$. The double prime indicates TTR results after the correction procedure described in Appendix is applied. The detailed fitting procedure for this case is given in Appendix C. It should be noted that no explicit information about d_g or d_m is needed in this correction procedure.

Table 4.3: Normalized complex propagation constant γ'_{MIM}/k_0 calculated by the TTR method, for the MIM structure shown in Fig. 4.8. The rigorous complex propagation constant for the TM_0 mode of the MIM structure without prism loaded ($d_m = \infty$) is $\gamma_{\text{MIM}}/k_0 = 2.11140 - j0.02967$.

d_g	d_m	TTR Method
0	80 nm	$2.1179 - j0.0326$
50 nm	"	$2.1191 - j0.0329$
100 nm	"	$2.1178 - j0.0305$
200 nm	"	$2.1167 - j0.0296$

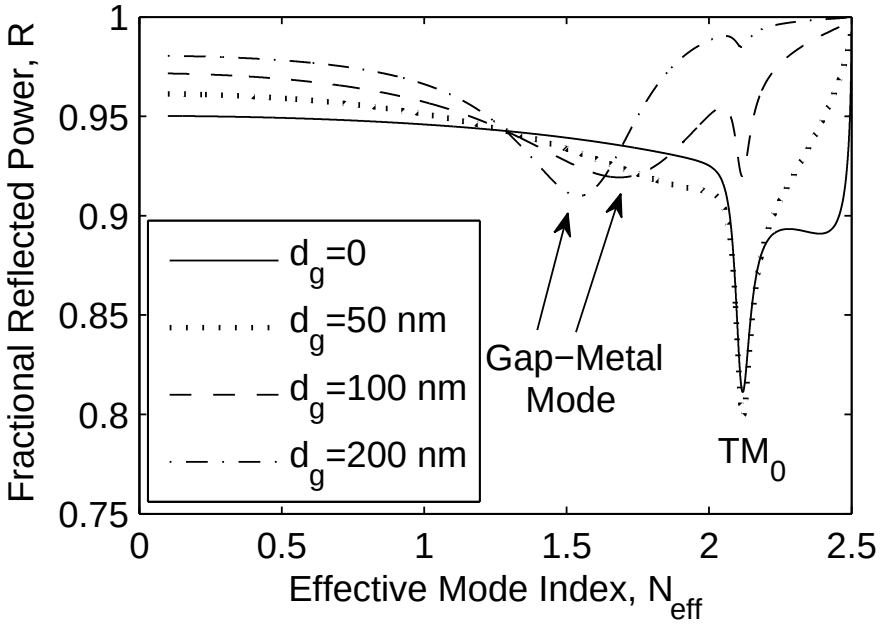

Figure 4.9: Angular reflection power spectrum for the structure in Fig. 4.8 with $d_m = 80$ nm. The resonances corresponding to the fluid gap-metal plasmonic mode and the TM_0 mode of the MIM structure are labeled.

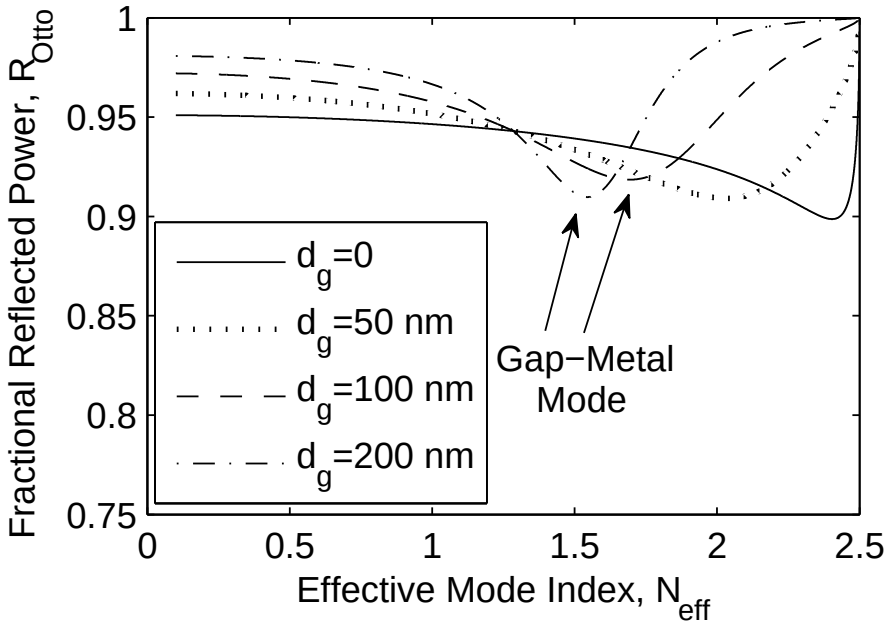

Figure 4.10: Angular reflection power spectrum for the structure in Fig. 4.8 with $d_m = \infty$. The structure is practically an Otto configuration.

4.4 Silver-Air-Silver Structure

Figure 4.11 shows an MIM structure with a 200 nm air core and silver claddings. At $\lambda = 0.6328$ μm, the silver has a complex dielectric constant $\widetilde{\varepsilon}_{\rm Ag} = -15.9 - j1.07$, or equivalently a refractive index $\widetilde{n}_{\rm Ag} = 0.135 - j3.99$ [90]. In this case, the skin depth of silver is $\delta \simeq 25$ nm. The normalized propagation constant $\gamma_{\rm MIM}/k_0$ of the $\rm TM_0$ mode calculated by APM is $1.13412 - j0.00505$, which corresponds to a loss of 0.44 dB/μm.

4.4.1 Sensitivity Analysis

In a TTR measurement, the thicknesses of the air gap (d_g) and the top metal cladding (d_m) are difficult to measure precisely: the former is controlled by the pressure between the prism and the MIM structure and cannot be straightforwardly translated into corresponding d_g values, and the latter is subject to an imprecise metal evaporation process and could be reduced due to an indentation on the soft metal surface created by the pressure between the prism and the MIM structure. Therefore, it is

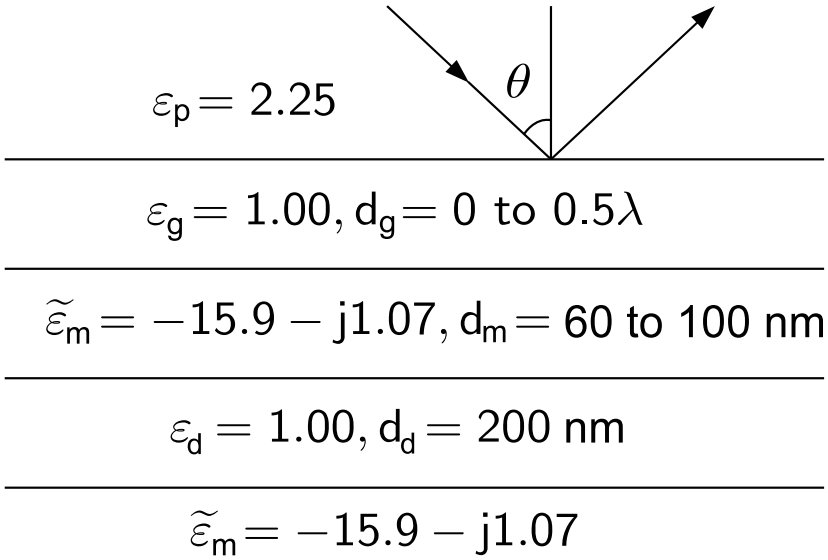

Figure 4.11: Schematic diagram of a prism-loaded MIM structure with a 200 nm air core. The metal is silver with complex dielectric constant $\widetilde{\varepsilon}_m = -15.9 - j1.07$, or equivalently refractive index $\widetilde{n}_m = 0.135 - j3.99$ [90]. The operating wavelength is 0.6328 μm.

important to ensure that the results obtained by the TTR method are insensitive to these parameters.

To determine the sensitivity when applying the TTR method to the MIM structure, a series of MIM structures with various metal cladding thicknesses d_m and air gap thicknesses d_g were simulated. The top metal cladding thicnkess d_m is varied from 60 nm to 100 nm, and the air gap thickness d_g is varied from 0 to 0.5λ. The prism index n_p has to be suitably larger than N_{MIM} and is chosen to be 1.5.

The angular reflection power spectra for the structure in Fig. 4.11 with $d_m =$ 100 nm, 80 nm, and 60 nm are plotted as functions of the effective index N_{eff} in Fig. 4.12, 4.13, and 4.14 respectively, and summarized in Table 4.4. The angular reflection power spectrum for the Otto configuation (Fig. 4.11 with $d_m = \infty$) is shown in Fig. 4.15. It is clear that R_{Otto} (Fig. 4.15) is simply the background variation in R (Fig. 4.12, 4.13, and 4.14). The N'_{MIM} and α'_{MIM} are obtained in the same manner as in Sec. 4.3. It is shown in Table 4.4 that, for the cases of $d_m = 100$ nm and 80 nm,

the results obtained by the TTR method are in good agreement with the rigorous result. The errors in α'_{MIM} are less than 5% in the case of $d_m = 100$ nm and are less than 10% in the case of $d_m = 80$ nm. The effective indices are also correct down to 10^{-3} in these cases. However, for the case of $d_m = 60$ nm, the error is high for all d_g values that are used in the simulation and is almost 40% when $d_g = 0.25\lambda$. The effective indices are also relatively incorrect compared with the cases of $d_m = 100$ nm and 80 nm. The high error is due to the small top metal cladding and therefore overly strong perturbation. Smaller d_m causes a larger TM_0 resonance intensity and stronger perturbation, in agreement with the analysis in Sec. 3.3 and 3.4. That is, the weak coupling condition [47,87–89] is not satisfied. The strong perturbation can be easily verified by noting either the strong resonance in the reflection spectrum or the clear dependence of α'_{MIM}/k_0 as a function of d_g as shown in Table 4.4. In the case that the weak coupling condition is satisfied (e.g. $d_m = 80$ nm or 100 nm), the dependence of α'_{MIM}/k_0 on d_g is indistinct.

Based on the simulation results, the top metal cladding should have a thickness larger than 3 skin depths to satisfy the weak coupling condition. Otherwise, the results obtained by the TTR method would be distorted by the strong perturbation. Provided this requirement is satisfied, the results obtained by the TTR method are shown to be insensitive to d_m and d_g. However, too thick a top metal cladding thickness leads to weak resonances and affects the accuracy of the measurement. Typically, a d_m value between 3 to 4 skin depths is optimal.

On the other hand, as described in Appendix B, the error in α'_{MIM} can be estimated. In the case of $d_m = 100$ nm, the error due to the finite thickness of the metal layer d_m is $\lesssim 2\%$. The phase shift is fitted as $\Delta\phi_V \simeq 15^\circ$ and the normalized attenuation coefficient after correction is $\alpha''_{\text{MIM}}/k_0 \simeq 0.00515$. Similarly, in the case of $d_m = 80$ nm, the error due to finite d_m is $\lesssim 8\%$. The fitted $\Delta\phi_V \simeq 15^\circ$ and $\alpha''_{\text{MIM}}/k_0 \simeq 0.0051$. It is shown that in both cases, the α''_{MIM}'s have less than 2% of error. It should be noted

that no explicit information about d_g or d_m is needed in the correction procedure.

Table 4.4: Normalized complex propagation constant γ'_{MIM}/k_0 calculated by the TTR method, for the MIM structure shown in Fig. 4.11. The rigorous complex propagation constant for the TM_0 mode of the MIM structure without prism loaded ($d_m = \infty$) is $\gamma_{\text{MIM}}/k_0 = 1.13412 - j0.00505$.

d_g	d_m	TTR Method
0	100 nm	$1.1348 - j0.0053$
0.25λ	"	$1.1350 - j0.0053$
0.50λ	"	$1.1348 - j0.0051$
0	80 nm	$1.1349 - j0.0054$
0.25λ	"	$1.1352 - j0.0055$
0.50λ	"	$1.1351 - j0.0052$
0	60 nm	$1.1352 - j0.0061$
0.25λ	"	$1.1373 - j0.0070$
0.50λ	"	$1.1375 - j0.0059$

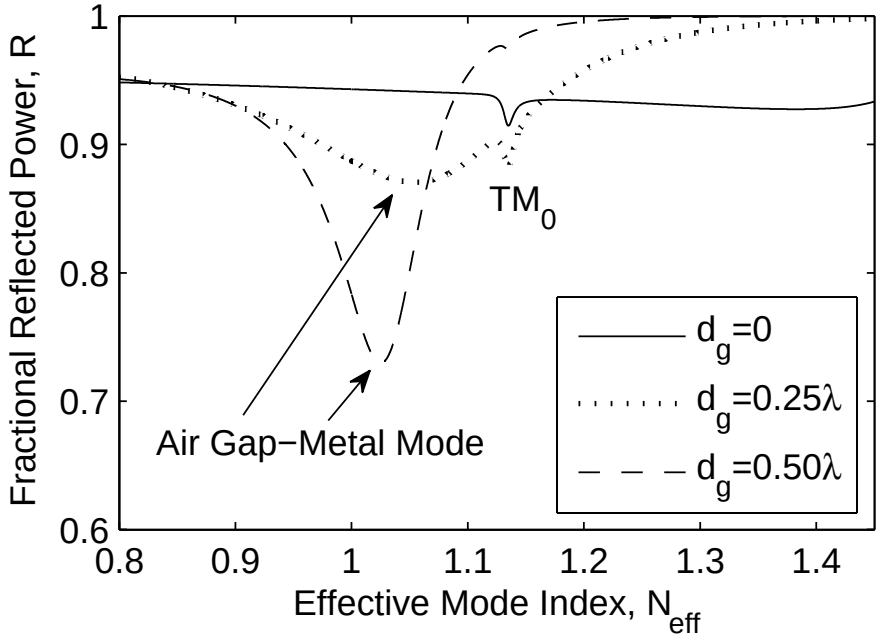

Figure 4.12: Angular reflection power spectrum for the structure in Fig. 4.11 with $d_m = 100$ nm. The resonances corresponding to the air gap-metal plasmonic mode and the TM_0 mode of the MIM structure are labeled.

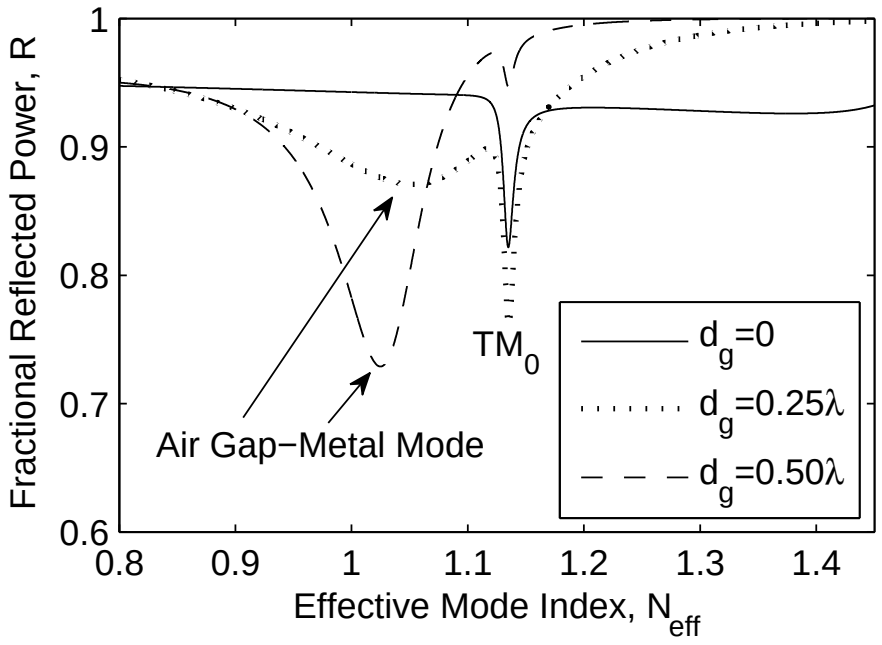

Figure 4.13: Angular reflection power spectrum for the structure in Fig. 4.11 with $d_m = 80$ nm.

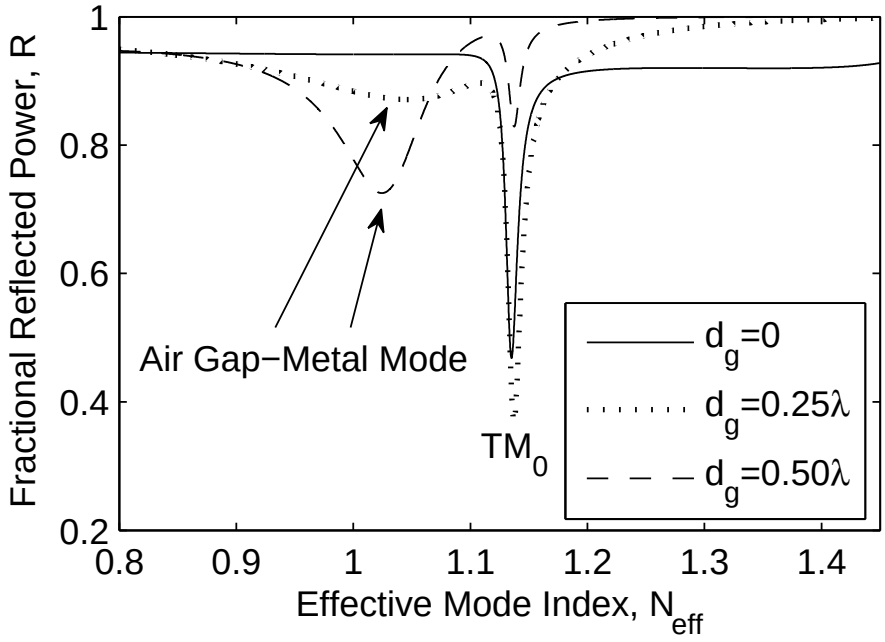

Figure 4.14: Angular reflection power spectrum for the structure in Fig. 4.11 with $d_m = 60$ nm.

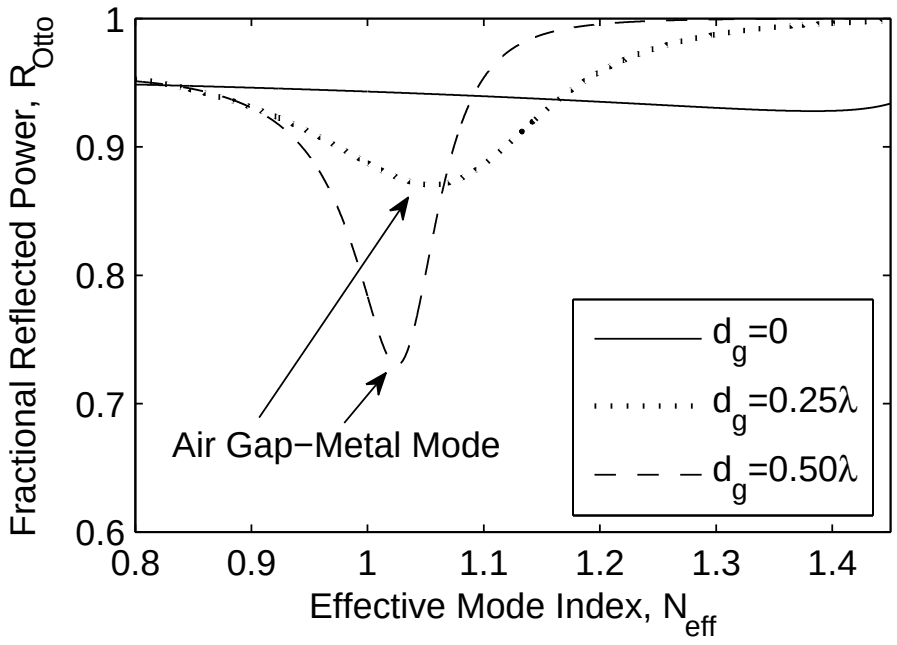

Figure 4.15: Angular reflection power spectrum for the structure in Fig. 4.11 with $d_m = \infty$. This structure is practically an Otto configuration.

4.5 Summary

In this chapter, the TTR simulations were applied to various waveguide structures, including a multimode AntiResonant Reflecting Optical Waveguide (ARROW), a lossy thin-film waveguide, and two MIM waveguides. All the TTR simulation results agree well with the rigorous theoretical propagation constants of the waveguides. It is shown that the TTR method is capable of detecting multiple modes with nearly equal effective mode indices (see Sec. 4.1) and detecting modes that are simultaneously leaky and lossy (see Sec. 4.2). When applying the TTR method to an MIM structure, one side of the metal claddings must be made thinner for light coupling. The thickness should be around 3 to 4 skin depths for appropriate coupling strength. Thin metal claddings will cause strong perturbation from the prism and distort the results, while thick claddings will lead to weak resonances. The resultant reflection spectra typically contain resonances corresponding to the SP mode at the air gap/metal interface and

the MIM plasmonic mode. The affect of the former can be removed by subtracting out the background variation, and the real and imaginary part of the propagation constant can then be obtained from the location and width of the resonance of the MIM plasmonic mode.

In a TTR measurement of an MIM structure, the thicknesses of the air gap and the top metal cladding are difficult to measure precisely, which may induce some concerns about the validity of the results. However, Sec. 4.4.1 shows that the results obtained by the TTR method are insensitive to these two parameters, provided the thickness of the metal cladding is sufficiently large. The fact that the TTR method is insensitive to these parameters is very important for its experimental application.

CHAPTER 5

EXPERIMENTAL VERIFICATION OF THE TTR METHOD

In this chapter, TTR measurement results for MIM (Au-SiO_2-Au) waveguides with subwavelength guiding layers are presented and discussed in detail. Two planar waveguide structures with 50 nm/200 nm SiO_2 cores were fabricated and investigated. The fabrication and characterization processes are discussed in detail. The TTR measurements for the MIM waveguides were performed using the Metricon Model 2010 Prism Coupler. At $\lambda = 1.55$ μm , the measured propagation lengths are 5.7 and 18 μm, respectively, in close agreement with the theoretical predictions.

5.1 Fabrication of MIM Structures

The MIM waveguides used in this chapter were fabricated using the facilities in the Nanotechnology Research Center cleanroom. The Au cladding layers were deposited by using the e-beam evaporator at a deposition rate of 0.05 nm/s. The SiO_2 cores were deposited using plasma-enhanced chemical vapor deposition (PECVD) at 250 °C, 900 mTorr, with 400 SCCM SiH_4 (2%) in N_2, 900 SCCM N_2O, and radio frequency (RF) power = 10 W. SCCM denotes cubic centimeters per minute at standard temperature and pressure. In this section, the optical properties of Au and SiO_2 will be reviewed.

5.1.1 Optical Constants of Silicon Dioxide

Silicon dioxide (chemical formula: SiO_2), also known as silica, is an extremely important optical material. For example, fused silica is the primary constituent in most glasses, which are used extensively in optical components such as prisms, lens, and optical fibers. The refractive index of fused silica is 1.470 at $\lambda = 404.7$ nm, 1.457 at

$\lambda = 632.8$ nm and 1.444 at $\lambda = 1550$ nm [90]. Because fused silica is amorphous, it does not exhibit optical anisotropy that is characteristic of many crystals [49]. It is worth mentioning that the dispersion is relatively small at visible and near-infrared wavelengths. Moreover, SiO_2 is transparent at wavelengths ranging from around 200 nm in the ultraviolet to beyond 2000 nm in the infrared [49].

Quartz, the second most abundant mineral in the Earth's continental crust, is the crystalline form of SiO_2. Unlike the amorphous fused silica, quartz is anisotropic. For α-quartz at $\lambda = 404.7$ nm, $n_o = 1.557$ and $n_e = 1.567$; at $\lambda = 632.8$ nm, $n_o = 1.542$ and $n_e = 1.551$; at $\lambda = 1550$ nm, $n_o = 1.528$ and $n_e = 1.536$.

In this work, SiO_2 is used as the insulator core of the MIM waveguides because of its insulating property and transparency at visible and near-infrared wavelengths. The SiO_2 layers were deposited using the Unaxis PECVD in the Nanotechnology Research Center cleanroom. The chemical equation for this deposition can be expressed as

$$SiH_4 + 2N_2O \longrightarrow SiO_2 + 2H_2 + 2N_2. \tag{5.1}$$

In this work, the deposition occurred at 250 °C, 900 mTorr, with 400 SCCM SiH_4 (2%) in N_2, 900 SCCM N_2O, and RF power = 10 W at 13.56 MHz. Although the refractive indices of fused silica and quartz are readily available, the refractive index of SiO_2 deposited by PECVD varies with the deposition conditions. Under some conditions, for example at lower RF power or smaller flow ratio of N_2O/SiH_4, the deposited oxide may contain insufficient oxide (also referred to as "Si-rich") [94, 95]. That is, the oxide has a chemical formula $SiO_{x<2}$, or equivalently, partially contains silicon monoxide (chemical formula: SiO), whose refractive index is between 1.85-2.15 from near-infrared to the visible spectrum [90]. As a result, the $SiO_{x<2}$ has a higher refractive index than regular fused silica. Figure 5.1 [94] and 5.2 [96] show the refractive index (measured at $\lambda = 632.8$ nm) variation of PECVD oxide deposited at various RF power. In the present case, the RF power = 10 W, which is relatively small, therefore a higher refractive index is expected.

In order to determine the refractive index of the PECVD oxide in the present case, a PECVD oxide thin film (deposition time = 100 min, thickness $\simeq 3$ μm) deposited on a Si wafer was analyzed by using the Metricon Model 2010 Prism Coupler [97]. The detailed configuration of the prism coupler will be discussed in Sec. 5.2. The schematic diagram of the oxide thin-film loaded with a prism is shown in Fig. 5.3(a),

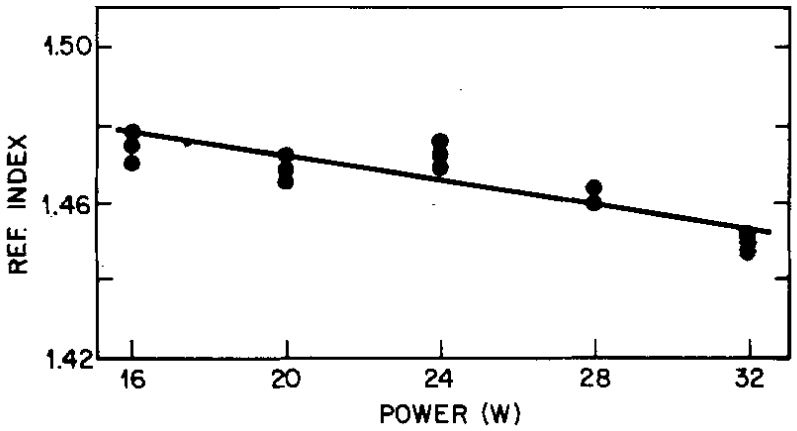

Figure 5.1: Refractive index of PECVD oxide (measured at $\lambda = 632.8$ nm) as a function of the RF power (13.56 MHz). The deposition occurred at 200 °C, 1 Torr, with 800 SCCM SiH_4 (3%) in Ar, 1560 SCCM N_2O [94].

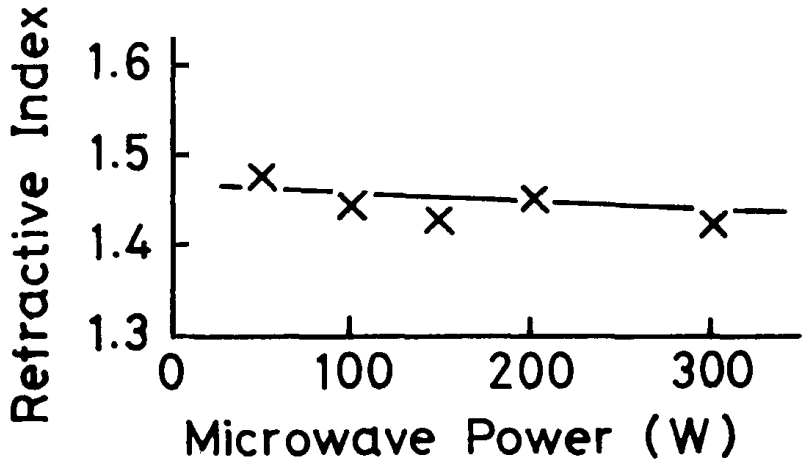

Figure 5.2: Refractive index of PECVD oxide (measured at $\lambda = 632.8$ nm) as a function of the RF power (2.45 GHz). The deposition occurred at room temperature, 2×10^{-4} Torr, with 10 SCCM SiH_4 and 10 SCCM O_2 [96].

and the measured angular TE reflection power spectrum at $\lambda = 1550$ nm is shown in Fig. 5.3(b). From the effective mode indices (i.e. the minima of the four downward resonances) of the leaky modes in this oxide thin-film structure, the refractive index n_{SiO_x} and thickness d_{SiO_x} of the PECVD oxide thin film can be derived [88, 89]. By using all the four effective mode indices (1.4678, 1.4071, 1.2997, and 1.1323) of the leaky TE_0 to TE_3 modes, the fitted $n_{SiO_x} = 1.4877 \pm 0.0001$ and $d_{SiO_x} = 2.9906 \pm 0.0091$ μm for the thin film. The values of n_{SiO_x} and d_{SiO_x} fitted by using only TE_0 to TE_2 and TE_0 to TE_1 modes are also summarized in Table 5.1. The fitted values n_{SiO_x} and d_{SiO_x} using different number of measured effective mode indices show very good self-consistency. Because PECVD oxide is amorphous, its refractive index is the same for TE and TM polarization. TE polarized light is used here because it produces more well-defined resonances in the spectrum; TM polarized light produces highly overlapping resonances, which makes it more difficult to determine the effective indices of the leaky modes. This measured refractive index of the PECVD oxide is higher than that of fused silica, but lies within the range of those of other PECVD oxides [94,96,98,99]. In all the following sections, 1.4877 will be used as the refractive index of all the PECVD oxide.

Table 5.1: Measured effective mode indices of TE_0 to TE_3 modes and the fitted refractive index n_{SiO_x} and thickness d_{SiO_x} of the PECVD oxide thin film in Fig. 5.3(a). The fitted values for n_{SiO_x} and d_{SiO_x} when using various number of measured effective mode indices are listed.

Effective mode indices used in fitting				Fitted	
TE_0	TE_1	TE_2	TE_3	n_{SiO_x}	d_{SiO_x}
1.4680	1.4082	1.3025	1.1417	1.4877 ± 0.0001	2.9906 ± 0.0091
1.4680	1.4082	1.3025	–	1.4876 ± 0.0001	2.9967 ± 0.0036
1.4680	1.4082	–	–	1.4876	3.0004

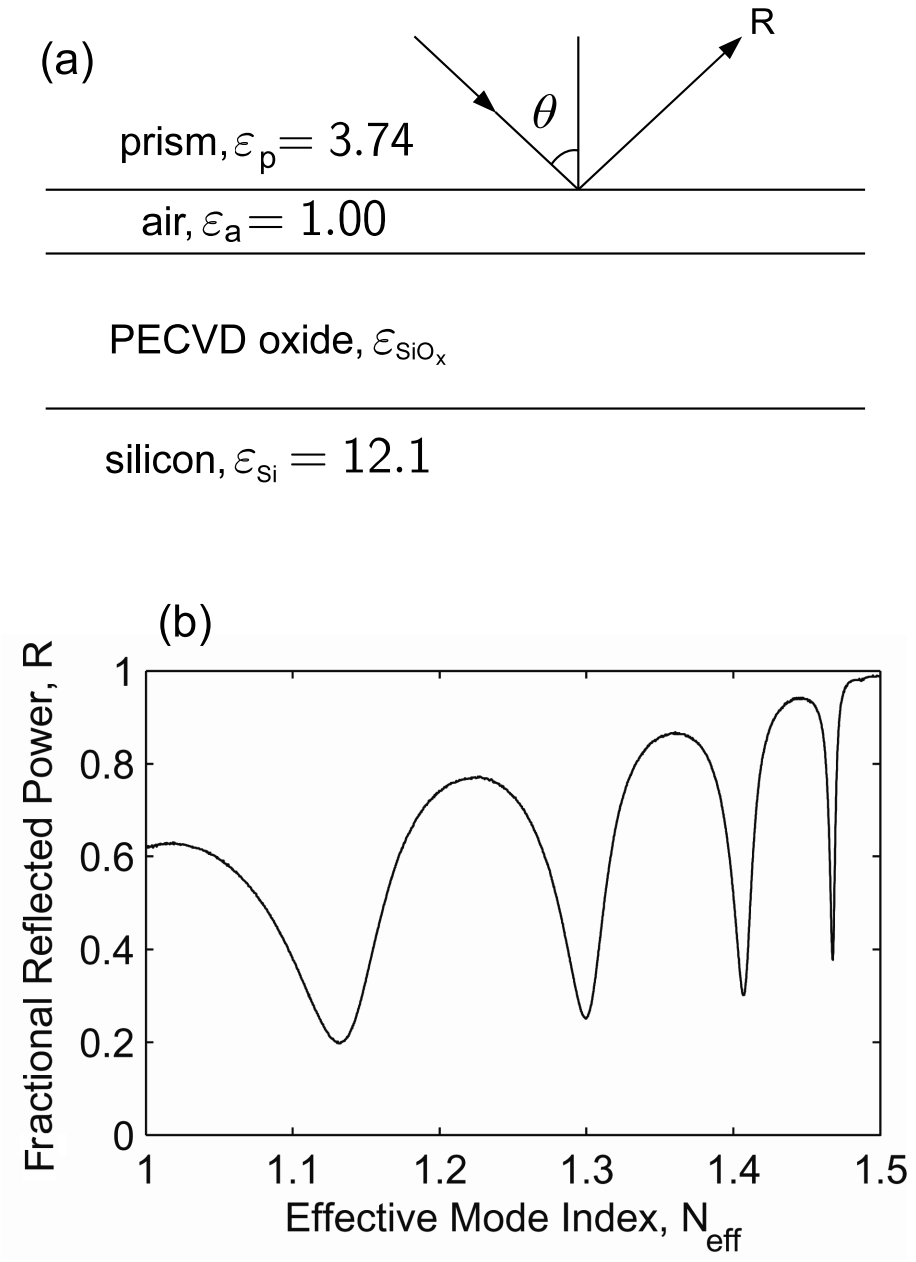

Figure 5.3: (a) Schematic diagram of a PECVD oxide thin-film (thickness $\simeq 3$ μm) structure with a prism on top. (b) The experimentally measured angular TE reflection power spectrum for the structure at $\lambda = 1550$ nm. The x-axis is the effective mode index $N_{\text{eff}} \equiv n_p \sin\theta$.

On the other hand, the same configuration is also applied to a thermal oxide thin film (thickness $\simeq 4$ μm) on a Si wafer. Thermal oxide is grown at very high temperature (~ 1100 °C) and the oxidation process is complete. As a result, thermal oxide can be regarded as pure SiO_2. The measured TE reflection power spectrum is shown in Fig. 5.4. The measured effective mode indices of the leaky mode and the fitted n_{SiO_2} and d_{SiO_2} are summarized in Table 5.2. Similarly, the fitted values of n_{SiO_2} and d_{SiO_2} show very good self-consistency. This measured refractive index is very close to that given in the literature, which is 1.444 according to [90]. The agreement reinforces the credibility of the refractive index measurement based on the prism coupler method.

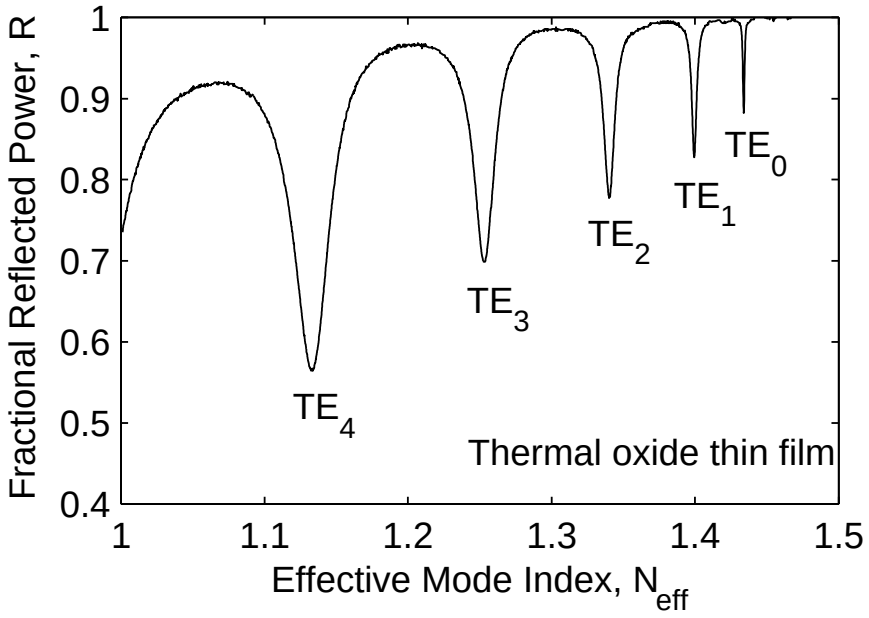

Figure 5.4: The experimentally measured angular TE reflection power spectrum for a thermal oxide thin-film (thickness $\simeq 4$ μm) structure at $\lambda = 1550$ nm.

Table 5.2: Measured effective mode indices of TE_0 to TE_4 modes and the fitted refractive index n_{SiO_2} and thickness d_{SiO_2} of the thermal oxide thin film. The fitted values for n_{SiO_2} and d_{SiO_2} when using various number of measured effective mode indices are listed.

Effective mode indices used in fitting					Fitted	
TE_0	TE_1	TE_2	TE_3	TE_4	n_{SiO_x}	d_{SiO_x}
1.4339	1.3995	1.3402	1.2531	1.1329	1.4452 ± 0.0001	4.0461 ± 0.0089
1.4339	1.3995	1.3402	1.2531	–	1.4452 ± 0.0001	4.0506 ± 0.0052
1.4339	1.3995	1.3402	–	–	1.4452 ± 0.0001	4.0538 ± 0.0029
1.4339	1.3995	–	–	–	1.4452 ± 0.0001	4.0567

5.1.2 Optical Constants of Gold

The dielectric constant of metal can be described by Drude free-electron-gas model [49, 67]. The dielectric constant of a metal can be written as

$$\widetilde{\varepsilon}_m(\omega) = 1 - \frac{\omega_p^2}{\omega^2 + j\gamma\omega}, \tag{5.2}$$

where γ is the damping rate (typically in the range of 10^{13} to 10^{14} Hz [49]) and

$$\omega_p = \left(\frac{Ne^2}{m^*\epsilon_0}\right)^{1/2} \tag{5.3}$$

is the the plasma frequency. N is the bulk electron charge density, e is the electronic charge, and m^* is the electron effective mass. Further, by algebraic manipulation, the real and imaginary parts of the dielectric constant can be written as

$$\varepsilon_R(\omega) = 1 - \frac{\omega_p^2}{\omega^2 + \gamma^2} \tag{5.4}$$

and

$$\varepsilon_I(\omega) = \frac{\omega_p^2\gamma}{\omega(\omega^2 + \gamma^2)}, \tag{5.5}$$

respectively. In the case that $\omega^2 \gg \gamma^2$ (e.g. visible or near-infrared wavelengths), $1 - \varepsilon_R$ is proportional to λ^2 and ε_I is proportional to λ^3.

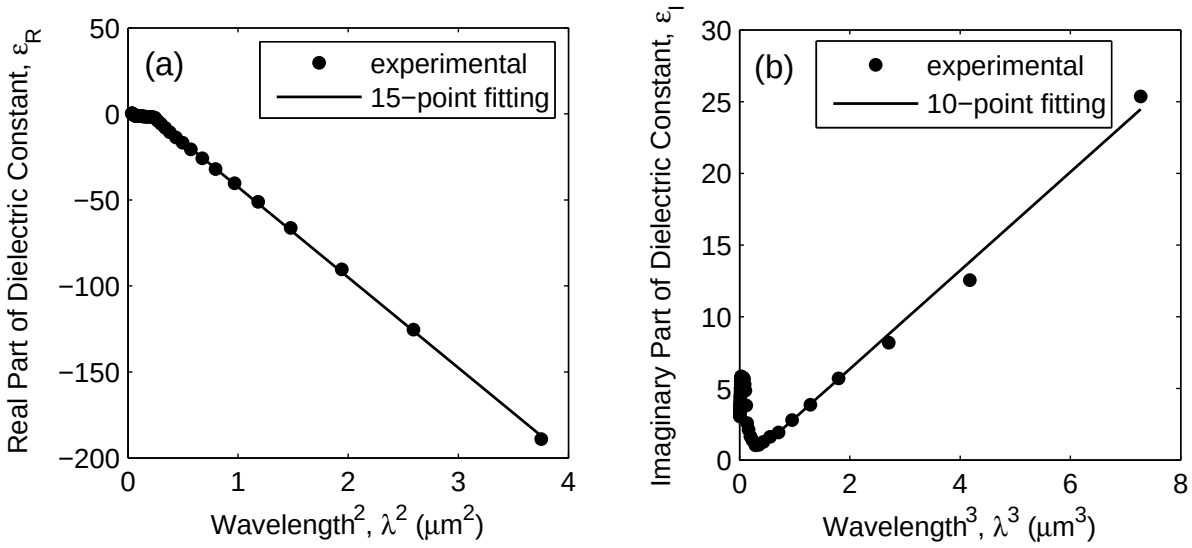

Figure 5.5: (a) Measured ε_R as a function of λ^2 and (b) ε_I as a function of λ^3 for Au [66]. The dots represent the experimental data points, and the lines are obtained by the least-square error fitting by the 15 data points in (a) and 10 data points in (b).

Figures 5.5(a) and (b) show the measured ε_R and ε_I of Au as functions of λ^2 (μm^2) and λ^3 (μm^3), respectively [66]. The dielectric constants were determined by inverting the normal-incidence reflection and transmission, simultaneously with the transmission for TM-polarized light incident at 60° [66, 100, 101]. The Au thin films (thickness $\simeq$ 40 nm) were deposited onto fused quartz substrates at room temperature by vacuum evaporation. This very small thickness of Au thin film allows detectable transmitted light, but is still larger than the critical thickness ($\simeq$ 25 nm for Au), under which the Au film may not be planar (e.g. islands) and would exhibit thickness-dependent optical property [66, 102]. The lines in Fig. 5.5 are plotted by the least-square error fitting by the 15 data points in (a) and 10 data points in (b). The proportionality agrees with Eq. (5.4) and (5.5). However, the values of the dielectric constants (especially ε_I) start to deviate from the line at short wavelength. The higher ε_I in this case corresponds to a higher loss than the prediction of the Drude free-electron-gap model. The extra loss can be explained by interband transitions in metals at sufficiently high frequency [49, 66]. Fortunately, in this work, the

wavelength of interest is $\lambda = 1550$ nm, which lies in the range where the Durde free-electron-gas model works fairly well. By using interpolation, the dielectric constant of Au is $\widetilde{\varepsilon}_{\text{Au}} = -115 - j11.3$, or equivalently, $\widetilde{n}_{\text{Au}} = 0.526 - j10.74$. This value will be used as the refractive index of Au in all the following sections.

5.2 Metricon Prism Coupler and Alignment of the Laser Beam

The experiments based on the TTR method were performed using the Metricon Model 2010 Prism Coupler [97]. The configuration of this instrument is shown in Fig. 5.6. The laser beam is linearly polarized after passing through a polarizer, and the polarization direction at 45° in between the fast and slow axes of the half-wave plate. Therefore, the TE/TM polarization of the light arriving at the prism coupler can be controlled. The prism coupler utilizes a coupling head to push the waveguide structure toward the prism to create an area where coupling can occur (a "coupling spot"). The laser beam is manually adjusted to be centered on the coupling spot (as shown in Fig. 5.7). The light reflected from the coupling spot refracts out of the prism and is measured by a photodetector. The prism, MIM waveguide, photodetector, and coupling head are fixed on a rotary table that can be rotated in angular steps of $\Delta\theta = 0.0075°$. This angular step size corresponds to an effective index resolution of $\Delta N_\theta \simeq 0.0001$. The measured reflected power is recorded at each angle and can be exported and analyzed using Matlab programs.

As shown in Fig. 5.7(a), for laser beams incident at various angles, the entering locations have to be correspondingly changed to ensure that the beams are incident on the center of the coupling spot. However, as the rotary table rotates during the measurement of the angular reflection spectrum, it requires complicated table movements to keep the incident laser beam centered on the coupling spot. The Metricon Prism Coupler system does not incorporate such a scheme, and the laser beam movement during the table rotation is illustrated in Fig. 5.7(b). Therefore,

in order to reduce the off-center effects, the laser beam should be initially adjusted to be incident on the center of the coupling spot for an angle of interest (effective index of interest), that is, near the resonance of the MIM plasmonic modes. The laser beam alignment can be realized by varying the position of the laser beam until the strongest resonance is observed in the reflection spectrum. It implies that the optimal laser beam alignment may vary from sample to sample and from prism to prism, as shown in Fig. 5.7(c) and (d). Figure 5.7(c) shows a laser alignment for a mode with a relatively high N_{eff}, and (d) is for a mode with a relatively low N_{eff}. It should also be noted that the coupling spot is typically near the corner edge of a prism, in order to reduce the laser spot movement during the stage rotation and therefore reduce the off-center effects.

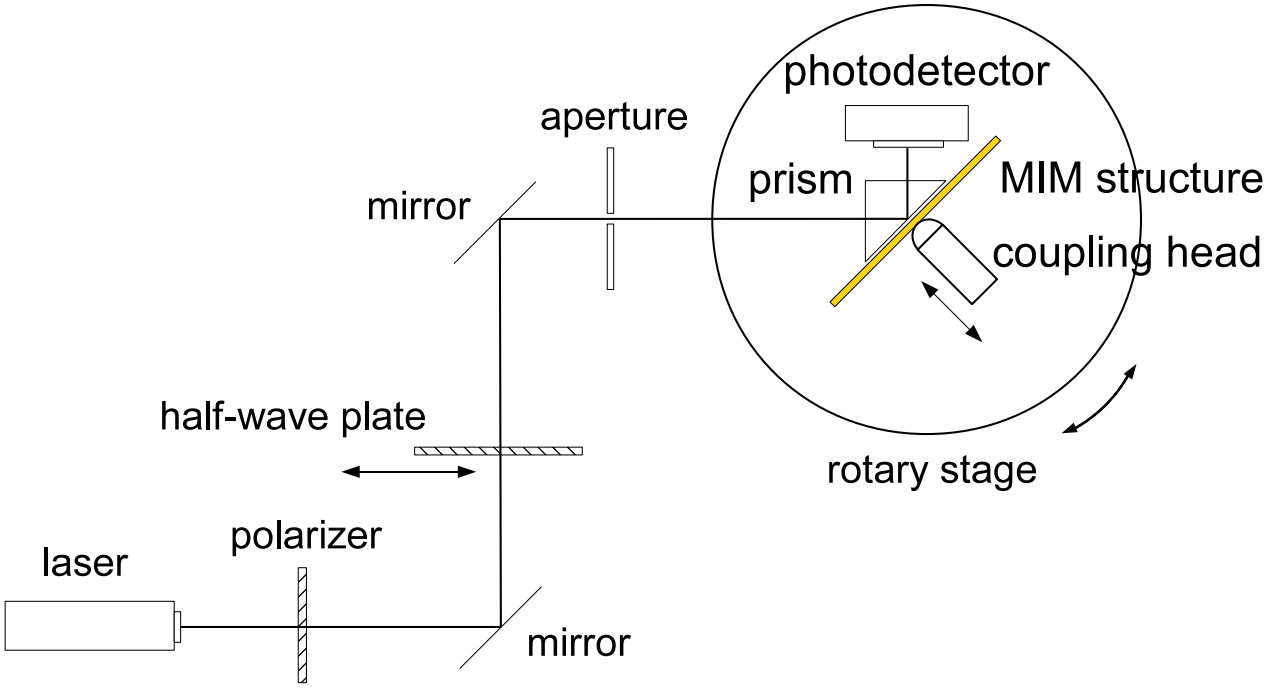

Figure 5.6: Schematic diagram of a Metricon Prism Coupler system.

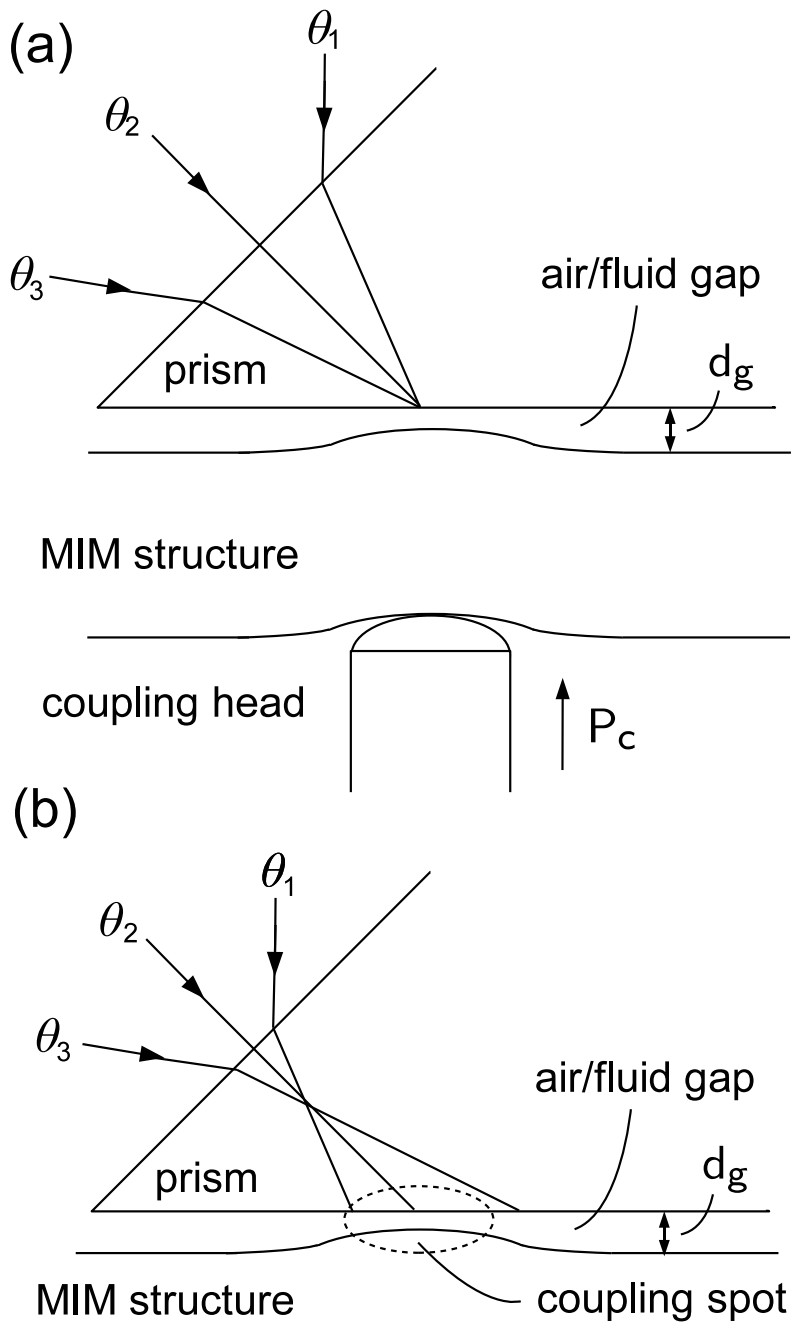

Figure 5.7: (a) Schematic diagram of a prism coupler near a coupling spot. The entering locations on the side of the prism have to be varied for light incident at various angles to be incident upon the coupling spot. The light incident at θ_1 corresponds to the minimum achievable effective index and θ_3 to maximum achievable effective index, i.e. $N_{\text{eff}}(\theta_1) = N_{\text{min}}$ and $N_{\text{eff}}(\theta_3) = N_{\text{max}}$. (b) Schematic diagram of an off-center laser beam during the table rotation. The laser beam is incident on the center of the coupling spot only at θ_2 in this case.

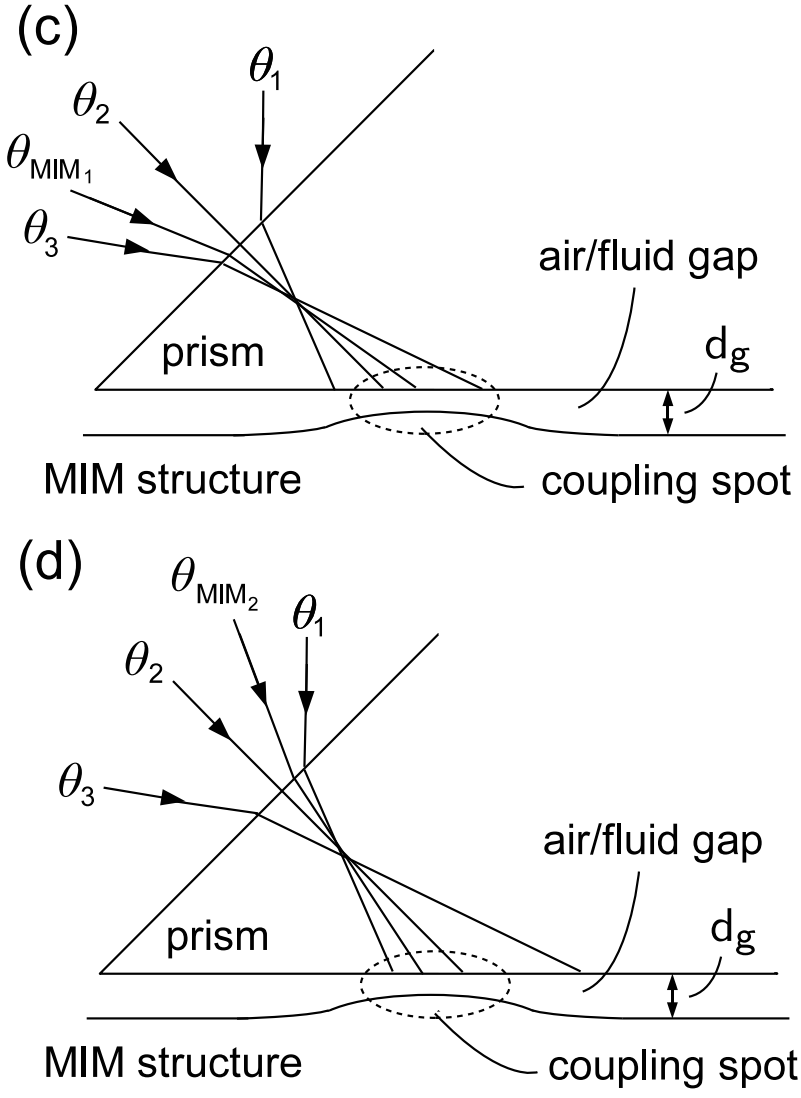

Figure 5.7 (cont.): (c) Schematic diagram of a laser beam alignment for a mode with a relatively high N_{eff}. The laser beam is incident on the center of the coupling spot only at θ_{MIM_1} in this case. (d) Schematic diagram of a laser beam alignment for a mode with a relatively low N_{eff}. The laser beam is incident on the center of the coupling spot only at θ_{MIM_2} in this case.

Figure 5.8 illustrates the reflection power spectrum measured at various fluid ($n_g = 1.4459$) gap thicknesses d_g for an MIM structure with a 75 nm top Au cladding and a 200 nm SiO_x core. In this case, the operating wavelength is $\lambda = 1550$ nm. The gap thickness d_g is changed by moving the center of the laser beam from the center of the coupling spot (d_{g1}) to off-center locations (d_{g2}, d_{g3}). For d_{g1}, the gap is small and the coupling between the prism and the TM_0 mode of the MIM structure is the strongest. For d_{g3}, the gap is the largest and the coupling to the TM_0 mode is negligible. The structure is essentially an Otto configuration [40, 41, 59] and a prominent SP mode at the fluid gap-metal interface is observed, with an effective index very close to the index of the fluid $n_g = 1.4459$. At the intermediate gap thickness d_{g2}, both the resonances of the fluid gap-metal SP mode and the TM_0 mode

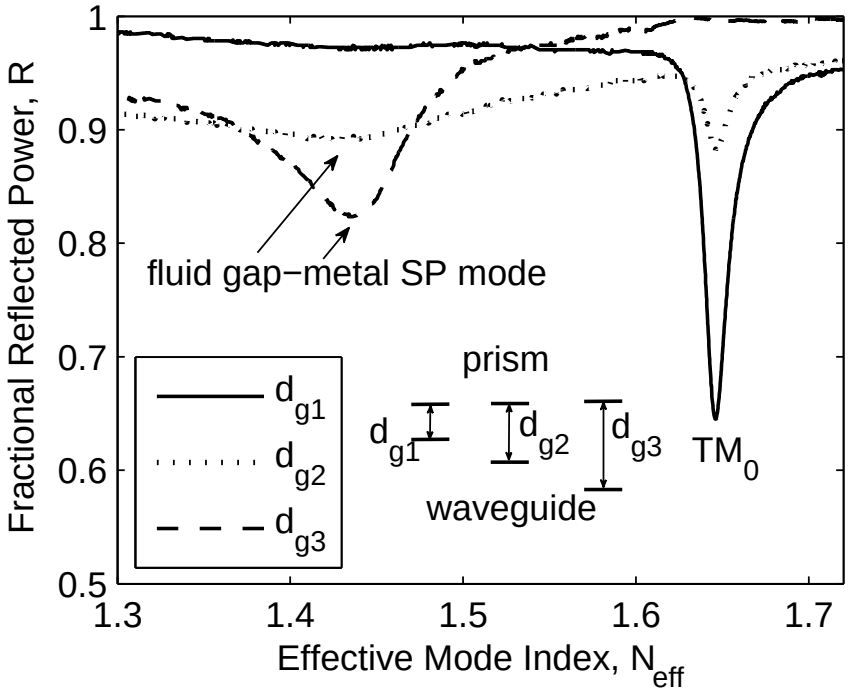

Figure 5.8: Experimental angular reflection power spectrum measured at various fluid ($n_g = 1.4459$) gap thickness d_g values. The resonances corresponding to the fluid gap-metal SP mode and the TM_0 mode of the MIM structure are labeled. The x-axis is the effective mode index $N_{\text{eff}} \equiv \beta/k_0$, where β is the wavevector in the waveguide propagation direction and k_0 is the freespace wavevector.

can be observed. It is clear from this measurement that a strong TM_0 resonance can only be observed and characterized when the laser beam is centered at or near the coupling spot. In all the following measurements for MIM structures, the laser beam is centered at the coupling spot.

5.3 TTR Measurements for Single-Mode MIM Waveguides

In this section, using the Metricon Model 2010 Prism Coupler [97], the TTR method is experimentally applied to two MIM (Au-SiO_x-Au) waveguide structures. The schematic diagram of the experimental configuration is shown in Fig. 5.9. A coupling head is used to push the waveguide structure toward the prism to create a coupling spot. The force is controlled by the pressure, P_c, which is adjustable from 15 to 50 psi (pounds per square inch). A laser beam can be manually adjusted to be centered on the coupling spot for a stronger coupling between the prism and the MIM plasmonic mode. Two MIM structures with two different SiO_x core thicknesses, d_i = 200 nm and 50 nm, were fabricated and characterized at $\lambda = 1.55$ μm. The Au layer on the top of the structure is 75 nm in thickness, which is about 3 skin depths, to ensure appropriate coupling strength. The Au layer substrate is 400 nm in thickness, which, for practical purposes, is optically semi-infinite. The SiO_x cores were deposited by using PECVD (see Sec. 5.1.1) and the Au cladding layers were deposited by using an e-beam evaporator (see Sec. 5.1.2).

The theoretical propagation constant of the MIM structure can be rigorously calculated by using the Argument Principle Method (APM) [91]. At $\lambda = 1.55$ μm, the refractive index of Au is $\widetilde{n}_{\text{Au}} = 0.526 - j10.74$ [66], and the refractive index of the PECVD oxide is $n_{\text{SiO}_x} = 1.4877$. The relatively high index of the PECVD oxide might be a result of incomplete oxidization at low RF power [94, 96]. The calculated normalized propagation constants are $(\beta_{\text{MIM}} - j\alpha_{\text{MIM}})/k_0 = 1.6556 - j0.0082$ and $2.0722 - j0.0259$ for the 200 nm- and the 50 nm-core structures, respectively. It

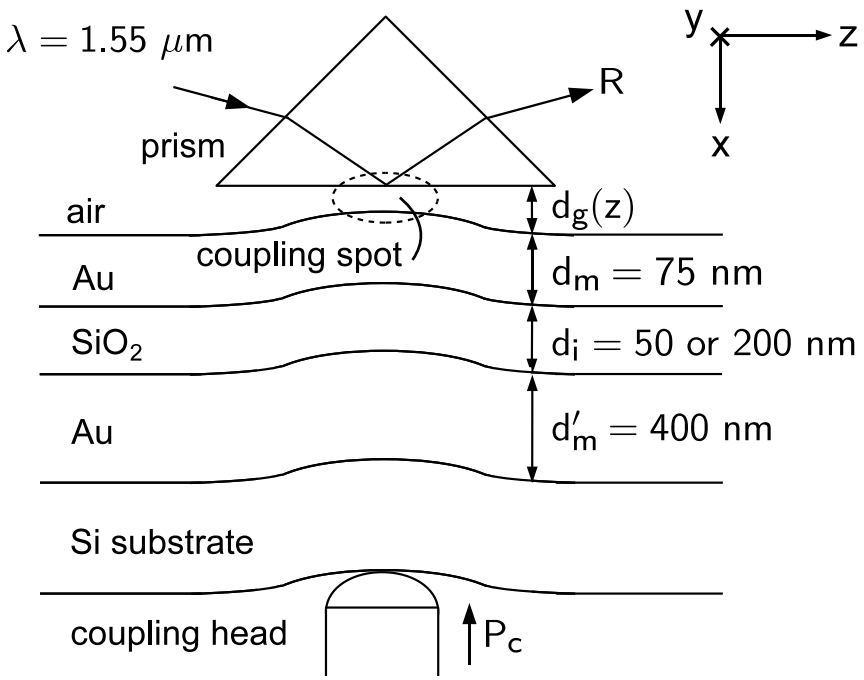

Figure 5.9: Schematic diagram of the ATR configuration applied to the MIM structures.

should be noted that in these calculations, it is assumed that the MIM structures have symmetric and semi-infinite claddings on both sides.

5.3.1 Oxide Core Thickness of 200 nm

The measured angular TM reflection power spectra of the structure in Fig. 5.9 with $d_i = 200$ nm is shown in Fig. 5.10(a). The x-axis is the effective mode index $N_{\text{eff}} \equiv \beta/k_0$, where β is the wavevector in the z-direction and k_0 is the freespace wavevector. In this case, the refractive index of the prism is $n_p = 1.9349$. By increasing the pressure of the coupling head, P_c, the air gap thickness d_g decreases and a series of spectra were measured. It is worth mentioning that explicit values of d_g are not necessary for mode characterization. The resonances of R correspond to the TM_0 mode of the MIM structure. Figure 5.10(b) shows the effective mode index $N'_{\text{MIM}} \equiv \beta'_{\text{MIM}}/k_0$ corresponding to the "resonance minima" of the TM_0 mode as a function of P_c, and the average of the measurements yields $N'_{\text{MIM}} = 1.6560$, with a standard

deviation $\sigma_\beta = 0.0001$. The prime denotes results obtained by the TTR method, in contrast to the rigorous theoretical results. Figure 5.10(c) shows the normalized attenuation coefficients $\alpha'_{\text{MIM}}/k_0 =$ HWHMs of the TM_0 mode as a function of P_c, and the average of the measurements yields $\alpha'_{\text{MIM}}/k_0 = 0.0070$, with a standard deviation $\sigma_\alpha = 0.0001$. This is equivalent to a loss of 0.25 dB/μm or a propagation length $L = 18$ μm. The resonance minima and HWHMs are obtained after removing the background variation in R; this can be done by leveling both sides of a resonance to unity. It can be observed from Fig. 5.10(b) and (c) that there is no apparent trend in the measured N'_{MIM} and α'_{MIM}/k_0 as functions of P_c. It implies that no requirement on P_c (and therefore d_g) is needed provided the TM_0 resonance is adequately observable. Moreover, since the measurement results are insensitive to d_g, the slightly non-planar coupling spot has little effect on them.

The experimental results, $(\beta'_{\text{MIM}} - j\alpha'_{\text{MIM}})/k_0 = 1.6560 - j0.0070$ on average, agree well with the theoretical result, $(\beta_{\text{MIM}} - j\alpha_{\text{MIM}})/k_0 = 1.6556 - j0.0082$. The $\sim 15\%$ smaller measured loss may be due to better film quality in the MIM structures [33]. The propagation calculation is sensitive to the complex dielectric constant $\widetilde{n}_{\text{Au}}$, which was determined by transmission/reflection measurements [66] or ellipsometry [33] for a Au thin film on a glass substrate. In both cases, the quality of the Au surface strongly affects the measured $\widetilde{n}_{\text{Au}}$. However, for MIM waveguides, the quality of the Au/oxide interfaces experienced by the waveguide mode is better than the quality of the Au surface deposited by vacuum evaporator. The protection of the Au claddings from environmental influences is a key attribute of MIM waveguides.

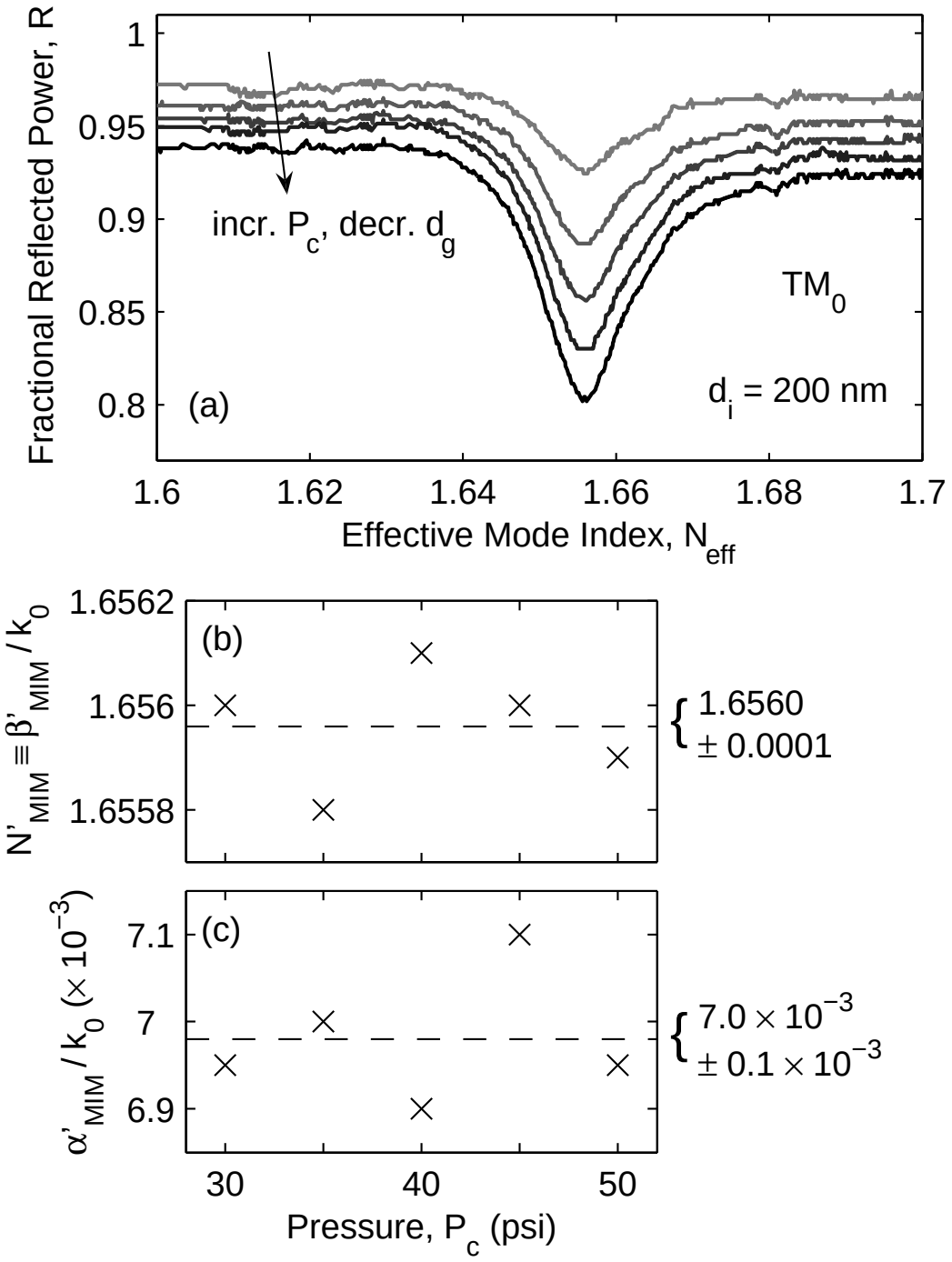

Figure 5.10: (a) TM reflection power spectra for the structure in Fig. 5.9 with $d_i = 200$ nm measured at various air gap thicknesses d_g, which correspond to pressures of the coupling head, $P_c = 30$, 35, 40, 45, and 50 psi. The x-axis is the effective mode index $N_{\text{eff}} \equiv \beta/k_0$, where β is the wavevector in the z-direction and k_0 is the freespace wavevector. (b) The normalized propagation constants $N'_{\text{MIM}} \equiv \beta'_{\text{MIM}}/k_0$ corresponding to the "resonance minima" and (c) the normalized attenuation coefficients $\alpha'_{\text{MIM}}/k_0 =$ HWHMs of the resonances at various values of P_c.

The measured angular TM reflection power spectra can also be compared with the theoretical calculations. Figure 5.11 shows the simulated angular TM reflection power spectra for the structure in Fig. 5.9 with $d_i = 200$ nm. The spectra are calculated for various air gap thicknesses $d_g = 0$, 20 nm, 40 nm, and 60 nm. It is observed that the simulated spectra are very similar to the measured ones, and they show the same trend. For example, as d_g increases, then R shifts up and the resonance strengths decreases. However, the measured spectra at higher pressure P_c have stronger resonances than predicted by the simulation. This may be due to the reduction of d_m caused by an indentation on the soft Au surface at high P_c. Figure 5.12 shows the simulation for the same structure except that d_m is changed to 66 nm, and the cases for $d_g = 0$, 20 nm, 40 nm, and 60 nm are calculated. Figure 5.12 exhibits stronger resonance strength compared with Fig. 5.11 and better agreement with the experimental results in Fig. 5.10(a) in terms of the resonance strength. It is also shown in Sec. 4.4 that smaller d_m produces stronger resonances; however, as long as d_m is sufficiently large (typically larger than 3 skin depths), the values of d_m and d_g do not affect the results obtained by the TTR method. Moreover, Fig. 5.13 illustrates the comparison between the experimental $P_c = 40$ psi curve and the calculated reflection spectrum for the MIM structure with $d_i = 200$ nm, $d_m = 66$ nm and $d_g = 39$ nm. The agreement between the two curves in Fig. 5.13 is excellent. Following a series of similar comparisons, the measured curves at $P_c = 30$, 35, 40, 45, and 50 psi correspond to $d_g = 65$, 48, 39, 29, and 20 nm, respectively. It is worth mentioning that since d_m is sufficiently large in this case, the values of d_m and d_g do not affect the results obtained by the TTR method. Therefore, no information about d_m or d_g is required.

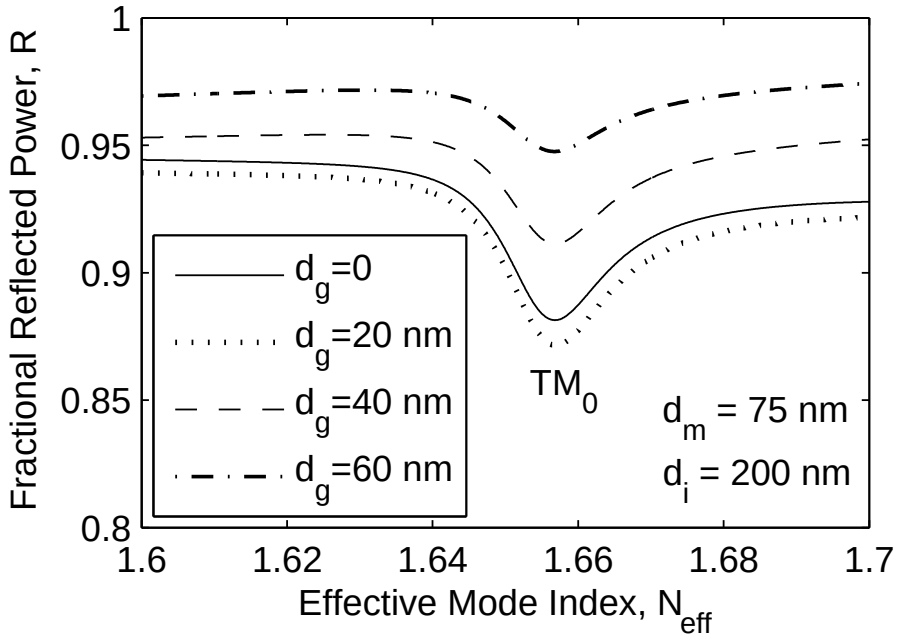

Figure 5.11: Simulated angular TM reflection power spectrum for the structure in Fig. 5.9 with $d_i = 200$ nm and $d_m = 75$ nm.

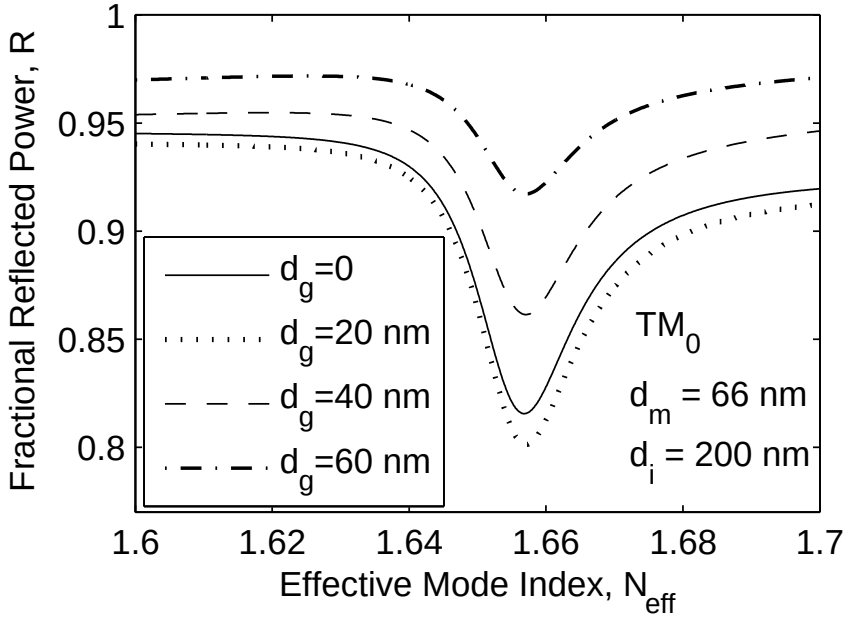

Figure 5.12: Simulated angular TM reflection power spectrum for the structure in Fig. 5.9 with $d_i = 200$ nm. The thickness of the top metal cladding, d_m, is changed to 66 nm.

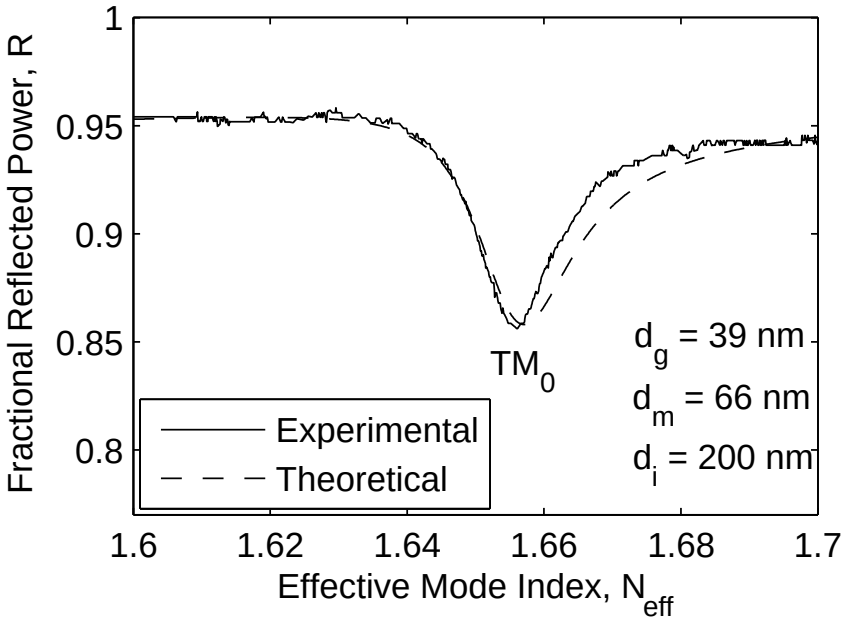

Figure 5.13: Comparison of the simulated reflection power spectrum and the measured reflection power spectrum for the structure in Fig. 5.9 with $d_i = 200$ nm at $P_c = 40$ psi. For the simulated spectrum, $d_m = 66$ nm and $d_g = 39$ nm are used.

5.3.2 Oxide Core Thickness of 50 nm

Figure 5.14(a) shows the TM reflection power spectra of the structure in Fig. 5.9 with $d_i = 50$ nm measured at various air gap thicknesses d_g. In this case, the refractive index of the prism is $n_p = 2.4441$. Figures 5.14(b) shows $N'_{\text{MIM}} \equiv \beta'_{\text{MIM}}/k_0$ of the TM_0 mode as a function of P_c, and the average of the measurements yields $N'_{\text{MIM}} = 2.0633$, with a standard deviation $\sigma_\beta = 0.0001$. Figure 5.14(c) shows the normalized attenuation coefficients α'_{MIM}/k_0 of the TM_0 mode as a function of P_c, and the average of the measurements yields $\alpha'_{\text{MIM}}/k_0 = 0.0217$, with a standard deviation $\sigma_\alpha = 0.0003$. This is equivalent to a loss of 0.76 dB/μm or $L = 5.7$ μm. The loss in this case is larger than the loss in the structure with $d_i = 200$ nm. This agrees with Fig. 2.5 in Sec. 2.2: the loss of the TM_0 mode decreases as the core thickness increases. Again there is no apparent trend in the measured N'_{MIM} and α'_{MIM}/k_0 as functions of P_c. The experimental results, $N'_{\text{MIM}} - j\alpha'_{\text{MIM}}/k_0 = 2.0633 - j0.0217$ on average, agree well with the theoretical result, $N_{\text{MIM}} - j\alpha_{\text{MIM}}/k_0 = 2.0722 - j0.0259$. Because of the

small core thickness, the theoretical N_{MIM} is sensitive to the core thickness used in the simulation. Therefore, compared with the previous case, the difference between the measured N'_{MIM} and the theoretical N_{MIM} in this case is slightly larger. Similar to the case of $d_i = 200$ nm, the measured loss is $\sim 15\%$ smaller than the theoretical result.

The measured angular TM reflection power spectra can also be compared with the theoretical calculations. Figure 5.15 shows the simulated angular TM reflection power spectra for the structure in Fig. 5.9 with $d_i = 50$ nm. The spectra are calculated for various air gap thicknesses $d_g = 0$, 20 nm, and 40 nm. Again the simulated spectra are very similar to the measured ones, and they show the same trend. Similar to the case in Sec. 5.3.1, a better agreement between the simulation and the experimental results can be obtained by using a smaller d_m. Figure 5.16 illustrates the comparison between the experimental $P_c = 40$ psi curve and the calculated reflection spectrum for the MIM structure with $d_i = 51$ nm, $d_m = 66$ nm, and $d_g = 28$ nm. The agreement between the two curves in Fig. 5.16 is very good.

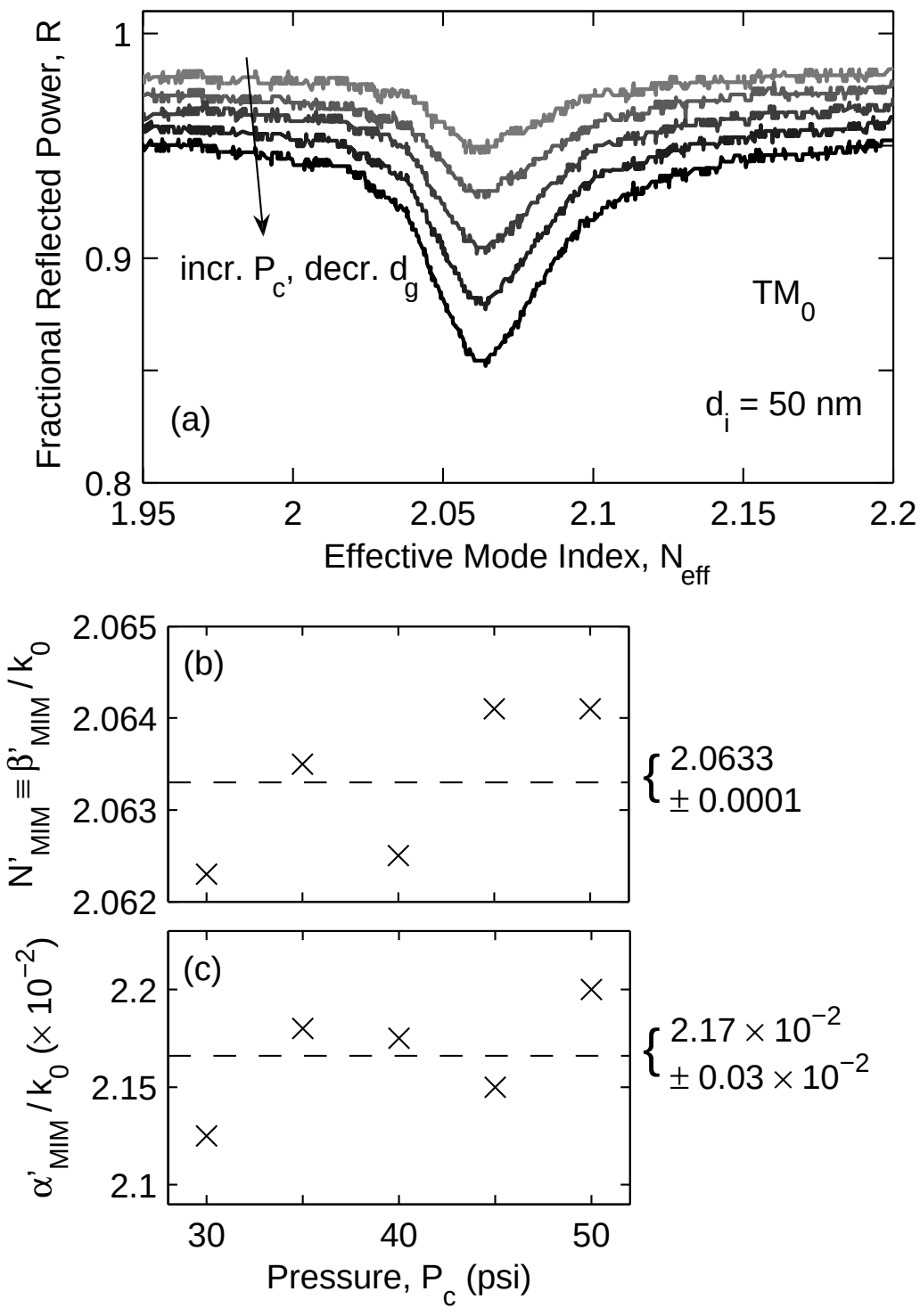

Figure 5.14: (a) TM reflection power spectra for the structure in Fig. 5.9 with $d_i = 50$ nm measured at various air gap thicknesses d_g corresponding to $P_c =$ 30, 35, 40, 45, and 50 psi. (b) The normalized propagation constants N'_{MIM} corresponding to the "resonance minima" and (c) the normalized attenuation coefficients $\alpha'_{\text{MIM}}/k_0 =$ HWHMs of the resonances at various values of P_c.

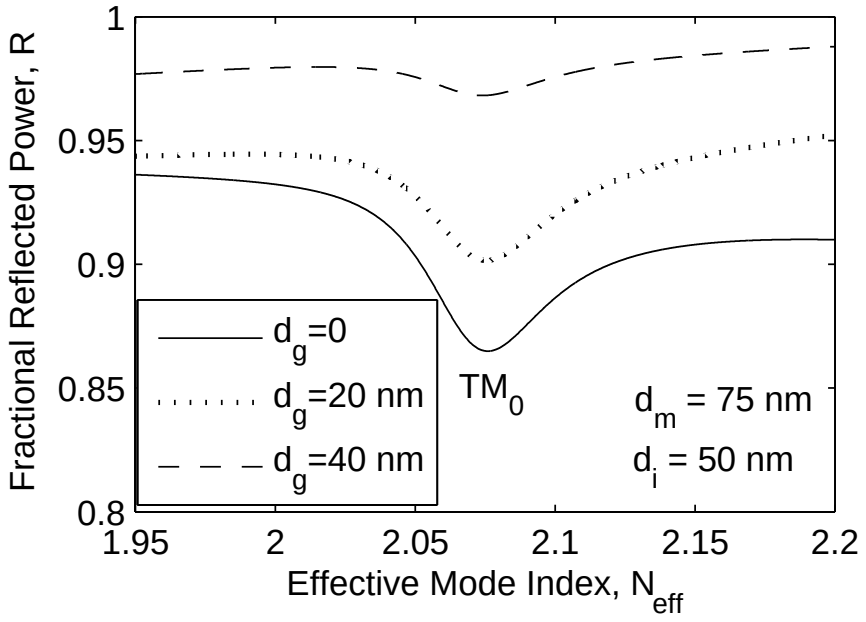

Figure 5.15: Simulated angular TM reflection power spectrum for the structure in Fig. 5.9 with $d_i = 50$ nm and $d_m = 75$ nm.

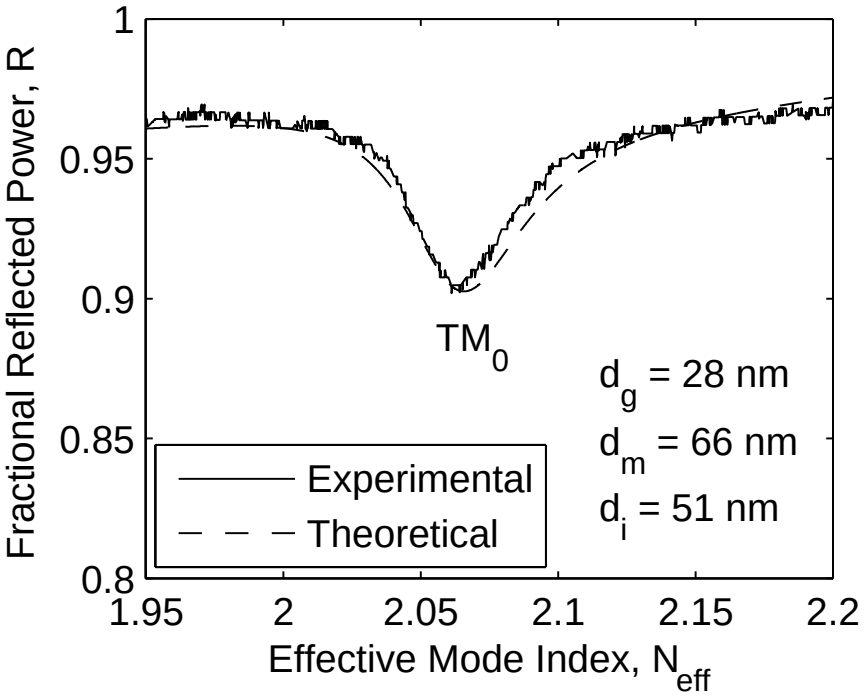

Figure 5.16: Comparison of the simulated reflection power spectrum and the measured reflection power spectrum for the structure in Fig. 5.9 with $d_i = 50$ nm at $P_c = 40$ psi. For the simulated spectrum, $d_i = 51$ nm, $d_m = 66$ nm and $d_g = 28$ nm are used for a better agreement with the experimental result.

5.4 Sensitivity Analysis

5.4.1 Effects of the Air-Gap Thickness Between the Prism and the Waveguide

In Sec. 5.3.1 and 5.3.2, it is shown that there is no apparent trend in the measured N'_{MIM} and α'_{MIM}/k_0 as functions of air gap thickness d_g. For N'_{MIM}, the standard deviation σ_β is about 0.0001 for both samples; for α'_{MIM}/k_0, the standard deviation σ_α is $< 2\%$ of the measured α'_{MIM}/k_0. This observation indicates that, despite the fact that the d_g values are not known, the TTR measurement results are very self-consistent as d_g varies. As a result, the configuration of the TTR method can be readily applied by using other similar ATR or prism-coupler configurations, without concern for the d_g-dependence on the measurement results.

5.4.2 Effects of the Thickness of the Top Metal Cladding

In addition to the air gap thickness d_g, the thickness of the top metal cladding d_m is also relatively difficult to quantify experimentally. In this section, MIM structures with various d_m values were fabricated and characterized by using the TTR method. The schematic diagram of the experimental configuration is shown in Fig. 5.17. Three MIM structures with $d_i = 190$ nm and $d_m = 85$, 75, and 65 nm were fabricated and characterized at $\lambda = 1.55$ μm. Using the rigorous numerical method, APM, the calculated normalization constants are $N_{\text{MIM}} - j\alpha_{\text{MIM}}/k_0 = 1.6638 - j0.0086$ for the TM_0 mode in the unperturbed MIM structure ($d_m = \infty$).

The measured angular TM reflection power spectrum for the structure in Fig. 5.17 with $d_m = 85$ nm is illustrated in Fig. 5.18(a). The refractive index of the prism is $n_p = 1.9349$ in this case. Figure 5.18(b) shows $N'_{\text{MIM}} \equiv \beta'_{\text{MIM}}/k_0$ of the TM_0 mode as a function of P_c, and the average of the measurements yields $N'_{\text{MIM}} = 1.6650$, with a standard deviation $\sigma_\beta = 0.0002$. Figure 5.18(c) shows the normalized attenuation coefficients α'_{MIM}/k_0 of the TM_0 mode as a function of P_c, and the average of the measurements yields $\alpha'_{\text{MIM}}/k_0 = 0.0073$, with a standard deviation $\sigma_\alpha = 0.00004$.

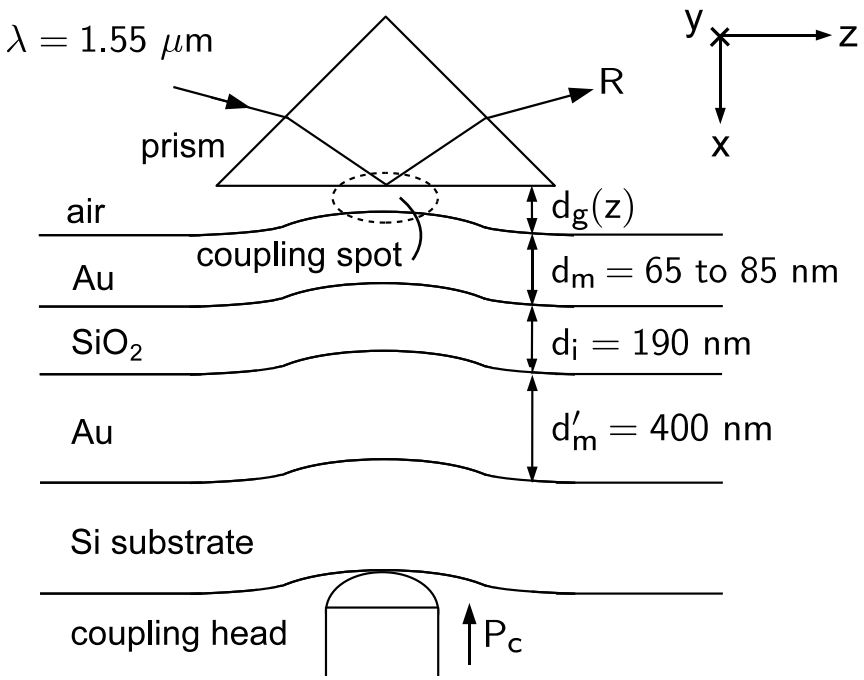

Figure 5.17: Schematic diagram of the ATR configuration applied to the MIM structures with $d_i = 190$ nm and various values of d_m.

This is equivalent to a loss of 0.26 dB/μm or $L = 17$ μm. The results for N'_{MIM} and α'_{MIM}/k_0 are only shown for $P_c = 40$, 45, and 50 psi because the resonances at lower P_c are too weak for the extraction of N'_{MIM} and α'_{MIM}/k_0. Similar to the results in Sec. 5.3, there is no apparent trend in the measured N'_{MIM} and α'_{MIM}/k_0 as functions of P_c. The experimental results, $N'_{\text{MIM}} - j\alpha'_{\text{MIM}}/k_0 = 1.6650 - j0.0073$ on average, agree well with the theoretical result, $N_{\text{MIM}} - j\alpha_{\text{MIM}}/k_0 = 1.6638 - j0.0086$. Similar to the cases in Sec. 5.3, the measured loss is $\sim 15\%$ smaller than the theoretical result.

Figure 5.19(a) shows the measured angular TM reflection power spectrum for a similar structure with $d_m = 75$ nm, and Figs. 5.19(b) and (c) show N'_{MIM} and α'_{MIM}/k_0 of the TM_0 resonance as functions of P_c. Due to the smaller d_m, the TM_0 resonances are stronger in this case. The experimental results, $N'_{\text{MIM}} - j\alpha'_{\text{MIM}}/k_0 = 1.6643 - j0.0074$ on average, agree very well with the experimental results for the structure with $d_m = 85$ nm. The similarity between these two sets of measurement results indicates the insensitivity of the TTR method to d_m.

On the other hand, Fig. 5.20(a) shows the measured angular TM reflection power spectrum for a similar structure with $d_m = 65$ nm, and Figs. 5.20(b) and (c) show N'_{MIM} and $\alpha'_{\mathrm{MIM}}/k_0$ of the TM_0 resonance as functions of P_c. The TM_0 resonances are further stronger than the case with $d_m = 75$ nm. However, in this case, the measured $\alpha'_{\mathrm{MIM}}/k_0$ values show a trend with P_c: the value of $\alpha'_{\mathrm{MIM}}/k_0$ is smaller at lower P_c and approaches a constant value at higher P_c (small d_g). Moreover, the measured $\alpha'_{\mathrm{MIM}}/k_0$ values in this case are larger than the cases with $d_m = 75$ or 85 nm. It is also shown in Sec. 4.4.1 that with overly small d_m, the results obtained by the TTR method are strongly perturbed, and this perturbation produces a higher $\alpha'_{\mathrm{MIM}}/k_0$.

In summary, the results obtained by the TTR method are insensitive to d_m for the case where d_m is sufficiently large. In such a case, both the measured values of N'_{MIM} and $\alpha'_{\mathrm{MIM}}/k_0$ exhibit no apparent trend as functions of P_c. However, if d_m is not sufficiently large, the results obtained by the TTR method are perturbed by the presence of the prism and may be unreliable. The strong perturbation is easily verified by noting either the presence of a strong resonance in the reflection spectrum or the clear dependence of $\alpha'_{\mathrm{MIM}}/k_0$ as a function of P_c as shown in Fig. 5.20(c).

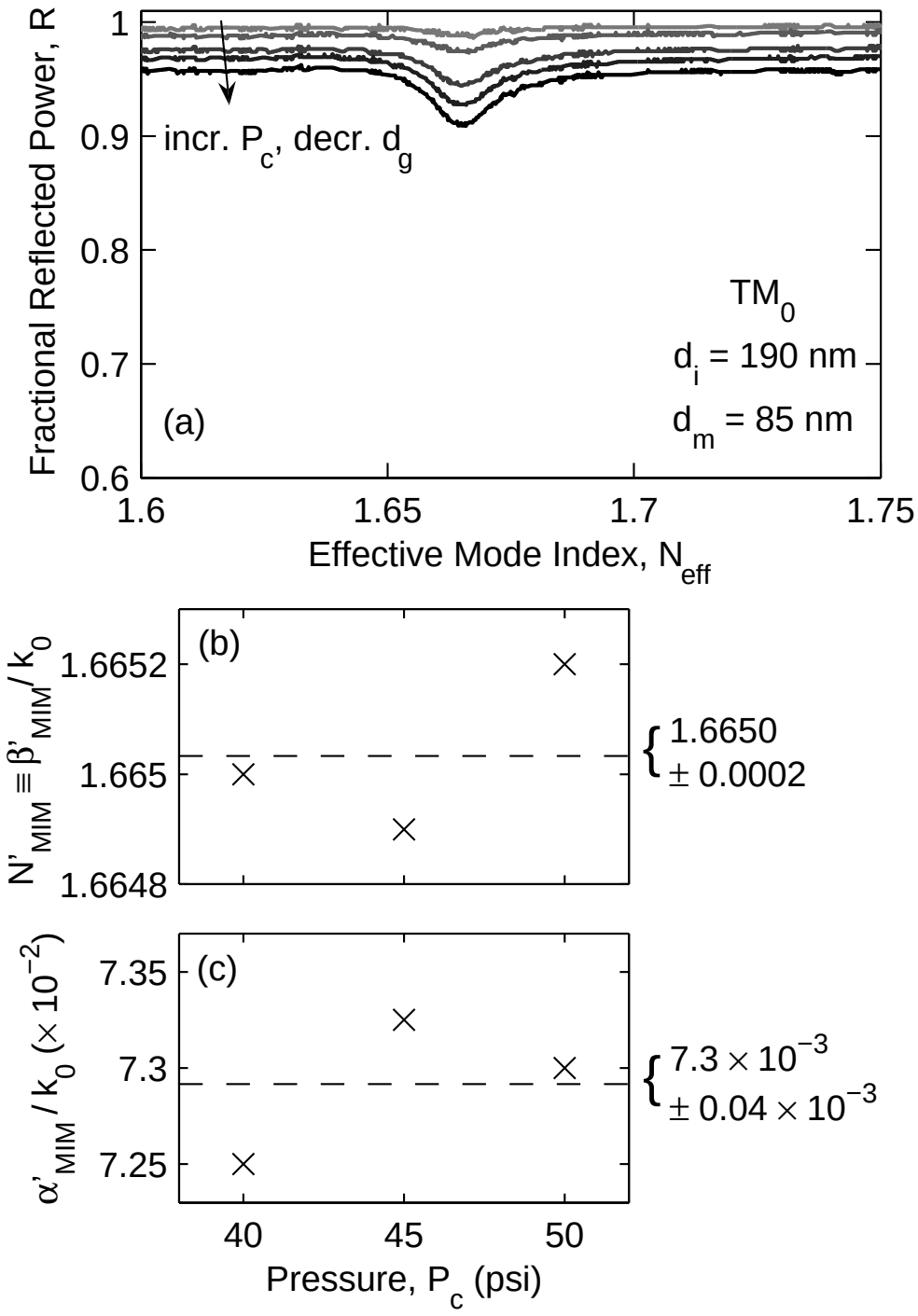

Figure 5.18: (a) TM reflection power spectra for the structure in Fig. 5.9 with $d_i = 190$ nm and $d_i = 85$ nm measured at various air gap thicknesses d_g corresponding to $P_c = 30$, 35, 40, 45, and 50 psi. (b) The normalized propagation constants N'_{MIM} and (c) the normalized attenuation coefficients α'_{MIM}/k_0 of the resonances at various values of P_c.

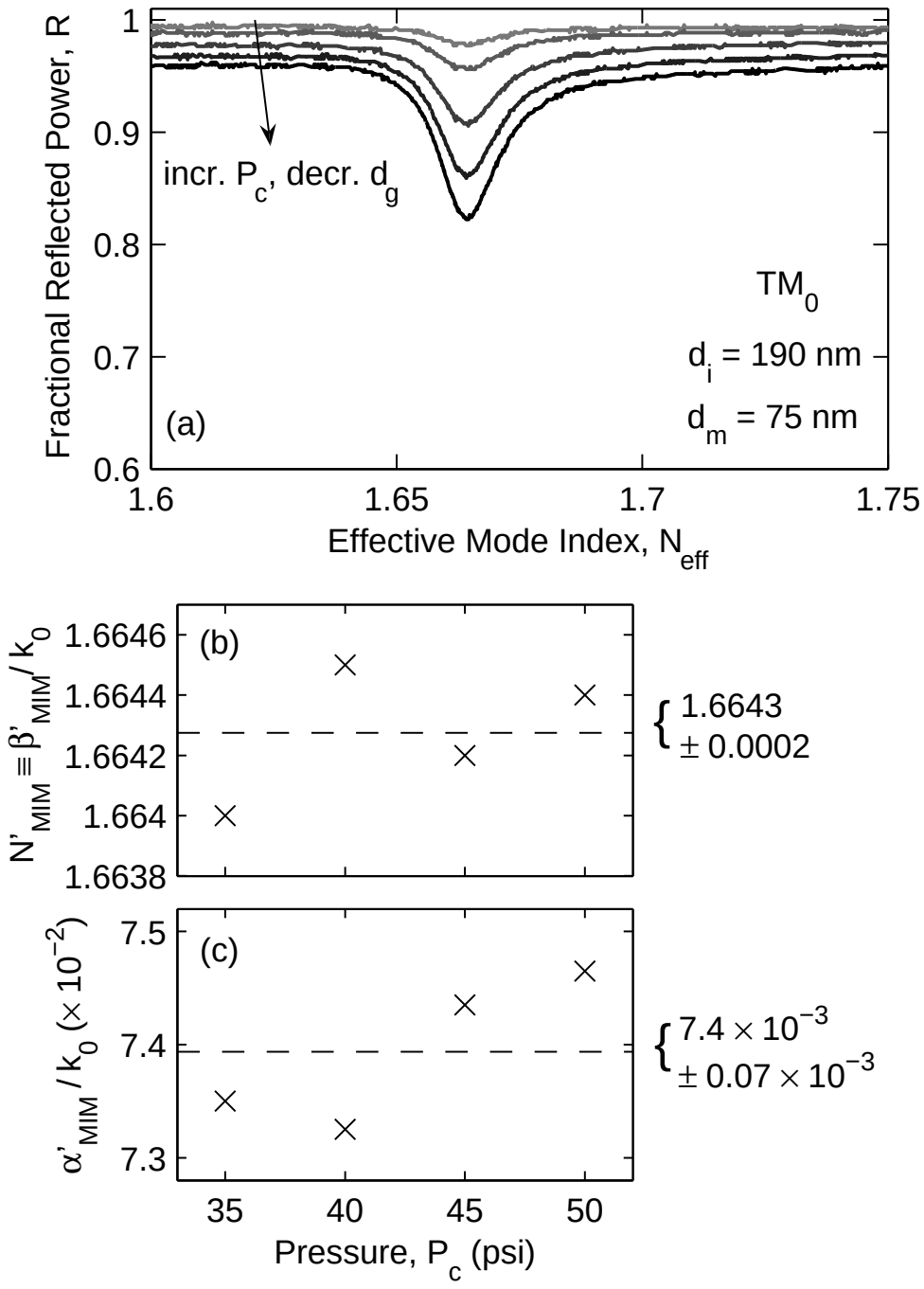

Figure 5.19: (a) TM reflection power spectra for the structure in Fig. 5.9 with $d_i = 190$ nm and $d_i = 75$ nm measured at various air gap thicknesses d_g corresponding to $P_c = 30$, 35, 40, 45, and 50 psi. (b) The normalized propagation constants N'_{MIM} and (c) the normalized attenuation coefficients α'_{MIM}/k_0 of the resonances at various values of P_c.

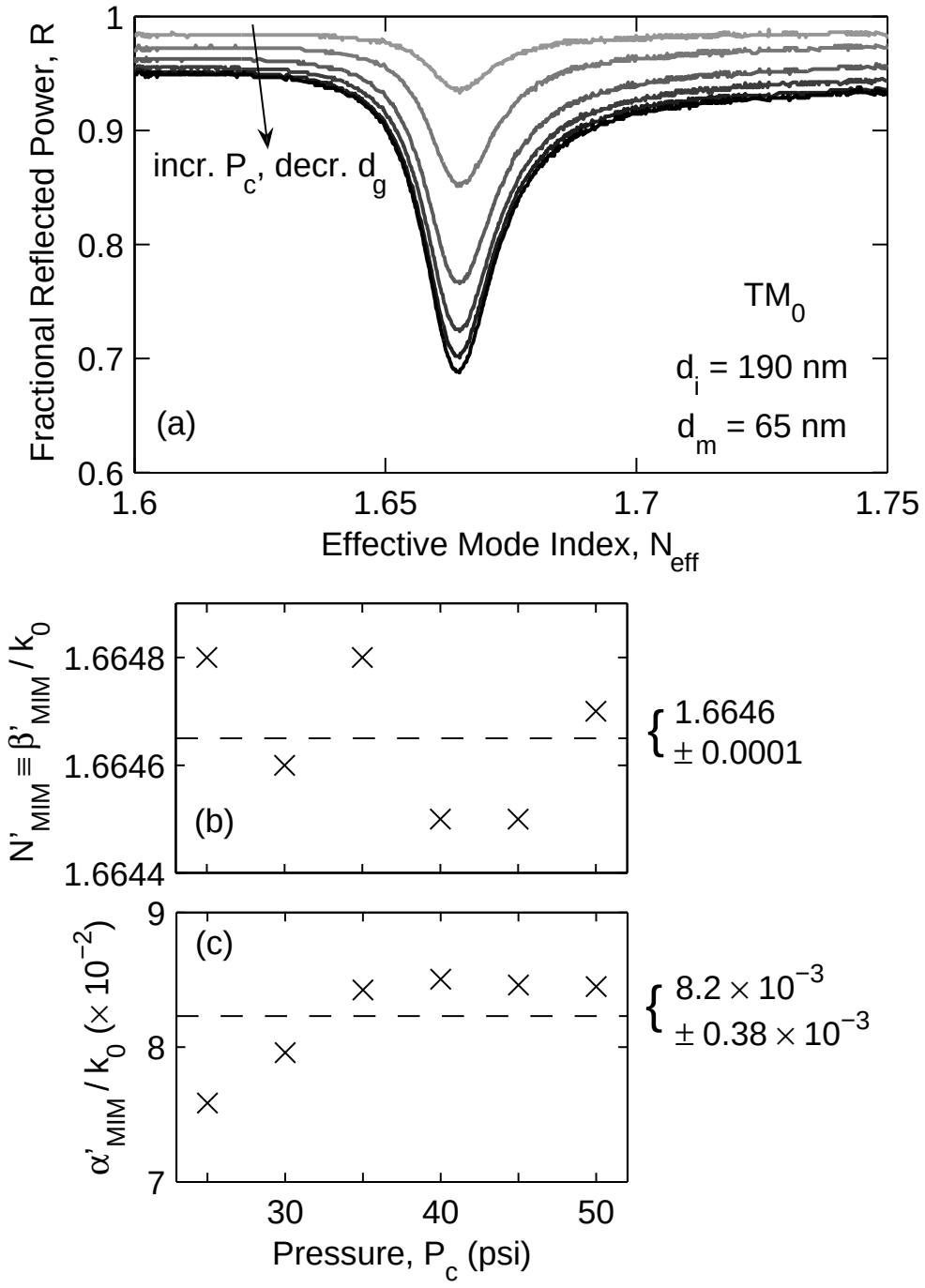

Figure 5.20: (a) TM reflection power spectra for the structure in Fig. 5.9 with $d_i = 190$ nm and $d_i = 65$ nm measured at various air gap thicknesses d_g corresponding to $P_c = 25$, 30, 35, 40, 45, and 50 psi. (b) The normalized propagation constants N'_{MIM} and (c) the normalized attenuation coefficients α'_{MIM}/k_0 of the resonances at various values of P_c.

5.5 Summary

In this chapter, two MIM (Au-SiO_x-Au) structures were fabricated and characterized using the Metricon Model 2010 Prism Coupler, which implements an ATR configuration. Both MIM structures have a 75 nm-thick top metal cladding and 400 nm-thick bottom metal cladding, and the core sizes are 200 nm and 50 nm. The oxide cores were deposited using PECVD and the metal claddings were deposited using an e-beam evaporator. The two MIM structures were characterized at wavelength $\lambda = 1550$ nm, and the results agree very well with the theoretical results in both the propagation constants β and the attenuation coefficients α. Moreover, the MIM structures were characterized at various air gap thicknesses d_g between the prism and the MIM structures, and the measured β and α shows no dependence on d_g values. MIM structures with various top metal cladding thicknesses d_m were also fabricated and characterized by the TTR method. The measurement results indicate that the TTR method is insensitive to d_m for the case when d_m is sufficiently large. The fact that the TTR method is insensitive to d_g and d_m demonstrates the robustness of the TTR method as a technique of characterizing MIM structures.

CHAPTER 6

MULTIMODE MIM WAVEGUIDES

MIM waveguides with subwavelength apertures are of great interest for researchers in the plasmonics area, primarily for their potential in realizing integrated optical nanocircuitry. However, the subwavelength dimensions also make experimental characterization difficult. In order to couple light into an MIM waveguide in a systerm/circuit, one possible way is to use a tapered MIM waveguide. Moreover, large-core MIM waveguides may also be used for lower-loss interconnects in SP-based optical nanocircuitry. Therefore, it is important to investigate MIM waveguides with larger core sizes. However, as discussed in Sec. 2.2, large-core MIM waveguides support higher-order TM modes. In conventional experimental characterization techniques, all the waveguide modes are excited simultaneously, therefore the propagation constant and attenuation coefficient of each mode cannot be easily extracted from the measurement data. In contrast, the TTR method, which uses the ATR configuration, inherently has very good angular selectivity and can be used to characterize each of the waveguide modes separately. In this chapter, the properties of the waveguide modes in multimode MIM waveguides will be simulated and discussed. Two MIM (Au-SiO_2-Au) structures with 730 nm and 1460 nm oxide cores were fabricated and characterized.

6.1 Theoretical Performance of Multimode MIM Waveguides

By using the characteristic equation of MIM structures developed in Sec. 2.2,

$$\tanh(\kappa_d d_d) = -\frac{2}{\left(\frac{\kappa_m}{\kappa_d}\frac{\varepsilon_d}{\varepsilon_m} + \frac{\kappa_d}{\kappa_m}\frac{\varepsilon_m}{\varepsilon_d}\right)}, \tag{6.1}$$

the complex propagation constants $\gamma_{\text{MIM}} = \beta_{\text{MIM}} - j\alpha_{\text{MIM}}$ can be calculated. Figure 6.1 shows the effective mode indices N_{eff} and propagation lengths L as functions of

dielectric core thickness for various modes in an MIM (Au-SiO_x-Au) waveguide. It can be observed from Fig. 6.1(a) that at small core thicknesses d_i, only the fundamental mode, TM_0, exists. As d_i increases, the MIM waveguide starts to support higher-order modes, and the cutoff thickness is larger for higher-order modes. Moreover, the two plasmonic modes, TM_0 and TM_1, become practically degenerate at large d_i, because the two Au/SiO_x interfaces become decoupled and the TM_0 and TM_1 modes propagate like independent SP modes at the Au/SiO_x interfaces. This can be observed from both the values of N_{eff} and L of the TM_0 and TM_1 modes, which approach the values of N_{eff} and L of the SP mode at a Au/SiO_x interfaces, respectively. On the other hand, the oscillatory modes, TM_2 and TM_3 modes, do not approach the SP mode at a Au/SiO_x interfaces. As d_i increases, the attenuations of the oscillatory modes always decreases. This property is also observed for the conventional modes in dielectric waveguides. It is worth mentioning that at larger d_i values, the attenuation of the fundamental mode exceeds the attenuation of the oscillatory modes (e.g. TM_2 and TM_3 modes). This differs from conventional dielectric waveguides, in which the fundamental mode always has the lowest attenuation. For data transmission purposes, it is favorable that the fundamental mode has dominantly low attenuation. Therefore, when other modes which have comparable attenuation exist, it is critical to determine the propagation constant and attenuation coefficient of each mode. In the next section, the TTR measurement results for two MIM waveguides with $d_i = 730$ nm and 1460 nm will be presented. According to Fig. 6.1(b), the TM_0 and TM_1 modes exist when $d_i = 730$ nm; when $d_i = 1460$ nm, the TM_{0-2} modes exist (the TM_3 mode is near cutoff and will not be included). In both cases, the TM_0 modes have the lowest attenuation among all supported modes, but the attenuations of all the modes are comparable.

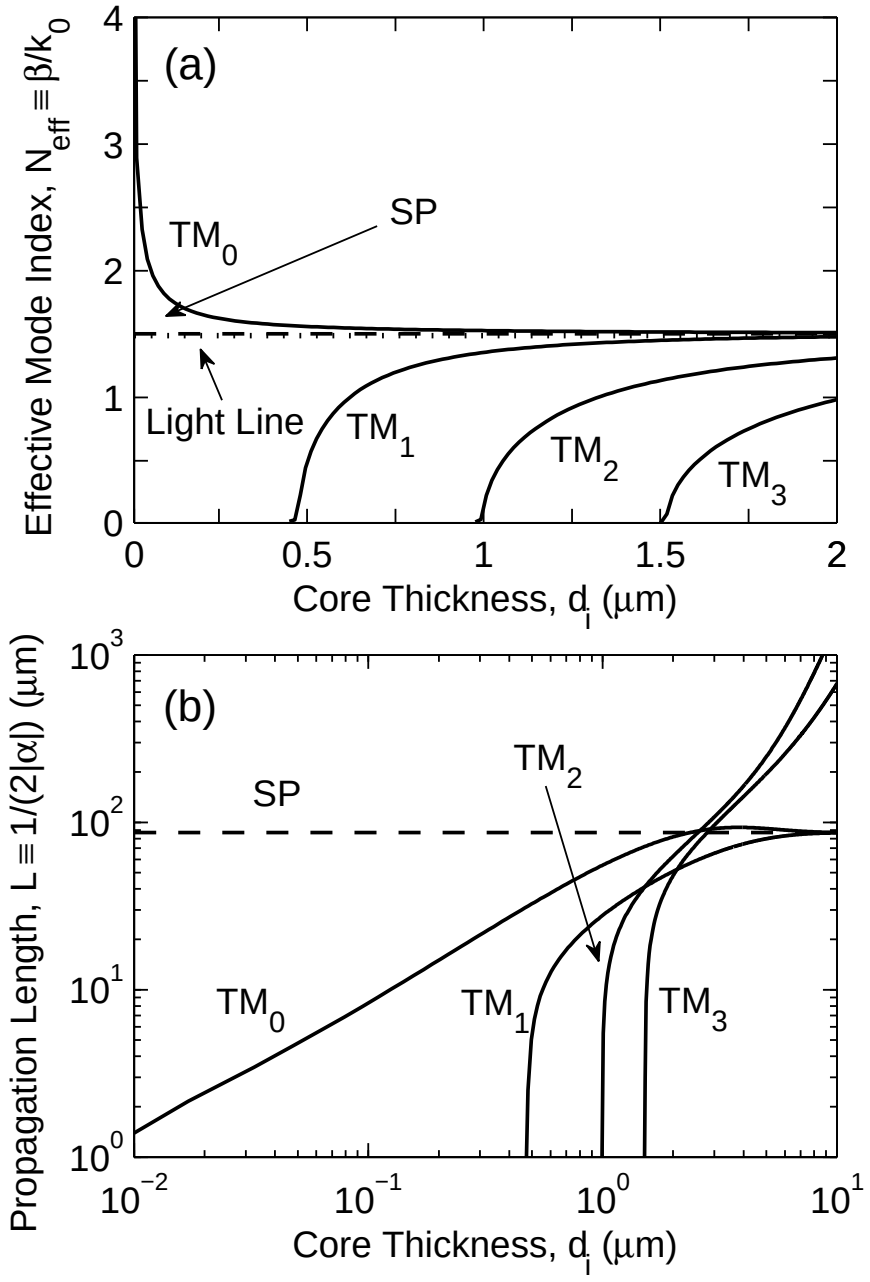

Figure 6.1: (a) Effective mode indices $N_{\text{eff}} \equiv \beta/k_0$ and (b) propagation lengths $L \equiv 1/(2|\alpha|)$ for the TM_{0-3} modes as functions of the dielectric core thickness d_i in an MIM (Au-SiO_x-Au) waveguide. In this case, the metal is Au at $\lambda = 1550$ nm, with a dielectric constant $\widetilde{\varepsilon}_{\text{Au}} = -115 - j11.3$ [66]. The dielectric constant of the SiO_x core is $\varepsilon_i = (1.4877)^2$. The curves for the MIM TM_{0-3} modes and the single gold/dielectric interface are labeled as TM_{0-3} and SP, respectively. The light line in (a) represents light propagation in bulk SiO_x, with an effective mode index $N_{\text{eff}} = 1.4877$. The effective mode index for the SP mode at a single gold/dielectric interface is $N_{\text{eff}} = 1.5020$.

6.2 TTR Measurements for Multimode MIM Waveguides

In this section, using the Metricon Model 2010 Prism Coupler [97], the TTR method is experimentally applied to two MIM (Au-SiO_x-Au) waveguide structures. The schematic diagram of the experimental configuration is shown in Fig. 6.2. Two MIM structures with two different SiO_x core thicknesses, $d_i = 730$ nm and 1460 nm, were fabricated and characterized at $\lambda = 1.55$ μm. To ensure the appropriate coupling strength, the Au layer on the top of the structure is 75 nm in thickness, which is about 3 skin depths. The Au layer substrate is 400 nm in thickness, which, for practical purposes, is optically semi-infinite. The SiO_x cores were deposited by using PECVD (see Sec. 5.1.1) and the Au cladding layers were deposited by using an e-beam evaporator (see Sec. 5.1.2).

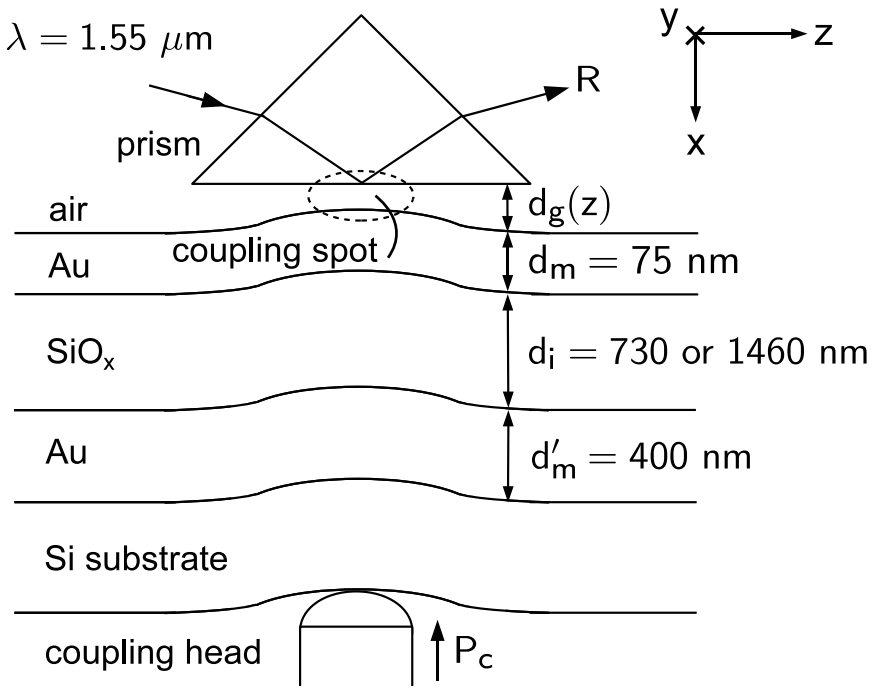

Figure 6.2: Schematic diagram of the ATR configuration applied to the MIM structures.

The theoretical propagation constant of the MIM waveguide can be rigorously calculated by using the APM [91]. At $\lambda = 1.55$ μm, the refractive index of Au is $\widetilde{n}_{\text{Au}} =$

$0.526 - j10.74$ [66], and the refractive index of the PECVD oxide is $n_{\mathrm{SiO}_x} = 1.4877$. The calculated normalized propagation constants are $(\beta_{\mathrm{TM}_0} - j\alpha_{\mathrm{TM}_0})/k_0 = 1.5392 - j0.00281$ and $(\beta_{\mathrm{TM}_1} - j\alpha_{\mathrm{TM}_1})/k_0 = 1.1764 - j0.00668$ for the 730 nm-core structures. For the 1460 nm-core structure, the calculated $(\beta_{\mathrm{TM}_0} - j\alpha_{\mathrm{TM}_0})/k_0 = 1.5167 - j0.00176$, $(\beta_{\mathrm{TM}_1} - j\alpha_{\mathrm{TM}_1})/k_0 = 1.4459 - j0.00310$, and $(\beta_{\mathrm{TM}_2} - j\alpha_{\mathrm{TM}_2})/k_0 = 1.1085 - j0.00321$. It should be noted that in these calculations, it is assumed that the MIM structures have symmetric and semi-infinite claddings on both sides.

6.2.1 Oxide Core Thickness of 730 nm

The measured angular TM reflection power spectra of the structure in Fig. 6.2 with and $d_i = 730$ nm is shown in Fig. 6.3(a). At $\lambda = 1550$ nm, the refractive index of the prism is $n_p = 1.9349$. By increasing the pressure of the coupling head, P_c, the air gap thickness d_g decreases and a series of spectra were measured. The resonances of R at higher and lower effective mode index N_{eff} correspond to the TM_0 and TM_1 modes in the MIM structure, respectively. Figure 6.3(b) shows the effective mode index $N'_{\mathrm{TM}_0} \equiv \beta'_{\mathrm{TM}_0}/k_0$, which corresponds to the resonance minima of the TM_0 resonance, as a function of P_c, and the average of the measurements yields $N'_{\mathrm{TM}_0} = 1.5333$, with a standard deviation $\sigma_\beta = 0.0001$. The prime denotes results obtained by the TTR method, in contrast to the rigorous theoretical results. Figure 6.3(c) shows the normalized attenuation coefficients $\alpha'_{\mathrm{TM}_0}/k_0 =$ HWHMs of the TM_0 mode as a function of P_c, and the average of the measurements yields $\alpha'_{\mathrm{TM}_0}/k_0 = 0.00247$, with a standard deviation $\sigma_\alpha = 0.00007$. This is equivalent to a loss of 0.087 dB/μm or $L = 50$ μm. The resonance minima and HWHMs are obtained after removing the background variation in R; this can be done by leveling both sides of a resonance to unity. It can be observed from Fig. 6.3(b) and (c) that there is no apparent trend in the measured N'_{TM_0} and $\alpha'_{\mathrm{TM}_0}/k_0$ as functions of P_c. The experimental results, $(\beta'_{\mathrm{TM}_0} - j\alpha'_{\mathrm{TM}_0})/k_0 = 1.5333 - j0.00247$ on average, agree well with the theoretical

result, $(\beta_{\mathrm{TM}_0} - j\alpha_{\mathrm{TM}_0})/k_0 = 1.5392 - j0.00281$. Similar to the cases of single-mode MIM waveguides, the measured attenuation is about 13% smaller than the theoretical value.

The N'_{TM_1} and α'_{TM_1} of the TM_1 mode can also be obtained in the same manner. Figure 6.3(d) shows N'_{TM_1} as a function of P_c, and the average of the measurements yields $N'_{\mathrm{TM}_1} = 1.1687$, with a standard deviation $\sigma_\beta = 0.0001$. Figure 6.3(e) shows $\alpha'_{\mathrm{TM}_1}/k_0$ as a function of P_c, and the average of the measurements yields $\alpha'_{\mathrm{TM}_1}/k_0 = 0.00588$, with a standard deviation $\sigma_\alpha = 0.00009$. This is equivalent to a loss of 0.21 dB/μm or $L = 21\ \mu$m. Again there is no apparent trend in the measured N'_{TM_1} and $\alpha'_{\mathrm{TM}_1}/k_0$ as functions of P_c. The experimental results, $(\beta'_{\mathrm{TM}_1} - j\alpha'_{\mathrm{TM}_1})/k_0 = 1.1687 - j0.00588$ on average, agree well with the theoretical result, $(\beta_{\mathrm{TM}_1} - j\alpha_{\mathrm{TM}_1})/k_0 = 1.1764 - j0.00668$. Similar to the case of the TM_0 mode, the measured attenuation is about 14% smaller than the theoretical value.

As predicted in Sec. 6.1, the loss of the fundamental TM_0 mode is smaller than the loss of the TM_1 mode in this case. However, the measured loss of the TM_1 mode is only 2.4 times the loss of the TM_0 mode. As a result, the consideration of higher-order modes is critical in the design of SP-based optical nanocircuitry, in which large-core, multimode MIM waveguides may be used as lower-loss interconnects or tapered end-couplers.

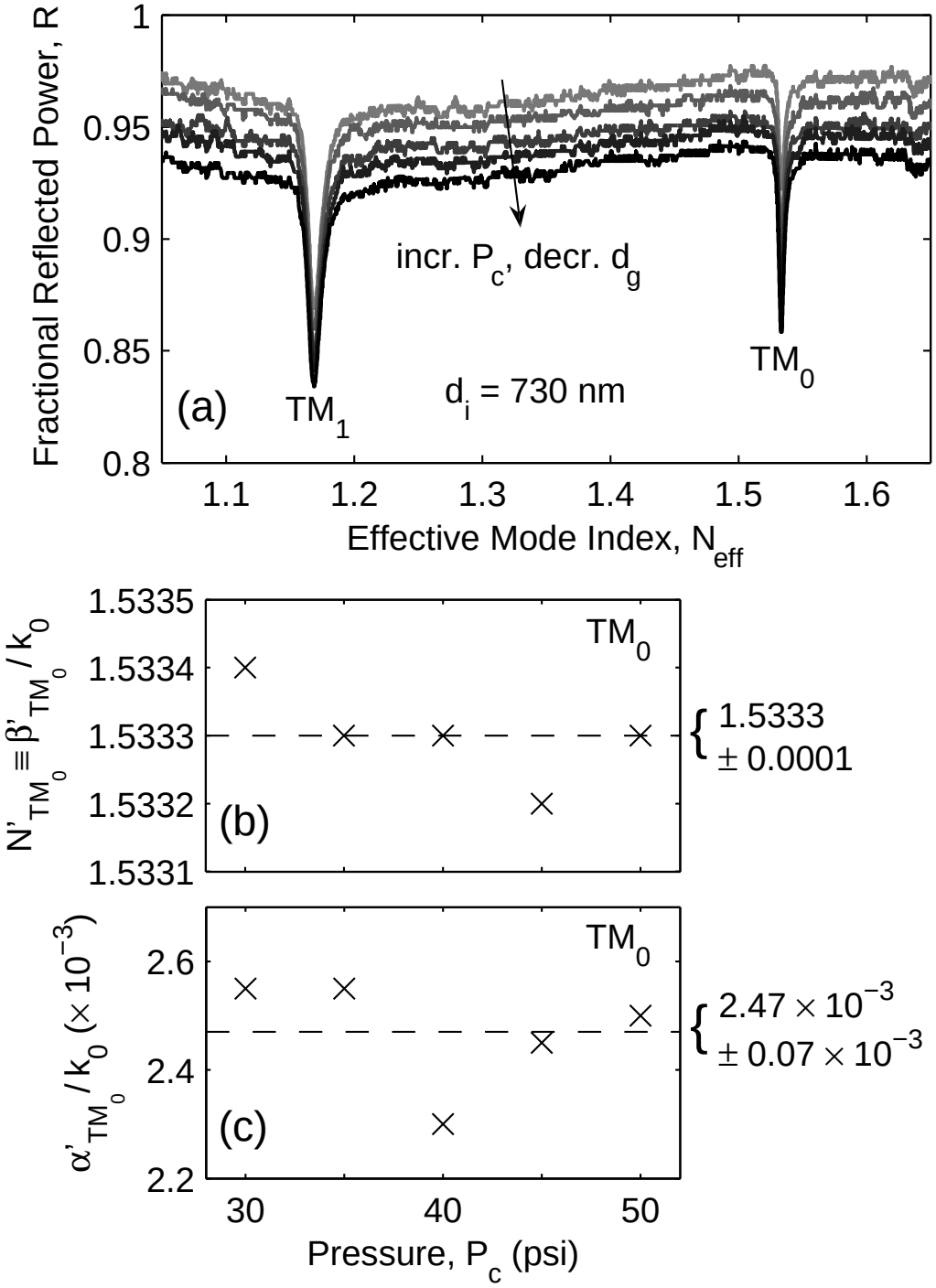

Figure 6.3: (a) TM reflection power spectra for the structure in Fig. 6.2 with d_i = 730 nm measured at various air gap thicknesses d_g, which correspond to pressures of the coupling head, P_c = 30, 35, 40, 45, and 50 psi. (b) The normalized propagation constants $N'_{\mathrm{TM}_0} \equiv \beta'_{\mathrm{TM}_0}/k_0$ corresponding to the "resonance minima" and (c) the normalized attenuation coefficients $\alpha'_{\mathrm{TM}_0}/k_0$ = HWHMs of the TM_0 resonances at various values of P_c.

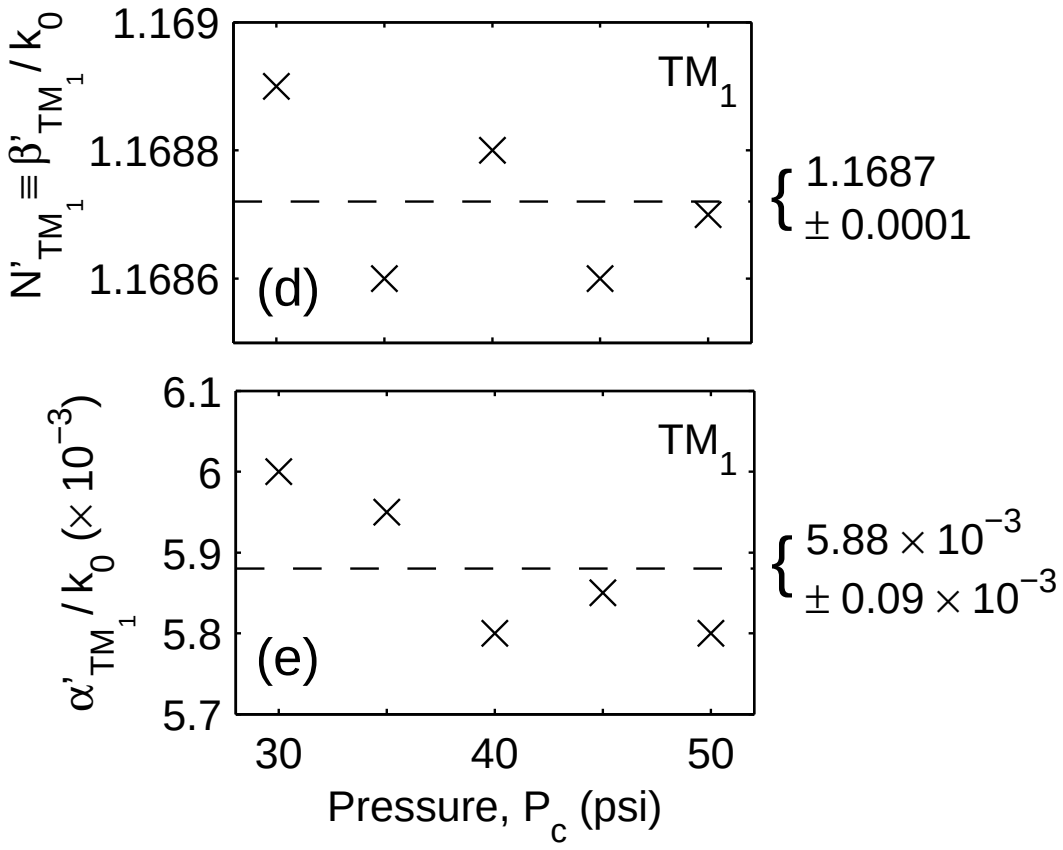

Figure 6.3 (cont.): (d) The normalized propagation constants N'_{TM_1} and (e) the normalized attenuation coefficients $\alpha'_{\mathrm{TM}_1}/k_0$ of the TM_1 resonances at various values of P_c.

6.2.2 Oxide Core Thickness of 1460 nm

The measured angular TM reflection power spectra of the structure in Fig. 6.2 with and $d_i = 1460$ nm is shown in Fig. 6.4(a). At $\lambda = 1550$ nm, the refractive index of the prism is $n_p = 1.9349$. The three resonances of R correspond to the TM_0, TM_1, and TM_2 modes in the MIM structure. It is shown that the resonances of the TM_0 and TM_1 modes are much weaker at larger d_g, while the resonance of the TM_2 mode is approximately independent of d_g. This is because the air gap thickness d_g has only a small effect on the coupling efficiency of a mode with low effective mode index.

Figure 6.4(b) shows the effective mode index $N'_{\mathrm{TM}_0} \equiv \beta'_{\mathrm{TM}_0}/k_0$ of the TM_0 mode as a function of P_c, and the average of the measurements yields $N'_{\mathrm{TM}_0} = 1.5166$, with a

standard deviation $\sigma_\beta = 0.0003$. Figure 6.4(c) shows the normalized attenuation coefficients $\alpha'_{\mathrm{TM}_0}/k_0$ = HWHMs of the TM_0 mode as a function of P_c, and the average of the measurements yields $\alpha'_{\mathrm{TM}_0}/k_0 = 0.00171$, with a standard deviation $\sigma_\alpha = 0.00007$. This is equivalent to a loss of 0.06 dB/μm or $L = 72$ μm. It can be observed from Fig. 6.4(b) and (c) that there is no apparent trend in the measured N'_{TM_0} and $\alpha'_{\mathrm{TM}_0}/k_0$ as functions of P_c. The experimental results, $(\beta'_{\mathrm{TM}_0} - j\alpha'_{\mathrm{TM}_0})/k_0 = 1.5166 - j0.00171$ on average, agree well with the theoretical result, $(\beta_{\mathrm{TM}_0} - j\alpha_{\mathrm{TM}_0})/k_0 = 1.5167 - j0.00176$. However, unlike the previous cases, in which the measured attenuations are about 15% smaller than the theoretical values, the difference between the measured and the theoretical attenuation is much less in this case. This can be ascribed to the angular distribution of the laser beam, which broadens the measured resonance. This broadening effect is stronger when the resonance is narrower. More details about the effect of angular distribution of the laser beam will be discussed in Sec. 7.1.

Figure 6.4(d) shows N'_{TM_1} as a function of P_c, and the average of the measurements yields $N'_{\mathrm{TM}_1} = 1.4473$, with a standard deviation $\sigma_\beta = 0.0001$. Figure 6.4(e) shows $\alpha'_{\mathrm{TM}_1}/k_0$ as a function of P_c, and the average of the measurements yields $\alpha'_{\mathrm{TM}_1}/k_0 = 0.00266$, with a standard deviation $\sigma_\alpha = 0.0001$. This is equivalent to a loss of 0.094 dB/μm or $L = 46$ μm. Again there is no apparent trend in the measured N'_{TM_1} and $\alpha'_{\mathrm{TM}_1}/k_0$ as functions of P_c. The experimental results, $(\beta'_{\mathrm{TM}_1} - j\alpha'_{\mathrm{TM}_1})/k_0 = 1.4473 - j0.00266$ on average, agree well with the theoretical result, $(\beta_{\mathrm{TM}_1} - j\alpha_{\mathrm{TM}_1})/k_0 = 1.4459 - j0.0031$. Similar to the cases of single-mode MIM waveguides, the measured loss is about 16% smaller than the theoretical prediction.

Moreover, Fig. 6.4(f) shows N'_{TM_2} as a function of P_c, and the average of the measurements yields $N'_{\mathrm{TM}_2} = 1.1149$, with a standard deviation $\sigma_\beta = 0.0001$. Figure 6.4(e) shows $\alpha'_{\mathrm{TM}_1}/k_0$ as a function of P_c, and the average of the measurements yields $\alpha'_{\mathrm{TM}_2}/k_0 = 0.0039$, with a standard deviation $\sigma_\alpha = 0.00004$. This is equivalent to a loss of 0.14 dB/μm or $L = 32$ μm. Similarly, there is no apparent trend in the

measured N'_{TM_2} and $\alpha'_{\mathrm{TM}_2}/k_0$ as functions of P_c. The experimental results, $(\beta'_{\mathrm{TM}_2} - j\alpha'_{\mathrm{TM}_2})/k_0 = 1.1149 - j0.0039$ on average, agree well with the theoretical result, $(\beta_{\mathrm{TM}_2} - j\alpha_{\mathrm{TM}_2})/k_0 = 1.1085 - j0.00321$. However, unlike any of the previous cases, the measured attenuation is about 20% larger than the theoretical prediction. This is probably due to loss mechanisms other than the absorption loss of the metal, which is the only mechanism taken into account in the theoretical calculation. For example, scattering loss caused by the rough Au/SiO_x interfaces is a possible reason for extra loss associated with the TM_2 mode. Scattering loss is much larger for higher-order modes which have large zigzag angles in the cores [87] and large penetration depths into the claddings. The further investigation of the scattering loss is one of the areas for future research.

In this case, the TM_0 and TM_1 modes have similar effective indices, and they also have comparable attenuation coefficients. Therefore, for the design and operation of a large-core, multimode MIM waveguide like this, it is important to investigate the effects of the two potentially competitive modes on the signal transmission.

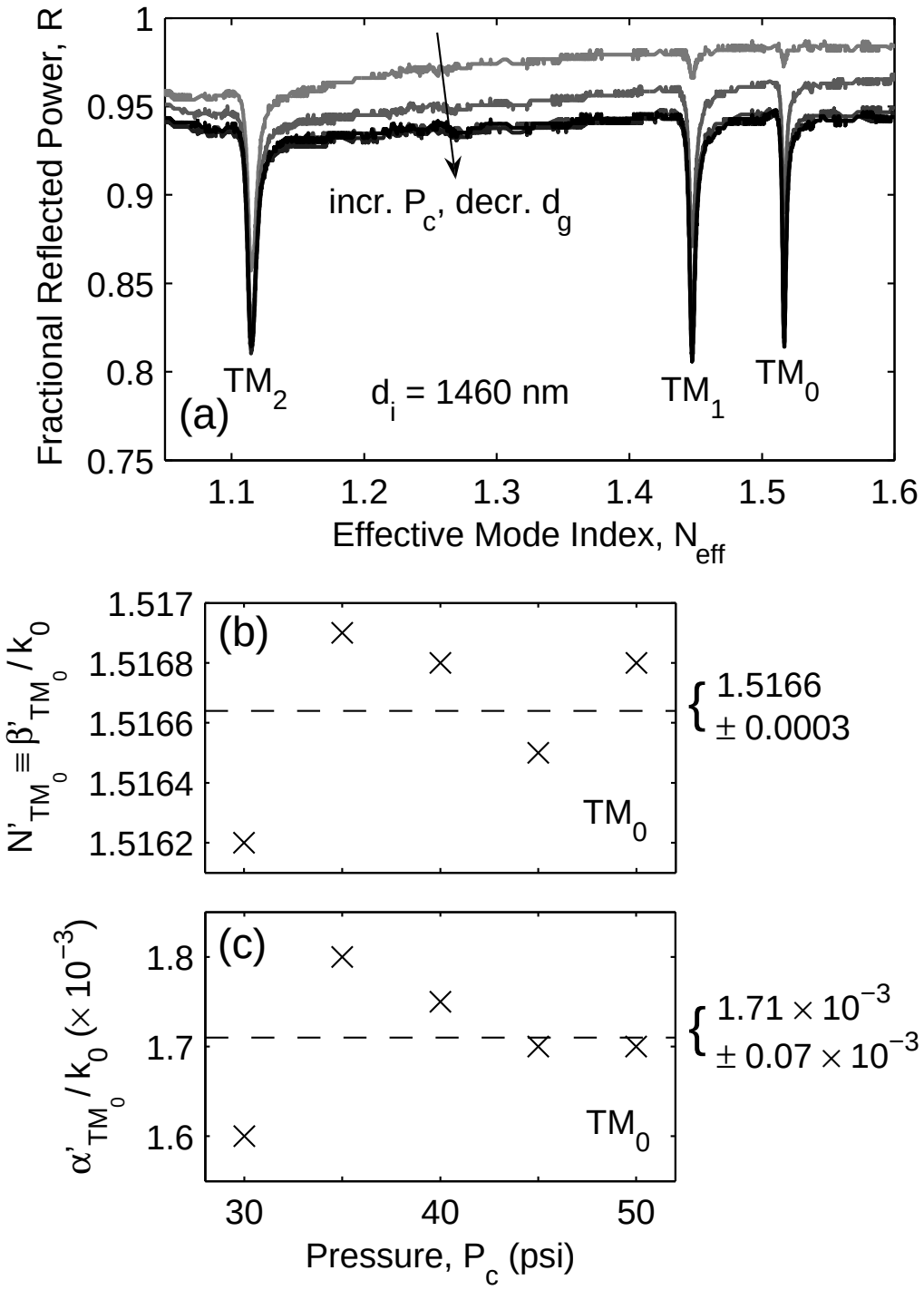

Figure 6.4: (a) TM reflection power spectra for the structure in Fig. 6.2 with d_i = 1460 nm measured at various air gap thicknesses d_g, which correspond to pressures of the coupling head, P_c = 30, 35, 40, 45, and 50 psi. (b) The normalized propagation constants N'_{TM_0} and (c) the normalized attenuation coefficients $\alpha'_{\mathrm{TM}_0}/k_0$ of the TM_0 resonances at various values of P_c.

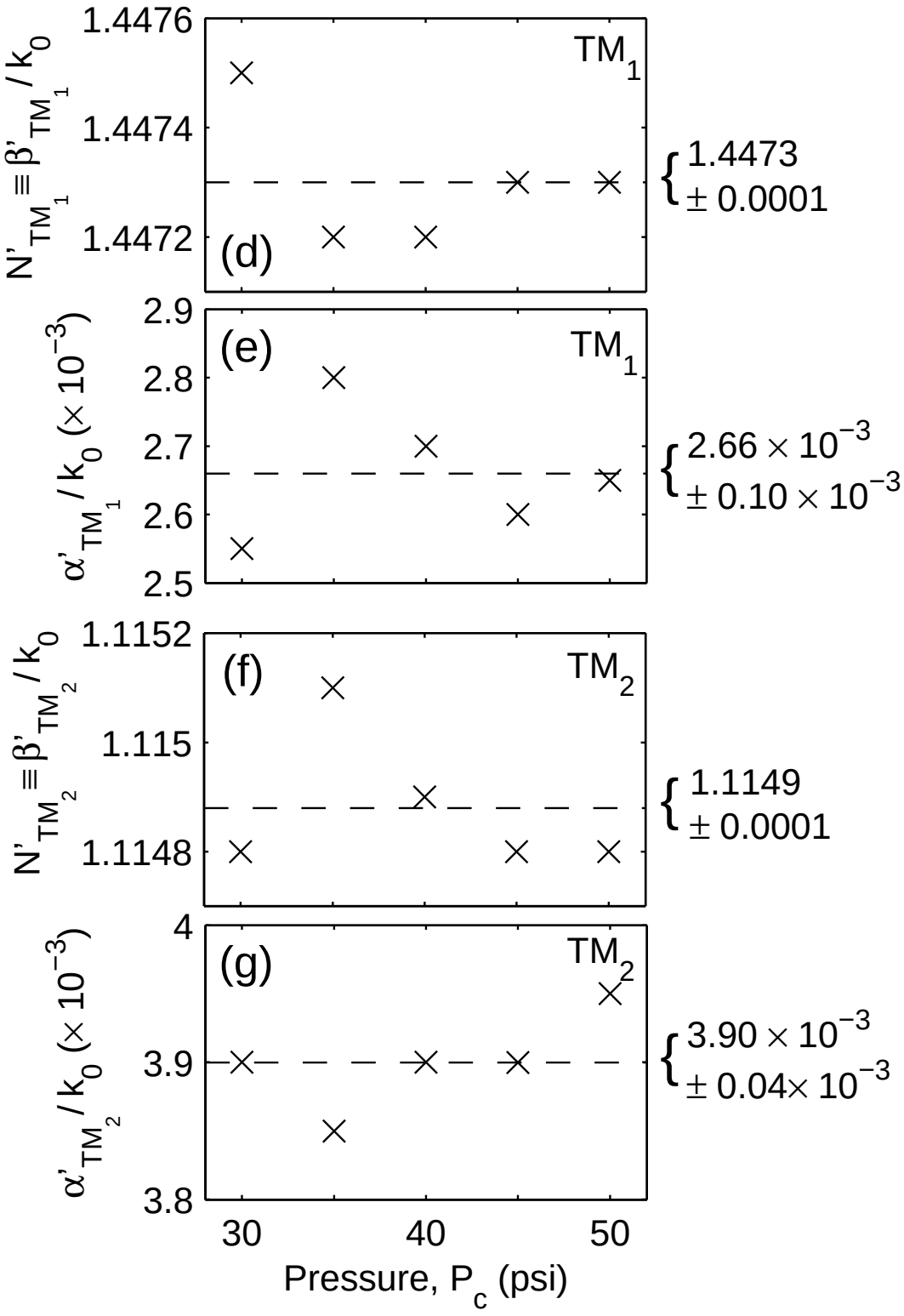

Figure 6.4 (cont.): (d) The normalized propagation constants N'_{TM_1} and (e) the normalized attenuation coefficients $\alpha'_{\mathrm{TM}_1}/k_0$ of the TM_1 resonances and (f) the normalized propagation constants N'_{TM_2} and (e) the normalized attenuation coefficients $\alpha'_{\mathrm{TM}_2}/k_0$ of the TM_2 resonances at various values of P_c.

6.3 Summary

In this chapter, the theoretical performance and experimental characterization of multimode Au-SiO_x-Au MIM structures were discussed. Large-core, multimode MIM waveguides may be used as low-loss interconnects or tapered end-couplers in SP-based optical nanocircuitry. Therefore, the experimental characterization of the propagation constants and attenuation coefficients of the modes in the multimode MIM waveguide are critically important. In this work, two multimode MIM waveguides were fabricated and characterized by using the TTR method. The effective mode indices and attenuation coefficients of all the modes in the multimode MIM waveguides can be separately obtained from the angle of resonance minima and the width of the resonance, respectively. To the best of the author's knowledge, this is the first time the propagation constant of each mode in a multimode MIM waveguide has been individually measured. Also, to the best of the author's knowledge, this is the first time the attenuation coefficient of each mode in a multimode MIM waveguide has been individually measured.

From the experimental results for both waveguide structures, it was shown that the losses of the fundamental TM_0 modes are the smallest among all modes. However, the losses of the other modes are only two to three times larger than the losses of the TM_0 modes. Therefore, the propagation constant and attenuation coefficient of each mode must be taken into account when a large-core, multimode MIM waveguide is used in the design of SP-based optical nanocircuitry.

CHAPTER 7

EFFECTS OF THE LASER BEAM ON THE EXPERIMENTAL RESULTS

In the TTR simulation, single-wavelength, plane-wave incidence is used; however, in the TTR measurements based on an ATR configuration, a realistic laser beam is not a plane wave and further contains more than one wavelength. Therefore, the effect of the angular distribution and linewidth of the incident laser beam needs to be quantified in order to validate the results obtained by the TTR method.

7.1 Effect of the Angular Distribution of Incident Laser Beam

As shown in Fig. 5.6, the laser beam passes a circular aperture before it is incident upon the prism coupler. The diameter of the aperture is 1.2 mm and the wavelength of the laser is 1550 nm. Figures 7.1(a) and (b) show the measured laser beam profiles that were measured at D_a = 700 mm and 350 mm, respectively, where D_a is the distance away from the aperture. The profiles are very similar to the well-known Airy disk, the diffraction pattern of a plane wave passing through a circular aperture. However, the measured profiles are neither perfectly circular nor azimuthally symmetric, which may be due to a non-circular aperture and/or an asymmetric laser beam profile. The axes in Figs. 7.1(a) and (b) can be translated into angles, and Fig. 7.1(c) shows the comparison of the angular beam profiles on the y axes in Figs. 7.1(a) and (b). The normalized Airy-disk profile I_a can be calculated by using [103]

$$I_a(\delta) = \left[\frac{2J_1(kr_a \sin\delta)}{kr_a \sin\delta}\right]^2, \tag{7.1}$$

where J_1 is the first-order Bessel function of the first kind, k is the freespace wavevector, r_a is the radius of the aperture, and δ is the field angle with $\delta = 0$ corresponds to

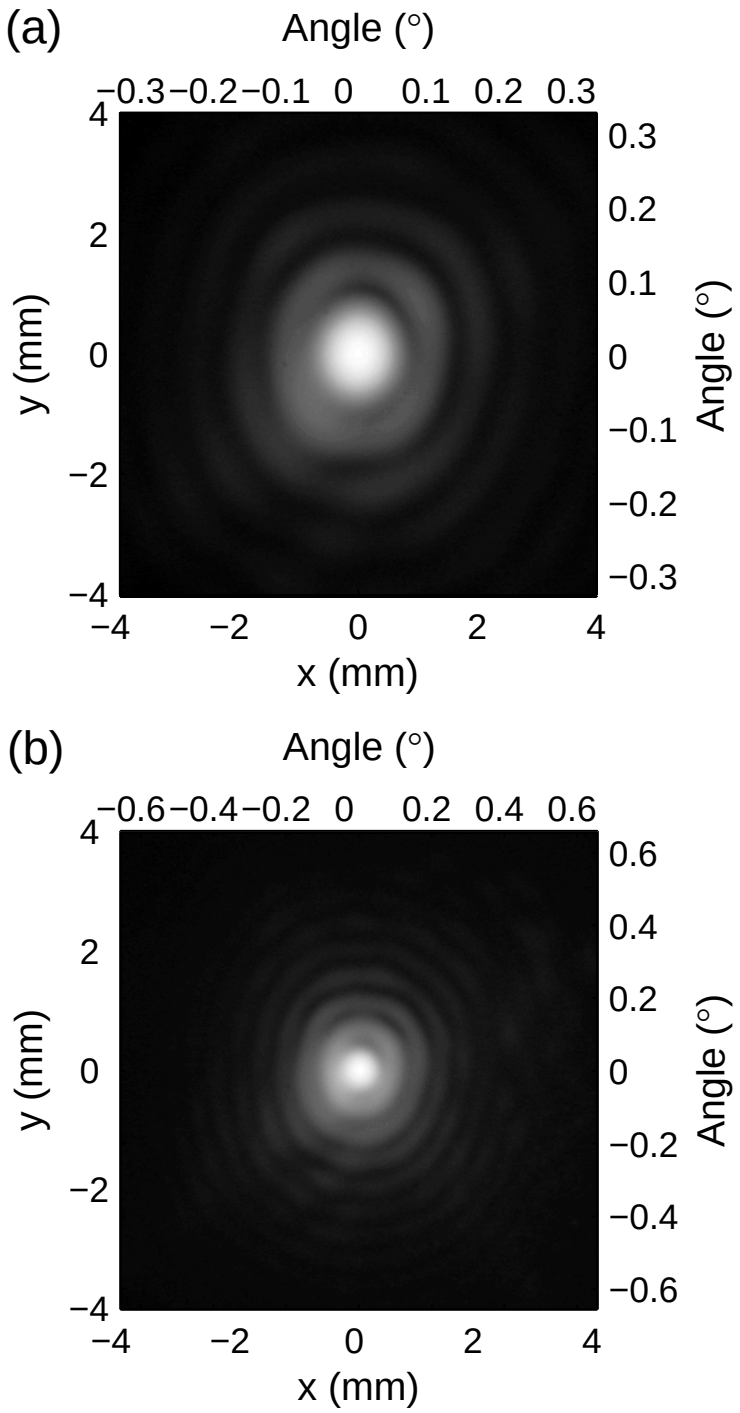

Figure 7.1: Intensity profile of the laser in the Metricon Prism Coupler measured at D_a = (a) 700 mm and (b) 350 mm. These images were obtained using Hamamatsu Infrared Camera Model C2741-03.

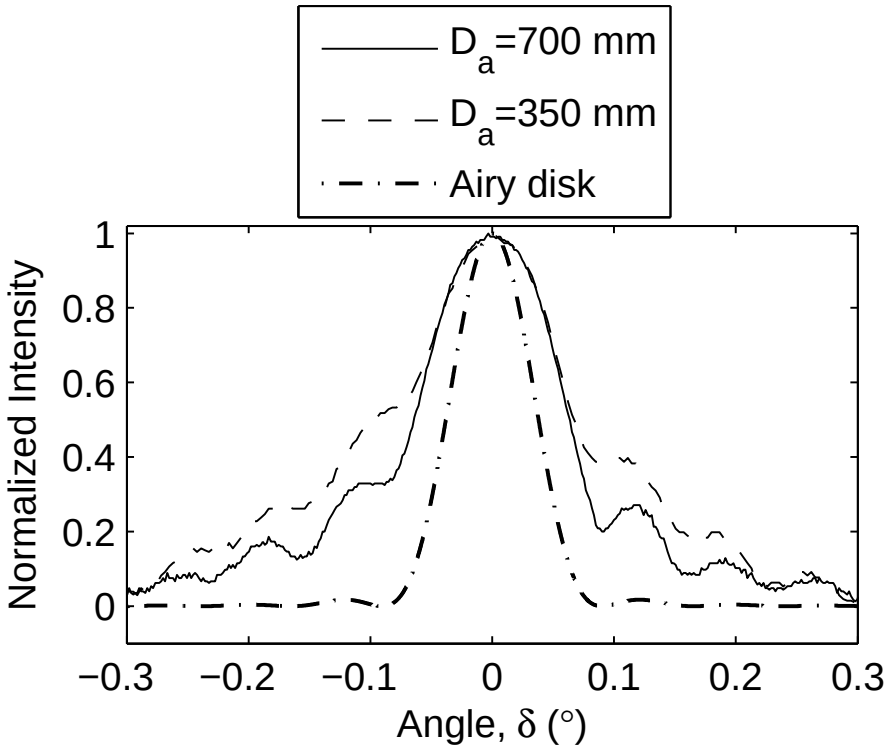

Figure 7.1 (cont.): (c) Comparison of the measured angular beam profiles on the y axes for $D_a = 700$ mm and 350 mm. The profile of the Airy disk is calculated for a 1.2 mm-diameter aperture. The first minimum of each profile occurs near $\delta = 0.089°$.

the center of the beam. The calculated profile for a 1.2 mm-diameter aperture is shown in Fig. 7.1(c). The two measured profiles are fairly similar and have similar minima locations. For example, the first minimum is about 0.089° from the center of the beam. Although the minima of the measured profiles are very close to those of the Airy disk, the measured profiles are wider than the Airy disk. This is because the incident laser beam is not a plane wave, while the calculated Airy disk is based on a plane-wave incidence upon a circular aperture. The similarity between the two measured beam profiles implies that the profiles are close to the far-field regime. The far-field criterion can also be examined by the following inequality [103],

$$D_a > \frac{\text{area of aperture}}{\lambda}, \tag{7.2}$$

where D_a is the distance between the detection plane and the aperture. In this case,

the value of D_a has to be larger than 730 mm to be in the far-field regime. Therefore, the profile measured at $D_a = 700$ mm [Fig. 7.1(a)] can be regarded as the far-field diffraction pattern in this case. In spite of the fact that the prism coupler is 350 mm away from the aperture, the far-field profile describes the angular distribution of the plane-wave components more accurately. The near-field contribution to the beam profile in Fig. 7.1(b) does not represent plane-wave components at the angles that are actually near the center of the beam. Since the prism coupler is extremely angularly selective, the light away from the center of the beam has negligible effect on the measurement. Therefore, the beam profile in Fig. 7.1(a) would be used as the angular distribution of the plane-wave components for further simulations.

The angular distribution in the incident laser beam is related to the effective index of the incident beam. Figure 7.2(a) is a schematic diagram of the light path in the prism coupler. The axes in Fig. 7.2 match those in Fig. 7.1. By algebraic manipulation, the angle of incidence from the air into the lateral surface of the prism (θ_a) can be related to the effective index in the z-direction (N_{eff}),

$$N_{\text{eff}} = n_p \sin\left[\phi_p - \sin^{-1}\left(\frac{\sin\theta_a}{n_p}\right)\right], \tag{7.3}$$

where n_p is the refractive index of the prism and ϕ_p is the angle of the prism base. In this chapter, $n_p = 1.9349$ and $\phi_p = 49.809°$ are used. It is worth mentioning that Eq. (7.3) only describes the light whose plane of incidence is the $x - z$ plane. Figure 7.2 (b) describes the 3D light incident away from the $x-z$ plane. By algebraic manipulation, the incident angle at the prism/air gap interface for light incident away from the $x - z$ plane [$\theta_p(\Delta y)$] can be related by its counterpart on the $x - z$ plane [$\theta_p(0)$],

$$\theta_p(\Delta y) = \tan^{-1}\left[\tan^2\theta_p(0) + \left(\frac{\Delta y}{700 n_p \cos\theta_p(0)}\right)^2\right], \tag{7.4}$$

where Δy (mm) is the distance difference in y direction between the two beams in

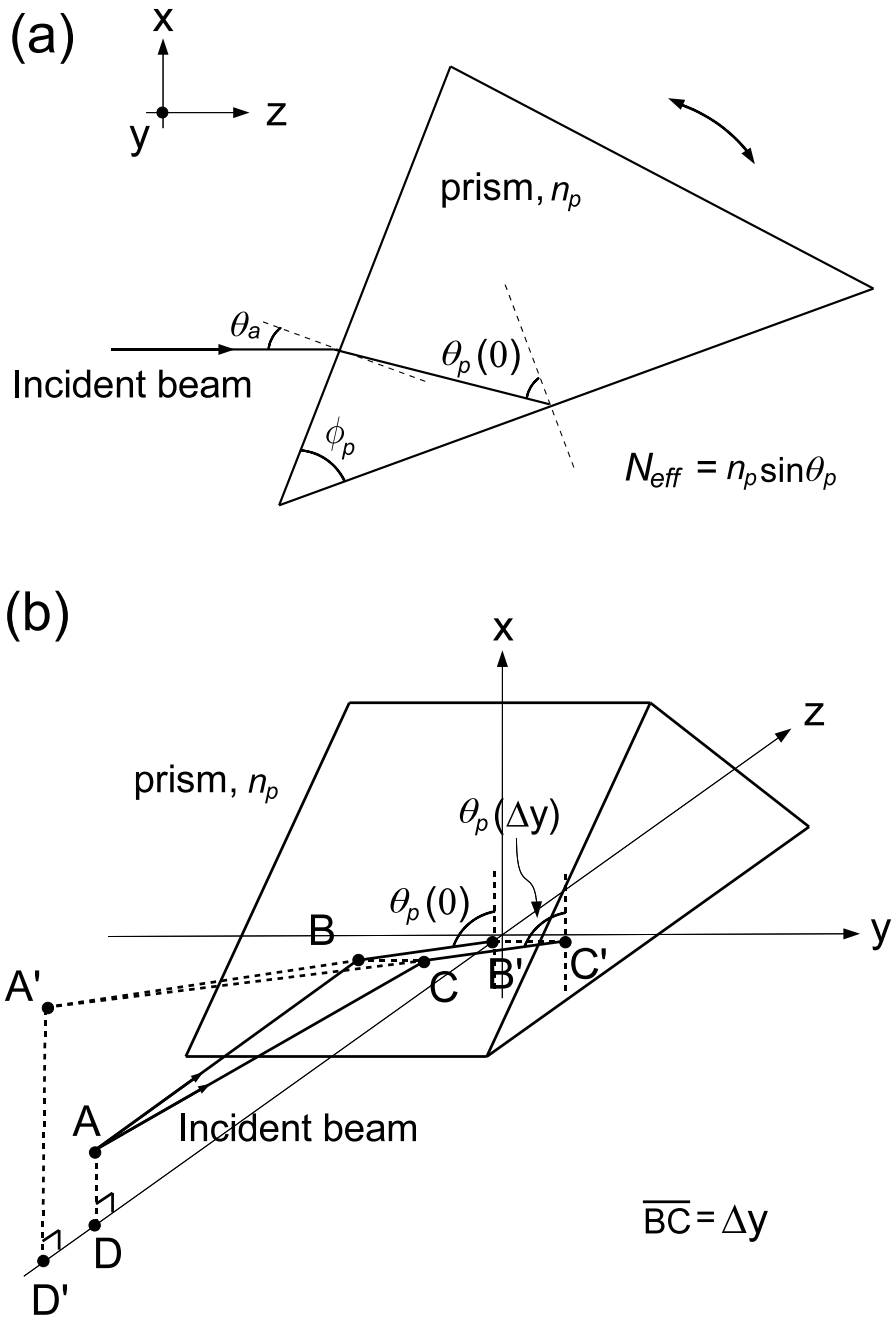

Figure 7.2: (a) Schematic diagram of the 2D light path in the prism coupler. As the prism rotates, the effective index $N_{\text{eff}} = n_p \sin\theta_p$ varies. (b) Schematic diagram of the 3D light path in the prism coupler when the prism base is on the $x - z$ plane. Point A represents the aperture, B is the center of the beam on the lateral surface of prism, C is near B with a Δy displacement in y direction, B$'$ and C$'$ are the location of the diffracted light from B and C on the prism base, respectively, and A$'$ is intersection of the elongated $\overline{\text{BC}}$ and $\overline{\text{B}'\text{C}'}$. D and D$'$ are the shadow points of A and A$'$ on the $x - z$ plane, respectively. In the case that $\Delta y \ll \overline{\text{AB}}$, $\overline{\text{A}'\text{B}} = n_p\overline{\text{AB}} = 700 n_p$ (mm). Moreover, because of the small size of the prism compared with $\overline{\text{AB}}$ and the small angle $\angle$BAC, $\overline{\text{B}'\text{C}'} \simeq \overline{\text{BC}} = \Delta y$.

the lateral surface of the prism and $\theta_p(0)$ can be written as

$$\theta_p(0) = \phi_p - \sin^{-1}\left(\frac{\sin\theta_a}{n_p}\right). \tag{7.5}$$

According to the laser beam profile in Fig. 7.1(a), Δy is smaller than 4 mm even for the weak outer rings. As a result, the difference between $\theta_p(0)$ and $\theta_p(\Delta y)$ is nearly negligible.

Based on the above analysis, the resultant effective index for each pixel point in the laser profile can be calculated for any angle of incidence. In order to analyze the effects of the incident laser beam, the MIM structure in Fig. 7.3 was used as the example in the simulation. The structure is the same as the one in Sec. 6.2.2. The air gap thickness d_g is assumed to be 50 nm and the top metal cladding thickness d_m is assumed to be 65 nm.

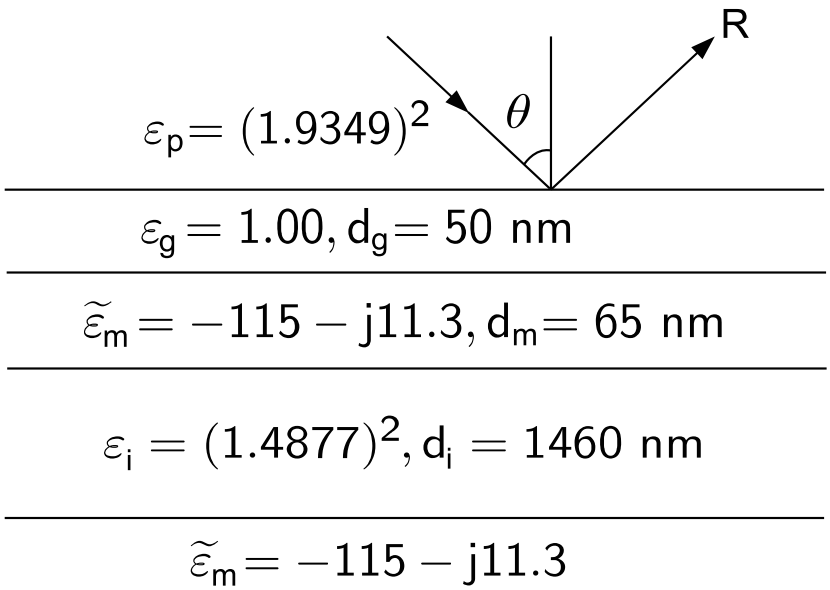

Figure 7.3: Schematic diagram of the prism-loaded MIM (Au-SiO_x-Au) structure used in the simulation. The structure is the same as the one in Sec. 6.2.2. The air gap thickness d_g is assumed to be 50 nm and the top metal cladding thickness d_m is assumed to be 65 nm.

Before simulating the effects of the incident laser profile, it should be noted that the size of the laser beam affects the results. This is intuitive since the wider the laser beam is, the wider the corresponding angular spread is, and the stronger the broadening effects on the resultant spectrum. However, the size of the laser beam that is incident upon the MIM structure is difficult to quantify because the size of the coupling spot over which the prism and the MIM structure have intimate contact is not known. The coupling spot size is also likely a function of the pressure of the coupling head, P_c. Therefore, various sizes of the laser beam are used in the simulation. Because the prism coupler is 350 mm away from the aperture while the laser beam profile in Fig. 7.1(a) was measured at $D_a = 700$ mm, the size of the beam profile is halved in the former. Laser beams with sizes (at $D_a = 350$ mm) 1 mm $\times$ 1 mm, 1.5 mm $\times$ 1.5 mm, 2 mm $\times$ 2 mm, and 3 mm $\times$ 3 mm are used in the simulation.

Figure 7.4(a) shows the 1 mm $\times$ 1 mm laser beam profile, which is a small portion of the measured laser beam profile in Fig. 7.1(a). The simulated angular TM reflection spectra for the MIM structure in Fig. 7.3 at $\lambda = 1550$ nm is illustrated in Fig. 7.4(b). The solid curve is for plane-wave incidence and the dashed curve is for the incidence of the 1 mm $\times$ 1 mm laser beam. It is worth mentioning that the spectrum for the laser beam incidence is a convolution of the angular distribution of the laser beam and the spectrum for plane-wave incidence. Since the angular distribution of the laser beam is fairly narrow in this case, the reflection spectra are very similar under the two different incidence condition. Figure 7.5(a) shows the 1.5 mm $\times$ 1.5 mm laser beam profile, and the simulated angular TM reflection spectra for the MIM structure in Fig. 7.3 at $\lambda = 1550$ nm is illustrated in Fig. 7.5(b). In the expanded Figs. 7.5(c), (d), and (e), it can be observed that the 1.5 mm $\times$ 1.5 mm laser beam incidence produces a shallower and wider resonance than the plane-wave incidence does. When larger laser beams are used, as in Fig. 7.6 and 7.7, the resultant resonances are wider.

Based on the TTR method, the normalized complex propagation constant $(\beta' - j\alpha')/k_0$ can be obtained by the location and width of each resonance. The prime denotes results obtained by the TTR method. Table 7.1 summarizes the results for plane-wave incidence and finite-size laser beam incidence. The variations in the propagation constant β' are negligible. For the laser beam incidence, it is shown that the broadening effect on the resonance, which causes an increase in α', is the most significant for a narrow resonance. Moreover, as the size of the laser beam increases, the resonance width also increases. Similar phenomena were also observed in the convolution of Voigt profile, which is the convolution of a Gaussian function and a Lorentzian function [104, 105].

In summary, the angular spread of the incident laser beam broadens the resonance width in the TTR method, which, in turn, increases the values of α'. This broadening effect is strongest when the resonance is narrow. Therefore, for the structure in Fig. 7.3, the TM_0 mode has the largest percentage of broadening. In Sec. 6.2.2, the measured α'_{TM_0} is only 3% smaller than the theoretical value, while most of the other α' values of the other modes are about 15% smaller than the theoretical values. Comparing Table 7.1 with the results in Sec. 6.2.2, it is estimated that the laser beam size is between 1 mm×1 mm and 2 mm×2 mm.

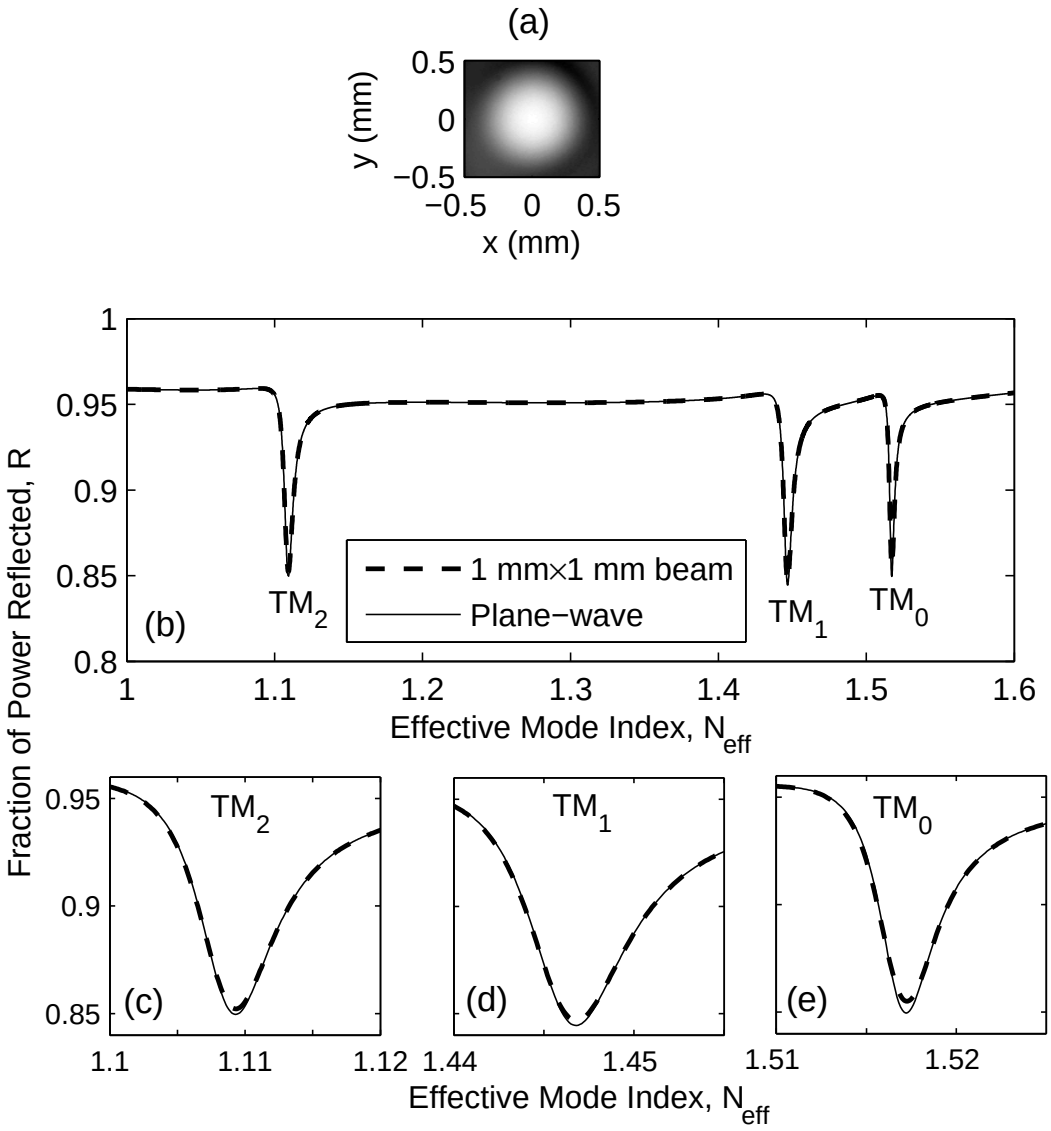

Figure 7.4: (a) The 1 mm×1 mm incident laser beam profile used in the simulation. The size of the laser beam is determined at $D_a = 350$ mm. (b) The simulated angular reflection spectra for the structure shown in Fig. 7.3. The solid curve is for plane-wave incidence and the dashed curve is for the 1 mm×1 mm laser beam incidence. Close view of (c) the TM_2 resonance, (d) the TM_1 resonance, and (e) the TM_0 resonance at plane-wave incidence and the 1 mm×1 mm laser beam incidence.

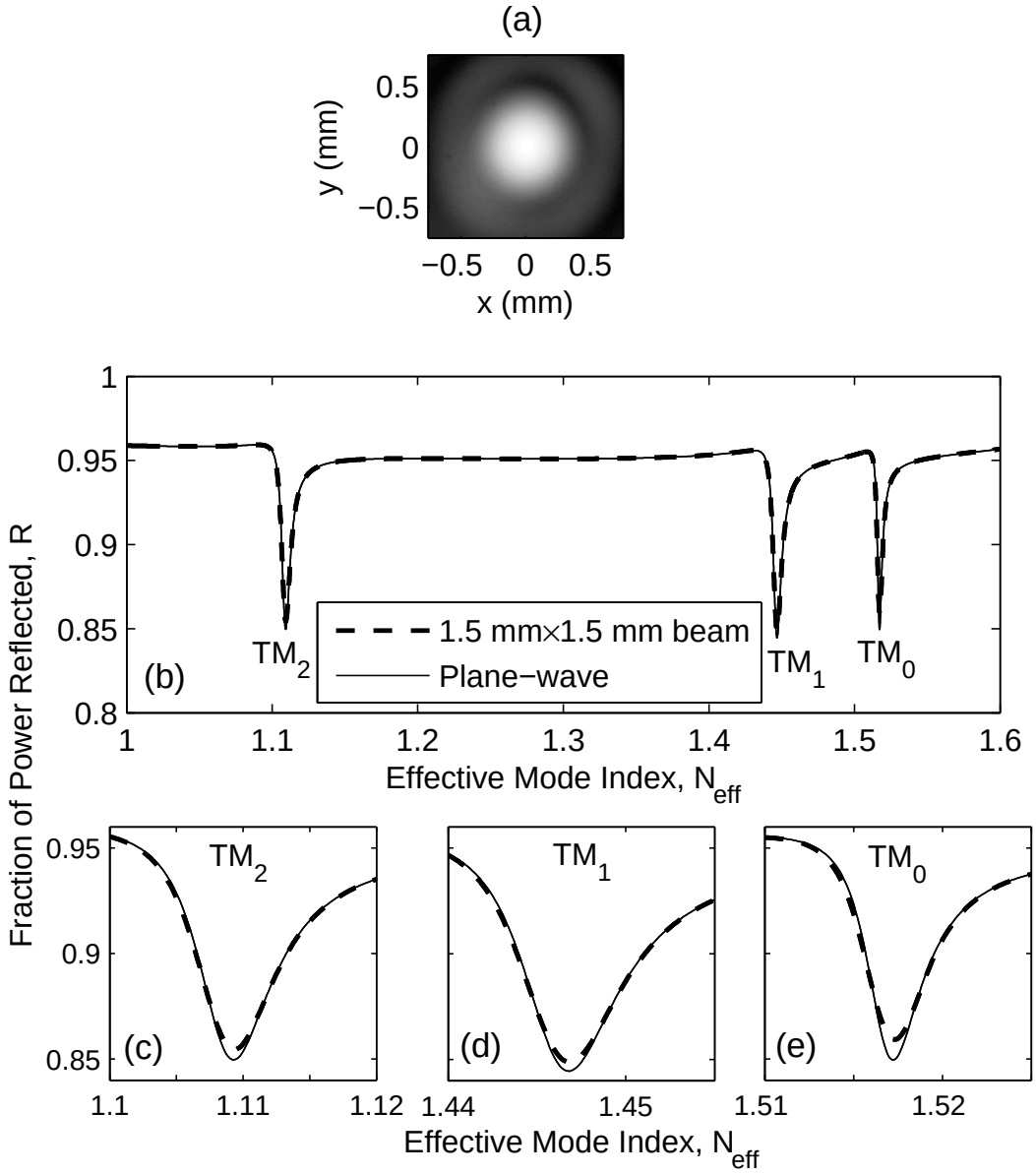

Figure 7.5: (a) The 1.5 mm×1.5 mm incident laser beam profile used in the simulation. The size of the laser beam is determined at $D_a = 350$ mm. (b) The simulated angular reflection spectra for the structure shown in Fig. 7.3. The solid curve is for plane-wave incidence and the dashed curve is for the 1.5 mm×1.5 mm laser beam incidence. Close view of (c) the TM_2 resonance, (d) the TM_1 resonance, and (e) the TM_0 resonance at plane-wave incidence and the 1.5 mm×1.5 mm laser beam incidence.

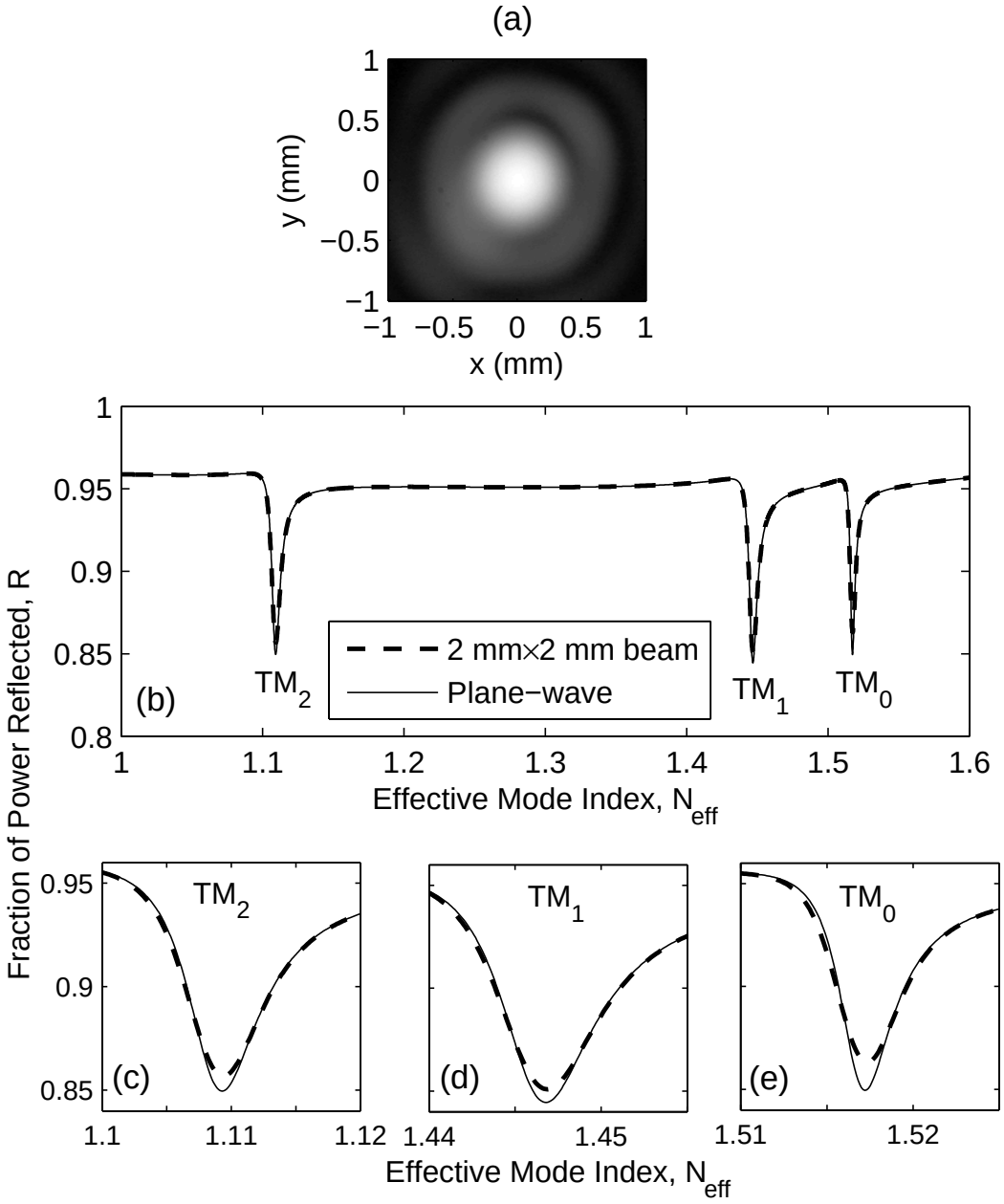

Figure 7.6: (a) The 2 mm×2 mm incident laser beam profile used in the simulation. The size of the laser beam is determined at $D_a = 350$ mm. (b) The simulated angular reflection spectra for the structure shown in Fig. 7.3. The solid curve is for plane-wave incidence and the dashed curve is for the 2 mm×2 mm laser beam incidence. Close view of (c) the TM_2 resonance, (d) the TM_1 resonance, and (e) the TM_0 resonance at plane-wave incidence and the 2 mm×2 mm laser beam incidence.

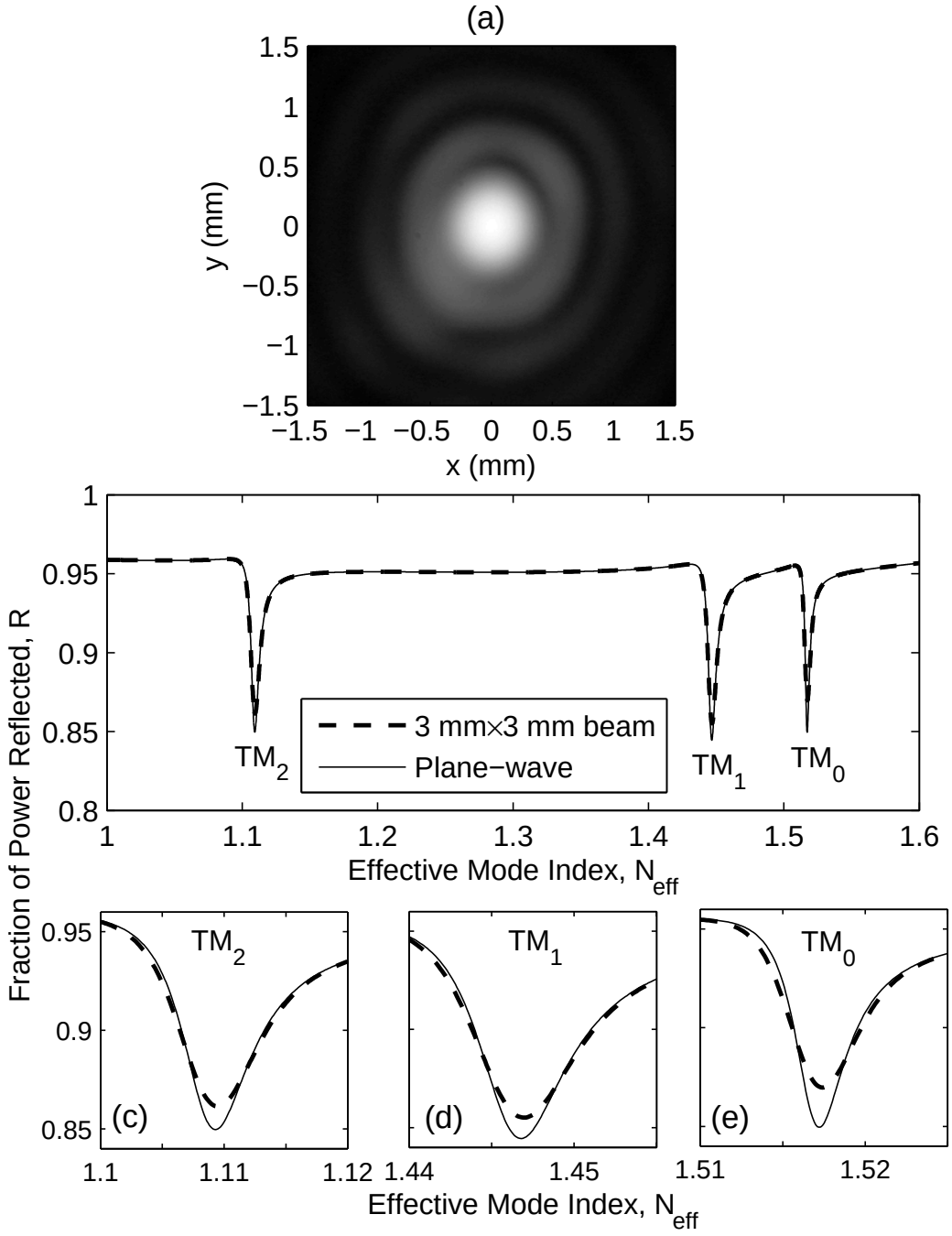

Figure 7.7: (a) The 3 mm×3 mm incident laser beam profile used in the simulation. The size of the laser beam is determined at $D_a = 350$ mm. (b) The simulated angular reflection spectra for the structure shown in Fig. 7.3. The solid curve is for plane-wave incidence and the dashed curve is for the 3 mm×3 mm laser beam incidence. Close view of (c) the TM_2 resonance, (d) the TM_1 resonance, and (e) the TM_0 resonance at plane-wave incidence and the 3 mm×3 mm laser beam incidence.

Table 7.1: TTR simulation results for the structure in Fig. 7.3 at various incidence condition. The broadening percentages compared with the plane-wave incidence are also listed.

Incidence Condition	Mode	Normalized Complex Propagation Constant $(\beta' - j\alpha')/k_0$	Broadening Percentage
Plane wave	TM_0	$1.5173 - j0.0020$	–
	TM_1	$1.4469 - j0.0035$	–
	TM_2	$1.1094 - j0.0036$	–
1 mm×1 mm beam	TM_0	$1.5175 - j0.0022$	8.4%
	TM_1	$1.4470 - j0.0036$	3.2%
	TM_2	$1.1095 - j0.0037$	4.8%
1.5 mm×1.5 mm beam	TM_0	$1.5175 - j0.0024$	16%
	TM_1	$1.4470 - j0.0037$	6.2%
	TM_2	$1.1095 - j0.0038$	7.2%
2 mm×2 mm beam	TM_0	$1.5175 - j0.0025$	23%
	TM_1	$1.4470 - j0.0038$	9.4%
	TM_2	$1.1095 - j0.0039$	11%
3 mm×3 mm beam	TM_0	$1.5175 - j0.0028$	37%
	TM_1	$1.4470 - j0.0040$	16%
	TM_2	$1.1095 - j0.0042$	19%

The broadening effects can be further generalized. Figure 7.8 illustrates the simulated broadening effects of various laser beams on Lorentzian functions with various HWHMs. The Lorentzian functions are assumed to be centered at $N_{\text{eff}} = 1.5$ and the prism has a refractive index $n_p = 1.9349$ and a base angle of $\phi_p = 49.809°$. As mentioned in the previous discussion, the broadening percentage is larger for a narrower resonance or an incident beam with a larger size and therefore wider angular spread. As shown in Fig. 7.8, the broadening percentage grows very rapidly as the normalized attenuation α/k_0 decreases. On the other, when α/k_0 is close to 0.01 or higher, the broadening percentage is about only 1% or less, which can be neglected.

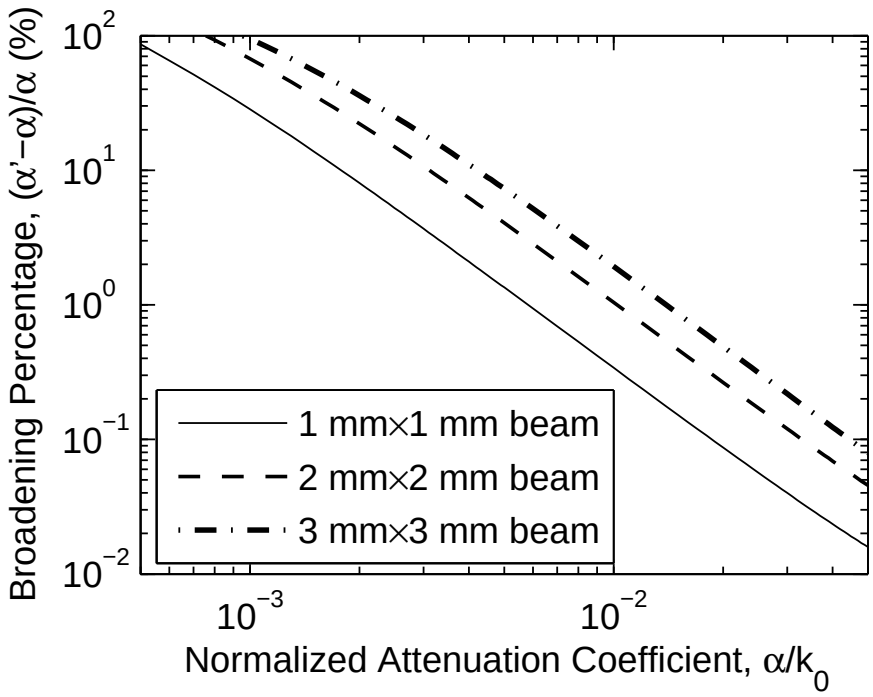

Figure 7.8: Simulated broadening effects for various laser beams on Lorentzian functions with various HWHMs. The values of α represent the HWHMs of original Lorentzian functions, while the values of α' represent the HWHMs of the resultant resonances. The Lorentzian functions are assumed to be centered at $N_{\text{eff}} = 1.5$ and the prism has a refractive index $n_p = 1.9349$ and a base angle of $\phi_p = 49.809°$.

7.2 Effect of the Laser Beam Linewidth

In the TTR simulation, the incident light is assumed to be single-wavelength. However, according to the famous Schawlow-Townes equation [106], the linewidth of a laser is not infinitesimal, there is always a nonzero linewidth due to the spontaneous emission and the bandwidth of the resonator. The linewidth will be further stretched by relaxation oscillation and other noise source (e.g. mechanical vibrations, temperature fluctuations, and pump power fluctuations) [107]. As a result, the effects of the laser linewidth on the results of the TTR method need to be investigated.

Figure 7.9 shows the simulated dispersion relation of the TM_0 mode in a 200 nm-core MIM (Au-SiO_x-Au) waveguide around $\lambda = 1550$ nm. The material dispersion is caused by the frequency-dependence of the dielectric constant of Au, and the

waveguide dispersion is caused by the structural factor (i.e. assuming the dielectric constant of Au is frequency-independent). The total dispersion is the combination of waveguide dispersion and material dispersion. It is shown that the variation in the effective mode index N_{eff} is less than 10^{-5} for even 10 GHz of frequency variation, which is a relatively large linewidth for a laser. As a result, it can be concluded that the linewidth of the laser has a negligible affect on the results of the TTR method.

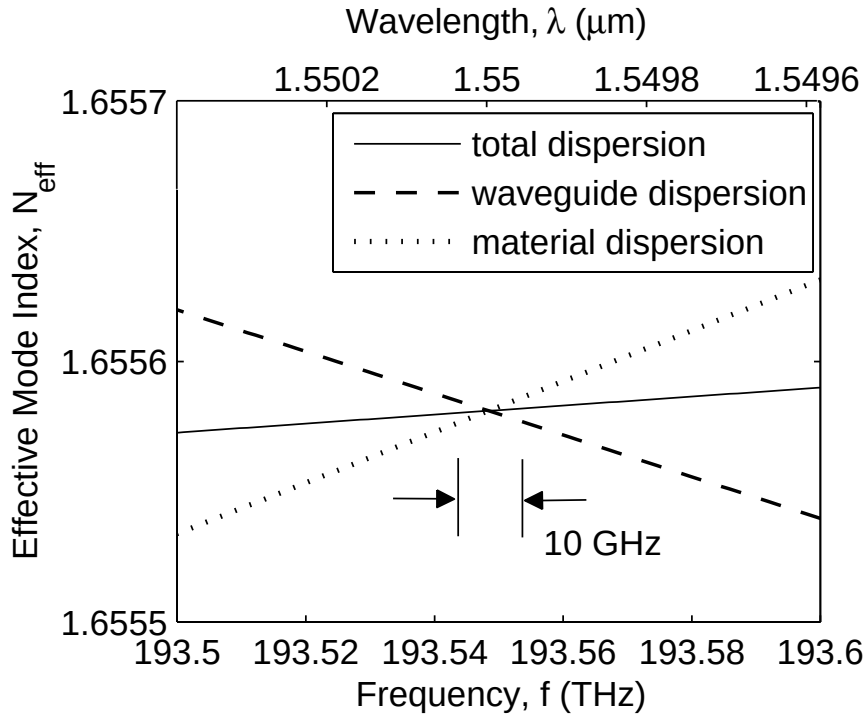

Figure 7.9: Simulated dispersion relation of the TM_0 mode in a 200 nm-core MIM (Au-SiO_x-Au) waveguide around $\lambda = 1550$ nm. The material dispersion is caused by the frequency-dependence of the dielectric index of Au, and the waveguide dispersion is caused by the structural factor.

7.3 Limitations on the Range of Detectable Loss

7.3.1 Lower Limit

The minimum detectable loss is primarily determined by the precision of the rotary table. In the Metricon Prism Coupler, the angular step of the rotary table is 7.5×10^{-3} degree, which corresponds to a effective mode index resolution of about 0.00005 to

0.0001. At $\lambda = 1550$ nm, $\alpha/k_0 = 0.00005$ to 0.0001 corresponds to a loss of 1.76 dB/mm to 3.52 dB/mm or a propagation length of 2.47 mm to 1.23 mm.

However, the angular distribution of the incident laser beam puts another lower limit on the detectable loss. According to the analysis in Sec. 7.1, the angular spread of the laser beam broadens the width of the resonance, and the broadening effect is the strongest for narrow resonances. That is, when a very narrow resonance is measured, the measured width is primarily determined by the angular spectral width of the incident laser beam. An issue that is even more difficult to take into account is that the size of the coupling spot, which determines the size of the laser beam incident into the MIM structure, is difficult to quantify. This uncertainty makes it difficult to remove the effect of the angular distribution of the laser beam. In Sec. 7.1, the TM_0 resonance, with an experimentally measured $\alpha/k_0 = \text{HWHMs} = 0.0017$, is estimated to be broadened by 10% to 20%. This mode corresponds to a loss of 0.06 dB/μm or a propagation length of 72 μm. A narrower resonance will be broadened by a larger percentage, and it will be more difficult to determine the exact amount. Figure 7.8 shows the simulated broadening percentage for various sizes of laser beams and Lorentzian functions with various HWHMs. This can be used as an estimate of the minimum detectable loss at various levels of tolerable errors.

7.3.2 Upper Limit

The maximum detectable loss is determined by the range of achievable effective mode index of the prism. Theoretically, the achievable effective mode index is from 0 to the refractive index of the prism. Of course, the edges of the range of achievable effective mode index are not necessarily achievable because of the geometrical arrangement. For example, the prism used in Chapter 6 has a refractive index $n_p = 1.9349$, and the achievable effective mode index in the Metricon Prism Coupler is 1 to 1.7. The geometrically limited range of effective mode index is about 0.63 to 1.9, but the edges

of this range are difficult to achieve because the laser beam is incident somewhere far from the center of the coupling spot (see Sec. 5.2 for details) and the air gap becomes too large for light coupling. The maximum detectable α/k_0 = HWHMs of the resonance is therefore approximately 0.1 to 0.2, which corresponds to a loss of 3.52 dB/μm to 7.04 dB/μm or a propagation length of 1.23 μm to 0.62 μm. An even larger upper limit may be achievable by using curve fitting, in which only a portion of the resonance is required to get the HWHM. However, as the measured angular spectrum covers such a wide range of effective mode index, the air gap thickness varies because the laser beam is not incident at the center of the coupling spot for all the effective mode indices (see Sec. 5.2 for details). This factor needs to be considered when curve fitting is performed over a wide range of effective mode index.

7.4 Summary

In this chapter, the effects of the angular distribution and linewidth of the incident laser beam have been treated. While the linewidth is typically too small to make any detectable difference, the angular spread of the laser beam broadens the width of the resonances in the angular reflection power spectrum, and the broadening effect is stronger for narrower resonances. The MIM structure measured in Sec. 6.2.2 was simulated for various incidence conditions of the laser beam, and it was shown that the TM_0 mode, which has the lowest loss among all supported modes, was broadened by the largest percentage. Comparing the simulation with the experimental results, it is estimated the size of the laser beam incident into the MIM structure is between 1 mm$\times$1 mm and 2 mm$\times$2 mm.

The broadening effect caused by the angular spread of the laser beam also limits the detectable loss of the Metricon Prism Coupler. Based on the simulation in Sec. 7.1, the TM_0 mode is estimated to be broadened by 10% to 20%. This mode corresponds to a loss of 0.06 dB/μm or a propagation length of 72 μm. Figure 7.8 provides an

estimation of detectable loss at various levels of tolerable loss. On the other hand, the upper limit of detectable loss is determined by the achievable effective mode index of the prism. It is estimated that a loss of 3.52 dB/μm to 7.01 dB/μm or a propagation length of 1.23 μm to 0.62 μm can be measured using the current experimental configuration.

CHAPTER 8

CONCLUSIONS

The objective of this thesis has been to develop an accurate and straightforward method of characterizing the plasmonic modes in an MIM waveguide. This has been accomplished by developing and applying the transverse transmission/reflection (TTR) method. By utilizing the attenuated total reflection (ATR) configuration or prism coupler arrangement, the TTR method has been implemented experimentally. In this chapter, the main accomplishments are summarized and potential areas of future research are discussed.

8.1 Summary of Results

8.1.1 Review of Surface Plasmons (Contribution No. 1)

The properties of the SP mode at a single metal/dielectric interface and TM and TE modes in an MIM waveguide were analyzed. It was shown that plasmonic modes in an MIM waveguide have nano-scale lateral confinement and slow-wave properties. Owing to these two properties, MIM-based devices and interconnects offer the potential of realizing integrated optical nanocircuitry. However, the subwavelength sizes of MIM waveguides also make the coupling and any further characterization challenging. It was shown that conventional characterization techniques, such as near-field scanning optical microscopy (NSOM) or usage of multiple samples with various propagation distances, have serious limitations. The former is very sensitive to environmental disturbances, and the measured signal is typically very noisy and sensitive to the surface conditions of the waveguide. In the latter, the sample-to-sample non-uniformity and the differences in coupling efficiencies among samples are difficult to quantify.

Owing to the limitations and unreliability of the conventional characterization techniques for plasmonic modes in MIM structures, the experiment-oriented facet of the research is less developed than its theoretical counterpart. The experimental challenges have greatly impeded the development of plasmonic technology. The main objective of this thesis is to develop a reliable and straightforward method of characterizing the plasmonic modes in MIM waveguides.

Moreover, the relation between MIM waveguides and the well-know parallel-plate waveguide in microwave technology was also discussed. It was shown that the parallel-plate waveguide is simply a special case of the MIM waveguide in microwave regime, in which metal is approximately a perfect conductor. The TEM mode in the parallel-plate waveguide can be guided with subwavelength confiment as can the TM_0 mode in the MIM waveguide. However, the TEM mode always propagates at light speed, whereas the TM_0 mode propagates more slowly, especially at higher frequencies.

8.1.2 Transverse Transmission/Reflection (TTR) Method [39] (Contributions Nos. 2 and 3)

By using the transmission matrix formulation, it was shown that the zeros of the m_{22} component in the transmission matrix correspond to the leaky/lossy modes in the waveguide structure. It was also shown that m_{22} is the denominator of the transmittance and reflectance for light incident from the transverse direction (i.e. cover or substrate). Therefore, when a waveguide mode is excited by light incident from the transverse direction, the transmittance and reflectance approach ∞, which is physically infeasible. In other words, the solutions of $m_{22} = 0$ do not correspond to physically measurable situations. However, by using an attenuated total reflection (ATR) configuration, which is also known as a prism coupler, the real and imaginary parts of the solutions to $m_{22} = 0$ can be transformed into the angles and the widths, respectively, of the resonances in the angular reflection power spectrum. The presence of the prism perturbs the condition of the waveguide mode and allows light to

be coupled into the waveguide from the transverse direction. In summary, by using the ATR configuration, the $m_{22} = 0$ condition for an unperturbed waveguide mode is transformed to the resonance condition in the angular reflection power spectrum for the ATR configuration.

In order to apply the ATR configuration to an MIM waveguide, one side of the metal claddings must be made sufficiently thin for light coupling. By using the transmission matrix formulation, it was shown that the angular reflection power spectrum can be written as the reflectance for the Otto configuration (i.e. prism-air-metal structure) multiplied by a downward resonance corresponding to the plasmonic mode in the MIM structure. The reflectance for the Otto configuration is typically much wider than the resonance for the plasmonic mode, therefore the latter can be extracted by subtracting out the background variation caused by the former. The propagation constant and the attenuation coefficient of the plasmonic mode can then be determined by the angle of the resonance minimum and the width of the resonance, respectively.

8.1.3 Theoretical Performance of the TTR Method [39,40] (Contribution No. 4)

The TTR simulation was applied to four waveguide structures in order to validate the theoretical performance of the TTR method. The four waveguide structures that have been simulated are a multimode AntiResonant Reflecting Optical Waveguide (ARROW), a lossy thin-film waveguide, and two MIM waveguides. All the TTR simulation results agree well with the rigorous theoretical propagation constants of the waveguides. The simulation for the ARROW structure demonstrates the performance of the TTR method in detecting all of the overlapping leaky modes. The lossy thin-film waveguide has a 1 μm cladding layer on a high-index substrate, therefore it is simultaneously leaky and lossy, and the TTR simulation is capable of characterizing such a mode that is simultaneously leaky and lossy.

When applying the TTR method to an MIM structure, one side of the metal

claddings must be made thinner for light coupling. The thickness should be around 3 to 4 skin depths for appropriate coupling strength. The resultant reflection spectra typically contain resonances corresponding to the SP mode at the air gap/metal interface (i.e. Otto configuration) and the MIM plasmonic mode. The latter can be extracted by subtracting out the background variation caused by the former, and the propagation constant and the attenuation coefficient of the plasmonic mode can then be determined by the angle of the resonance minimum and the width of the resonance, respectively. Moreover, the TTR simulation was applied at various thicknesses of the air gap and the top metal claddings, both of which are difficult to measure precisely. It was shown that the results obtained by the TTR method are insensitive to these two parameters, provided the thickness of the metal cladding is sufficiently large. The fact that the TTR method is insensitive to those parameters is very important for its experimental application.

8.1.4 Experimental Verification of the TTR Method [41] (Contributions Nos. 5 and 6)

By using the Metricon Prism Coupler, the TTR method was experimentally applied to two MIM (Au-SiO_x-Au) waveguides. The MIM waveguides have 50 nm and 200 nm cores, and both support only the fundamental TM_0 mode at $\lambda = 1550$ nm. The measured results agree very well with the theoretical results in both the propagation constants and the attenuation coefficients. Moreover, the MIM waveguides were experimentally characterized at various thicknesses of the air gap and the top metal claddings, and it was shown that the results are not sensitive to these two parameters, provided the thickness of the metal cladding is sufficiently large. This fact illustrates the robustness of the TTR method as a technique for characterizing MIM waveguides.

8.1.5 Multimode MIM Waveguides (Contributions Nos. 7 and 8)

MIM waveguides with subwavelength dimensions are the fundamental building element in realizing SP-based integrated optical nano-circuitry. However, MIM waveguides with larger core sizes may also be used as low-loss interconnects or tapered end-couplers. As for conventional dielectric waveguides, the number of modes increases as the core thickness of the MIM waveguides increases. In such cases, the experimental characterization of the propagation constants and attenuation coefficients of all the modes in the multimode MIM waveguides are critically important. Two multimode MIM (Au-SiO_x-Au) waveguides with 730 nm and 1460 nm cores were fabricated and experimentally characterized by using the TTR method. The measured results agree very well with the theoretical results in both the propagation constants and the attenuation coefficients. To the best of the author's knowledge, this is the first time the propagation constant of each mode in a multimode MIM waveguide has been individually measured. Also, to the best of the author's knowledge, this is the first time the attenuation coefficient of each mode in a multimode MIM waveguide has been individually measured.

The experimental results showed that the losses of the fundamental TM_0 modes are smaller than the other modes for both waveguides. However, the losses of the other modes are only two to three times larger than the losses of the TM_0 modes. As a result, the inclusion of the higher-order modes is essential when a large-core, multimode MIM waveguide is used in any practical applications.

8.1.6 Effects of the Laser Beam on the Experimental Results (Contributions Nos. 9 and 10)

In the TTR method, it is assumed that the incident light is a single-wavelength plane wave. However, a realistic laser beam is not a plane wave and contains more than one wavelength. Therefore, the angular distribution and linewidth of the incident laser

beam were investigated and their affect on an MIM (Au-SiO_x-Au) structure with a 1460 nm core were simulated. The simulation shows that the linewidth of the laser beam has negligible effect on the TTR measurement even for a linewidth of 10 GHz. On the other hand, the laser beam profile was measured and transformed into the angular distribution. By using the angular distribution of the laser beam, the angular reflection power spectrum for laser beam incidence was calculated. Since the size of the laser beam that is incident upon the MIM structure is difficult to quantify, various sizes of the laser beams were used in the simulation. It was shown that the reflection resonances are broadened due to the angular spread of the laser, and the broadening effect is larger for wider angularly spread beams and for narrower resonances.

Moreover, the range of detectable loss for the experimental configuration is also estimated. The lower limit is determined by the broadening effect caused by the angular spread of the laser beam. For example, it was shown that for a mode with a loss of 0.06 dB/μm or a propagation length of 72 μm, the broadening percentage is about 10% to 20%. On the other hand, the upper limit is primarily determined by the achievable effective index of the prism. It is estimated that a loss of 3.52 dB/μm to 7.04 dB/μm or a propagation length of 1.23 μm to 0.62 μm can be measured using the current experimental configuration. The range of detectable loss mentioned above is sufficient for nearly all types of MIM waveguides.

8.2 Future Work

In order to realize fully the potential of the TTR method in the characterization and development of SP-based optical nanocircuitry, further research is required. In this section, several potential directions of research are highlighted.

8.2.1 Application of the TTR Method to Ridge or Channel MIM Waveguides

Research to date has been solely focused on the 1D, symmetric MIM waveguides. For applications in integrated, SP-based optical nanocircuitry, MIM waveguides that are confined in two dimensions are essential. Therefore, it is critically important to extend the capability of the TTR method to the characterization of 2D MIM waveguides.

Figure 8.1 shows the schematic diagram of applying the TTR method to an array of parallel channel MIM waveguides. Because of the small width (typically a few microns) of 2D MIM waveguides compared with the laser beam width ($\sim$ 1 mm to 2 mm) in the y direction, the strength of the reflection resonance in the TTR method is very weak from a single channel waveguide. Therefore, by using an array of parallel, identical channel MIM waveguides, the reflection resonance can be multiplied [108]. Of course, the MIM waveguides has to be sufficiently far apart to avoid coupling between neighboring waveguides. The angle of incidence on the prism/air gap interface, θ, can be varied to excite various modes in the MIM waveguides, the same manner as for the TTR method for 1D waveguides discussed in previous chapters.

On the other hand, the angle between the prism axis and the waveguide axis, ϕ, is unique and important for the application of the TTR method to 2D MIM waveguides [108]. The angle ϕ is effectively zero for any alignment of 1D MIM waveguides. Hovever, in 2D MIM waveguides, there exists modes with antisymmetric modal profile in the y direction. According to coupled mode theory [109], at $\theta \simeq 0$, these modes are barely excited. Therefore, in order to characterize all the modes accurately, it is necessary to perform measurements at various values of ϕ. By using the boundary condition that k_z is continuous at each interface, the effective mode index when $\phi = 0$ is $N(0) = N(\phi)\cos\phi$. It is shown in [108] that all the effective indices of the modes can be detected by varying ϕ within a range of $\pm 10^\circ$.

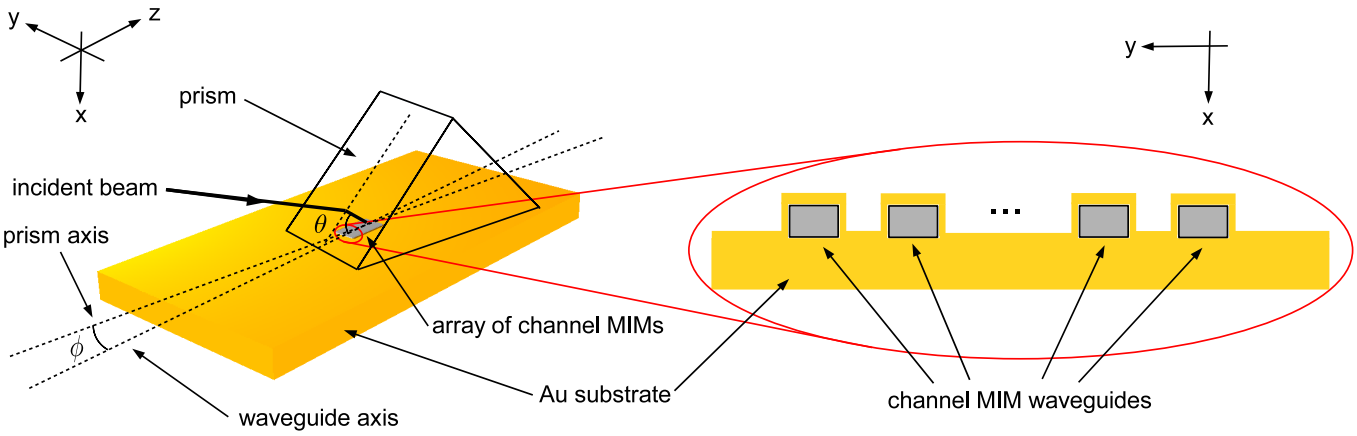

Figure 8.1: Schematic diagram of applying the TTR method to an array of parallel channel MIM waveguides. Multiple identical and parallel waveguides is used to enhance the reflection resonance strength. The angle between the prism axis and the waveguide axis, ϕ, and the angle of incidence on the prism/air gap interface, θ, can be adjusted for the incident beam to excite various modes in the MIM waveguides [108].

8.2.2 Application of the TTR Method to Asymmetric MIM Structures

In the present work, the MIM structures that have been analyzed and discussed are exclusively symmetric, that is, both sides of the claddings are made of the same metal. For a symmetric MIM structure, there exists a fundamental TM_0 at any core thickness, and the core size is the only parameter to control the propagation properties (e.g. cutoff condition, propagation constants, etc.) of the waveguide modes. The asymmetric MIM structures provide another dimension of engineering. For example, [26] proposed that there exists a "negative refractive index" (NI) band for Ag-Si_3N_4-Ag MIM structures (with a core thickness of 50 nm) in ultraviolet regime. The NI band is featured by the negative group velocity within the spectrum. This NI band can be tailored to the visible spectrum by using an asymmetric Au-Si_3N_4-Ag MIM structure. Figure 8.2 illustrates the dispersion diagram for both types of aforementioned MIM structures, and Fig. 8.3 [26] shows the proposed NI prism based on this concept. The NI prism ("W1" region in Fig. 8.3) is composed of a Au-Si_3N_4-Ag structure with a 50 nm core, and the rest of the region is composed of a Au-Si_3N_4-Ag structure with

a 500 nm core ("W2" region). When light is incident into the NI prism, the light is refracted as if the prism has a negative refractive index.

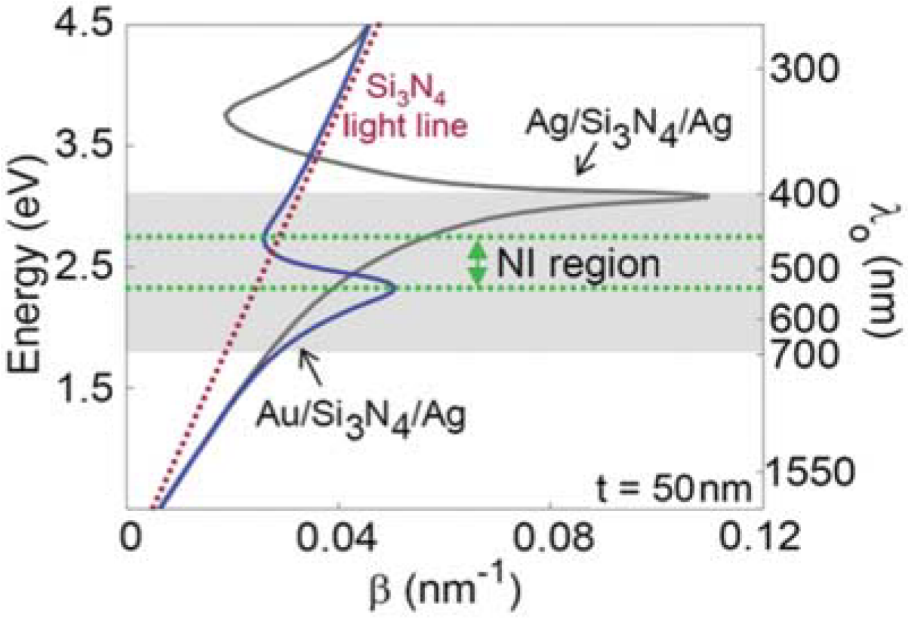

Figure 8.2: Calculated dispersion curves for Ag-Si_3N_4-Ag and Au-Si_3N_4-Ag MIM structures with 50 nm cores [26].

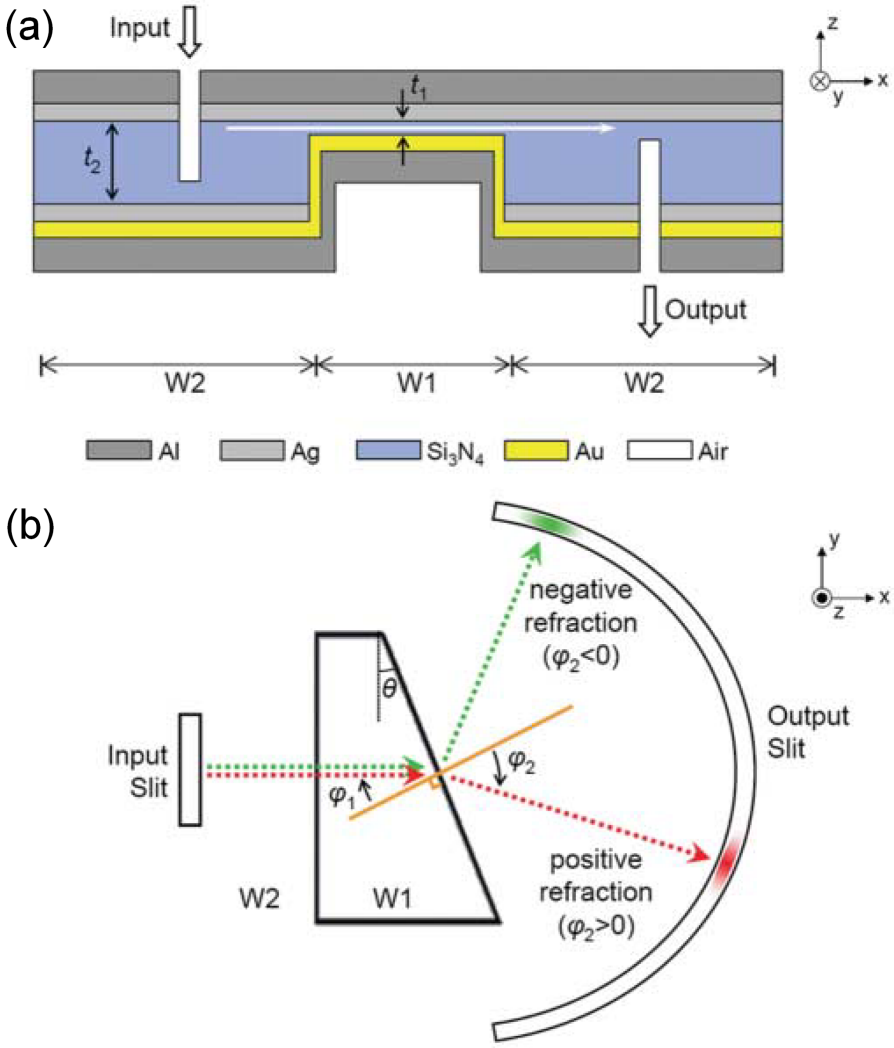

Figure 8.3: Schematic diagram of the structure fabricated to demonstrate negative refraction. A prism-shaped segment ("W1") of Au-Si_3N_4-Ag waveguide with core thickness $t_1 = 50$ nm is embedded in an region of Au-Si_3N_4-Ag waveguide with core thickness $t_1 = 500$ nm ("W2"). Two slits extending into the waveguide core are used to excited and intercept the light. (a) Cross section showing the light path through structure (white arrow). (b) Hypothetical path of the guided mode at two different frequencies illustrating positive refraction (red arrow) and negative refraction (green arrow) [26].

The TTR method can provide a simpler and more accurate way to characterized such an asymmetric MIM structure. As discussed in the previous chapters, the effective indices of the waveguide modes can be obtained for the resonances in the angular reflection power spectrum. By varying the wavelength of the incident beam, a band structure like Fig. 8.2 can be measured. In addition to the high accuracy due to the high angular selectivity of the TTR method, another advantage of the TTR measurement is that only the structure of interest (i.e. Au-Si_3N_4-Ag structure with a 50 nm core in this case) is characterized and no extra structure (like that shown in Fig. 8.3) is required.

8.2.3 Scattering Loss induced by Surface/Interface Roughness

Historically, scattering loss in waveguides induced by slight surface/interface roughness has been a difficult problem to analyze [110–113]. Brute-force types of simulation such as finite-difference time-domain (FDTD) analyses are not feasible since the feature size of surface roughness is much smaller than the wavelength. One of the most well-known treatments of this problem was proposed by D. Marcuse [110], who calculated the loss by the "mode conversion" from the fundamental mode into the higher-order modes and leaky modes. For a conventional dielectric waveguide, leaky modes have effective indices smaller than the refractive index of the cover or substrate, therefore the wave is propagating away from the cover or substrate. For a particular dielectric waveguide, leaky modes exist for any value of effective index smaller than the refractive index of the cover or substrate. In contrast, guided modes can only exist for certain discrete values of effective indices. Because of the presence of surface roughness, the orthogonality between the waveguide modes is lost, and energy can be coupled from one mode to another. However, the derivation does not consider all possible modes that can be coupled to, such as modes with complex effective indices. Such modes contain evanescent wave in particular directions and

may play an important role in scattering loss induced by surface/interface roughness. As a result, some of the conclusions are paradoxical. For example, the derivation in [110, 114, 115] shows that the waveguide is lossless when the root mean square (r.m.s.) surface/interface roughness is nonzero and the roughness is completely uncorrelated (i.e. zero correlation length).

A potentially simpler way to approach this issue is to start from the theory of electromagnetic waves scattered from a slightly rough surface [87,116–119]. While the diffusely scattered light is extremely complicated to analyze, the specularly reflected light has a much simpler form. For a waveguide structure, the diffusely scattered light does not corresponds to a guided mode and may be ignored for further analysis. One of the primary advantages of this approach is that it is potentially compatible with the transmission matrix formulation [120–122] and therefore can be readily applied to a structure with arbitrary numbers of layers. Further, the application of the TTR method to characterize the scattering loss serves as a potential area of future research.

8.3 Concluding Remarks

Surface plasmon technology will continue to be one of most promising candidates in realizing optical nanocircuitry. Among the family of plasmonic waveguides, the MIM waveguide provides the best lateral confinement, and is naturally the primary building element in such optical nanocircuitry. However, owing to the subwavelength dimension, the experimental characterization has been one of the major issues in the development of plasmonic devices. The conventional experimental characterization techniques, such as near-field scanning optical microscopy (NSOM) and the usage of multiple waveguides with various propagation distances, have some fundamental reliability issues, which inevitably limit the credibility of the measured propagation constants and/or attenuation coefficients. In this thesis, the transverse transmission/reflection (TTR) method is theoretically developed based on the transmission

matrix formulation, and experimentally implemented using an attenuated total reflection (ATR) configuration. Unlike the conventional techniques, in which light is coupled into the MIM waveguide via a tapered fiber or waveguide and the light propagation properties can then be determined, the TTR method relies on coupling from the transverse direction via a nearby prism and the light propagation properties can be obtained by the angular reflection spectrum. Therefore, the TTR method obviates the needs of sensitive detection in NSOM or the issue of coupling-efficiency variation when using multiple waveguide samples in the measurement. All the aforementioned properties make the TTR method a more reliable and accurate characterization technique than the conventional ones. Moreover, the TTR method has outstanding angular selectivity and is inherently capable of characterizing various waveguide mode in a multimode waveguide separately. This ability is unique to the TTR method. Lastly, the application of the TTR method can be further strengthened by extending the TTR method to 2D MIM waveguides, asymmetric MIM waveguides, and inclusion of scattering loss. Taking full advantage of the TTR method, the development of plasmonic devices can be potentially accelerated.

8.4 Summary

The main objectives and the major contributions of the research presented in this thesis were reviewed and summarized, and potential areas of future research were highlighted.

APPENDIX A

COMPARISON OF THE EXACT MODE PROFILE WITH THE FIELD PROFILE EXCITED AT RESONANT ANGLE

For a leaky waveguide structure with a high-index cover or loaded by a high-index layer as shown in Fig. 3.2, assume there exists a leaky mode with propagation constant $\beta_m - j\alpha_m$ that satisfies the equation $m_{22} = 0$; the corresponding mode profile therefore contains waves that propagate away from the waveguide into the high-index cover and the substrate, while there is no wave incident upon the waveguide in these two regions. If the same structure is excited by a wave incident from the cover, with an angle of incidence θ_q such that $n_c' \sin\theta = \beta_q/k_0$, the transmission matrix for the ith layer, $M_i(\beta_q)$, can be represented by

$$M_i(\beta_q) = \frac{1}{2}\begin{pmatrix} (1+f_i\frac{\kappa_{x,i}}{\kappa_{x,i+1}})\exp(-\kappa_{x,i}d_i) & (1-f_i\frac{\kappa_{x,i}}{\kappa_{x,i+1}})\exp(\kappa_{x,i}d_i) \\ (1-f_i\frac{\kappa_{x,i}}{\kappa_{x,i+1}})\exp(-\kappa_{x,i}d_i) & (1+f_i\frac{\kappa_{x,i}}{\kappa_{x,i+1}})\exp(\kappa_{x,i}d_i) \end{pmatrix} \text{ for } i = 0, \cdots, j-1. \tag{A.1}$$

In the case that $\alpha_q \ll \beta_q$, the transmission matrix for the leaky waveguide mode, $M_i(\beta_q - j\alpha_q)$, is again Eq. (A.1), but with $M_i(\beta_q)$ replaced by $M_i(\beta_q - j\alpha_q)$, $\kappa_{x,i}$ replaced by $\kappa_{x,i}'$, and $\kappa_{x,i+1}$ replaced by $\kappa_{x,i+1}'$ where $\kappa_{x,i}' = [(\beta_q - j\alpha_q)^2 - k_0^2 n_i^2]^{1/2} \simeq$

$\kappa_{x,i} - j\beta_q\alpha_q/\kappa_{x,i}$. Thus $M_i(\beta_q - j\alpha_q)$ can be approximated by the first-order perturbation of α_q as

$$M_i(\beta_q - j\alpha_q) \simeq \frac{1}{2}\times$$
$$\left(\begin{array}{c} \left[\left(1+f_i\frac{\kappa_{x,i}}{\kappa_{x,i+1}}\right)+f_i\frac{\alpha_q\beta_q}{\kappa_{x,i+1}^2}\left(\frac{\kappa_{x,i}}{\kappa_{x,i+1}}-\frac{\kappa_{x,i+1}}{\kappa_{x,i}}\right)+j\left(1+f_i\frac{\kappa_{x,i}}{\kappa_{x,i+1}}\right)\frac{\alpha_q\beta_q}{\kappa_{x,i}}d_i\right]\exp(-\kappa_{x,i}d_i) \\ \left[\left(1-f_i\frac{\kappa_{x,i}}{\kappa_{x,i+1}}\right)-f_i\frac{\alpha_q\beta_q}{\kappa_{x,i+1}^2}\left(\frac{\kappa_{x,i}}{\kappa_{x,i+1}}-\frac{\kappa_{x,i+1}}{\kappa_{x,i}}\right)+j\left(1-f_i\frac{\kappa_{x,i}}{\kappa_{x,i+1}}\right)\frac{\alpha_q\beta_q}{\kappa_{x,i}}d_i\right]\exp(-\kappa_{x,i}d_i) \\ \left[\left(1-f_i\frac{\kappa_{x,i}}{\kappa_{x,i+1}}\right)-f_i\frac{\alpha_q\beta_q}{\kappa_{x,i+1}^2}\left(\frac{\kappa_{x,i}}{\kappa_{x,i+1}}-\frac{\kappa_{x,i+1}}{\kappa_{x,i}}\right)-j\left(1-f_i\frac{\kappa_{x,i}}{\kappa_{x,i+1}}\right)\frac{\alpha_q\beta_q}{\kappa_{x,i}}d_i\right]\exp(\kappa_{x,i}d_i) \\ \left[\left(1+f_i\frac{\kappa_{x,i}}{\kappa_{x,i+1}}\right)+f_i\frac{\alpha_q\beta_q}{\kappa_{x,i+1}^2}\left(\frac{\kappa_{x,i}}{\kappa_{x,i+1}}-\frac{\kappa_{x,i+1}}{\kappa_{x,i}}\right)-j\left(1+f_i\frac{\kappa_{x,i}}{\kappa_{x,i+1}}\right)\frac{\alpha_q\beta_q}{\kappa_{x,i}}d_i\right]\exp(\kappa_{x,i}d_i) \end{array}\right)$$
$$\text{for } i = 0, \cdots, j-1. \tag{A.2}$$

It should be noted that $\kappa_{x,i}$ is imaginary when $n_i > \beta_q/k_0$ and real when $n_i < \beta_q/k_0$. Comparing Eq. (A.1) and (A.2), it is clear that the difference is small (on the order of α_q) unless $\kappa_{x,i}d_i$ has a significant real part, which exponentially amplifies the first-order perturbation of α_q. Since in either case, the field in the substrate is a wave propagating away from the waveguide with similar transverse wavevector (i.e. $\kappa_{x,s}$ and $\kappa'_{x,s}$), by equating the magnitude and phase of these two waves in the substrate, the two profiles between substrate and the cover ($n_1 = n_c$) will be very similar if $\mathrm{Re}(\kappa_{x,i}d_i) \ll \mathrm{Re}(\kappa_{x,1}d_1)$ for all $i \neq 1$. It is noteworthy that the two profiles agree more closely when the value of α_q is smaller. Moreover, if a high-index layer is added, the two profiles both agree with the mode profile in the absence of the high-index layer if the low-index gap between that layer and the waveguide is large enough to satisfy the weak coupling condition. Although the discussion above assumes that the structure is composed of lossless materials, the same argument can be applied to lossy materials by treating the extinction coefficient as α_q.

APPENDIX B

DETAILED ERROR ANALYSIS

The attenuation coefficient $\alpha'_{\rm MIM}$ obtained from the TTR method is specified by the HWHM of $R/R_{\rm Otto}$, which equals to $\alpha'_{\rm MIM}/k_0$. Following Sec. 3.4, the quantity $\alpha'_{\rm MIM}$ differs from the rigorously calculated attenuation coefficient $\alpha_{\rm MIM}$. The error in $\alpha'_{\rm MIM}$ has three sources: 1) the finite metal thickness d_m, 2) the phase shift of $V(\beta)$ due to loss in the metal, and 3) the background variation in $V(\beta)$. A step-by-step procedure for obtaining the value of the attenuation coefficient $\alpha''_{\rm MIM}$ corrected for these errors is given in Appendix C.

The first error is caused by the approximation $A \equiv (m_{21}m'_{12})/(m_{22}m'_{22})\exp(-2\kappa_m d_m) = 0$ in Eq. (3.29). Because of the m_{22} in the denominator, $|A|$ has a peak near where m_{22} has a pole which is also near where $R/R_{\rm Otto}$ has a minimum. In the worst case, the resonance strength of $R/R_{\rm Otto}$ is decreased by $100|A|_{max}\%$, and its HWHM is broadened by a similar percentage. $|A|_{max}$ can be estimated by comparing with the value of $(m_{21}/m_{22})[(m'_{11}m'_{22} - m'_{12}m'_{21})/(m'_{22}m'_{21})]\exp(-2\kappa_m d_m) = V(\beta)/(\beta - \gamma_{\rm MIM})$, which is the resonance strength of $R/R_{\rm Otto}$. The transmission matrix $M_{\rm Otto}$ when the gap dielectric thickness $d_g \to 0$ may be expressed as

$$M_{\rm Otto}(d_g \to 0) = \frac{1}{2}\begin{pmatrix} 1 + m'_{\rm Otto} & 1 - m'_{\rm Otto} \\ 1 - m'_{\rm Otto} & 1 + m'_{\rm Otto} \end{pmatrix}, \tag{B.1}$$

where $m'_{\rm Otto} = (n_m^2\kappa_p)/(n_p^2\kappa_m)$, which is imaginary for a lossless metal. For a low-loss metal, $|(m'_{11}m'_{22} - m'_{12}m'_{21})/(m'_{22}m'_{21})| = |4m'_{\rm Otto}/(1 - m'^2_{\rm Otto})|$ has values between 1 and 2 for $N_{\rm eff} = 0$ to $[n_m^2 n_p^2(n_m^2 + n_p^2)/(n_m^4 + n_p^4)]^1/2 \simeq n_p$. Therefore, based on Eq. (3.30), the value of $|(m_{21}/m_{22})\exp(-2\kappa_m d_m)|$ is between 1/4 to 1/2 times the resonance strength of $R/R_{\rm Otto}$ when $d_g \to 0$. Since the value of $|m'_{12}/m'_{22}|$ is between

1 and 2 for any d_g, $|A|_{max}$ at any d_g is smaller than or equal to 1/2 times the resonance strength of R/R_{Otto} when $d_g \to 0$. It should be noted that α'_{MIM} obtained without the approximation $A = 0$ [Eq. (3.30)] is always larger than that with the approximation [Eq. (3.29)].

The second source of error is caused by the material loss in the metal. In the case of a lossless metal, $\phi_V = 3\pi/2$. However, ϕ_V is shifted when the metal is lossy. Based on Eq. (3.30) and assuming $V(\beta) = V\exp[(3\pi/2)+\Delta\phi_V]$ where V is a positive constant, β_{min} at the minimum of the phase-shifted Lorentzian R/R_{Otto} can be represented as

$$\beta_{min} = \beta_{\text{MIM}} + \alpha_{\text{MIM}}\frac{\cos(\Delta\phi_V) - 1}{\sin(\Delta\phi_V)} \tag{B.2}$$

and β_{hm} values at the half-minimum points are

$$\beta^{\pm}_{hm} = \beta_{\text{MIM}} + \alpha_{\text{MIM}}\frac{-2\sin(\Delta\phi_V) \pm \{2[1+\cos(\Delta\phi_V)] + \sin^2(\Delta\phi_V)\}^{1/2}}{1+\cos(\Delta\phi_V)}, \tag{B.3}$$

where the positive and negative signs correspond to the right and left half-minimum points, respectively. Figure B.1(a) shows the variation of β_{min} and β_{hm} values, and Fig. B.1(b) shows the broadening effect of α'_{MIM} as a function of $\Delta\phi_V$.

The third source of error is caused by background variation of $V(\beta)$ and the effect is dependent on $\Delta\phi_V$. Assuming the phase-shifted Lorentzian is multiplied by a linearly varying function $V(\beta)$, Fig. B.2 shows the variation of α'_{MIM} as a function of the percentage background variation, $|V(\beta_{\text{MIM}}+\alpha_{\text{MIM}})/V(\beta_{\text{MIM}}-\alpha_{\text{MIM}})|-1$, at various $\Delta\phi_V$ values.

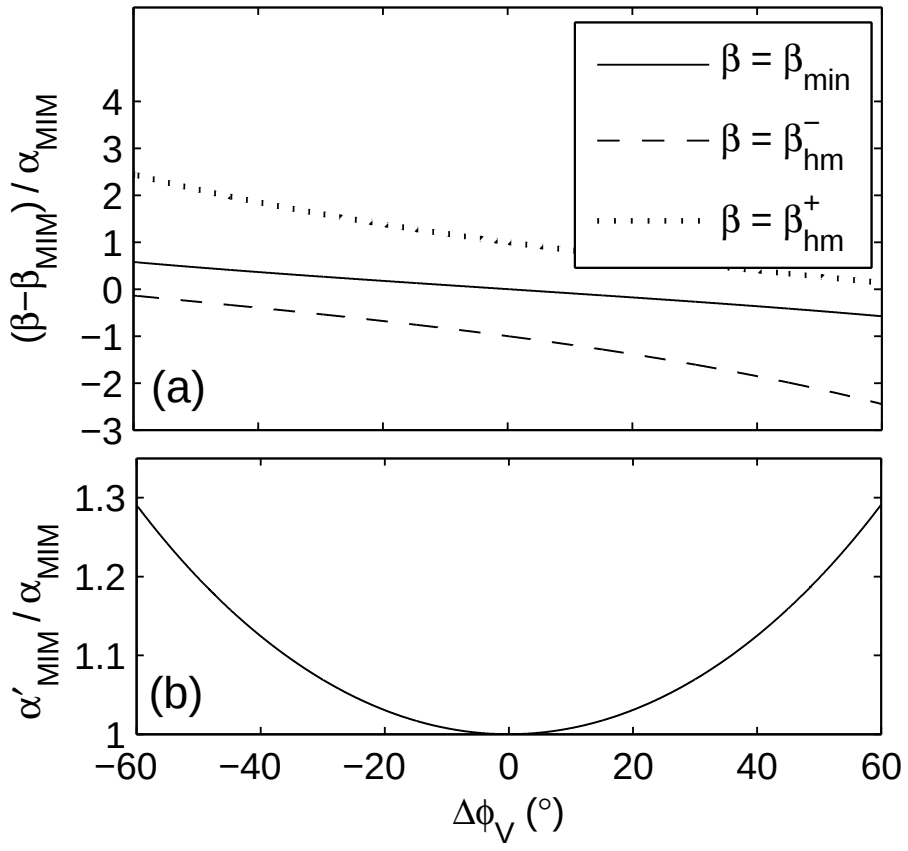

Figure B.1: (a) Variation of β_{min} and $\beta_{hm}^{\pm}$ values as a function of the phase shift $\Delta\phi_V$ caused by the material loss of the metal. The lower β_{hm}^{-} corresponds to the left half-minimum point and the upper β_{hm}^{+} to the right half-minimum point. (b) Broadening of α'_{MIM} as a function of $\Delta\phi_V$.

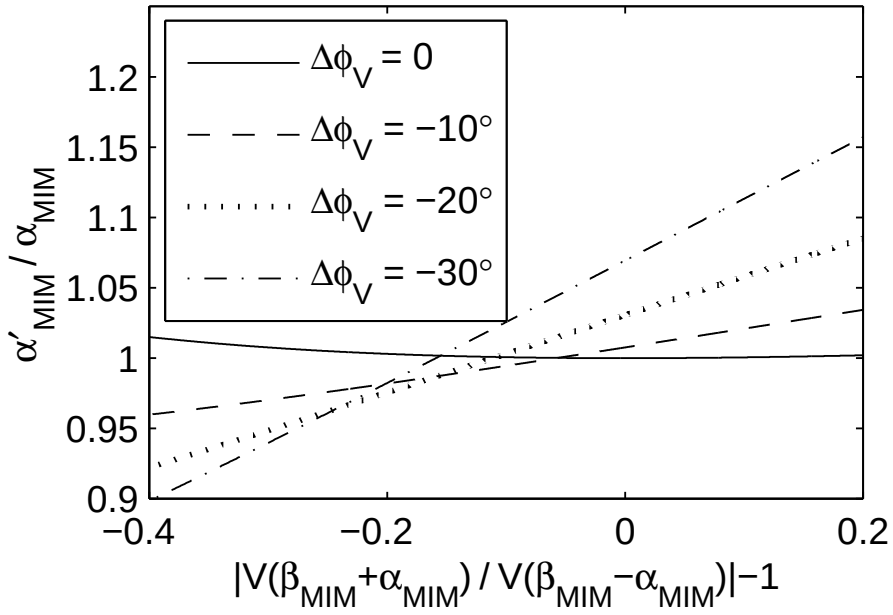

Figure B.2: Variation of α'_{MIM} as a function of the linear background variation at various phase shift $\Delta\phi_V$.

APPENDIX C

METHOD OF DETERMINING CORRECTED ATTENUATION COEFFICIENTS

Based on the discussion in Appendix B, the corrected α''_{MIM} can be obtained by using multiple R curves at various gap dielectric thicknesses d_g, utilizing the fact that the variation of α'_{MIM} is proportional to the percentage background variation and that the slopes depend on the phase shift $\Delta\phi_V$ (Fig. B.2). From various α'_{MIM} values obtained from the $V(\beta)$ variations, the quantity $\Delta\phi_V$ and the corrected α''_{MIM} can be estimated by the slope of the α'_{MIM} versus the percentage background variation. By definition, the variation of $|V(\beta)|$ is determined by the variation of $|(m'_{11}m'_{22} - m'_{12}m'_{21})/(m'_{22}m'_{21})|$ and $|(m_{21}/m_{22})\exp(-2\kappa_m d_m)|$; the former is related to the prism-dielectric-metal structure and the latter is related to the MIM structure. Therefore, the variation of $|V(\beta)|$ can be controlled by varying the values of d_g, while the variation of $|(m_{21}/m_{22})\exp(-2\kappa_m d_m)|$ stays constant and does not affect the slope of Fig. B.2. The variation of $|(m'_{11}m'_{22} - m'_{12}m'_{21})/(m'_{22}m'_{21})|$ can be obtained by using

$$\left|\frac{m'_{11}m'_{22} - m'_{12}m'_{21}}{m'_{22}m'_{21}}\right| = \left|\frac{t_{\text{c,Otto}}t_{\text{s,Otto}}}{r_{\text{s,Otto}}}\right| \simeq T_{\text{Otto}} \propto 1 - R_{\text{Otto}}, \tag{C.1}$$

where R_{Otto} can be obtained by qualitatively subtracting out the TM_0 resonance. It should be noted that no explicit information about d_g or d_m is needed, which means the correction procedure can be implemented by simply using multiple R curves at various d_g values.

The correction procedure of α'_{MIM} is given by the following steps. For illustration purpose, the procedure is applied to the example case in Sec. 4.3.

1) Calculate/plot R vs. N_{eff} at various d_g values.

2) Produce R_{Otto} vs. N_{eff} by qualitatively subtracting out the TM_0 resonance from R for each d_g.

3) From R/R_{Otto} vs. N_{eff}, estimate the error due to the finite d_m, which is the half resonance strength as $d_g \to 0$. The error $\simeq 6\%$ in this case.

4) From R/R_{Otto} vs. N_{eff}, calculate β'_{MIM} from the location of the minimum and α'_{MIM} from the HWHM for each d_g. The quantity α'_{MIM} should be subtracted by the broadening error due to the finite d_m obtained in step 3.

5) From R_{Otto} vs. N_{eff} in step 2, calculate the background variation, $[1 - R_{\text{Otto}}(\beta'_{\text{MIM}} + \alpha'_{\text{MIM}})]/[1 - R_{\text{Otto}}(\beta'_{\text{MIM}} - \alpha'_{\text{MIM}})] - 1$, for each d_g. The background variation is proportional to $|V(\beta'_{\text{MIM}} + \alpha'_{\text{MIM}})/V(\beta'_{\text{MIM}} - \alpha'_{\text{MIM}})| - 1$ according to Eq. (C.1). In this case, the background variation $\simeq 4\%$, -3%, -27%, and -30% for $d_g = 0$, 50 nm, 100 nm, and 200 nm, respectively.

6) From the plot of α'_{MIM} vs. the background variation (Fig. C.1), estimate $\Delta\phi_V$ by comparing with Fig. B.2. In this case, $\Delta\phi_V \simeq 20^\circ$.

7) Calculate the corrected attenuation α''_{MIM} from

$$\alpha''_{\text{MIM}} = \frac{\alpha'_{\text{MIM}} \text{ (Fig. C.1)}}{(\alpha'_{\text{MIM}}/\alpha_{\text{MIM}}) \text{ (Fig. B.2)}}. \tag{C.2}$$

In this case, $\alpha''_{\text{MIM}}/k_0 \simeq 0.0297$.

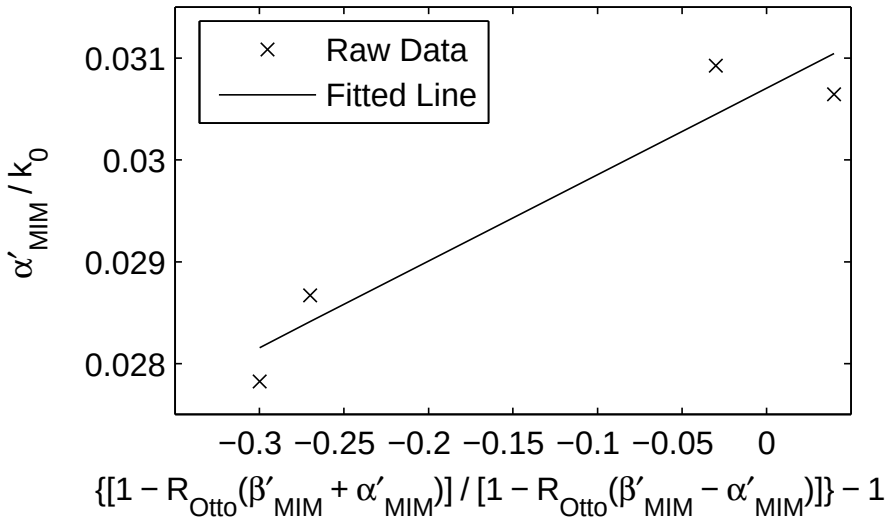

Figure C.1: Variation of α'_{MIM} as a function of the linear background variation for the example case in Sec. 4.3. β'_{MIM} and α'_{MIM} are obtained by using Table 4.3, while the latter is subtracted by the estimated broadening error due to finite d_m, which is $\simeq 6\%$ in this case.

REFERENCES

[1] E. Ozbay, "Plasmonics: Merging photonics and electronics at nanoscale dimensions," *Science*, vol. 311, no. 5758, pp. 189–193, Jan. 2006.

[2] W. L. Barnes, A. Dereux, and T. W. Ebbesen, "Surface plasmon subwavelength optics," *Nature*, vol. 424, no. 6950, pp. 824–830, Aug. 2003.

[3] R. Zia, J. A. Schuller, A. Chandran, and M. L. Brongersma, "Plasmonics: The next chip-scale technology," *Mater. Today*, vol. 9, no. 7-8, pp. 20–27, Jul.-Aug. 2006.

[4] S. A. Maier and H. A. Atwater, "Plasmonics: Localization and guiding of electromagnetic energy in metal/dielectric structures," *J. Appl. Phys.*, vol. 98, no. 1, p. 011101, Jul. 2005.

[5] M. L. Brongersma and V. M. Shalaev, "The case for plasmonics," *Science*, vol. 328, no. 5977, pp. 440–441, Apr. 2010.

[6] T. W. Ebbesen, H. J. Lezec, H. F. Ghaemi, T. Thio, and P. A. Wolff, "Extraordinary optical transmission through sub-wavelength hole arrays," *Nature*, vol. 391, no. 6668, pp. 667–669, Feb. 1998.

[7] J. R. Krenn and J. C. Weeber, "Surface plasmon polaritons in metal stripes and wires," *Philos. Trans. Roy. Soc. A*, vol. 362, no. 1817, pp. 739–756, Apr. 2004.

[8] S. I. Bozhevolnyi, V. S. Volkov, E. Devaux, J. Y. Laluet, and T. W. Ebbesen, "Channel plasmon subwavelength waveguide components including interferometers and ring resonators," *Nature*, vol. 440, no. 7083, pp. 508–511, Mar. 2006.

[9] P. Berini, R. Charbonneau, N. Lahoud, and G. Mattiussi, "Characterization of long-range surface-plasmon-polariton waveguides," *J. Appl. Phys.*, vol. 98, no. 4, p. 043109, Aug. 2005.

[10] D. F. P. Pile, T. Ogawa, D. K. Gramotnev, T. Okamoto, M. Haraguchi, M. Fukui, and S. Matsuo, "Theoretical and experimental investigation of strongly localized plasmons on triangular metal wedges for subwavelength waveguiding," *Appl. Phys. Lett.*, vol. 87, no. 6, p. 061106, Aug. 2005.

[11] S. A. Maier, "Plasmonics: The promise of highly integrated optical devices," *IEEE J. Sel. Top. Quant.*, vol. 12, no. 6, pp. 1671–1677, Nov.-Dec. 2006.

[12] S. A. Maier, M. D. Friedman, P. E. Barclay, and O. Painter, "Experimental demonstration of fiber-accessible metal nanoparticle plasmon waveguides for planar energy guiding and sensing," *Appl. Phys. Lett.*, vol. 86, no. 7, p. 071103, Feb. 2005.

[13] J. Vuckovic, M. Loncar, and A. Scherer, "Surface plasmon enhanced light-emitting diode," *IEEE J. Quantum Electron.*, vol. 36, no. 10, pp. 1131–1144, Oct. 2000.

[14] S. Wedge, J. A. E. Wasey, W. L. Barnes, and I. Sage, "Coupled surface plasmon-polariton mediated photoluminescence from a top-emitting organic light-emitting structure," *Appl. Phys. Lett.*, vol. 85, no. 2, pp. 182–184, Jul. 2004.

[15] J. Hashizume and F. Koyama, "Plasmon enhanced optical near-field probing of metal nanoaperture surface emitting laser," *Opt. Express*, vol. 12, no. 25, pp. 6391–6396, Dec. 2004.

[16] J. B. Pendry, L. Martin-Moreno, and F. J. Garcia-Vidal, "Mimicking surface plasmons with structured surfaces," *Science*, vol. 305, no. 5685, pp. 847–848, Aug. 2004.

[17] J. B. Pendry, "Negative refraction makes a perfect lens," *Phys. Rev. Lett.*, vol. 85, no. 18, pp. 3966–3969, Oct. 2000.

[18] N. Fang, H. Lee, C. Sun, and X. Zhang, "Sub-diffraction-limited optical imaging with a silver superlens," *Science*, vol. 308, no. 5721, pp. 534–537, Apr. 2005.

[19] J. Homola, S. S. Yee, and G. Gauglitz, "Surface plasmon resonance sensors: review," *Sens. Actuat. B-Chem.*, vol. 54, no. 1-2, pp. 3–15, Jan. 1999.

[20] K. Kneipp, H. Kneipp, I. Itzkan, R. R. Dasari, and M. S. Feld, "Surface-enhanced Raman scattering and biophysics," *J. Phys.-Condens. Mat.*, vol. 14, no. 18, pp. R597–R624, May 2002.

[21] K. Kneipp, Y. Wang, H. Kneipp, L. T. Perelman, I. Itzkan, R. Dasari, and M. S. Feld, "Single molecule detection using surface-enhanced Raman scattering (SERS)," *Phys. Rev. Lett.*, vol. 78, no. 9, pp. 1667–1670, Mar. 1997.

[22] S. M. Nie and S. R. Emery, "Probing single molecules and single nanoparticles by surface-enhanced Raman scattering," *Science*, vol. 275, no. 5303, pp. 1102–1106, Feb. 1997.

[23] S. Pillai, K. R. Catchpole, T. Trupke, and M. A. Green, "Surface plasmon enhanced silicon solar cells," *J. Appl. Phys.*, vol. 101, no. 9, p. 093105, May 2007.

[24] M. Westphalen, U. Kreibig, J. Rostalski, H. Luth, and D. Meissner, "Metal cluster enhanced organic solar cells," *Sol. Energ. Mat. Sol. C.*, vol. 61, no. 1, pp. 97–105, Feb. 2000.

[25] D. Derkacs, S. H. Lim, P. Matheu, W. Mar, and E. T. Yu, "Improved performance of amorphous silicon solar cells via scattering from surface plasmon polaritons in nearby metallic nanoparticles," *Appl. Phys. Lett.*, vol. 89, no. 9, p. 093103, Aug. 2006.

[26] H. J. Lezec, J. A. Dionne, and H. A. Atwater, "Negative refraction at visible frequencies," *Science*, vol. 316, no. 5823, pp. 430–432, Apr. 2007.

[27] V. M. Shalaev, W. S. Cai, U. K. Chettiar, H. K. Yuan, A. K. Sarychev, V. P. Drachev, and A. V. Kildishev, "Negative index of refraction in optical metamaterials," *Opt. Lett.*, vol. 30, no. 24, pp. 3356–3358, Dec. 2005.

[28] V. M. Shalaev, "Optical negative-index metamaterials," *Nat. Photonics*, vol. 1, no. 1, pp. 41–48, Jan. 2007.

[29] A. Karalis, E. Lidorikis, M. Ibanescu, J. D. Joannopoulos, and M. Soljacic, "Surface-plasmon-assisted guiding of broadband slow and subwavelength light in air," *Phys. Rev. Lett.*, vol. 95, no. 6, p. 063901, Aug. 2005.

[30] E. Feigenbaum and M. Orenstein, "Modeling of complementary (void) plasmon waveguiding," *J. Lightwave Technol.*, vol. 25, no. 9, pp. 2547–2562, Sep. 2007.

[31] H. Raether, *Surface Plasmons on Smooth and Rough Surfaces and on Gratings*. Springer-Verlag, 1988.

[32] M. Born and E. Wolf, *Principles of Optics (Seventh Edition)*. Cambridge University Press, 1999. Chapter 8.

[33] J. A. Dionne, H. J. Lezec, and H. A. Atwater, "Highly confined photon transport in subwavelength metallic slot waveguides," *Nano Lett.*, vol. 6, no. 9, pp. 1928–1932, Sep. 2006.

[34] Z. Han, A. Y. Elezzabi, and V. Van, "Experimental realization of subwavelength plasmonic slot waveguides on a silicon platform," *Opt. Lett.*, vol. 35, no. 4, pp. 502–504, Feb. 2010.

[35] T. Goto, Y. Katagiri, H. Fukuda, H. Shinojima, Y. Nakano, I. Kobayashi, and Y. Mitsuoka, "Propagation loss measurement for surface plasmon-polariton modes at metal waveguides on semiconductor substrates," *Appl. Phys. Lett.*, vol. 84, no. 6, pp. 852–854, Feb. 2004.

[36] U. Durig, D. W. Pohl, and F. Rohner, "Near-field optical-scanning microscopy," *J. Appl. Phys.*, vol. 59, no. 10, pp. 3318–3327, May 1986.

[37] J. C. Weeber, Y. Lacroute, and A. Dereux, "Optical near-field distributions of surface plasmon waveguide modes," *Phys. Rev. B*, vol. 68, no. 11, p. 115401, Sep. 2003.

[38] S. I. Bozhevolnyi, V. S. Volkov, E. Devaux, and T. W. Ebbesen, "Channel plasmon-polariton guiding by subwavelength metal grooves," *Phys. Rev. Lett.*, vol. 95, no. 4, p. 046802, Jul. 2005.

[39] C.-I. Lin and T. K. Gaylord, "Attenuation and mode profile determination of leaky/lossy modes in multilayer planar waveguides by a coupling simulation method," *Appl. Opt.*, vol. 48, no. 19, pp. 3603–3613, Feb. 2009.

[40] C.-I. Lin and T. K. Gaylord, "Characterization of the loss of plasmonic modes in planar metal-insulator-metal waveguides by a coupling-simulation approach," *Appl. Opt.*, vol. 49, no. 6, pp. 936–944, Feb. 2010.

[41] C.-I. Lin and T. K. Gaylord, "Loss measurement of plasmonic modes in planar metal-insulator-metal waveguides by an attenuated total reflection method," *Opt. Lett.*, vol. 35, no. 22, pp. 3814–3816, Nov. 2010.

[42] A. E. Craig, G. A. Olson, and D. Sarid, "Experimental-observation of the long-range surface-plasmon polariton," *Opt. Lett.*, vol. 8, no. 7, pp. 380–382, Jul. 1983.

[43] J. C. Quail, J. G. Rako, and H. J. Simon, "Long-range surface-plasmon modes in silver and aluminum films," *Opt. Lett.*, vol. 8, no. 7, pp. 377–379, Jul. 1983.

[44] F. Z. Yang, G. W. Bradberry, and J. R. Sambles, "Long-range surface-mode supported by very thin silver films," *Phys. Rev. Lett.*, vol. 66, no. 15, pp. 2030–2032, Apr. 1991.

[45] P. K. Tien and R. Ulrich, "Theory of prism-film coupler and thin-film light guides," *J. Opt. Soc. Am.*, vol. 60, no. 10, pp. 1325–1337, Oct. 1970.

[46] R. Ulrich, "Theory of prism-film coupler by plane-wave analysis," *J. Opt. Soc. Am.*, vol. 60, no. 10, pp. 1337–1350, Oct. 1970.

[47] J. Cardin and D. Leduc, "Determination of refractive index, thickness, and the optical losses of thin films from prism-film coupling measurements," *Appl. Opt.*, vol. 47, no. 7, pp. 894–900, Mar. 2008.

[48] E. N. Economou, "Surface plasmons in thin films," *Phys. Rev.*, vol. 182, no. 2, pp. 539–554, Jun. 1969.

[49] M. Fox, *Optical Properties of Solids*. Oxford University Press, 2001.

[50] J. K. S. Poon, J. Scheuer, Y. Xu, and A. Yariv, "Designing coupled-resonator optical waveguide delay lines," *J. Opt. Soc. Am. B*, vol. 21, no. 9, pp. 1665–1673, Sep. 2004.

[51] F. N. Xia, L. Sekaric, and Y. Vlasov, "Ultracompact optical buffers on a silicon chip," *Nat. Photonics*, vol. 1, no. 1, pp. 65–71, Jan. 2007.

[52] Y. Hamachi, S. Kubo, and T. Baba, "Slow light with low dispersion and nonlinear enhancement in a lattice-shifted photonic crystal waveguide," *Opt. Lett.*, vol. 34, no. 7, pp. 1072–1074, Apr. 2009.

[53] R. Charbonneau, P. Berini, E. Berolo, and E. Lisicka-Shrzek, "Experimental observation of plasmon-polariton waves supported by a thin metal film of finite width," *Opt. Lett.*, vol. 25, no. 11, pp. 844–846, Jun. 2000.

[54] G. Veronis and S. H. Fan, "Bends and splitters in metal-dielectric-metal subwavelength plasmonic waveguides," *Appl. Phys. Lett.*, vol. 87, no. 13, p. 131102, Sep. 2005.

[55] Y. Matsuzaki, T. Okamoto, M. Haraguchi, M. Fukui, and M. Nakagaki, "Characteristics of gap plasmon waveguide with stub structures," *Opt. Express*, vol. 16, no. 21, pp. 16 314–16 325, Oct. 2008.

[56] S. E. Kocabas, G. Veronis, D. A. B. Miller, and S. H. Fan, "Transmission line and equivalent circuit models for plasmonic waveguide components," *IEEE J. Sel. Top. Quant.*, vol. 14, no. 6, pp. 1462–1472, Nov.-Dec. 2008.

[57] S. I. Bozhevolnyi and K. V. Nerkararyan, "Analytic description of channel plasmon polaritons," *Opt. Lett.*, vol. 34, no. 13, pp. 2039–2041, Jul. 2009.

[58] P. Ginzburg, D. Arbel, and M. Orenstein, "Gap plasmon polariton structure for very efficient microscale-to-nanoscale interfacing," *Opt. Lett.*, vol. 31, no. 22, pp. 3288–3290, Nov. 2006.

[59] A. Otto, "Excitation of nonradiative surface plasma waves in silver by method of frustrated total reflection," *Z. Phys.*, vol. 216, no. 4, pp. 398–410, 1968.

[60] E. Kretschmann and H. Raether, "Radiative decay of non radiative surface plasmons excited by light," *Z. Naturforsch. Pt. A*, vol. A 23, no. 12, pp. 2135–2136, 1968.

[61] R. H. Ritchie, E. T. Arakawa, J. J. Cowan, and R. N. Hamm, "Surface-plasmon resonance effect in grating diffraction," *Phys. Rev. Lett.*, vol. 21, no. 22, pp. 1530–1533, 1968.

[62] R. W. Wood, "On a remarkable case of uneven distribution of light in a diffraction grating spectrum," *Philos. Mag.*, vol. 4, no. 19-24, pp. 396–402, Jul-Dec. 1902.

[63] B. Hecht, H. Bielefeldt, L. Novotny, Y. Inouye, and D. W. Pohl, "Local excitation, scattering, and interference of surface plasmons," *Phys. Rev. Lett.*, vol. 77, no. 9, pp. 1889–1892, Aug. 1996.

[64] H. Ditlbacher, J. R. Krenn, N. Felidj, B. Lamprecht, G. Schider, M. Salerno, A. Leitner, and F. R. Aussenegg, "Fluorescence imaging of surface plasmon fields," *Appl. Phys. Lett.*, vol. 80, no. 3, pp. 404–406, Jan. 2002.

[65] B. Prade, J. Y. Vinet, and A. Mysyrowicz, "Guided optical waves in planar heterostructures with negative dielectric-constant," *Phys. Rev. B*, vol. 44, no. 24, pp. 13 556–13 572, Dec. 1991.

[66] P. B. Johnson and R. W. Christy, "Optical-constants of noble-metals," *Phys. Rev. B*, vol. 6, no. 12, pp. 4370–4379, Dec. 1972.

[67] M. F. Chen and H. C. Chang, "Plasmonic states from visible light to microwaves," *IEEE J. Quantum Electron.*, vol. 45, no. 12, pp. 1558–1562, Dec. 2009.

[68] N. N. Rao, *Elements of Engineering Electromagnetics*. Prentice Hall, 2000.

[69] R. Ramaswami and K. N. Sivarajan, *Optical Networks – A Practical Perspective.* Morgan Kaufmann, 2002.

[70] E. Betzig and J. K. Trautman, "Near-field optics - microscopy, spectroscopy, and surface modification beyond the diffraction limit," *Science*, vol. 257, no. 5067, pp. 189–195, Jul. 1992.

[71] J. W. Goodman, *Introduction to Fourier Optics.* McGraw-Hill, 1968.

[72] G. A. Massey, "Microscopy and pattern generation with scanned evanescent waves," *Appl. Opt.*, vol. 23, no. 5, pp. 658–660, Mar. 1984.

[73] E. Betzig, J. K. Trautman, T. D. Harris, J. S. Weiner, and R. L. Kostelak, "Breaking the diffraction barrier - optical microscopy on a nanometric scale," *Science*, vol. 251, no. 5000, pp. 1468–1470, Mar. 1991.

[74] D. W. Pohl, W. Denk, and M. Lanz, "Optical stethoscopy - image recording with resolution $\lambda/20$," *Appl. Phys. Lett.*, vol. 44, no. 7, pp. 651–653, Apr. 1984.

[75] E. A. Ash and G. Nicholls, "Super-resolution aperture scanning microscope," *Nature*, vol. 237, no. 5357, pp. 510–512, Jun. 1972.

[76] J. K. Trautman, E. Betzig, J. S. Weiner, D. J. Digiovanni, T. D. Harris, F. Hellman, and E. M. Gyorgy, "Image-contrast in near-field optics," *J. Appl. Phys.*, vol. 71, no. 10, pp. 4659–4663, May 1992.

[77] E. Betzig and R. J. Chichester, "Single molecules observed by near-field scanning optical microscopy," *Science*, vol. 262, no. 5138, pp. 1422–1425, Nov. 1993.

[78] S. Bourzeix, J. M. Moison, F. Mignard, F. Barthe, A. C. Boccara, C. Licoppe, B. Mersali, M. Allovon, and A. Bruno, "Near-field optical imaging of light propagation in semiconductor waveguide structures," *Appl. Phys. Lett.*, vol. 73, no. 8, pp. 1035–1037, Aug. 1998.

[79] G. H. Vander Rhodes, B. B. Goldberg, M. S. Unlu, S. T. Chu, W. Pan, T. Kaneko, Y. Kokobun, and B. E. Little, "Measurement of internal spatial modes and local propagation properties in optical waveguides," *Appl. Phys. Lett.*, vol. 75, no. 16, pp. 2368–2370, Oct. 1999.

[80] A. L. Campillo, J. W. P. Hsu, C. A. White, and C. D. W. Jones, "Direct measurement of the guided modes in $LiNbO_3$ waveguides," *Appl. Phys. Lett.*, vol. 80, no. 13, pp. 2239–2241, Apr. 2002.

[81] S. I. Bozhevolnyi, V. S. Volkov, T. Sondergaard, A. Boltasseva, P. I. Borel, and M. Kristensen, "Near-field imaging of light propagation in photonic crystal waveguides: Explicit role of Bloch harmonics," *Phys. Rev. B*, vol. 66, no. 23, p. 235204, Dec. 2002.

[82] S. I. Bozhevolnyi, I. Smolyaninov, and A. V. Zayats, "Near-field microscopy of surface-plasmon polaritons - localization and internal interface imaging," *Phys. Rev. B*, vol. 51, no. 24, pp. 17 916–17 924, Jun. 1995.

[83] E. Verhagen, J. A. Dionne, L. Kuipers, H. A. Atwater, and A. Polman, "Near-field visualization of strongly confined surface plasmon polaritons in metal-insulator-metal waveguides," *Nano Lett.*, vol. 8, no. 9, pp. 2925–2929, Sep. 2008.

[84] T. Tamir and F. Y. Kou, "Varieties of leaky waves and their excitation along multilayered structures," *IEEE J. Quantum Electron.*, vol. 22, no. 4, pp. 544–551, Apr. 1986.

[85] E. Anemogiannis, E. N. Glytsis, and T. K. Gaylord, "Determination of guided and leaky modes in lossless and lossy planar multilayer optical waveguides: Reflection pole method and wavevector density method," *J. Lightwave Technol.*, vol. 17, no. 5, pp. 929–941, May 1999.

[86] J. Q. Xia, A. K. Jordan, and J. A. Kong, "Inverse-scattering view of modal structures in inhomogeneous optical waveguides," *J. Opt. Soc. Am. A*, vol. 9, no. 5, pp. 740–748, May 1992.

[87] P. K. Tien, "Light waves in thin films and integrated optics," *Appl. Opt.*, vol. 10, no. 11, pp. 2395–2413, Nov. 1971.

[88] R. Ulrich and R. Torge, "Measurement of thin-film parameters with a prism coupler," *Appl. Opt.*, vol. 12, no. 12, pp. 2901–2908, Dec. 1973.

[89] R. T. Kersten, "Prism-film coupler as a precision instrument Part I. Accuracy and capabilities of prism couplers as instruments," *Opt. Acta*, vol. 22, no. 6, pp. 503–513.

[90] E. D. Palik, *Handbook of Optical Constants of Solids.* Academic Press, 1985.

[91] E. Anemogiannis and E. N. Glytsis, "Multilayer waveguides - efficient numerical-analysis of general structures," *J. Lightwave Technol.*, vol. 10, no. 10, pp. 1344–1351, Oct. 1992.

[92] M. A. Duguay, Y. Kokubun, T. L. Koch, and L. Pfeiffer, "Antiresonant reflecting optical waveguides in SiO_2-Si multilayer structures," *Appl. Phys. Lett.*, vol. 49, no. 1, pp. 13–15, Jul. 1986.

[93] T. Baba and Y. Kokubun, "Dispersion and radiation loss characteristics of antiresonant reflecting optical waveguides - numerical results and analytical expressions," *IEEE J. Quantum Electron.*, vol. 28, no. 7, pp. 1689–1700, Jul. 1992.

[94] A. C. Adams, F. B. Alexander, C. D. Capio, and T. E. Smith, "Characterization of plasma-deposited silicon dioxide," *J. Electrochem. Soc.*, vol. 128, no. 7, pp. 1545–1551, Jul. 1981.

[95] J. R. Hollahan, "Deposition of plasma silicon-oxide thin-films in a production planar reactor," *J. Electrochem. Soc.*, vol. 126, no. 6, pp. 930–934, Jun. 1979.

[96] S. Matsuo and M. Kiuchi, "Low-temperature chemical vapor-deposition method utilizing an electron-cyclotron resonance plasma," *Jpn. J. Appl. Phys. 2*, vol. 22, no. 4, pp. L210–L212, Apr. 1983.

[97] Metricon Corporation, http://www.metricon.com/.

[98] C. Dominguez, J. A. Rodriguez, F. J. Munoz, and N. Zine, "Plasma enhanced CVD silicon oxide films for integrated optic applications," *Vacuum*, vol. 52, no. 4, pp. 395–400, Apr. 1999.

[99] V. A. Dao, V. D. Nguyen, J. Heo, H. Choi, Y. Kim, N. Lakshminarayan, and J. Yi, "Effect of N_2O/SiH_4 flow ratios on properties of amorphous silicon oxide thin films deposited by inductively-coupled plasma chemical vapor deposition with application to silicon surface passivation," *Vacuum*, vol. 84, no. 3, pp. 410–414, Nov. 2009.

[100] J. E. Nestell and R. W. Christy, "Derivation of optical-constants of metals from thin-film measurements at oblique-incidence," *Appl. Opt.*, vol. 11, no. 3, pp. 643–651, Mar. 1972.

[101] J. E. Nestell and R. W. Christy, "Optics of thin metal films," *Am. J. Phys.*, vol. 39, no. 3, pp. 315–320, Mar. 1971.

[102] C. Reale, "Optical constants of vacuum deposited thin metal films in near infrared," *Infrared Phys.*, vol. 10, no. 3, pp. 173–181, 1970.

[103] P. L. Pedrotti and F. L. Pedrotti, *Introduction to Optics*. Prentice Hall, 1993.

[104] J. J. Olivero and R. L. Longbothum, "Empirical fits to Voigt line-width - brief review," *J. Quant. Spectrosc. Ra.*, vol. 17, no. 2, pp. 233–236, 1977.

[105] J. F. Kielkopf, "New approximation to Voigt function with applications to spectral-line profile analysis," *J. Opt. Soc. Am.*, vol. 63, no. 8, pp. 987–995, Aug. 1973.

[106] A. L. Schawlow and C. H. Townes, "Infrared and optical masers," *Phys. Rev.*, vol. 112, no. 6, pp. 1940–1949, Dec. 1958.

[107] P. Bhattacharya, *Semiconductor Optoelectronic Devices*. Prentice Hall India, 2002.

[108] K. S. Chiang and S. Y. Cheng, "Technique of applying the prism-coupler method for accurate measurement of the effective indices of channel waveguides," *Opt. Eng.*, vol. 47, no. 3, p. 034601, Mar. 2008.

[109] A. Yariv, "Coupled-mode theory for guided-wave optics," *IEEE J. Quantum Electron.*, vol. 9, no. 9, pp. 919–933, Sep. 1973.

[110] D. Marcuse, "Mode conversion caused by surface imperfections of a dielectric slab waveguide," *Bell Sys. Tech. J.*, vol. 48, no. 10, pp. 3187–3215, Dec. 1969.

[111] M. Imai, S. Miyanaga, and T. Asakura, "Mode conversion and radiation loss caused by refractive-index fluctuations in an asymmetric slab waveguide," *IEEE J. Quantum Electron.*, vol. 13, no. 4, pp. 255–262, Apr. 1977.

[112] J. M. Elson, "Propagation in planar waveguides and the effects of wall roughness," *Opt. Express*, vol. 9, no. 9, pp. 461–475, Oct. 2001.

[113] K. K. Lee, D. R. Lim, L. C. Kimerling, J. Shin, and F. Cerrina, "Fabrication of ultralow-loss Si/SiO_2 waveguides by roughness reduction," *Opt. Lett.*, vol. 26, no. 23, pp. 1888–1890, Dec. 2001.

[114] J. P. R. Lacey and F. P. Payne, "Radiation loss from planar waveguides with random wall imperfections," *IEE Proc.-J*, vol. 137, no. 4, pp. 282–288, Aug. 1990.

[115] F. P. Payne and J. P. R. Lacey, "A theoretical-analysis of scattering loss from planar optical waveguides," *Opt. Quant. Electron.*, vol. 26, no. 10, pp. 977–986, Oct. 1994.

[116] T. M. Elfouhaily and C. A. Guerin, "A critical survey of approximate scattering wave theories from random rough surfaces," *Wave. Random Media*, vol. 14, no. 4, pp. R1–R40, Oct. 2004.

[117] I. Filinski, "Effects of sample imperfections on optical spectra," *Phys. Status Solidi B*, vol. 49, no. 2, pp. 577–588, 1972.

[118] H. E. Bennett and J. O. Porteus, "Relation between surface roughness and specular reflectance at normal incidence," *J. Opt. Soc. Am.*, vol. 51, no. 2, pp. 123–129, Feb. 1961.

[119] H. Davies, "The reflection of electromagnetic waves from a rough surface," *Proc. Inst. Electr. Eng.*, vol. 101, no. 7, pp. 209–214, Jan. 1954.

[120] C. C. Katsidis and D. I. Siapkas, "General transfer-matrix method for optical multilayer systems with coherent, partially coherent, and incoherent interference," *Appl. Opt.*, vol. 41, no. 19, pp. 3978–3987, Jul. 2002.

[121] J. S. C. Prentice, "Coherent, partially coherent and incoherent light absorption in thin-film multilayer structures," *J. Phys. D Appl. Phys.*, vol. 33, no. 24, pp. 3139–3145, Dec. 2000.

[122] C. L. Mitsas and D. I. Siapkas, "Generalized matrix-method for analysis of coherent and incoherent reflectance and transmittance of multilayer structures

with rough surfaces, interfaces, and finite substrates," *Appl. Opt.*, vol. 34, no. 10, pp. 1678–1683, Apr. 1995.

VITA

Chien-I Lin was born in 1987 in Kaohsiung, Taiwan. He entered National Taiwan University in 2001 and received his Bachelor of Science from the Department of Electrical Engineering in 2005. He entered Georgia Institute of Technology in 2005 and received his Master of Science in 2006. Chien-I is a member of the Institute of Electrical and Electronics Engineers and the Optical Society of America.